ANALYSIS OF 11 JUNE 2003 MESOSCALE CONVECTIVE VORTEX GENESIS USING WEATHER SURVEILLANCE RADAR – 1988 DOPPLER (WSR-88D)

A Thesis

by

AMBER ELIZABETH REYNOLDS

Submitted to the Office of Graduate Studies of
Texas A&M University
in partial fulfillment of the requirements for the degree of

MASTER OF SCIENCE

December 2007

Major Subject: Atmospheric Sciences

ANALYSIS OF 11 JUNE 2003 MESOSCALE CONVECTIVE VORTEX GENESIS USING WEATHER SURVEILLANCE RADAR – 1988 DOPPLER (WSR-88D)

A Thesis

by

AMBER ELIZABETH REYNOLDS

Submitted to the Office of Graduate Studies of
Texas A&M University
in partial fulfillment of the requirements for the degree of

MASTER OF SCIENCE

Approved by:

Co-Chairs of Committee,	Larry Carey
	Fuqing Zhang
Committee Members,	Chris Davis
	Shari Yvon-Lewis
Head of Department,	Kenneth Bowman

December 2007

Major Subject: Atmospheric Sciences

ABSTRACT

Analysis of the 11 June 2003 Mesoscale Convective Vortex Genesis Using Weather Surveillance Radar – 1988 Doppler (WSR-88D). (December 2007)

Amber Elizabeth Reynolds, B.S., The Pennsylvania State University

Co-Chairs of Advisory Committee: Dr. L. Carey
Dr. F. Zhang

Mesoscale convective vortices (MCVs), which typically form within the stratiform rain of some mesoscale convective systems (MCSs), may persist for days, often regenerating convection daily. Long-lived MCVs can produce as much precipitation as a landfalling hurricane and lead to catastrophic flooding. The number of studies using multi-Doppler radar observations for validation of the kinematics, or three-dimensional (3-D) wind structure, of MCV genesis is limited. For this study, the Oklahoma City (KTLX) and Tulsa, Oklahoma (KINX) Weather Surveillance Radar – 1988 Doppler (WSR-88D) were used to examine the genesis of a long-lived MCV from 0000 to 0300 UTC on 11 June 2003. Traditional dual-Doppler techniques were used to determine the 3-D wind field. To relate MCV genesis within the associated larger MCS, time series of convective and stratiform precipitation, divergence, vertical vorticity, and vertical velocity were created for multiple levels within the MCS. The role of vertical vorticity generated in the convective region in MCV development was determined using vertical profiles of the terms in the vorticity tendency equation at 15 minute temporal resolution during the three hour period of investigation. The results of this study provide a detailed three hour examination for the initiation and early evolution of a long-lived MCV and can provide model validation of MCV generation.

DEDICATION

I would like to dedicate this work in loving memory of my grandmother, Marjorie C. Bidwell. Although she is unable to be here with me as I finish this journey, she set an example for me by pursuing her love of mathematics at a time when many women were not encouraged to follow their dreams. Thanks for encouraging me to always follow mine, Gram.

ACKNOWLEDGEMENTS

There are many people whom I wish to thank for their help and support. I would like to thank my co-chairs Larry Carey and Fuqing Zhang for both their financial and intellectual support through these last three years. I have learned a lot from each of you in your different areas of expertise in dynamics and radar meteorology which greatly contributed to a thorough discussion of my thesis subject. I would like to thank Chris Davis, Raj Pandya, and the Significant Opportunities in Atmospheric Research and Science (SOARS) Program at NCAR where this research began two summers ago. Your encouragement of my interest in atmospheric science and particularly severe storms, radar meteorology, and field projects from my time as an undergraduate definitely contributed to the scientist I have become and am becoming. I would also like to thank Shari Yvon-Lewis and Andrew Klein for their participation on my committee. Thanks for your different points of view – sometimes it really helps to take a step back and realize that as atmospheric scientists we sometimes need to clarify our thinking so that everyone can understand what we are talking about. And finally, I would like to thank my family and friends for their constant support, especially my Mom and the love of my life, Marlon. I never would have made it through the hard times if you hadn't been there for me.

TABLE OF CONTENTS

LIST OF FIGURES

FIGURE Page

FIGURE Page

FIGURE Page

1. INTRODUCTION

1.1 Mesoscale Convective Systems

A mesoscale convective system (MCS) is defined as a cloud system that occurs in connection with a group of thunderstorms that produces a continuous precipitation region on the order of 100 km in horizontal scale in at least one direction (Houze 1993). MCSs are the largest of the convective storms and contain regions of both convective and stratiform precipitation (Houze 2004). The convective region consists of intense, vertically extending cores, while the stratiform region is more uniform with lighter precipitation.

MCSs account for a large proportion of precipitation in both the tropics and midlatitudes and thus are important from a climatological standpoint (Fritsch et al. 1986). MCSs are also associated with severe weather, from flooding associated with long-lasting, slow moving precipitation, to hail, damaging straight-line winds, frequent lightning (Rutledge and MacGorman 1988; Rutledge et al. 1990), and even tornadoes. Although the rain rate in the stratiform region is less than that in the convective region, the much larger area covered by continuous stratiform rain implies a large total rainfall over the stratiform region (Houze 1993).

Large MCSs can usually be recognized in infrared (IR) satellite images by their cold cloud top (see Fig. 1.1). However, it is difficult to derive further information on the internal structure of MCSs using satellite data. The cloud top tends to be uniform, masking the structure of the storm beneath the cloud top from view. Precipitation, which

---

This thesis follows the style of *Monthly Weather Review*.

can be scanned by radar, gives the most detailed information about the three-dimensional (3-D) storm structure of MCSs. Radar has the dual advantage of both broad coverage and high resolution to capture the spatial pattern of radar reflectivity from precipitation, which is a good indicator of storm organization (Houze 1993).

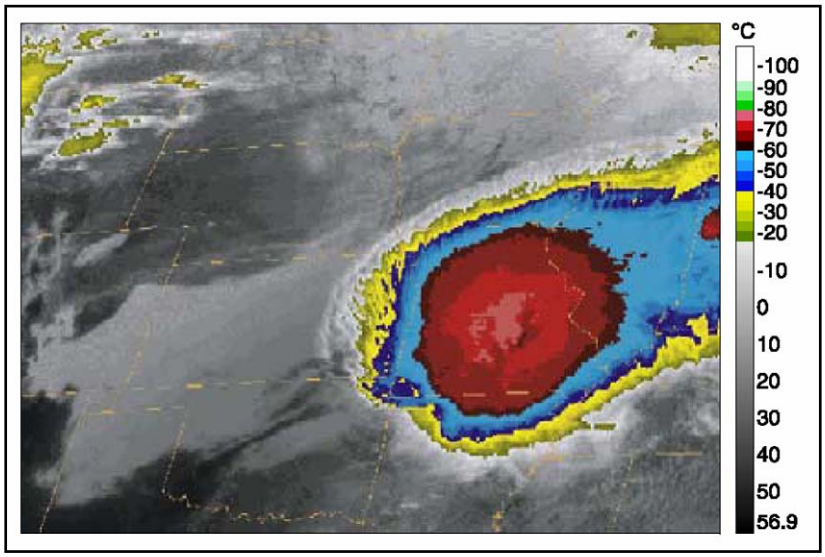

Figure 1.1. Infrared satellite image of a mesoscale convective system over Missouri (Houze 2004).

Fig. 1.2 illustrates a conceptual model of a vertical cross section through an MCS with a trailing stratiform precipitation region. The heavy dark line indicates the boundary of the storm that can be delineated by conventional weather radar. The scalloped line indicates the clouds associated with an MCS as determined from aircraft and satellite observations. Medium and dark shading indicates regions of enhanced radar reflectivity.

A general trend of upward motion starts in the boundary layer near the gust front and extends up through the convective region, where it slopes more gently into the

trailing stratiform cloud region at mid- to upper-levels. New convective cells tend to form just ahead of the leading edge of the convective region. As these developing convective cells mature, they are characterized by deep, strong reflectivity cores and are associated with heavy surface rainfall. Mature cells have a strong, narrow updraft that can overshoot the top of the broad cloud shield. Once mature cells begin to weaken, they are located at increasingly higher altitudes as they are advected rearward over a layer of dense, subsiding, storm-relative rear inflow (Houze et al. 1989).

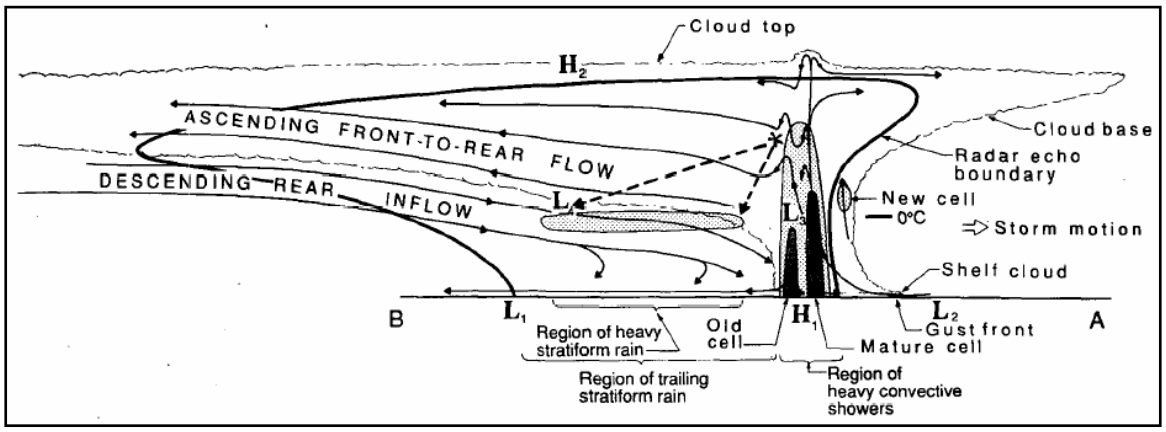

Figure 1.2. A conceptual model of the kinematic, microphysical, and radar echo structure of an MCS with a leading convective line and trailing stratiform precipitation viewed in a vertical cross section oriented perpendicular to the convective line. Moderate and strong radar reflectivity is indicated by medium and dark shading, respectively. H and L indicate areas of mesoscale positive and negative pressure perturbations, respectively. Dashed-line arrows indicate fallout trajectories of ice particles passing through the melting layer (Houze et al. 1989).

A layer of upward-sloping, front-to-rear flow that emanates from the upper portions of the convective line advects ice particles rearward. The fallspeed of the ice particles is generally larger than that of the ascending mesoscale updraft (Rutledge et al. 1988). The ice particles slowly fall as they are carried rearward in the ascending front-to-

rear flow and grow by vapor deposition. As the ice particles reach warmer air, they form aggregates. As these aggregates fall through the melting level (0°C), they develop a water coating. Water is approximately nine times more reflective than ice at microwave wavelengths, so large wet aggregates produce high reflectivity. As the aggregates continue to fall and melt, they collapse into rain drops. These drops are smaller and fall faster, so both the size of the particles and their concentration decrease, reducing radar reflectivity. These processes lead to the formation of a region of high reflectivity near the melting level, known as the "bright band" (Houze 1989).

Fig. 1.3 shows another conceptual model of a radar "bright band" (a band of high reflectivity) just below the melting level in the trailing stratiform rain region and a layer of subsiding rear-to-front flow, which enters the stratiform rain region just below the trailing stratiform cloud. As the rear inflow enters the stratiform rain region, it descends to the level of the bright band and passes through the melting level, where it finally reaches the rear of the convective line at low-levels (Houze et al. 1989; Biggerstaff and Houze 1991). The mesoscale downdraft is initiated by evaporative cooling as precipitation falls from the overlying mesoscale updraft. The melting of precipitation may also accelerate the downdraft (Leary and Houze 1979). Stratiform precipitation is also eroded by the intrusion of dry air in the midlevel rear inflow. Fig. 1.4 shows that this erosion sometimes appears as a small notch in the low-level reflectivity at the back of the stratiform rain region (Smull and Houze 1985), or, when a strong vortex is present, the southern portion of the stratiform rain region may be missing entirely. Later studies showed that linear convection with trailing stratiform precipitation often evolve from symmetric (left panel) to asymmetric (right panel) with the maturity of the MCS (Houze

et al. 1990; Parker and Johnson 2000). The presence of a vortex and asymmetric organization of precipitation often indicates a mature MCS.

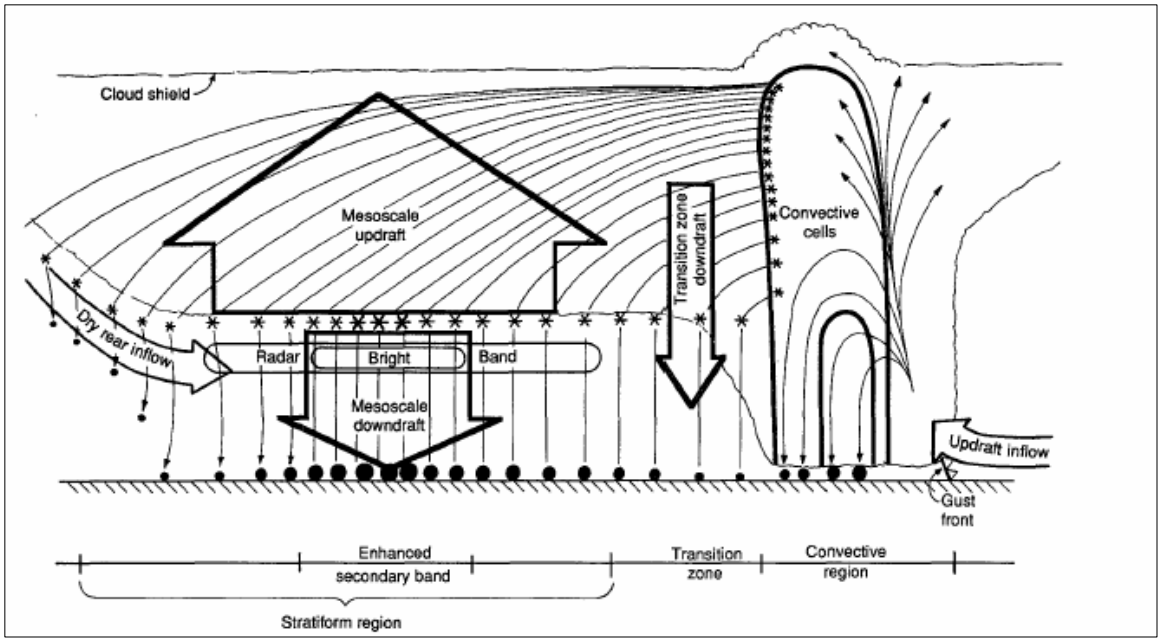

Figure 1.3. A conceptual model of hydrometeor trajectories through the stratiform region of an MCS and associated radar bright band, mesoscale updraft, and mesoscale downdraft that result from the melting of frozen precipitation (Biggerstaff and Houze 1991).

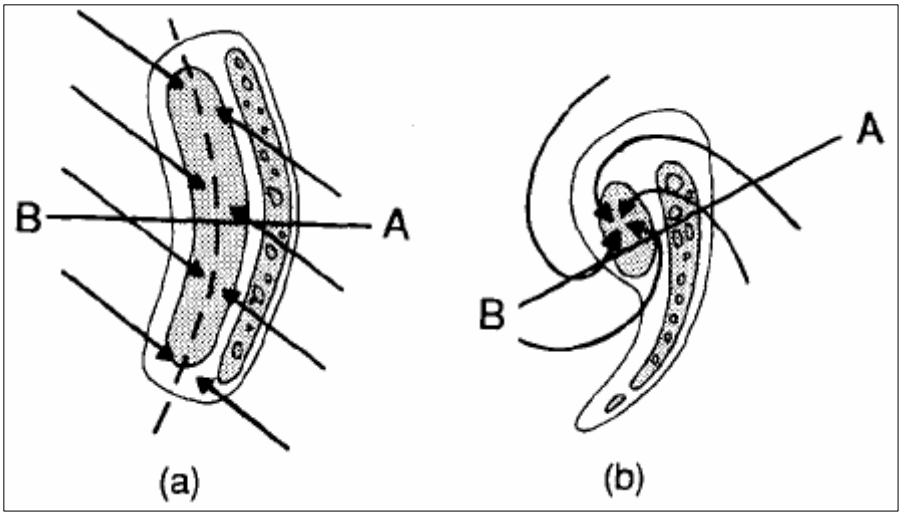

Figure 1.4. A conceptual model of mid-level horizontal storm-relative flow and low-level radar reflectivity through (a) a two-dimensional MCS, and (b) an MCS with a well-defined mesoscale vortex in the stratiform rain region. Shading indicates regions of higher reflectivity (Houze et al. 1989).

A six-year radar climatology of MCSs that occurred during the spring in Oklahoma (Houze 1990) gave the following characteristics to the leading convective line:

1. Arc shaped and convex toward the leading edge.
2. Oriented generally from the northeast to southwest.
3. Storm motion with an east and/or south component.
4. A series of intense reflectivity cells connected by an echo of moderate intensity.
5. Strong reflectivity gradient at the leading edge of the convective region.
6. The leading edge of the convective region is also non-uniform as new cells are continuously formed and integrated into the leading line.

The trailing stratiform region, however, has the following characteristics:

1. Large size ($>10^4$ km^2 in horizontal area).
2. Notch-like concavity of reflectivity at the rear edge of the stratiform region caused by the entrainment of dry air.
3. A second relative maximum in reflectivity which is separated from the convective line by a channel of low reflectivity, called the transition zone.

The dynamics of MCSs are often more complex than those of individual or lines of thunderstorms because additional phenomena appear when thunderstorms group together in these cloud systems. In particular, MCSs often contain a large region of stratiform precipitation. As MCSs mature, mesoscale circulations tend to develop within the stratiform region.

1.2 Mesoscale Convective Vortices

On occasion mesoscale convective vortices (MCVs) are observed within the stratiform rain region of MCSs (Brandes 1990). Although most MCVs dissipate as the parent MCS decays, there are occasions in which the MCV can persist long after the parent MCS dissipates and even retrigger convection (Zhang and Fritsch 1987; Bartels and Maddox 1991; Trier and Davis 2007). They can initiate and focus subsequent heavy rainfall, which can lead to flooding with local amounts in excess of 200 mm over swaths of 1000 km or more. Fig. 1.5 shows an example of a long-lived MCV that occurred from 20 to 22 August 1998. The swirling cloud pattern evident in visible satellite imagery (Figure 1.5a) is the signature of an MCV spawned by an MCS that occurred the previous evening. By late afternoon, convection formed near the MCV center (Figure 1.5b), moved eastward (Figure 1.5c), and evolved into another MCS before dissipating the following evening. Mesoscale convection redeveloped overnight near the remnant vortex and left another MCV in its wake the following day (Figure 1.5d). Convection over eastern Nebraska during the early morning hours of 21 August was associated with reports of widespread flash flooding (Trier et al. 2000).

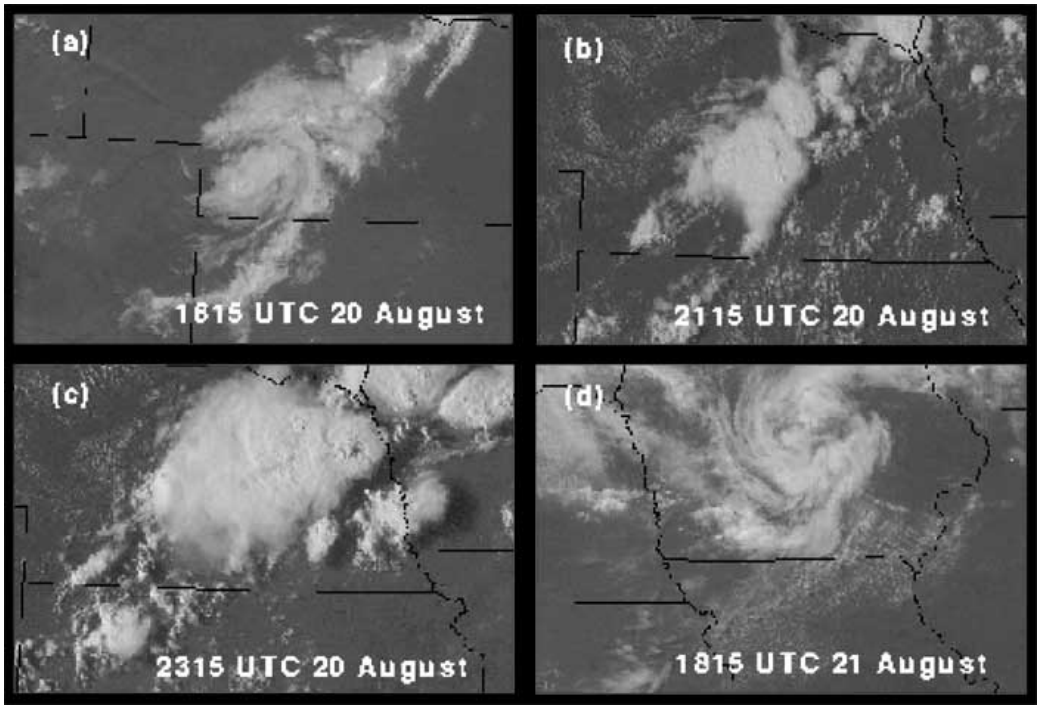

Figure 1.5. GOES-8 visible satellite imagery depicting a long-lived MCV at (a) 1615 UTC 20 August, (b) 2115 UTC 20 August, (c) 2315 UTC 20 August, and (d) 1815 UTC 21 August 1998. (Adapted from Trier et al. 2000.)

Fig. 1.6 shows the evolution of an MCS and an associated MCV at the (a) initial stage, (b) MCV genesis stage, and (c) MCV intensification stage (Chen and Frank 1993). Once a well developed stratiform rain region forms, MCV generation can occur and forms near the cloud base in the well developed stratiform rain region of the MCS. Figure 1.7 is a schematic showing how an MCS generates a mature MCV (Johnson and Bartels 1992). Initially, at time *t*, the precipitation is characterized by a leading convective line and trailing stratiform region. Within a shortwave trough at 500 mb, cyclonic circulation then developed. Convergence produced by vorticity at mid-levels, associated with front-to-rear flow ahead of the system and a rear-inflow jet behind, contributed to an intensification of the MCV. At time *t*, the MCV was confined to the mid-troposphere

between 3 and 8 km and was positioned above the cold pool produced by evaporation of precipitation in the stratiform region. The cold pool produced an area of localized high pressure behind the leading convective line, often called a mesohigh. Four hours later (*t* + *4h*), the storm completely dissipated and precipitation ceased, but the cyclonic circulation at 500 mb persisted and expanded. In addition, a pronounced surface low developed beneath the MCV, which may indicate that MCV amplification can cause cyclonic vorticity at mid-levels to grow downward to the surface.

Long-lived midlatitude MCSs that tend to produce MCVs are often observed in weak, shallow shear and high convective available potential energy (CAPE) (i.e., 2500 J kg^{-1}) environments (Skamarock et al 1994). CAPE is the amount of energy a parcel of air would have if lifted from the level of free convection (LFC) to the equilibrium level (EL) vertically through the atmosphere. CAPE is measured in joules per kilogram of air (J/kg). Any value greater than 0 J/kg indicates instability and the possibility of thunderstorms, while values less than 0 J/kg indicate stability or convective inhibition (CIN). CAPE is calculated by integrating vertically the local buoyancy of a parcel from the LFC to the level of neutral buoyancy (EL):

$$CAPE = \int_{z_f}^{z_n} g\left(\frac{T_{parcel} - T_{env}}{T_{env}}\right) dz \qquad (1.1)$$

where z_f and z_n are, respectively, the heights of the levels of free convection and neutral buoyancy, T_{parcel} and T_{env} are the air temperatures, respectively, of the specific parcel and the environment, and g is the acceleration due to gravity. CAPE for a given region is most often calculated from a thermodynamic or sounding diagram (e.g., a skew-T thermodynamic diagram) using air temperature and humidity data measured by a weather balloon.

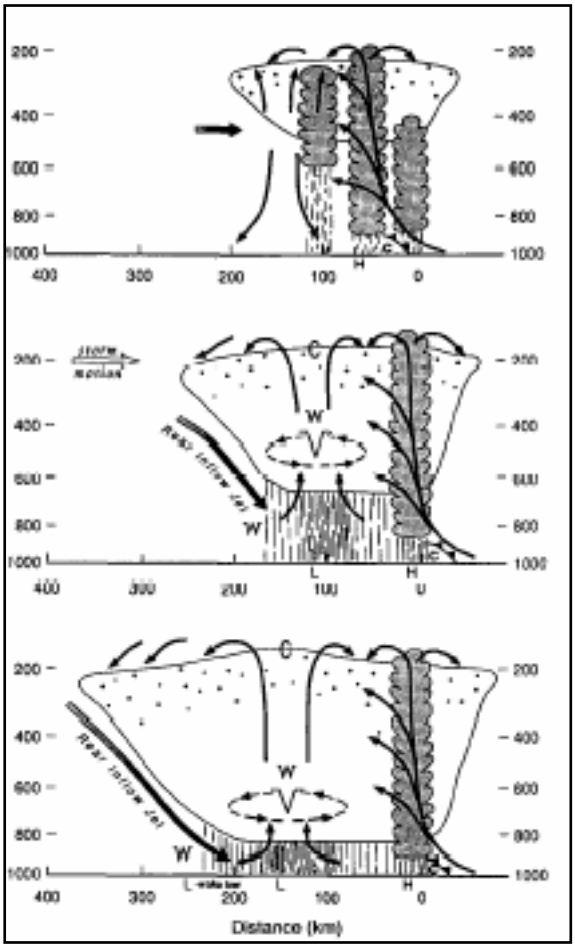

Figure 1.6. Diagram of an MCS structure with a leading convective line (dark shading) and the trailing stratiform rain region (outlined). The associated MCV is shown at the (a) initial stage, (b) genesis stage, and (c) intensification stage. The solid arrows indicate mesoscale circulation. Positive and negative temperature anomalies are shown as W and C, respectively; the mid-level MCV is denoted by a V with dashed arrows (Chen and Frank 1993).

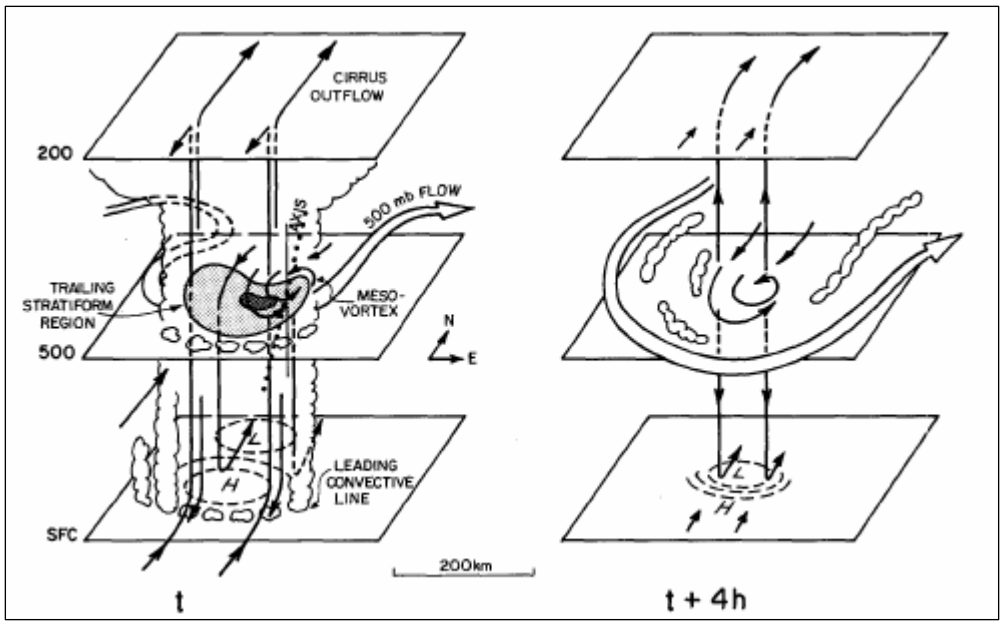

Figure 1.7. Idealized cloud and system-relative flow structure during decaying convective line stage (*t*) and fully developed MCV stage (*t + 4h*). Solid arrows denote storm-relative flow, and open arrows denote large-scale 500 mb flow (Johnson and Bartels 1992).

Bartels and Maddox (1991) found that MCVs were favored by weak background flow and relative vorticity, weak vertical shear, and strong gradients of humidity from a satellite-based climatology of MCVs over the United States and associated sounding data. Trier et al. (2002) found that CAPE averaged 1895 J kg^{-1} among MCVs that fostered a second MCS. In the five cases studied in Davis and Trier (2007), which includes the 11 June 2003 case studied here, the environments were characterized by weak shear and widespread conditional instability with values of convective available potential energy in excess of 2000 J kg^{-1}.

Skamarock et al (1994) showed that trailing "bookend" vortices form on each end of a squall line and that a midlatitude cyclonic MCV can develop from a bookend vortex

which is favored by the Coriolis force. Fig. 1.8 shows a conceptual model of an MCS that evolved with and without Coriolis forcing.

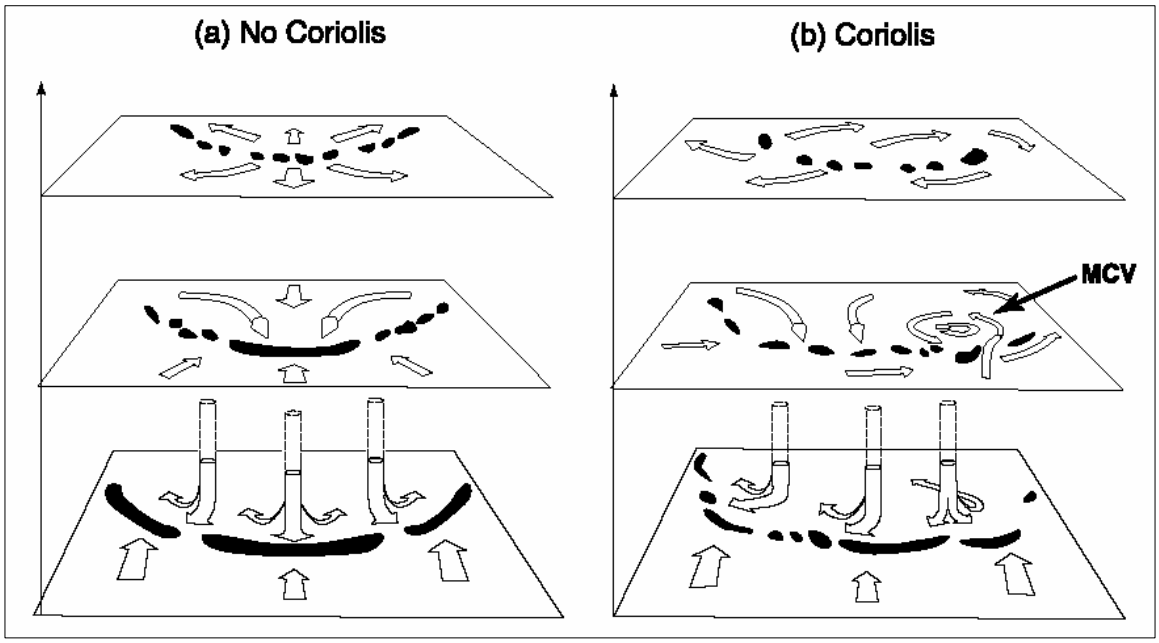

Figure 1.8. A conceptual model of a Northern Hemisphere MCS that has evolved with and without Coriolis forcing. The view is from standing in front of the MCS as it progresses toward the viewer. The planes represent surface, middle, and upper level cross sections of the storm. Two-dimensional arrows denote flow in the plane, while three-dimensional tubes denote vertical air motion. Solid areas denote regions of convection (Adapted from Skamarock et al. 1994).

Raymond and Jiang (1990) provided a theoretical framework for long-lived MCSs associated with MCVs. They suggested that an environment of weak mid-level shear but stronger low-level shear (as observed by Bartels and Maddox 1991) could support a mesoscale circulation within an MCS. The circulation consisted of a warm core vortex characterized by a positive potential vorticity (PV) anomaly (i.e., MCV) in middle levels beneath a negative potential vorticity anomaly at upper-levels. The idealized MCV was

located above a cold pool formed by precipitation evaporation and melting associated with the MCS. Raymond and Jiang (1990) further postulated that lifting associated with positive PV anomalies in vertical shear may explain some cases of long-lived MCVs. In addition to generally exhibiting a warm core, MCVs are characterized by low- and mid-level cyclonic rotation associated with positive PV anomalies and capped by an anticyclonic circulation at high levels associated with negative PV anomalies (Brandes 1990; Verlinde and Cotton 1990; Knievel and Johnson 2002).

Fritsch et al. (1994) combined concepts from Raymond and Jiang (1990) and their own mesoanalysis of a major MCS. They found that the MCV that developed in the stratiform region of the MCS grew larger and was much longer lived than the parent MCS. Their results suggested that long-lived MCVs may achieve a state of near balanced flow. Thus, in some extreme cases, an MCS can foster the development of a long-lived MCV that can, in turn, support the development of new MCSs.

Research in the past two decades has yielded dramatic advances in understanding MCVs, such as the heightened awareness among forecasters to the strong relevance of MCVs triggering convection which exceeds previous precipitation forecasts (Davis et al. 2002). Despite such advances in the understanding of MCVs, several important aspects of MCVs remain poorly understood. These include: the development of MCVs within organized MCSs, the redevelopment of convection or lack thereof within MCV cases, the feedback of convective redevelopment on MCV lifecycles, and how MCV amplification may cause cyclonic vorticity at mid-levels to grow downward to the surface.

To gain a better understanding of MCVs, the Bow Echo and MCV Experiment (BAMEX) field project sampled numerous MCSs at high spatial and temporal resolution

(Davis et al. 2004). One of the two primary objectives of BAMEX was to observe the spectrum of circulation structures believed to exist within MCSs and to document their life cycles (Davis and Trier 2007). The emphasis was on vortices with length scales between 50 and 200 km, although a broad spectrum of characteristic length scales has been identified within MCSs (Wakimoto et al. 2006).

The number of studies using multi-Doppler radar observations for validation of the kinematics, or three-dimensional (3D) wind structure, of MCV genesis is limited. The modeling studies of Weisman (1993), Davis and Weisman (1994), Skamarock et al. (1994), and Weisman and Davis (1998) proposed that tilting of horizontal vorticity into the vertical by convective updrafts is the primary mechanism for the genesis of MCV circulations, which are subsequently enhanced by horizontal convergence. Here the simulated convection resembles the frequently observed asymmetric squall-type MCS (Houze et al. 1989, 1990; Blanchard 1990; Loehrer and Johnson 1995), which consists of a leading convective region followed by an expansive region of stratiform precipitation on its poleward end, wherein the MCV develops. However, while convective organization is common, the few published observations of MCVs spawned from this type of MCS (Brandes 1990; Scott and Rutledge 1995; Knievel and Johnson 2002) have lacked the spatial and temporal data coverage to confirm the basic vorticity generation mechanisms deduced from the simulations. Clearly, additional observations of MCVs in their formative stages are required to improve the understanding and relative importance of convective and stratiform processes influencing the formation and longevity of MCVs.

1.3 Synoptic Overview of 11 June 2003 Case

The synoptic environment in the South Plains of the 11 June 2003 case was conducive to MCV formation with moderate to high levels of convective instability and weak shear at low-levels as shown in Raymond and Jiang (1990) and Fritsch et al. (1994). The precursors to the MCV were two nocturnal MCSs which occurred on consecutive nights, both triggered by a shortwave disturbance embedded within the subtropical jet (Galarneau and Bosart 2005). As shown by Davis and Trier (2007), the first MCS formed over eastern New Mexico on the evening of 9 June and produced an MCV over western Texas in the early morning hours of 10 June (Figure 1.9). This vortex moved northeastward over western Oklahoma and new convection developed northwest of Norman, OK around 0000 UTC 11 June and evolved into another MCS overnight.

Fig.1.10 shows a composite map of infrared satellite imagery, low-level radar reflectivity, and surface analyses valid at 0000 UTC 11 June 2003. The MCS in which the MCV developed initiated ahead of a frontal boundary which extended from the Minnesota/Wisconsin border into eastern Iowa and Missouri and further south into the panhandles of Oklahoma and Texas. Similar to what Trier et al. (2000) found, the MCS that generated the 11 June 2003 MCV formed near a synoptic surface front. There was strong advection of warm, moist air from the south into the environment where MCV genesis occurred which can be seen from the stations in Norman, Oklahoma (temperature: 82°F; dew point: 65°F) and Dallas/Fort Worth (temperature: 86°F; dew point: 69°F). Fig. 1.11 shows an 850 mb forecast analysis in which a low-level jet with 25 knot southerly winds advected air with high (60 to 90%) relative humidity into the environment where the 11 June 2003 MCV formed. Fig. 1.12 shows surface to 3 km wind

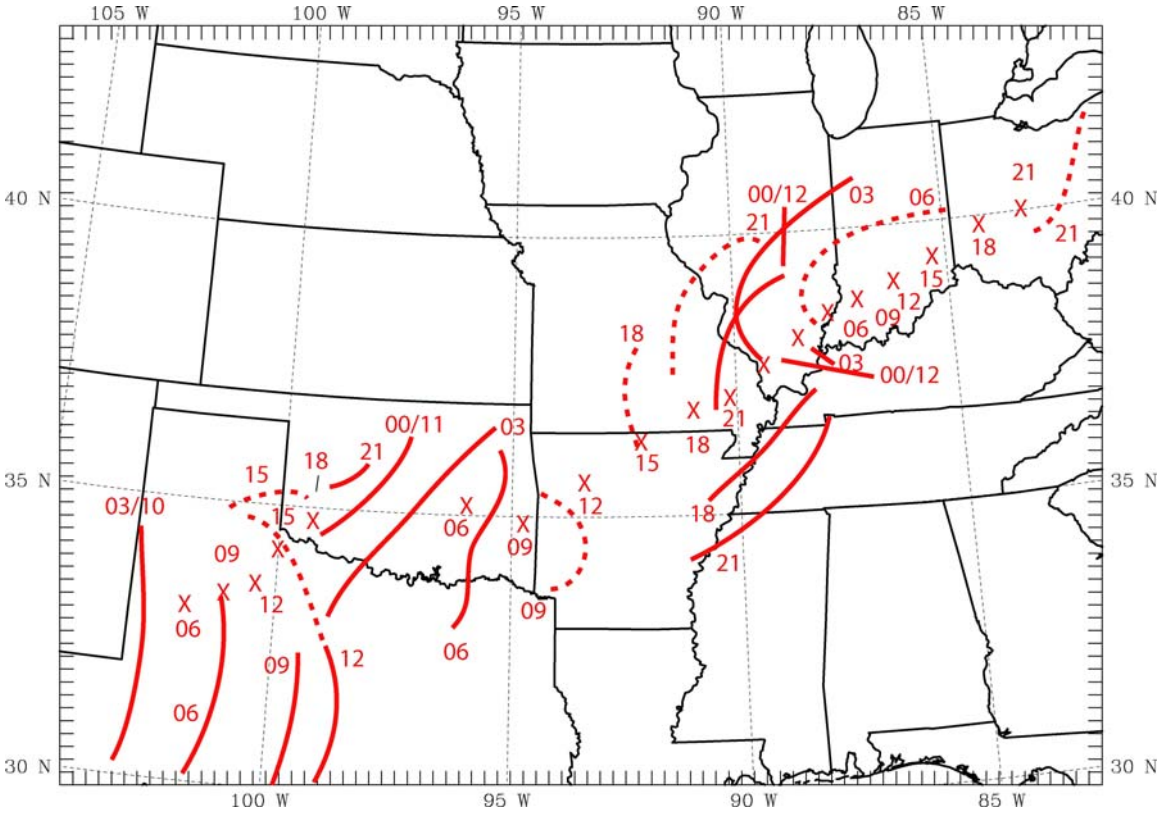

Figure 1.9. Isochrones of leading convective lines (solid = solid line of reflectivity > 40 dBZ, dashed = broken line consisting of cells with reflectivity > 40 dBZ) and positions of MCV (X's) at 3 hour intervals for the 11 June 2003 MCV. Two digit numerical labels refer to time (UTC), while the first symbol of the day is marked by both hour and day (HH/DD) (Davis and Trier 2007).

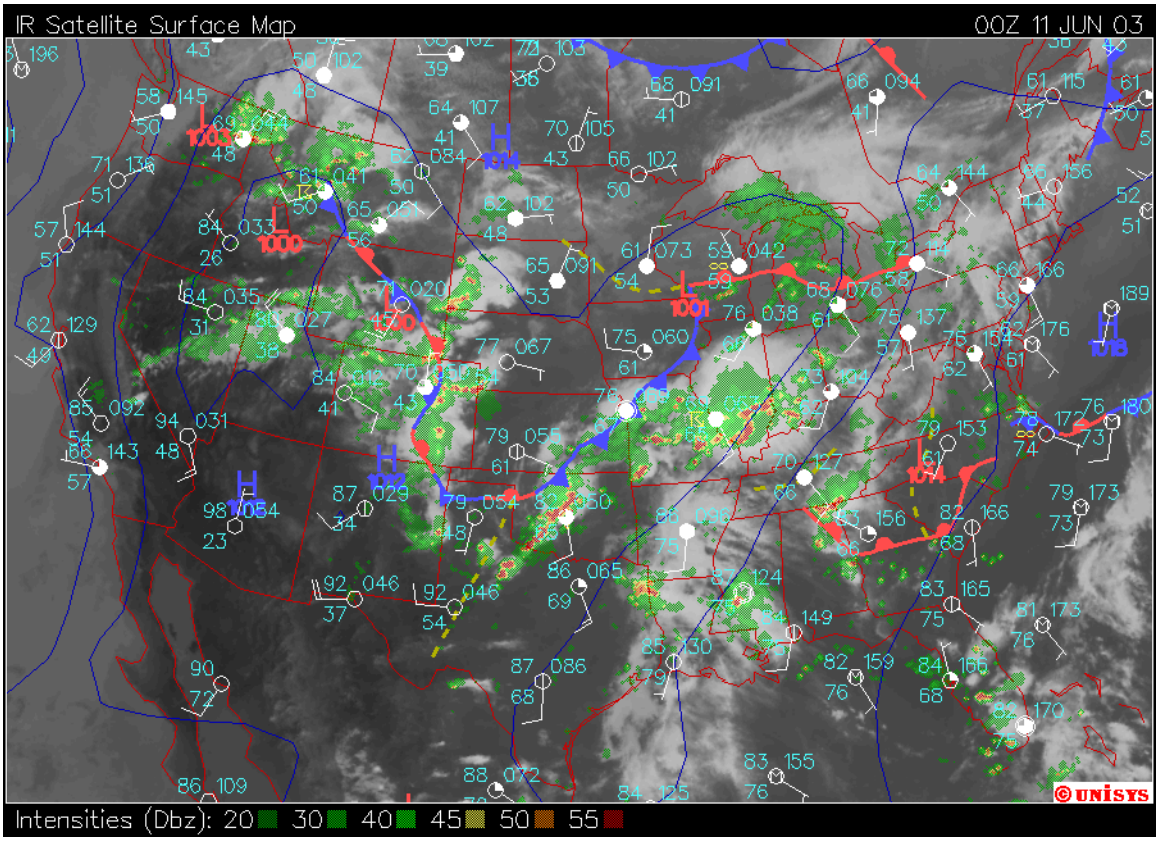

Figure 1.10. An infrared satellite, radar, and surface analysis of the synoptic environment valid at 0000 UTC 11 June 2003 (Courtesy of UNISYS).

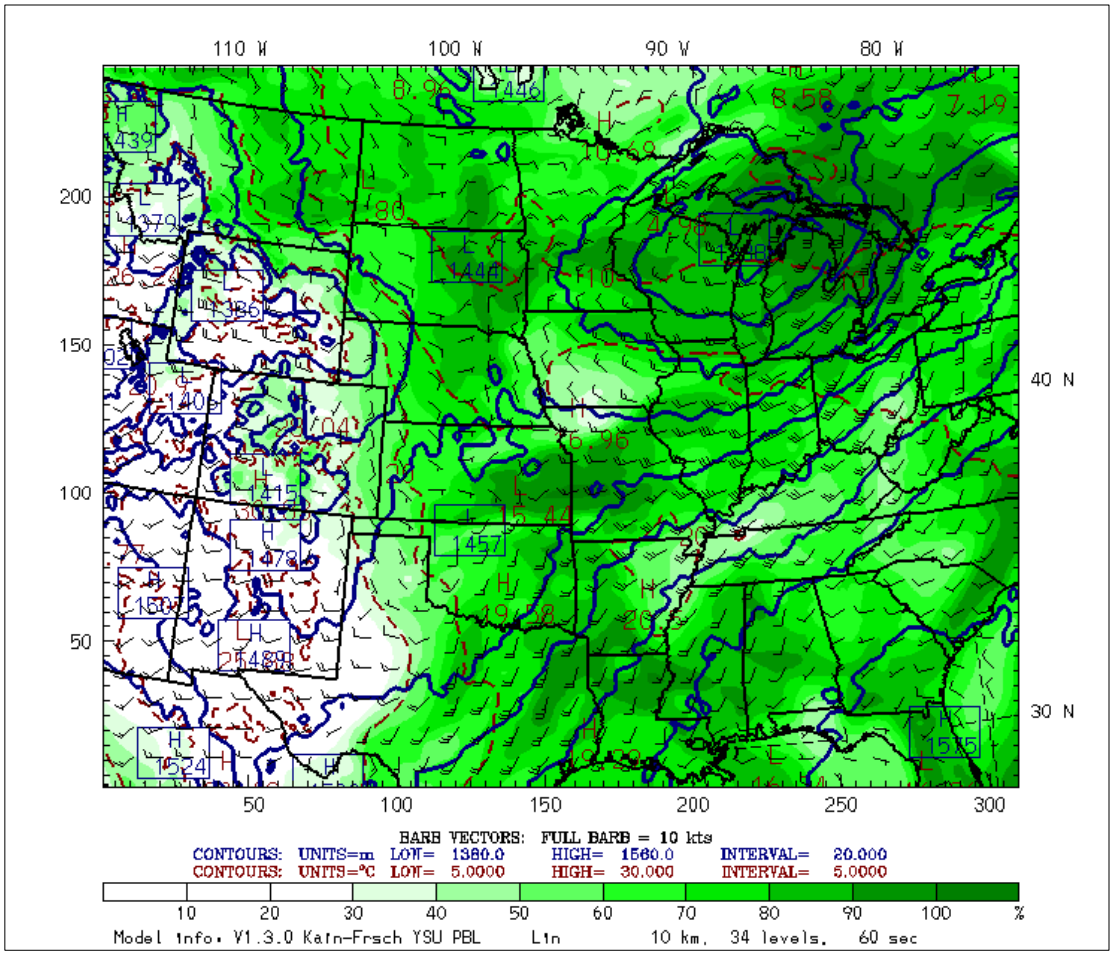

Figure 1.11. 850 mb WRF 10 km resolution forecast model for 0000 UTC 11 June 2003. Relative humidity with respect to water is shaded green, temperature is denoted by brown dashed lines, geopotential heights are marked by blue lines, and wind vectors are in black (Courtesy of Model/Forecast Products from JOSS/BAMEX field catalog).

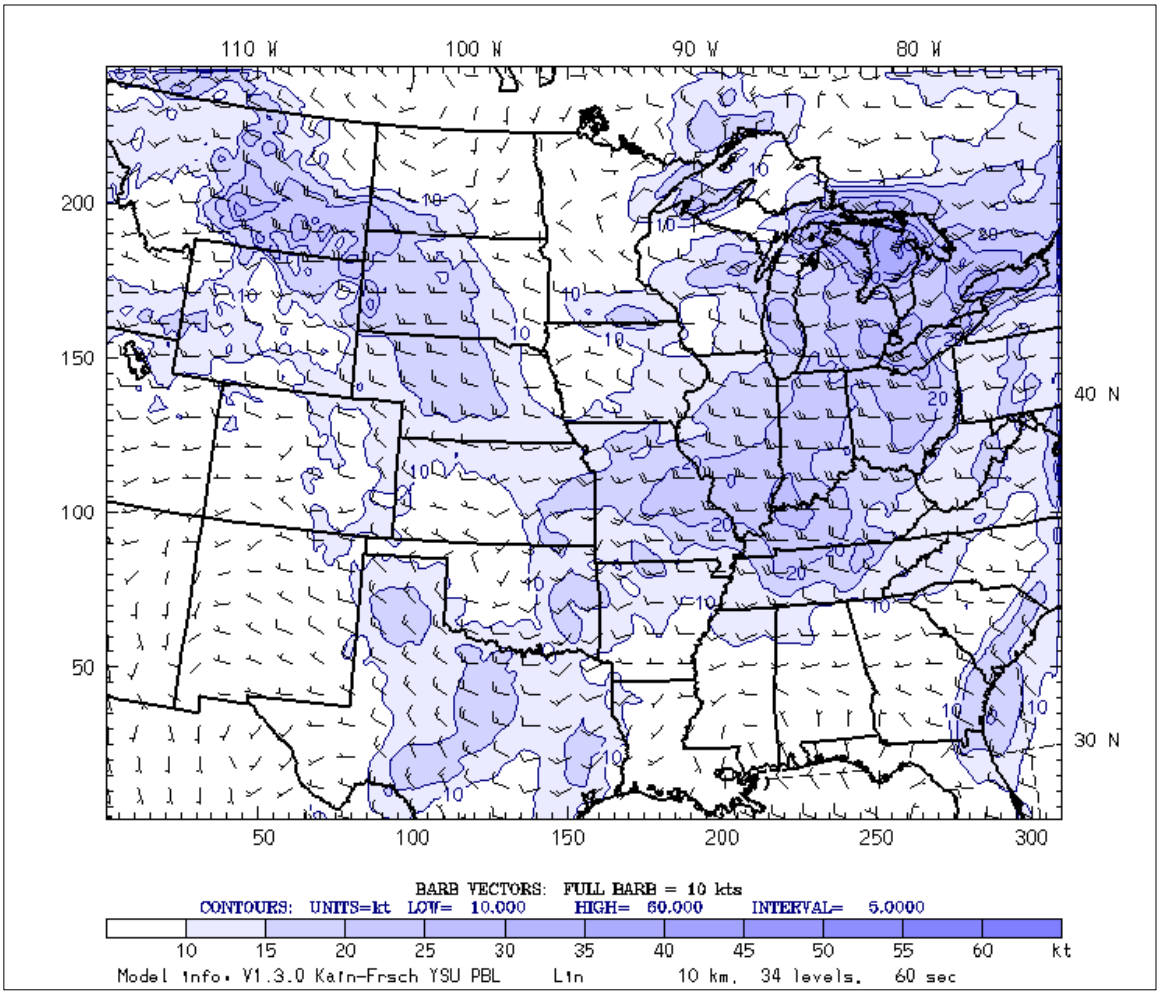

Figure 1.12. Surface to 3 km wind shear WRF 10 km resolution forecast model for 0000 UTC 11 June 2003. Surface to 3 km shear is shaded in light blue and shear vectors are in black (Courtesy of Model/Forecast Products from JOSS/BAMEX field catalog).

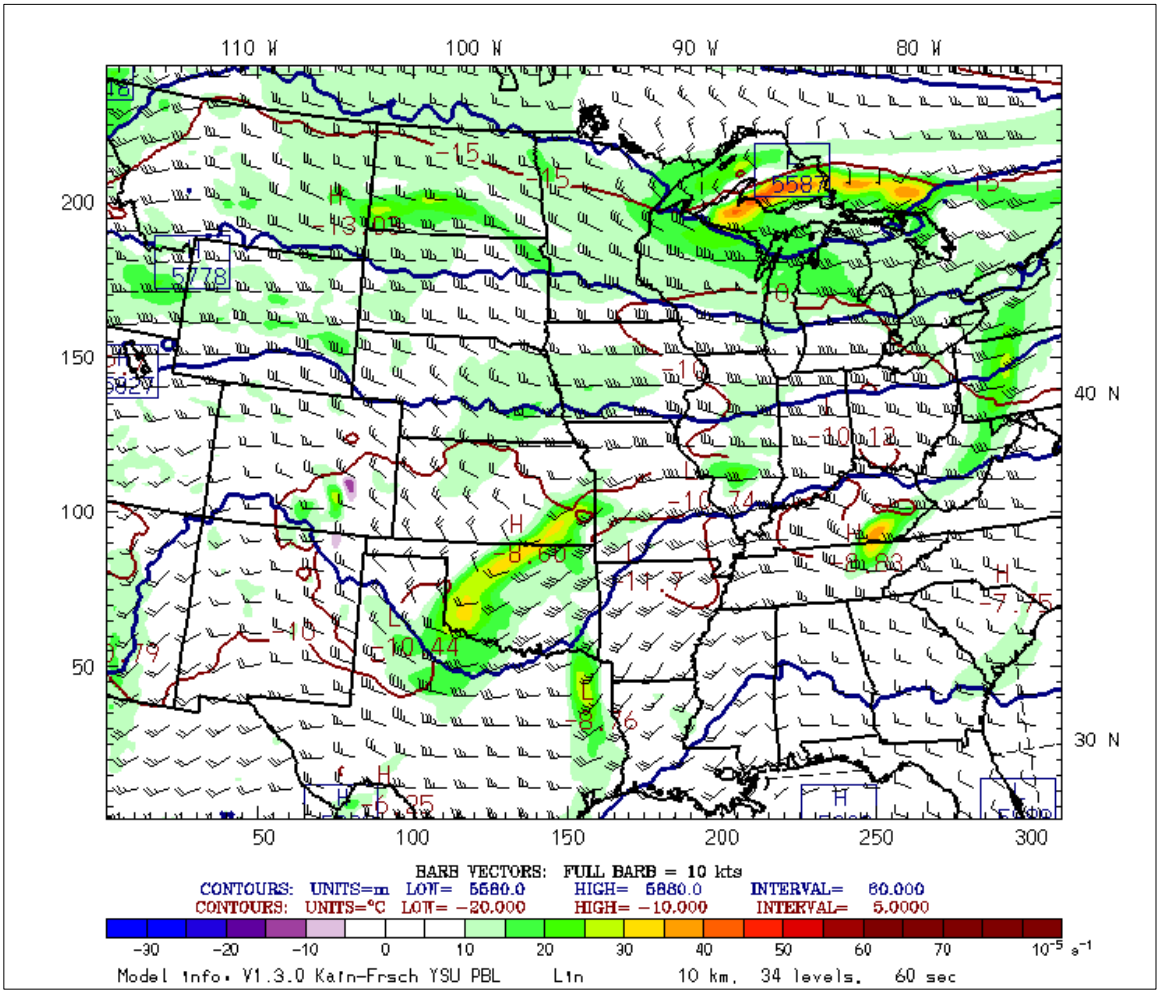

Figure 1.13. 500 mb WRF 10 km resolution forecast model for 0000 UTC 11 June 2003. Absolute vorticity is shaded, temperature is indicated by brown lines, geopotential heights are blue lines, and wind vectors are in black (Courtesy of Model/Forecast Products from JOSS/BAMEX field catalog).

shear. Similar to what Raymond and Jiang (1990) hypothesized and found by others (e.g., Bartels and Maddox 1991), the 11 June 2003 MCV formed in a region of <10 knot shear in western Oklahoma. Fig. 1.13 shows a 500 mb forecast analysis where the MCV developed within a shortwave trough with high absolute vorticity.

Fig. 1.14 is the 0000 UTC 11 June 2003 sounding from station KOUN in Norman, Oklahoma. The environment in which the MCV formed was characterized by nearly 2000 J kg^{-1} of CAPE and weak flow from the surface to 700 mb (3 km) as discussed above. Fig. 1.15 and 1.16 show model predictions for values of CAPE and CIN for the environment in which the 11 June 2003 MCV formed. In northwestern Oklahoma, the environment produced CAPE values of approximately 1500 J kg^{-1}. The region also lacked strong shear from the surface to 6 km which is also conducive to MCV formation. The 11 June 2003 MCV formed in an area of northwestern Oklahoma just ahead of higher values of CIN in a region characterized by only 0 to 25 J kg^{-1} of CIN as shown in Fig. 1.16.

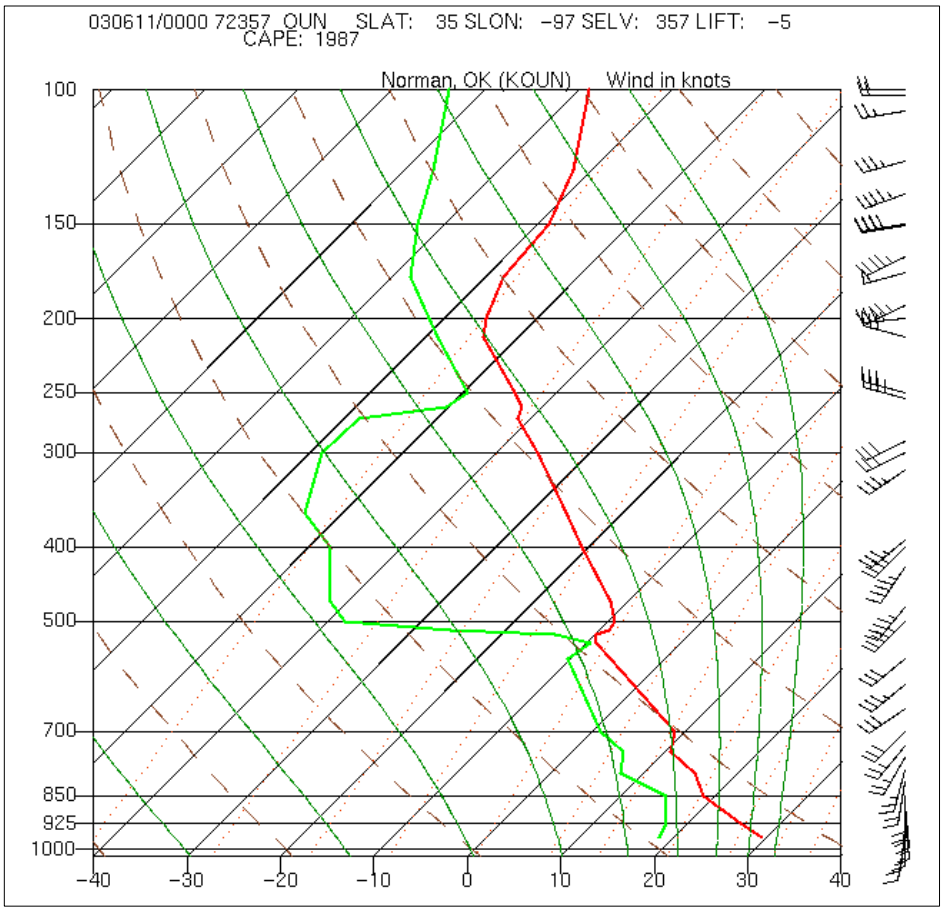

Figure 1.14. 0000 UTC 11 June 2003 skew-T diagram from Norman, OK (Courtesy of Operational Products from JOSS/BAMEX field catalog).

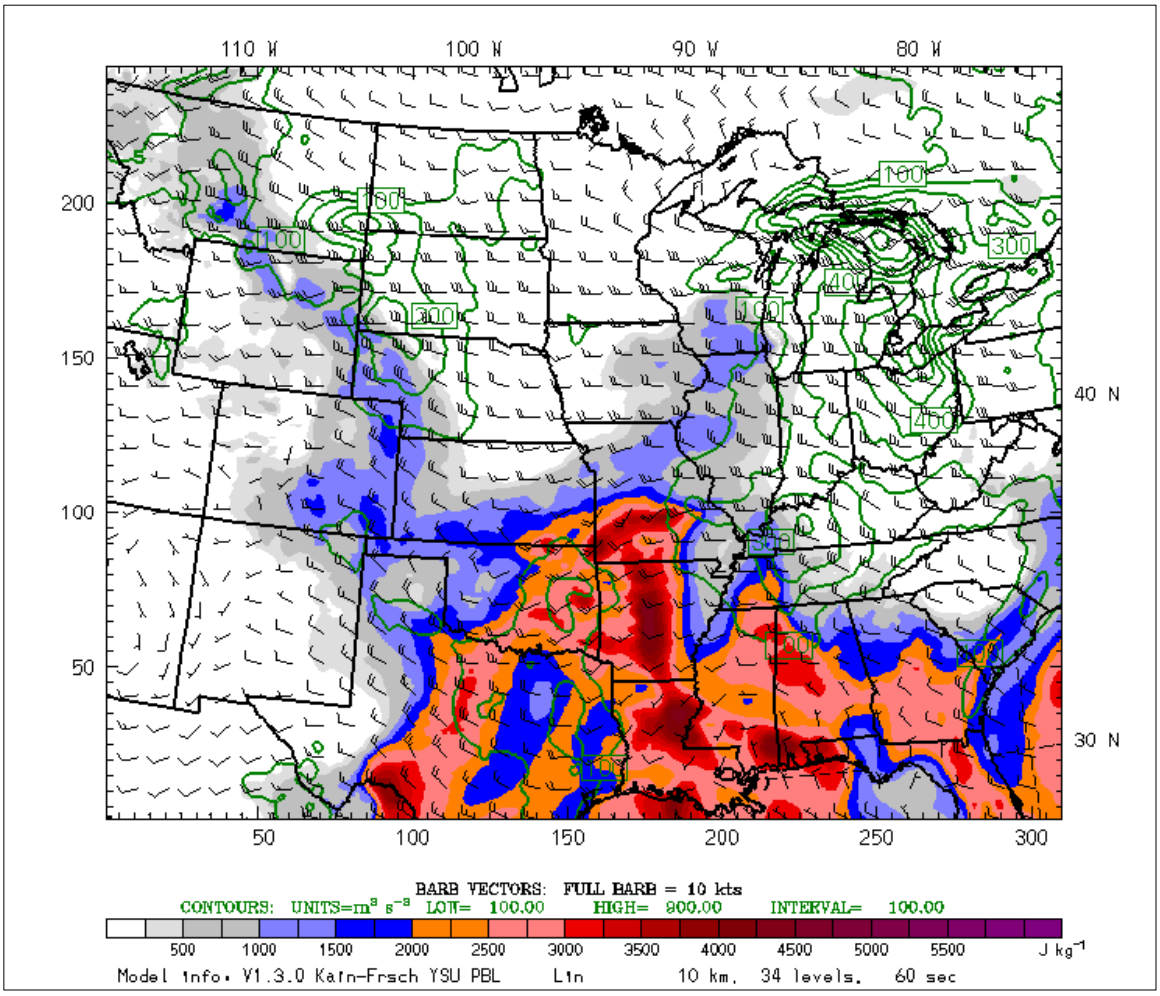

Figure 1.15. Surface based CAPE WRF 10 km resolution forecast model for 0000 UTC 11 June 2003. CAPE (J kg^{-1}) is shaded, surface to 3 km storm relative helicity (m^3 s^{-3}) is contoured in green, and surface to 6 km wind shear vectors are in black (Courtesy of Model/Forecast Products from JOSS/BAMEX field catalog).

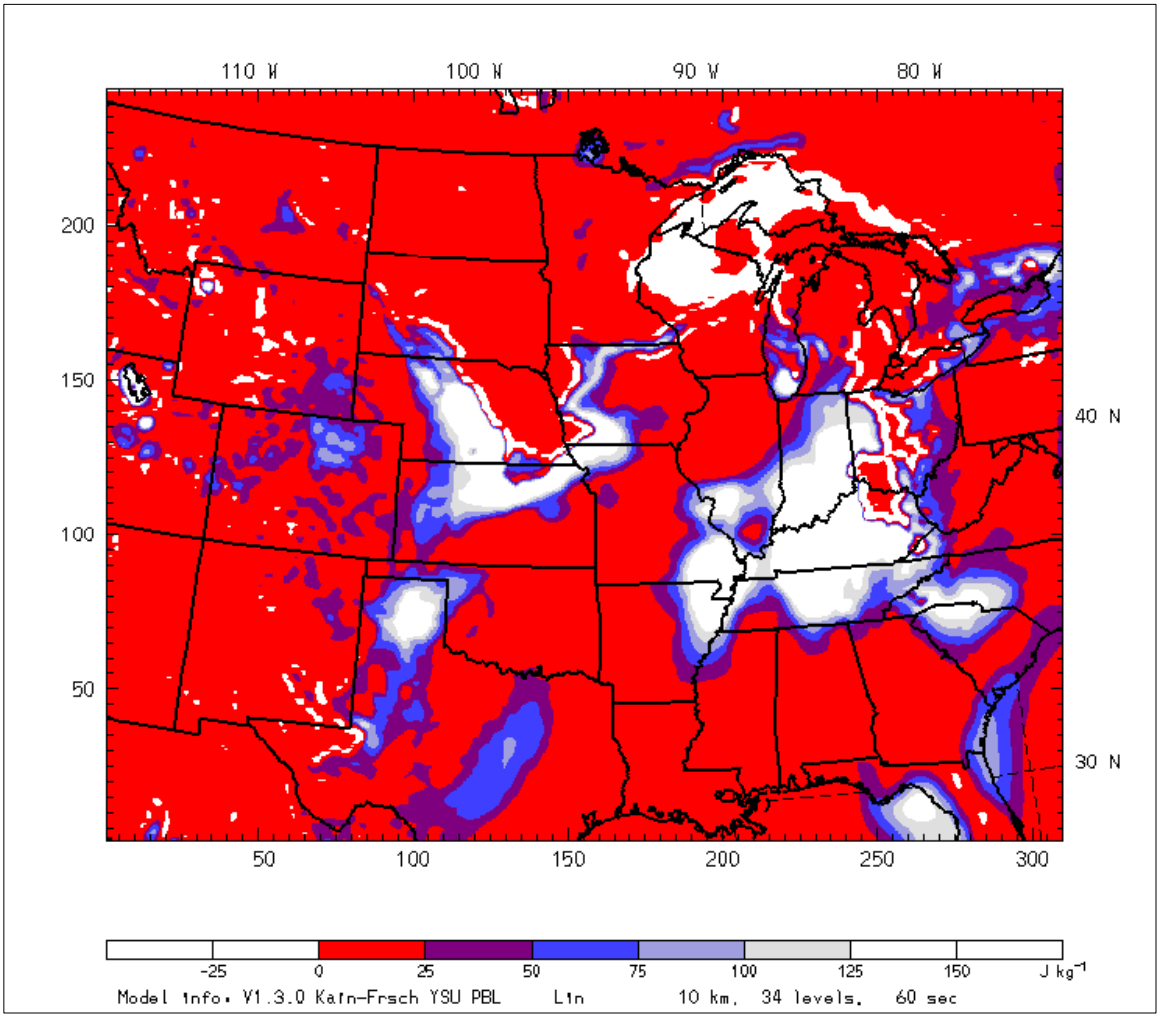

Figure 1.16. Surface based CIN WRF 10 km resolution forecast model for 0000 UTC 11 June 2003. CIN (J kg^{-1}) is shaded (Courtesy of Model/Forecast Products from JOSS/BAMEX field catalog).

1.4 Scientific Objectives and Hypothesis

The main hypothesis is that vorticity generated in the convective leading line is advected rearward and causes the rapid formation and enhancement of the 11 June 2003 MCV. The objective is to document the development of the 11 June 2003 MCV within an organized MCS and to verify the proposed basic vorticity generation mechanisms from previous numerical simulations and observational studies. This will be accomplished by relating MCS internal structure, with particular focus on mesoscale horizontal and vertical motion fields, to the MCV genesis and evolution. The objectives to document the mesoscale development of the 11 June 2003 MCV, relate MCV genesis to the overall MCS environment, and to verify the vertical vorticity generation mechanisms are listed in the next three subsections.

1.4.1 Document Mesoscale Development of 11 June 2003 MCV

During the time of initial MCV formation, airborne Doppler radar platforms were not available so it is necessary to rely on two radars from the WSR-88D network to determine the 3D wind structure in the developing MCV. For this study, the Oklahoma City (KTLX) and Tulsa, Oklahoma (KINX) WSR-88D were used to examine the genesis of a long-lived MCV from 0000 UTC to 0300 UTC on 11 June 2003. This case presents a unique opportunity to resolve mesoscale circulation within the developing 11 June 2003 MCV using the KTLX and KINX WSR-88D radars which have a baseline of 180.7 km. Due to the rapid formation of the MCV at early times during the analysis, high temporal resolution analyses were created at fifteen minute increments for the 0000 to 0300 UTC time period. Contours of positive vertical vorticity were created at 1.0, 4.5, and 7.0 km. North-south vertical transects were also taken of the MCV from x = -15.0 km (with

respect to KTLX) to x = 30.0 km. East-West vertical transects were also taken along y = 100.0 (again, with respect to KTLX) as the MCV propagated approximately eastward for each fifteen minute interval between 0000 and 0300 UTC.

1.4.2 Document Quantitative Changes in Reflectivity, Divergence, Vorticity, and Vertical Velocity within MCS

To relate MCV genesis within the trailing stratiform region of the associated larger MCS, time series of convective and stratiform precipitation and average divergence, vertical vorticity, and vertical velocity were created for multiple levels in the MCS. Low-level is defined, in this case, as 1.0 to 3.0 km. Mid-level is defined as 4.5 to 7.0 km, and upper-level is represented by 10.0 km.

1.4.3 Investigation of Mechanisms Responsible for Generation of Vertical Vorticity within MCV

To better understand the role of convection in MCV development, a budget may be formulated to evaluate various terms in the vorticity tendency equation using 3D wind fields derived from dual-Doppler analyses. According to the vertical vorticity tendency equation:

$$\frac{\partial \zeta}{\partial t} = -\left(u\frac{\partial \zeta}{\partial x} + v\frac{\partial \zeta}{\partial y}\right) - w\frac{\partial \zeta}{\partial z} - (\zeta + f)\left(\frac{\partial u}{\partial x} + \frac{\partial v}{\partial y}\right) - \left(\frac{\partial w}{\partial x}\frac{\partial v}{\partial z} - \frac{\partial w}{\partial y}\frac{\partial u}{\partial z}\right) + \frac{1}{\rho^2}\left(\frac{\partial \rho}{\partial x}\frac{\partial p}{\partial y} - \frac{\partial \rho}{\partial y}\frac{\partial p}{\partial x}\right) \quad (1.2)$$

LC HADV VADV DIV TILT SOL

where u, v, and w are the three components of the wind; p is the pressure; ρ is air density; and ζ is the vertical component of relative vorticity. If friction is ignored, then the local change (LC) in vertical vorticity within an MCV must originate from some combination of horizontal advection of vorticity (HADV), vertical advection of vorticity (VADV), the divergence (or stretching) term (DIV) which represents amplification/reduction of

preexisting vertical vorticity by horizontal convergence/divergence, and the tilting term (TILT) which represents the vertical vorticity created by tilting horizontal vorticity with vertical motion (Scott and Rutledge 1995; Yu et al. 1999; Knievel and Johnson 2003). The solenoidal term (SOL) can be ignored in this case, as it is assumed to be on the order of 10^3 times smaller than the other terms in the equation (Skamarock et al. 1994). All other terms on the right-hand side of Equation 1 can be calculated at each grid point within the dual-Doppler analysis domain. The sum of four terms therefore represents the estimated magnitude of the local change of vorticity at each grid point. An estimate of the domain average for each term may be obtained by taking the arithmetic mean over the area of analysis at each level.

Figs. 1.17 and 1.18 show examples of vorticity budgets created for previous work on other MCVs. Fig. 1.17 shows vertical profiles of domain-averaged values of various terms in the vorticity budget for an MCV that occurred from 1520-1529 UTC 16 June 1987. Yu et al. (1999) found that contrary to previously documented MCVs, which have generally been fully developed and observed in the stratiform region of mature MCSs, the vorticity budgets suggested that the mechanisms responsible for the formation of a long-lived MCV are related to the convective, rather than stratiform, precipitation of the developing MCS. According to domain averaged vorticity budgets, Yu et al. (1999) concluded that vertical stretching in the convective region was a primary mechanism contributing to the development of a vortex at low-levels and that the source of vertical vorticity contributing to the initiation of the MCV was likely tilting of horizontal vorticity in the convective region. The vorticity budgets shown in Figure 1.18 from Knievel and Johnson (2003) suggest that tilting may have been mostly responsible for the formation

of the 1 August 1996 MCV, although the vortex's origin could not be proved. Their results were consistent with Zhang (1992), whose simulated MCV began primarily from tilting, and then in maturity strengthened from convergence. Bartels and Maddox (1991) concluded that MCVs intensified by the stretching term of the vorticity equation. Brandes (1990) found that stretching of preexisting vorticity seemed to be the primary amplification mechanism at mid-levels, while tilting of horizontal vorticity generated by baroclinicity in the rear inflow was given as an explanation for low-level vorticity. The proposed 11 June 2003 case will provide a unique chance to document the mechanisms responsible for vorticity generation within a long-lived MCV because dual-Doppler analyses from which the vorticity budgets are created are available over a three-hour period during which the MCV formed.

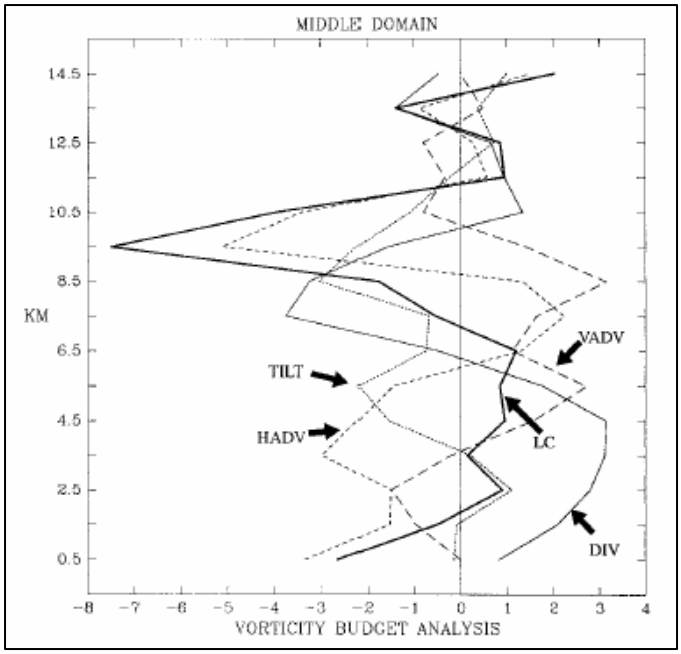

Figure 1.17. Vertical profiles of domain-averaged values of various terms in the vorticity budget for an MCV that occurred 1520-1529 UTC 16 June 1987. Units are 10^{-7} s^{-2} (Yu et al. 1999).

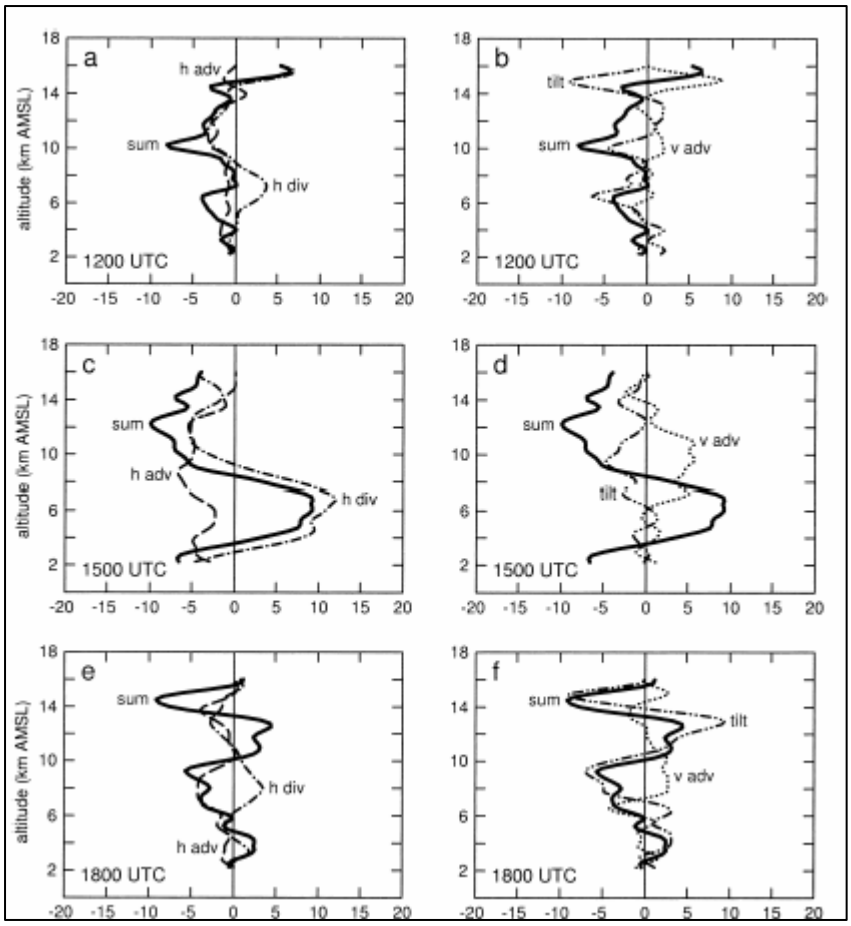

Figure 1.18. Vorticity budgets for 1 August 1996 MCV. (a), (c), (e) Horizontal advection (dashed) and horizontal divergence (dot-dashed). (b), (d), (f) Vertical advection (dotted) and tilting (dot-dot-dashed). The sum of all four terms (heavy solid) appears in each panel (Knievel and Johnson 2003).

2. DATA AND METHODOLOGY

2.1 KTLX and KINX WSR-88D Radar Data

The following data were used in the analysis of the 11 June 2003 MCV:

1.) Oklahoma City (Twin Lakes) (KTLX) Level II WSR-88D radar data

The KTLX radar is located at 35.33° N, 97.28° W, and 1.213 km above sea level.

2.) Tulsa, Oklahoma (KINX) Level II WSR-88D radar data

The KINX radar is located at 36.17° N, 95.56° W, and 0.668 km above sea level.

The radar data were obtained from the National Climatic Data Center (NCDC).

The Weather Surveillance Radar – 1988 Doppler (WSR-88D) is an S-band radar with a 10.71 cm wavelength that can detect hydrometeors larger than the size of cloud droplets. The WSR-88D has a beam width of 0.95° and a gate spacing of 250 m, which is the distance between consecutive measurements along a radial. The radial velocity spatial resolution is therefore 0.95° by 0.25 km, while the reflectivity spatial resolution is 0.95° by 1.0 km because radar data are averaged every four gates to reduce noise (Crum et al. 1993).

During the time period of interest (0000 through 0300 UTC 11 June 2003), both the KTLX and KINX WSR-88D were using Volume Coverage Pattern 11 (VCP-11). Both radars made sixteen 360° azimuthal sweeps at fourteen predetermined elevation scan angles from 0.5 to 19.5° in approximately five minutes (see Fig. 2.1).

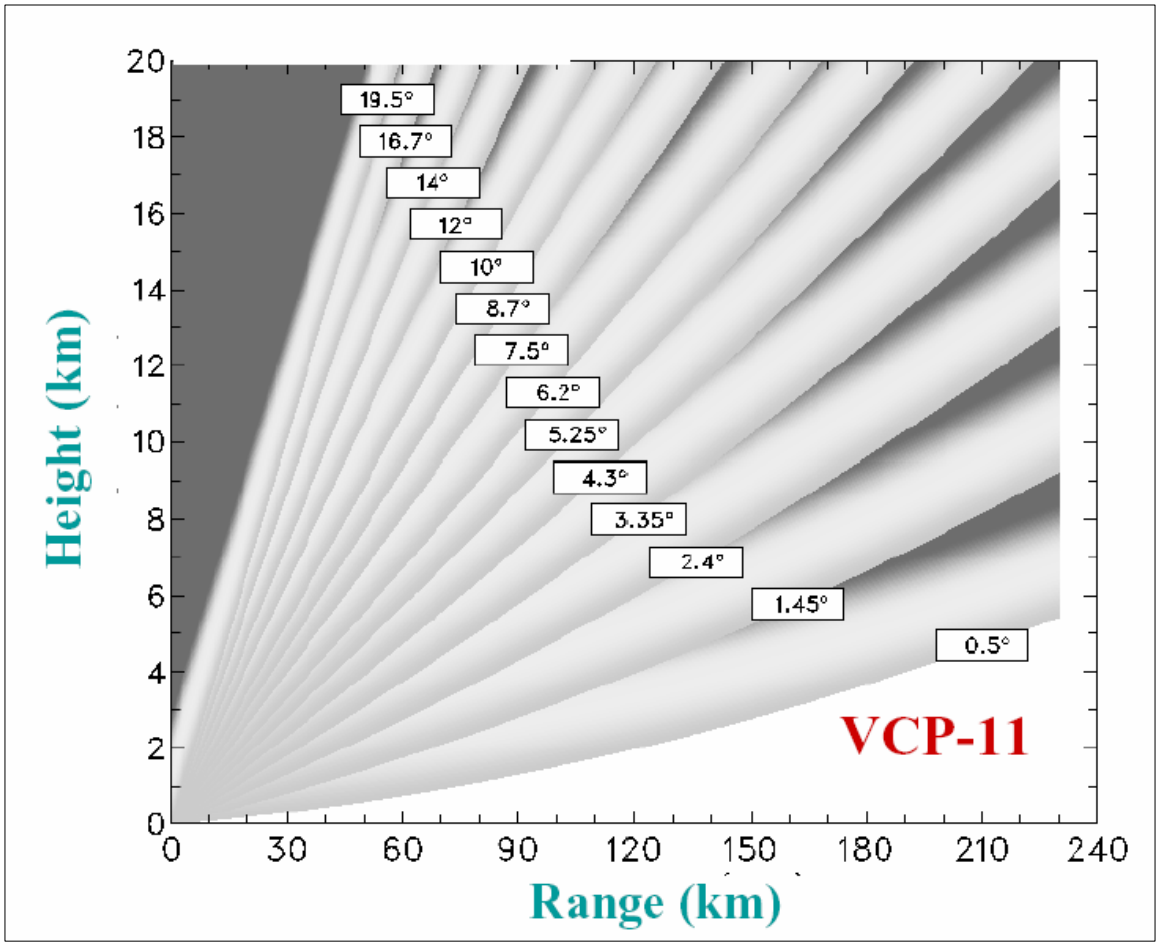

Figure 2.1. The range and height of elevation angles in Volume Coverage Pattern 11 (VCP-11) (Federal Meteorological Handbook No. 11 (FMH-11) Doppler Radar Meteorological Observations).

At the two lowest elevation angles (0.5° and 1.45°), the radar completes two sweeps. The first sweep uses a pulse width of 4.7 μs to detect reflectivity out to 460 km range. The next sweep uses a pulse width of 1.57 μs to determine the velocity field out to a reduced range of 230 km. At the remaining twelve elevation angles the smaller pulse width is used (Crum et al. 1993). The VCP-11 scanning strategy provides the best coverage of a storm because volume scans are performed quickly (one every approximately five minutes) and the storm detail in a radar volume is well resolved using

the fourteen elevation scans. Although VCP-11 provides the best coverage of storms with WSR-88D, gaps in data coverage do occur, especially at higher altitudes with increasing distance from the radar. These data gaps are easily seen in "ring" structures of missing reflectivity at higher altitudes.

The WSR-88D provides information on reflectivity, radial velocity, and spectrum width for each gate within the radar volume. These three variables are explained in the following three subsections.

2.1.1 Reflectivity

When the radar beam intercepts a hydrometeor, some of the energy is absorbed and some is scattered. The amount of energy that is backscattered depends on the size, shape, dielectric properties of the hydrometeor (refractive index), and the ratio of the wavelength of the transmitted energy to the size of the hydrometeor. When the diameter of a hydrometeor is small when compared to the wavelength, Rayleigh scattering occurs. For Rayleigh scattering conditions, backscattered energy (as measured by a parameter called "reflectivity") is proportional to the sixth power of the diameter of the hydrometeor. Reflectivity, Z, has units of $mm^6\ m^{-3}$, and is usually expressed in decibels ($dBZ = 10 \log_{10} Z$). Reflectivity also depends on the number of targets encountered by the radar beam. In other words, high reflectivity generally implies heavier precipitation (Rinehart 2001).

2.1.2 Velocity

In Doppler radars, the phase of the backscattered signal is detected, and when compared to the phase of the transmitted signal, a radial wind speed can be computed from the phase shift. If hydrometeors, which are carried by the wind, are moving toward

or away from the radar, the frequency of the returned signal changes slightly from the transmitted frequency. The faster the hydrometeors move in this direction, the larger the Doppler shift is. The shift will have higher frequency if the hydrometeors are moving toward the radar and lower frequency if they are moving away. The change in frequency is proportional to the wind speed along the direction of the beam, which is called radial velocity. Motions toward (away from) the radar are defined to have negative (positive) radial velocity. A maximum unambiguous velocity exists and is related to a radar's PRF, the frequency at which pulses are transmitted by the radar, and wavelength (λ) by the following equation:

$$v_{max} = \pm \left(\frac{PRF \ \lambda}{4} \right) \tag{2.1}$$

All velocities that exceed v_{max} are aliased or "folded" onto other portions of the velocity spectrum having velocities of integer multiples of $2v_{max}$ away (Brown 1976). The interval given by (2.1) is also called the "Nyquist interval" with v_{max} also called the "Nyquist velocity".

2.1.3 Spectrum Width

Spectrum width ω_s is a measure of the variability of wind within a single pulse volume of the radar. It can be related to the spread of the terminal fallspeeds of hydrometeors, turbulence within the sample volume, wind shear along or across the beam, and the rotation rate of the antenna (Nathanson 1969). Turbulence and wind shear are the major producers of spectrum width (Sirmans and Doviak 1973), although at ranges greater than 30 km shear is expected to predominate (Nathanson 1969). Sirmans

and Doviak (1973) showed, for small elevation angles and a Gaussian-shaped antenna pattern, that spectrum width is given by

$$\omega_s = 0.3 K_t r_1 \theta_w \qquad (2.2)$$

where K_t is the transverse shear of the radial velocity, r_1 is the pulse volume range, and θ_w is the 3 dB beamwidth in radians.

2.2 SOLOII: Radar Data Editing Software

SOLOII, a software package developed at the National Center for Atmospheric Research (NCAR), was used to edit radar data for radar volumes every fifteen minutes during the time period 0000 to 0300 UTC 11 June 2003 from both the KTLX and KINX radars. Editing primarily involved only velocity as errors in velocity could produce significantly large errors in later dual-Doppler analyses. Reflectivity data in the WSR-88D are also edited to remove ground clutter by algorithms (Steiner and Smith 2002). SOLOII was used to remove artificial noise from the data by setting a maximum spectral width threshold of 4.0 m s^{-1} on the raw velocity data. SOLOII was also used to unfold ambiguous velocities around a predetermined Nyquist velocity of 28.0 m s^{-1}.

2.3 REORDER

The REORDER software program (Mohr et al. 1986; Oye and Case 1995) was used to interpolate and grid the radar data from its original spherical (radar) coordinates (r, φ, Θ) onto a Cartesian grid (x,y,z). The analysis domain was a 450 km by 450 km box ($-150.0 < x < 300.0$, $-150.0 < y < 300.0$, $0.0 < z < 19.0$) centered on the KTLX radar (35.33° N, -97.28° W, and 1.213 km above sea level). The Cartesian grid was given a horizontal and vertical resolution of 3.0 km and 0.5 km, respectively. The horizontal radius of influence was set to 6.0 km while the vertical radius of influence was set to 3.0

km. Both the grid resolution and radii of influence were chosen due to the interest in resolving mesoscale phenomena with WSR-88D over a large area. Unfortunately, the use of two WSR-88D radars does not allow a dual-Doppler analysis to resolve motions at convective scales. A three-dimensional Cressman weighting scheme (Cressman 1959) was used to derive Cartesian grid points from the polar radar data. The Cressman weighting scheme is a function of both grid spacing and radius of influence. The radius of influence is defined as:

$$R^2 = dX^2 + dY^2 + dZ^2 \tag{2.3}$$

The weighting function, W, for a particular gate value is defined as:

$$W = \frac{R^2 - r^2}{R^2 + r^2} \tag{2.4}$$

where *r* is the distance between the gate and the grid point (Oye and Case 1995).

2.4 CEDRIC

A single Doppler radar can measure the radial component of a target but cannot give its complete three-dimensional (3D) velocity components. Traditional dual-Doppler processing is particularly useful because it requires only two radars instead of three. However, the requirement for having three different components of motion for a target to obtain 3D wind structure cannot be eliminated. With two radars, it is only possible to directly determine two components of the velocity field. It is still possible to combine radial velocity data from only two radars and obtain 3D wind fields if other assumptions are included in the processing. There are actually four unknowns that must be solved for: u, v, w, and V_t where u, v, and w are the components of velocity in the x, y, and z directions and V_t is the terminal velocity of the precipitation. Unless an accurate measurement of particle type (i.e., liquid or frozen) and size distribution can be made, the

error variance of V_t should be assumed to be equal to 1 m s^{-1} associated with rain drops. It should be noted that large errors, up to several meters per second, in V_t estimates can be caused by relating regions of hail with a V_t-Z relation appropriate for liquid water (Doviak et al. 1976).

Two Doppler radars provide velocity estimates for u and v in the horizontal xy-plane. To supplement these two measurements, the mass continuity equation and the assumption that the terminal velocity is a function of the radar reflectivity are used (Rinehart 2001). The relationship of terminal velocity to radar reflectivity is based on a Marshall-Palmer drop size distribution which determines terminal velocity as a function of drop size diameter (Gunn and Kinzer 1949). By adding these assumptions to radar measurements of the horizontal components of the wind, it is possible to calculate the 3D wind components at every point within the storm.

The Custom Editing and Display of Reduced Information in Cartesian space (CEDRIC) software program (Miller and Fredrick 1998) was used to combine the grids created from REORDER for each of the radars and to solve for the horizontal wind components (u, v) and the vertical wind component (w) using the continuity equation. The continuity equation is used to estimate the vertical velocity by calculating horizontal divergence at each height and then integrating the divergence with respect to height. This integration of divergence with height can be performed upward or downward. Downward integration was used because vertical velocity is dependent upon the density of hydrometeors and, since the density of hydrometeors generally decreases with height, the errors associated with assuming vertical velocity is zero at the top of the grid and then integrating downward are less than errors accumulated with upward integration.

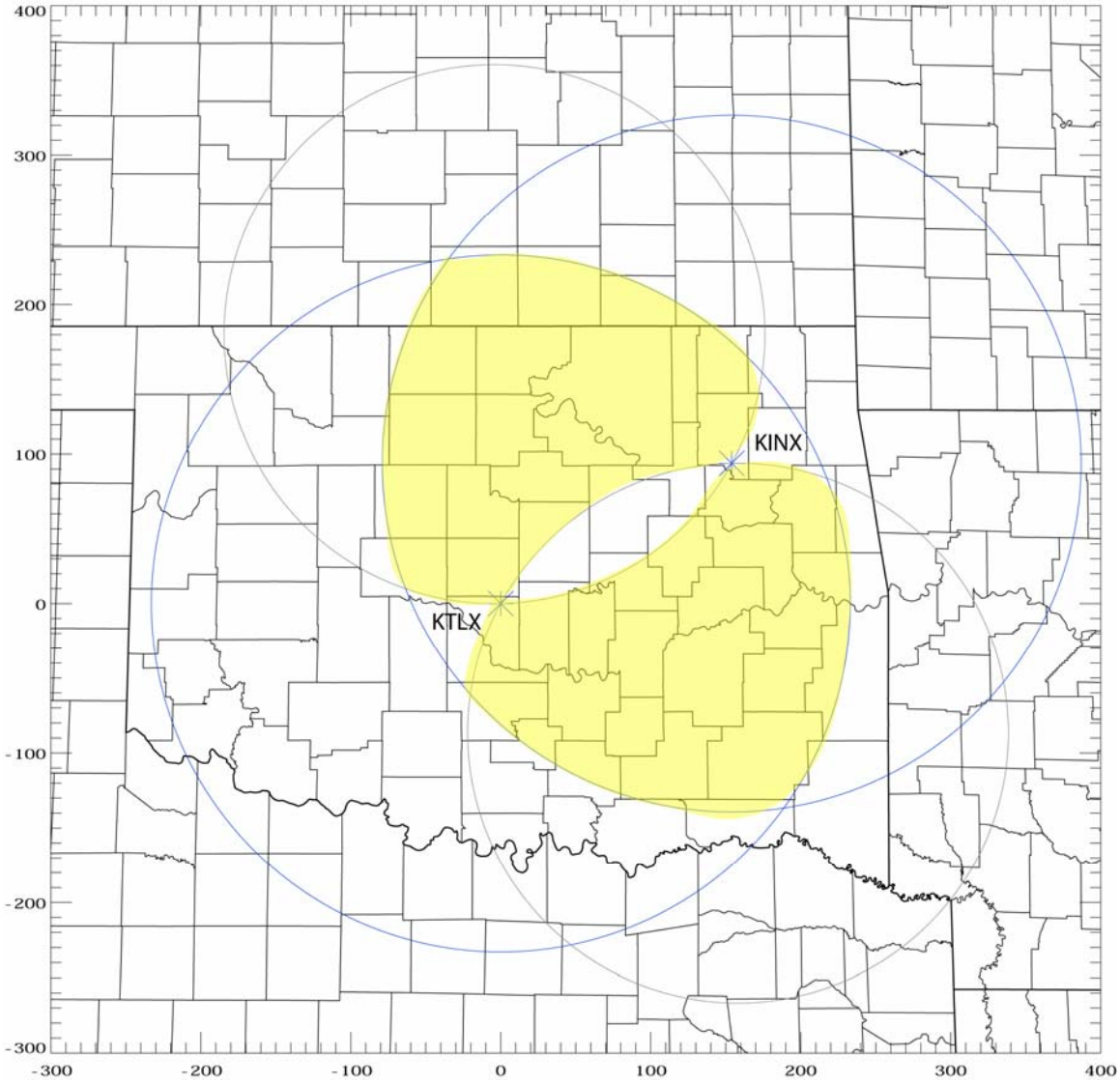

Figure 2.2. Dual-Doppler lobes of KTLX and KINX WSR-88D with a 30° beam crossing angle.

The coverage area of the dual-Doppler lobes using the KTLX and KINX radars is the yellow area shown in Fig. 2.2. The two smaller circles in Fig. 2.2 oriented to the northwest and southeast are given by Eqn. 2.5 and are associated with beam crossing angle constraints. The two larger circles, with one of each of the radars at the center, have

a radius of 230 km and indicate the area where reflectivity and velocity measurements are taken.

$$A_1(\beta) = 2(d \csc \beta)^2 (\pi - 2\beta + 2 \sin 2\beta) \quad (2.5)$$

where β is the angle between intersecting beams from the radars ($0 \leq \beta \leq 90°$) and d is half the distance of the baseline (180.7 km, in this case) (Davies-Jones 1976). The coverage area is the intersection of the circles defined related to beam crossing angle constraints and the circles of fixed (230 km) radius from both radars related to resolution (Davies-Jones 1979). β is also related to the sum of the error variances for the u and v components divided by the sum of the mean velocity variances of the two radars as shown in the following equation:

$$\frac{\sigma_u^{\,2} + \sigma_v^{\,2}}{\sigma_1^{\,2} + \sigma_2^{\,2}} = \csc^2 \beta \equiv b \quad (2.6)$$

Wind error is minimum when $\beta = 90°$, however this reduces the amount of data that can be incorporated within a dual-Doppler analysis (Lhermitte and Miller 1970; Davis-Jones 1979). To adequately determine velocity components, β must be 30° or greater (i.e., $b \leq 4$) (Davies-Jones 1979; Bluestein et al. 1994). Doviak et al. (1976) found that dual-Doppler coverage area can be increased to any desired size without increasing wind estimate variance, but that the resolution of vertical velocity would be linearly proportional to d. Vertical wind has variance larger than horizontal wind for most grid locations as errors in vertical wind calculations are due to the accumulation of errors in the integration of the continuity equation. Vertical velocity can be estimated with a standard deviation of less than a few meters per second up to heights near 14 km for extended regions of space (Doviak et al. 1976). Dual-Doppler coverage area can be increased by increasing the distance between radars without increasing wind estimate

variance, but increased coverage area is compromised by poorer resolution (Doviak et al. 1976). Increasing the radar baseline reduces spatial resolution close to the radars, while greatly increasing the area over which velocity components can be determined (Davies-Jones 1979).

The spatial resolution (S) of a given point within a dual-Doppler lobe is defined as:

$$S = \frac{R\pi\Delta}{180} \tag{2.7}$$

where R is the range to the farthest radar and Δ is the radar's half-power beamwidth (Davies-Jones 1979).

2.4.1 Dual-Doppler Analysis Images

Dual-Doppler analyses of maximum reflectivity and storm-relative wind vectors were created every fifteen minutes at 1.0, 3.0, 4.5, 5.5, 7.0, and 10.0 km during the 0000 to 0245 UTC time period of 11 June 2003 to allow a detailed examination of the MCV evolution. The analysis domain was a 450 km by 450 km box ($-150.0 < x < 300.0$, $-150.0 < y < 300.0$) with KTLX at the origin (0.0, 0.0). Contours of maximum reflectivity were made in increments of 10 dBZ starting from 0 dBZ up to 50 dBZ. The average storm motion during the 0000 to 0300 UTC time period, determined by tracking the farthest eastward extending region in the convective leading line on an hourly basis from both radars, was from 288° at 10.5 m s^{-1}. The advective part of the wind (average storm motion) was subtracted from the total wind to obtain storm relative motion. Storm-relative wind vectors, which were made proportional to a 20 m s^{-1} scale vector, were then overlaid on reflectivity.

2.4.2 Vorticity Calculation within Analysis Domain

The vertical component of relative vorticity, ζ, is given by the following equation:

$$\zeta = \frac{\partial v}{\partial x} - \frac{\partial u}{\partial y} \tag{2.8}$$

where u and v are the x- and y-components of the horizontal wind and $\partial x/\partial y$ is equal to 6km for this case. Unlike u, v, w, and divergence, vertical vorticity is not a variable automatically calculated in and output from CEDRIC, so a computer program was created in IDL to calculate it at every grid point with valid wind data. Both horizontal and vertical cuts were made at 15 minute intervals from 0000 to 0245 UTC to examine the vertical vorticity structure of the developing MCV. Horizontal cross-sections of vertical vorticity contours were made at 1.0, 4.5, and 7.0 km. The analysis domain covered a smaller region ($-50.0 < x < 100.0$, $50.0 < y < 150.0$) than the dual-Doppler analyses themselves to show more detail within the northwestern dual-Doppler lobe where the MCV developed (Fig. 2.2). Vertical vorticity in the horizontal cross-sections was first contoured at 1×10^{-5} s^{-1}, then 1×10^{-4} s^{-1} and increased up to 5×10^{-3} s^{-1} in increments of 1×10^{-4} s^{-1}.

At each fifteen minute interval for the North-South vertical cross-sections of vertical vorticity, the location of x was subjectively chosen from the analysis of horizontal contours of vertical vorticity. The analysis domain was ($0.0 < y < 150.0$, $0.0 < z < 17.0$) because the MCV developed in the northwestern dual-Doppler lobe relative to the KTLX radar. For the East-West vertical transects, y = 100.0 km (relative to KTLX at the origin) was subjectively chosen to capture the MCV evolution as it propagated basically eastward in time. The analysis domain was ($-100.0 < x < 100.0$, $0.0 < z < 17.0$) and covered a large portion of the northwestern dual-Doppler lobe to capture the

evolution of the MCV. Vorticity in the vertical cross-sections was first contoured at 1 x 10^{-4} s^{-1} and increased up to 5 x 10^{-3} s^{-1} in increments of 2 x 10^{-4} s^{-1}.

2.5 Time Series

Time series were created to document the quantitative changes in reflectivity, divergence, vertical vorticity, and vertical velocity within the MCS as it related to MCV genesis. The total number of data points, the number of convective data points (loosely defined as having reflectivity greater than 40 dBZ), the number of stratiform precipitation points (loosely defined as having reflectivity greater than 0 dBZ but less than 40 dBZ), average divergence, average vertical vorticity, and average vertical velocity at 2.0, 3.0, 4.5, 5.5, 7.0, and 10.0 km were calculated every fifteen minutes from 0000 to 0300 UTC 11 June 2003. Data for each of the previously stated items were generated using the same IDL program to generate the dual-Doppler analyses and then imported into an Excel spreadsheet. At each height, the total number of data points was defined as all grid points within the MCS having reflectivity greater than 0 dBZ. The number of convective data points was defined as all grid points having reflectivity greater than 40 dBZ. Note that there are more precise methods of determining convective versus stratiform precipitation type (Steiner et al. 1995), in which classifications of convective regions within an MCS involve the 40 dBZ reflectivity threshold, strong gradients of reflectivity, or location relative to another echo that has been previously classified as convective based on the 40 dBZ threshold. Although enhanced reflectivity from the bright band at mid-levels (i.e., 4.5 km near the melting level) may exceed the 40 dBZ threshold, the simple classification criterion used herein was able to adequately distinguish between convective and stratiform regions within the MCS over the time period of analysis. The number of

stratiform convective points was defined as the total number of data points minus the number of convective data points, or those data points having reflectivity greater than 0 dBZ but less than 40 dBZ. Averages of divergence, vertical vorticity, and vertical velocity were calculated by adding each term separately at a given height for each valid data point within the dual-Doppler domain and then dividing by the total number of valid data points.

2.6 Vorticity Budgets

To investigate the possible mechanisms responsible for the generation of an MCV, a vorticity budget was formulated to evaluate various terms in the vorticity tendency equation using 3D wind fields derived from dual-Doppler analyses. The terms of the vertical vorticity tendency equation ignoring the solenoidal term were calculated using the following equation:

$$\frac{\partial \zeta}{\partial t} = -\left(u\frac{\partial \zeta}{\partial x} + v\frac{\partial \zeta}{\partial y} \right) - w\frac{\partial \zeta}{\partial z} - (\zeta + f)\left(\frac{\partial u}{\partial x} + \frac{\partial v}{\partial y} \right) - \left(\frac{\partial w}{\partial x}\frac{\partial v}{\partial z} - \frac{\partial w}{\partial y}\frac{\partial u}{\partial z} \right) \qquad (2.9)$$

LC HADV VADV DIV TILT

where u, v, and w are the three components of the wind, ζ is the vertical component of relative vorticity, and f is the Coriolis parameter. The Coriolis parameter ($f \equiv 2\ \Omega \sin\varphi$) was assumed to be a constant ($8.52 \times 10^{-5}\ s^{-1}$) based on the average latitudes of the KTLX and KINX radars approximately where MCV genesis occurred. If friction is ignored, then the local change (LC) in vertical vorticity within an MCV must originate from some combination of horizontal advection of vorticity (HADV), vertical advection of vorticity (VADV), the divergence (or stretching) term (DIV) which represents amplification/reduction of preexisting vertical vorticity by horizontal convergence/divergence, and the tilting term (TILT) which represents the vertical

vorticity created by tilting horizontal vorticity with vertical motion (e.g., Scott and Rutledge 1995; Yu et al. 1999; Knievel and Johnson 2003). All the terms on the right-hand side of Equation 2.9 were calculated at each grid point within the dual-Doppler analysis domain using centered finite differencing. The sum of each of the four terms therefore represents the estimated magnitude of the local change of vorticity at each grid point. An estimate of the domain average for each term was obtained by taking the arithmetic mean over the area of analysis at each level.

The analysis domain for the vorticity budgets was a 150.0 km by 150.0 km box centered over the region where the MCV developed that extended 19.0 km in altitude and that moved east at two separate times to follow the convective line of the MCS and the region where the MCV developed. The storm motion of the MCS was approximately 10 m s^{-1} from the west (270°), which translates to approximately 36 km per hour. The horizontal analysis domain for the 0000 to 0045 time period was ($-100.0 < x < 50.0$, $0.0 < y < 150.0$). For the next hour (0100 to 0145 UTC), the horizontal analysis domain was ($-75.0 < x < 75.0$, $0.0 < y < 150.0$). For the final hour of analysis, the horizontal domain was ($-50.0 < x < 100.0$, $0.0 < y < 150.0$). A minimum threshold of 250 points at each level was required to calculate the terms of the vorticity tendency equation. This reduced noise at upper and lower levels near the boundaries of the dual-Doppler analysis domain. In addition, all the terms in the tendency equation had to be valid in order for the tendency equation to be computed at a given level. This further reduced noise within the calculation and removed additional error. At each level in the analysis domain, the average of a term was computed by summing that term at all valid grid points and then dividing by the number of valid grid points.

3. RESULTS

The results section is organized based on the objectives stated in Section 1. Section 3.1 discusses reflectivity and storm-relative dual-Doppler winds at 1.0, 3.0, 4.5, 5.5, 7.0, and 10.0 km altitude. The altitude of 1.0 km, which corresponds to approximately 900 mb, is the lowest height able to be seen with adequate data coverage based on the geometry of the dual-Doppler analysis with radars spaced 180 km apart. The altitudes of 2.0, 3.0, 5.5, 7.0, and 10.0 km correspond to approximately 800, 700, 500, 400, and 250 mb pressure levels, respectively. The altitude of 4.5 km is chosen because it represents the melting level. Horizontal cross sections of vertical vorticity are contoured at 1.0, 4.5, and 7.0 km to represent low- and mid- to upper-levels within the MCV environment. Vertical cross-sections of vertical vorticity along North-South and East-West transects through the developing MCV document the mesoscale development of the 11 June 2003 MCV from 0000 to 0245 UTC. Section 3.2 contains time series to document quantitative changes in reflectivity, divergence, vorticity, and vertical velocity within the environment of the developing MCV. Section 3.3 contains vorticity budget analyses for fifteen minute intervals between 0000 and 0245 UTC as well as time series that display the number of data points used within the analysis, average horizontal advection of vorticity, average horizontal divergence of vorticity, average vertical advection of vorticity, average tilting term of vorticity, and the average sum of the four vorticity budget terms at 2.0, 3.0, 4.5, 5.5, 7.0, and 10.0 km altitude to investigate the mechanisms responsible for the generation of vertical vorticity within the MCV. These vorticity budget analyses are done in a subjectively determined analysis domain around the MCV that developed within the northwest dual-Doppler lobe (Fig. 2.2).

3.1 Dual-Doppler Analyses and Horizontal/Vertical Cross-Sections of Vertical Vorticity

Fig. 3.1 shows reflectivity and storm-relative wind vectors derived from dual-Doppler analysis at 1.0 km altitude for fifteen minute intervals between 0000 and 0245 UTC. At this altitude during early times (0000 and 0015 UTC), the area of the MCS within the dual-Doppler lobe is predominantly convective. However, by 0030 UTC there is a suggestion of circulation immediately behind the convective line (x = -5.0, y = 80.0). By 0045 UTC, rotation becomes evident and is centered on (x = -5.0, y = 90.0). Although the rotation is near the edge of the dual-Doppler lobe, development of cyclonic rotation from 0015 to 0030 UTC continued in the same storm-relative location which suggests that the analysis reveals a real circulation. An approximately 30 km diameter MCV developed in the stratiform region in the same location relative to the convective line which can be seen at 0100 and 0115 UTC. The magnitude of wind vectors associated with the MCV are small (5 m s^{-1} or less), but this is reasonable for MCVs in the initial stages of formation (Brandes 1990; Knievel and Johnson 2002; Davis and Trier 2007). By 0145 UTC, the MCV takes on an elliptical shape and is not fully enclosed within the dual-Doppler lobe which suggests that the area of the MCV has increased. At 0245 UTC, the center of the MCV is located at (x = -25.0, y = 55.0). While both the MCS and MCV propagate to the east, the MCV appears to move rearward relative to the leading convective line because the MCV propagates at a slower rate than the advancement of the convective line.

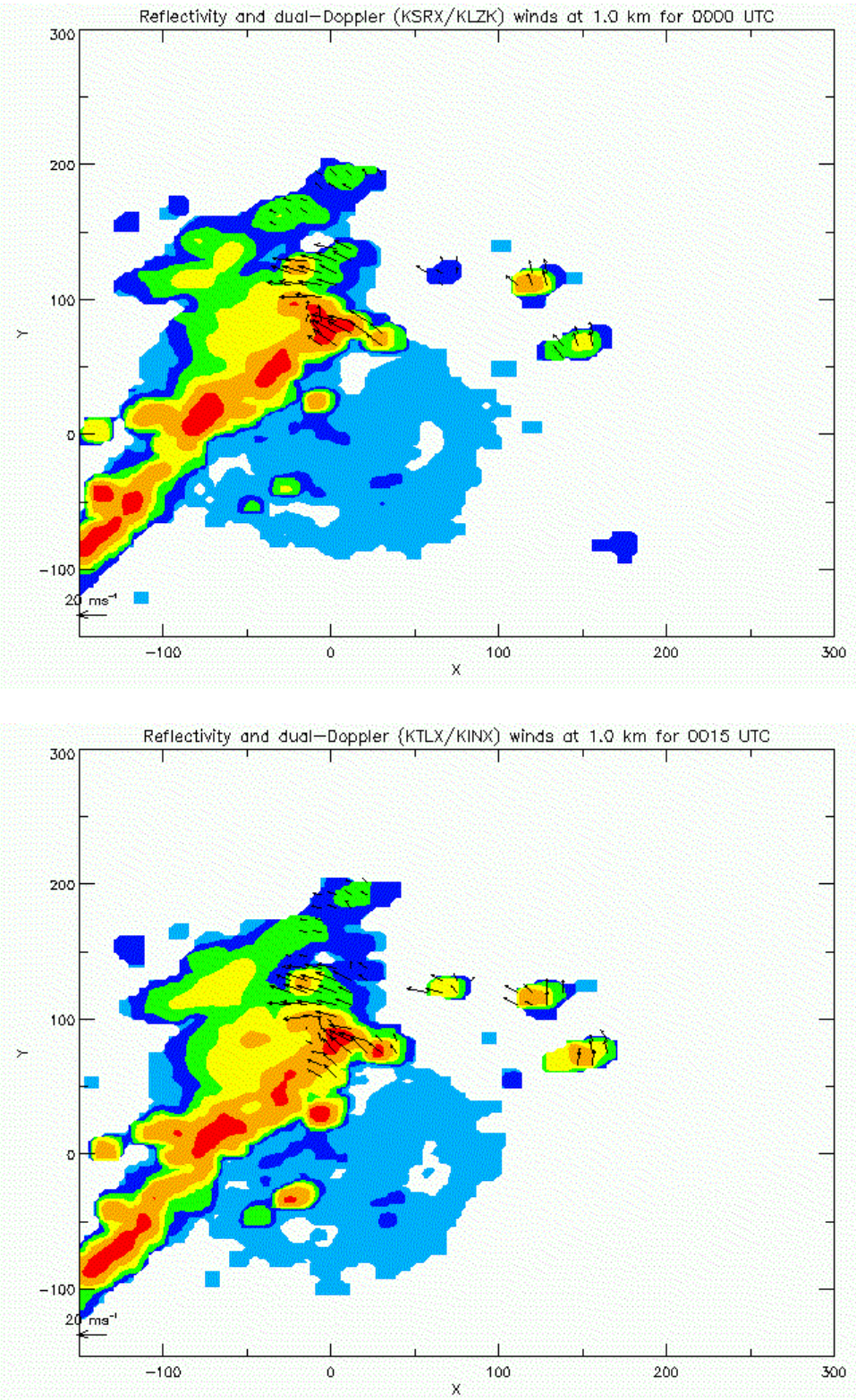

Figure 3.1. Reflectivity and storm-relative wind vectors for fifteen minute intervals between 0000 and 0245 UTC at 1.0 km altitude. Reflectivity scaled in 10 dBZ increments from 0 dBZ (light blue) to 50 dBZ (red).

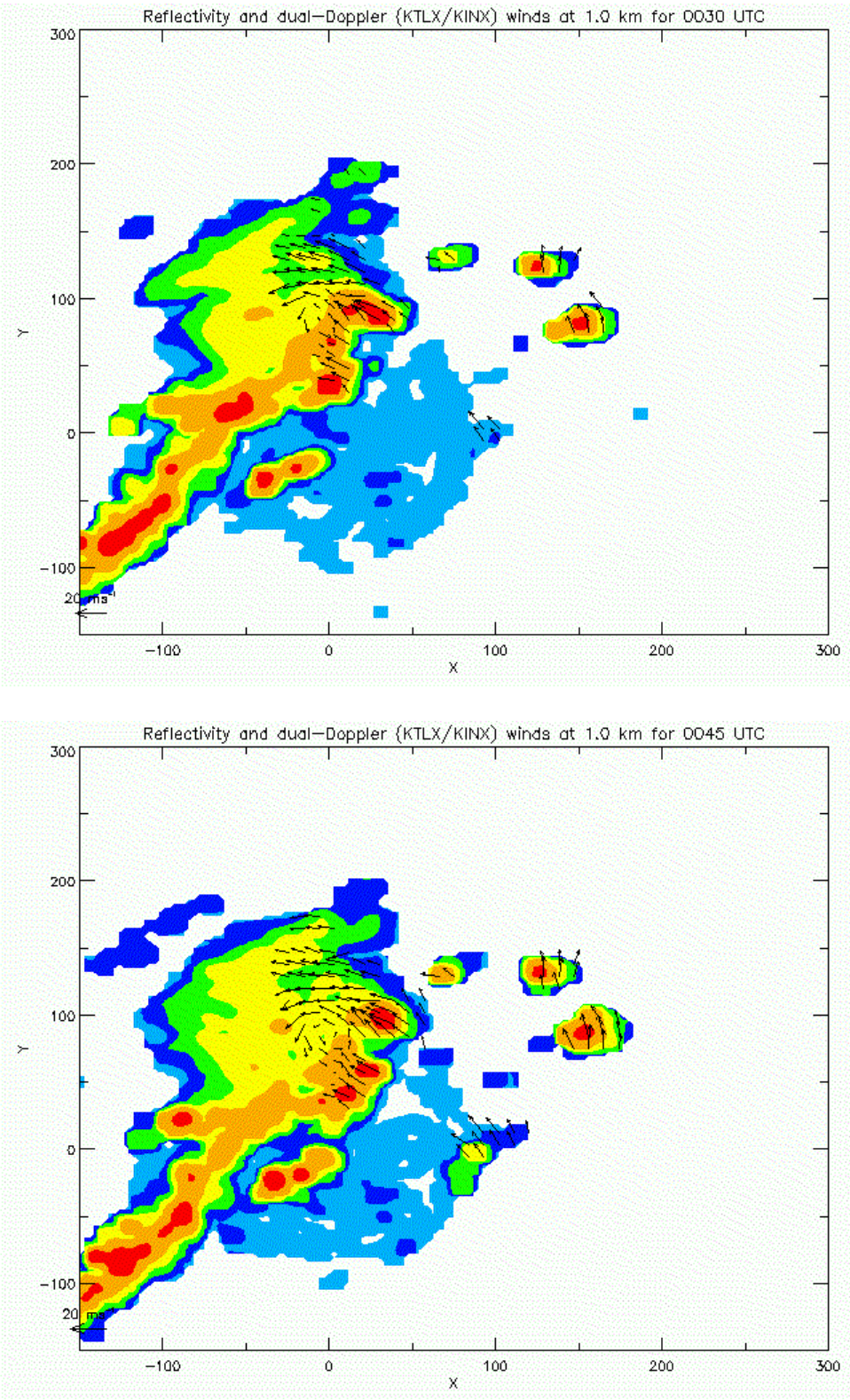

Figure 3.1 continued.

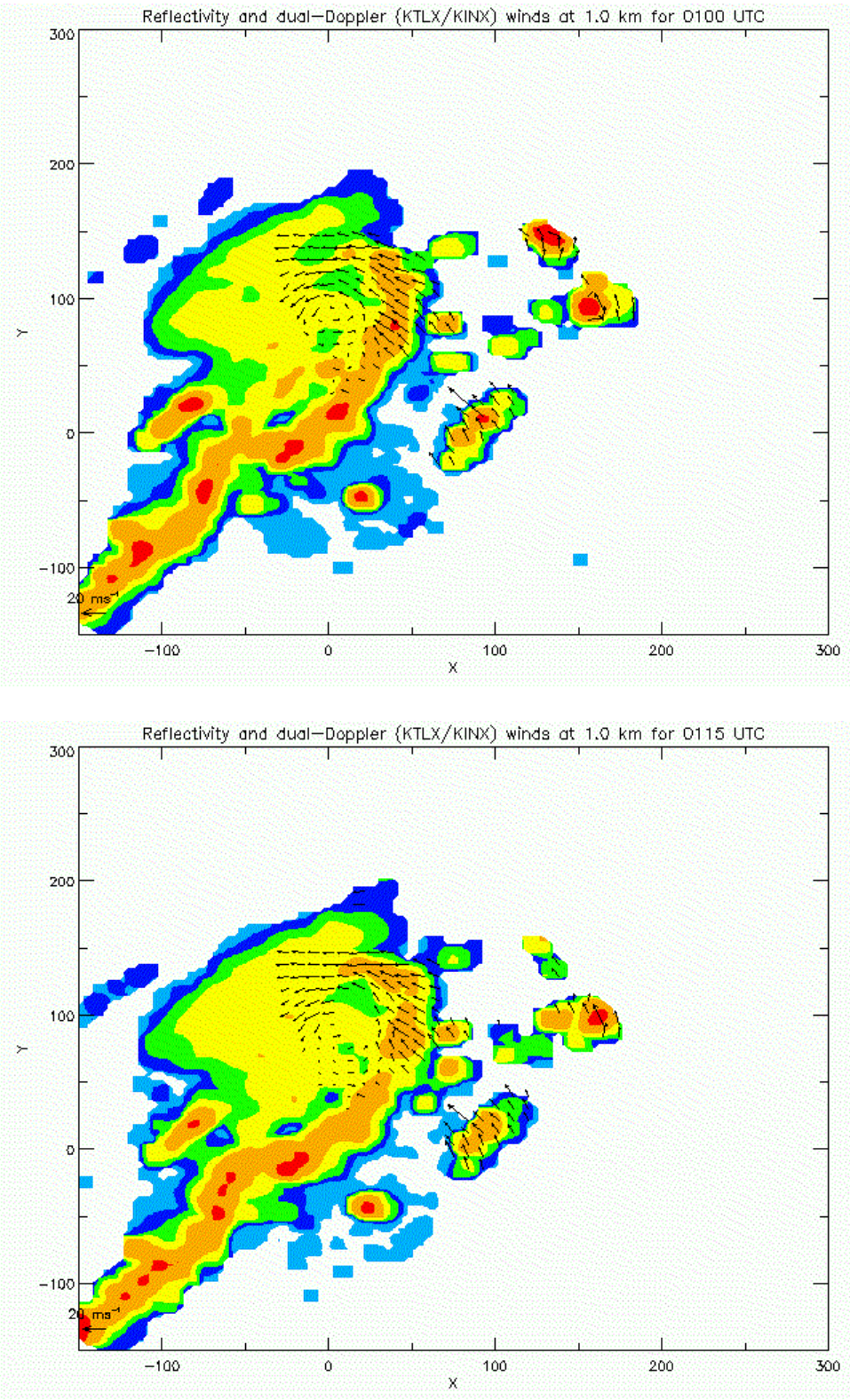

Figure 3.1 continued.

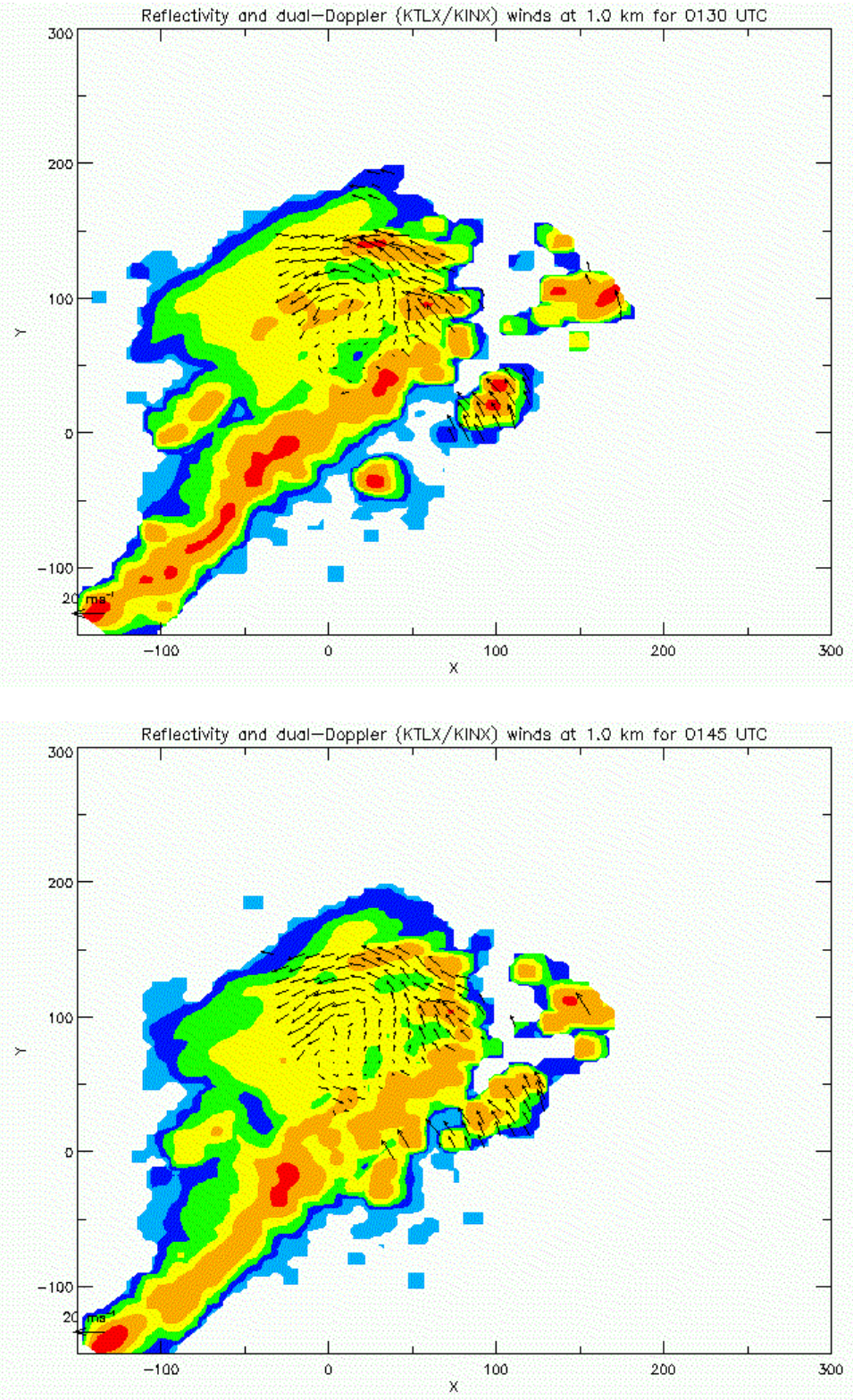

Figure 3.1 continued.

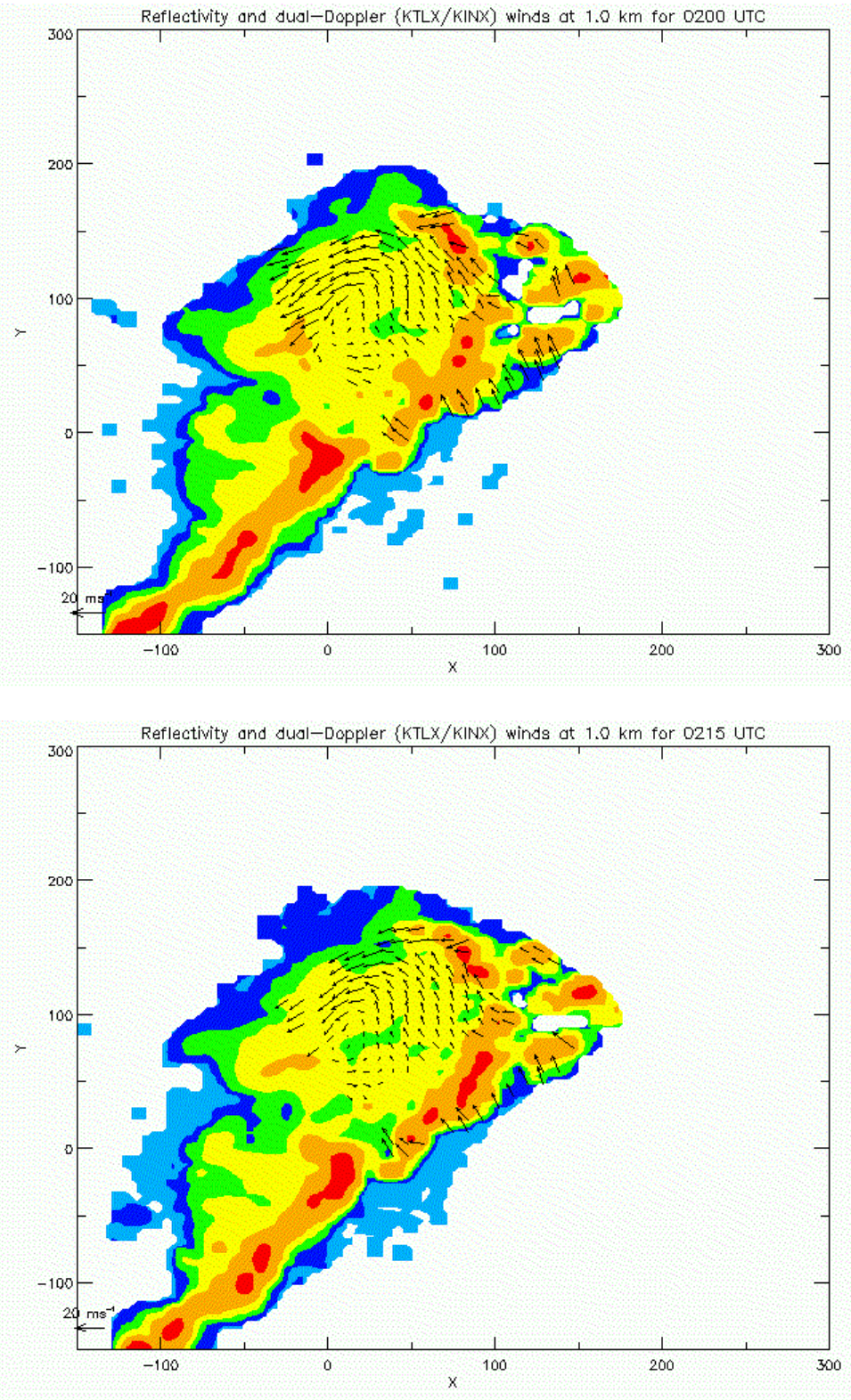

Figure 3.1 continued.

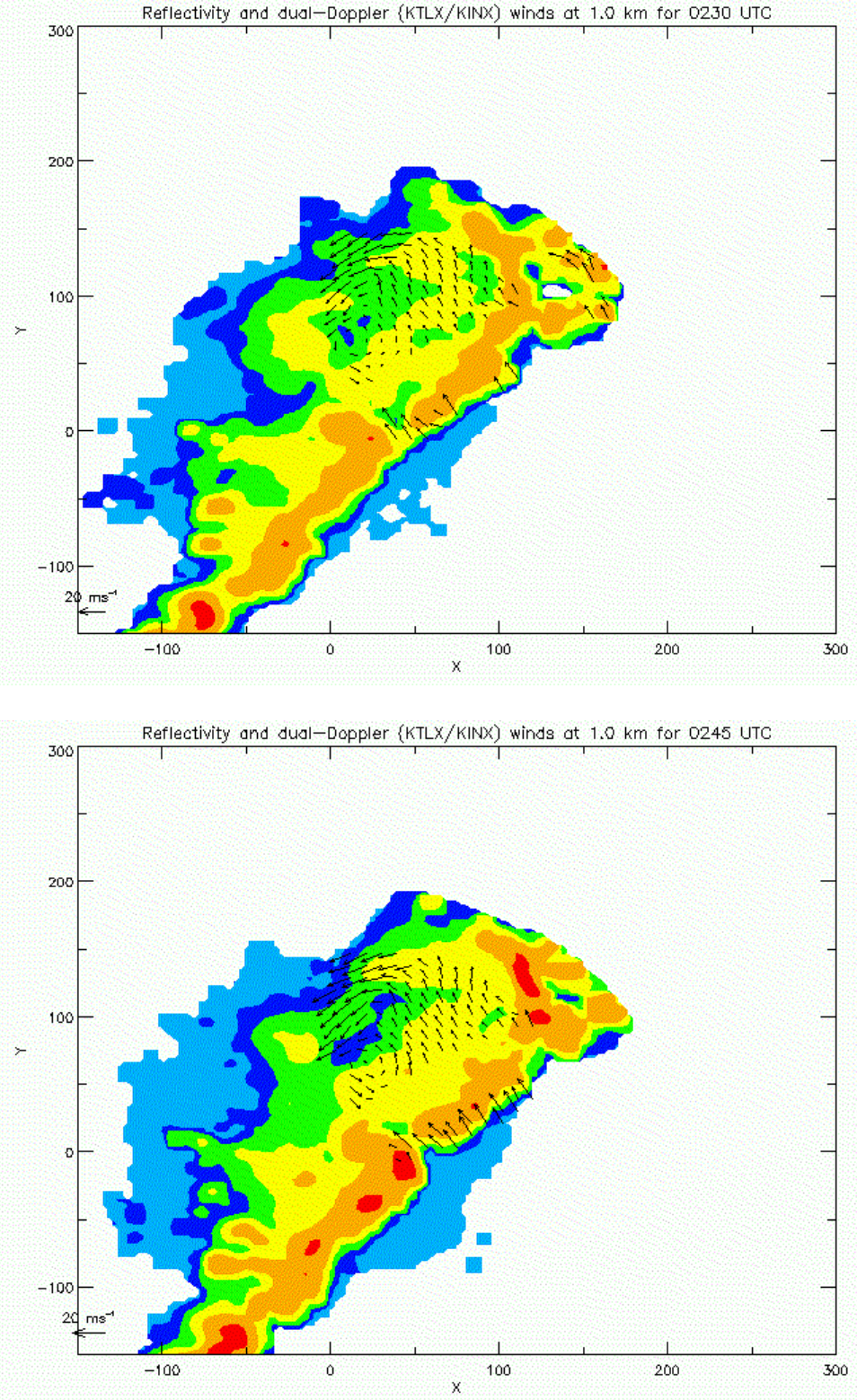

Figure 3.1 continued.

Fig.3.2 shows reflectivity and storm-relative wind vectors derived from dual-Doppler analysis at 3.0 km altitude for fifteen minute intervals between 0000 and 0245 UTC. At 0000 UTC, cyclonic rotation appears to be forming in a hook-like appendage from the convective line which extended back into the stratiform region. These hook echoes were first documented by Fujita (1978), but were associated with bow echoes. Mature MCVs are generally larger than most bow echoes, but the cyclonic rotation evident in both phenomena are included among the spectrum of circulation structures seen within MCSs (Wakimoto et al. 2006). At this altitude, by 0015 UTC a weak but closed circulation is evident just to the rear of the convective line (x = -20.0, y = 85.0). Half an hour later at 0045 UTC, the circulation was not as pronounced as it was at earlier times, but it does appear to become larger (approximately 30 km as was seen at 0100 and 0115 UTC at 1.0 km altitude in Fig. 3.1). By 0130 UTC, the MCV takes on an elliptic shape centered approximately around (x = 0.0, y = 50.0) and is oriented from the southwest to northeast although the circulation does not appear to be closed. This may be due to constraints from the size of the dual-Doppler lobe. At 0215 and 0230 UTC there is a gap in the data at x = -10.0 km although the MCV retains its elliptical shape. At 0245 UTC, there is another rotation evident in a reflectivity hook near KTLX (x = 0.0, y = 0.0). As the circulation takes on a more elliptical shape, it appears to move southwest in a storm-relative sense. This is consistent with other observations of long-lived MCVs. Once an MCV is generated, it can sometimes move independently of the parent MCS that spawned it, even outlasting it to go on and produce secondary convection (Raymond and Jiang 1990; Fritsch et al. 1994; Trier and Davis 2007).

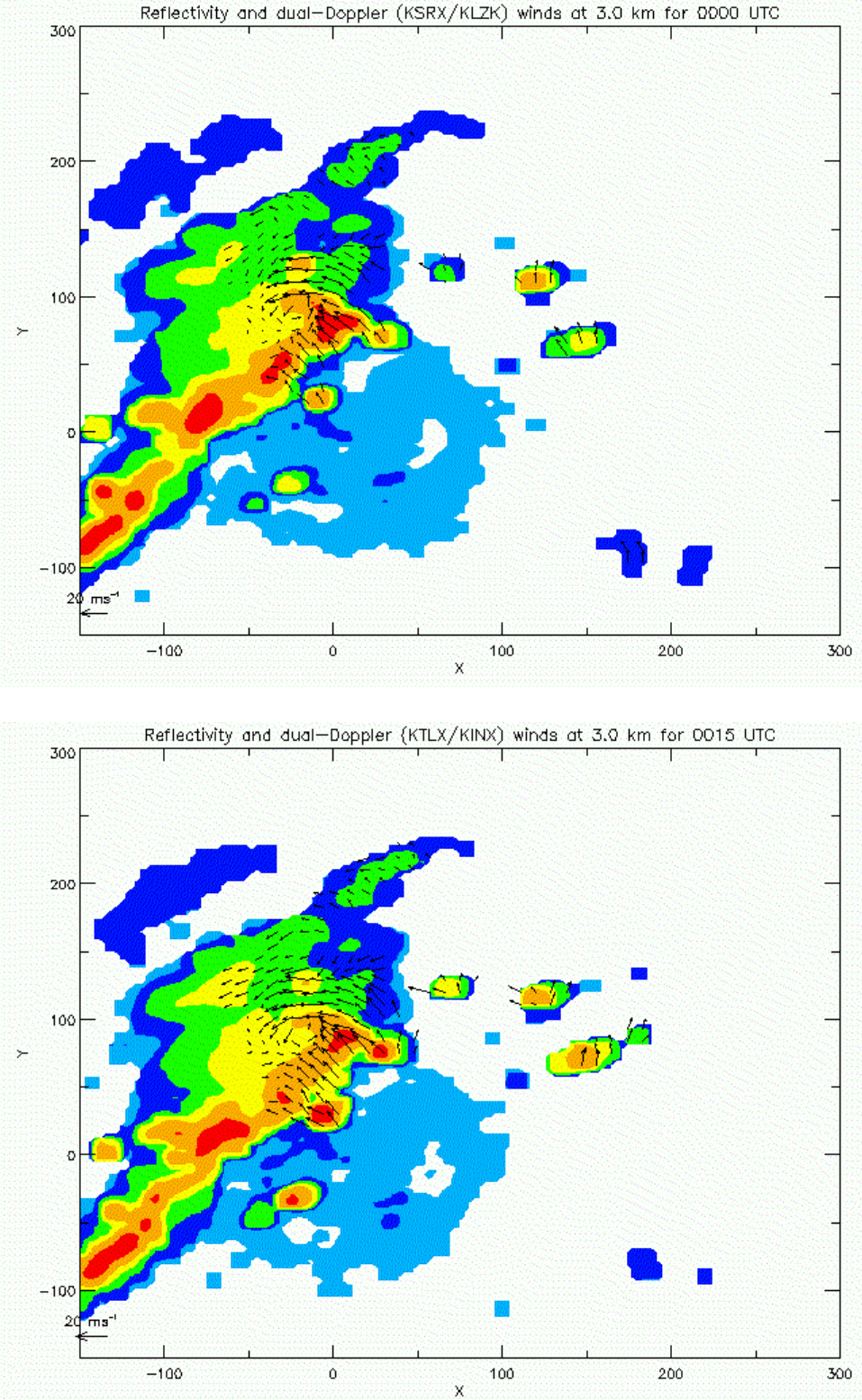

Figure 3.2. Reflectivity and storm-relative wind vectors for fifteen minute intervals between 0000 and 0245 UTC at 3.0 km altitude. Reflectivity scaled in 10 dBZ increments from 0 dBZ (light blue) to 50 dBZ (red).

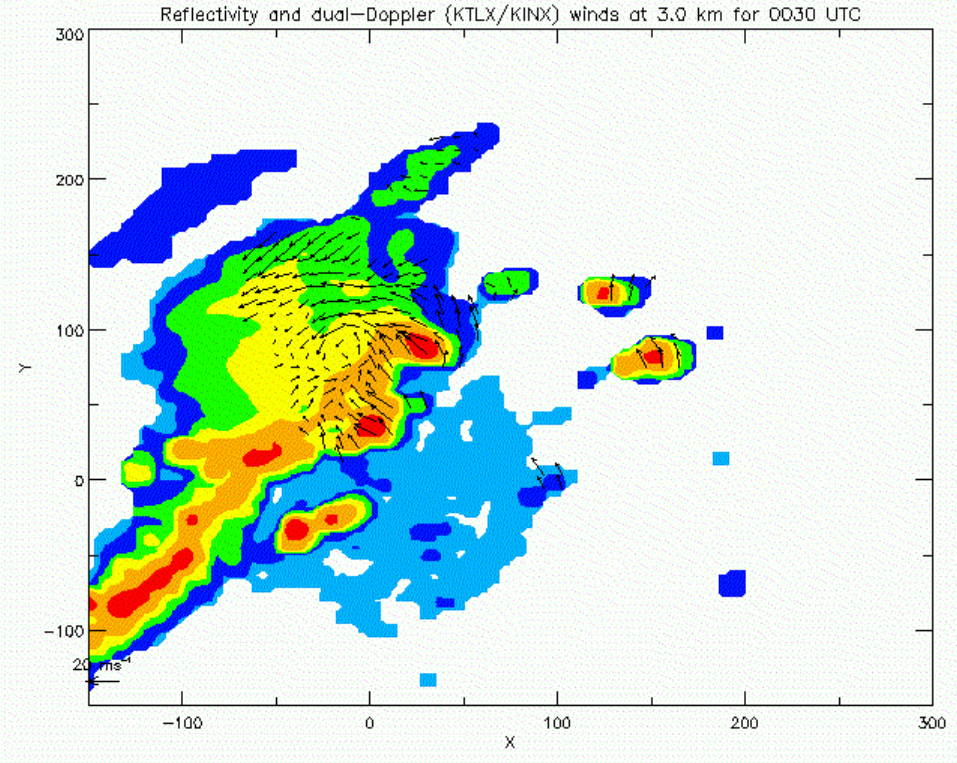

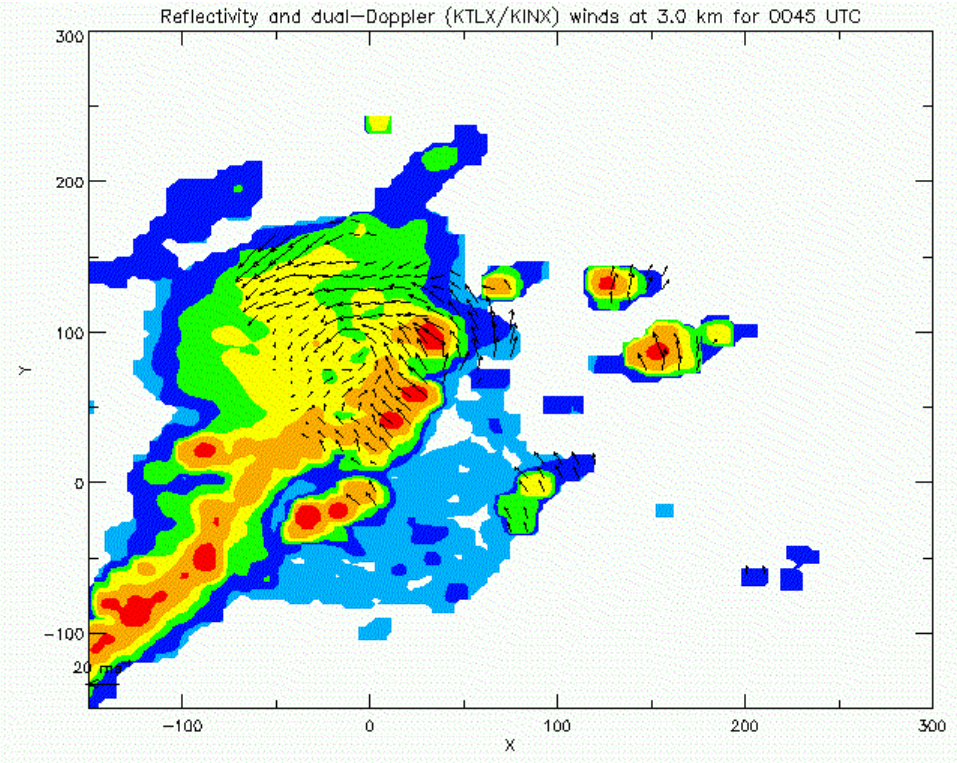

Figure 3.2 continued.

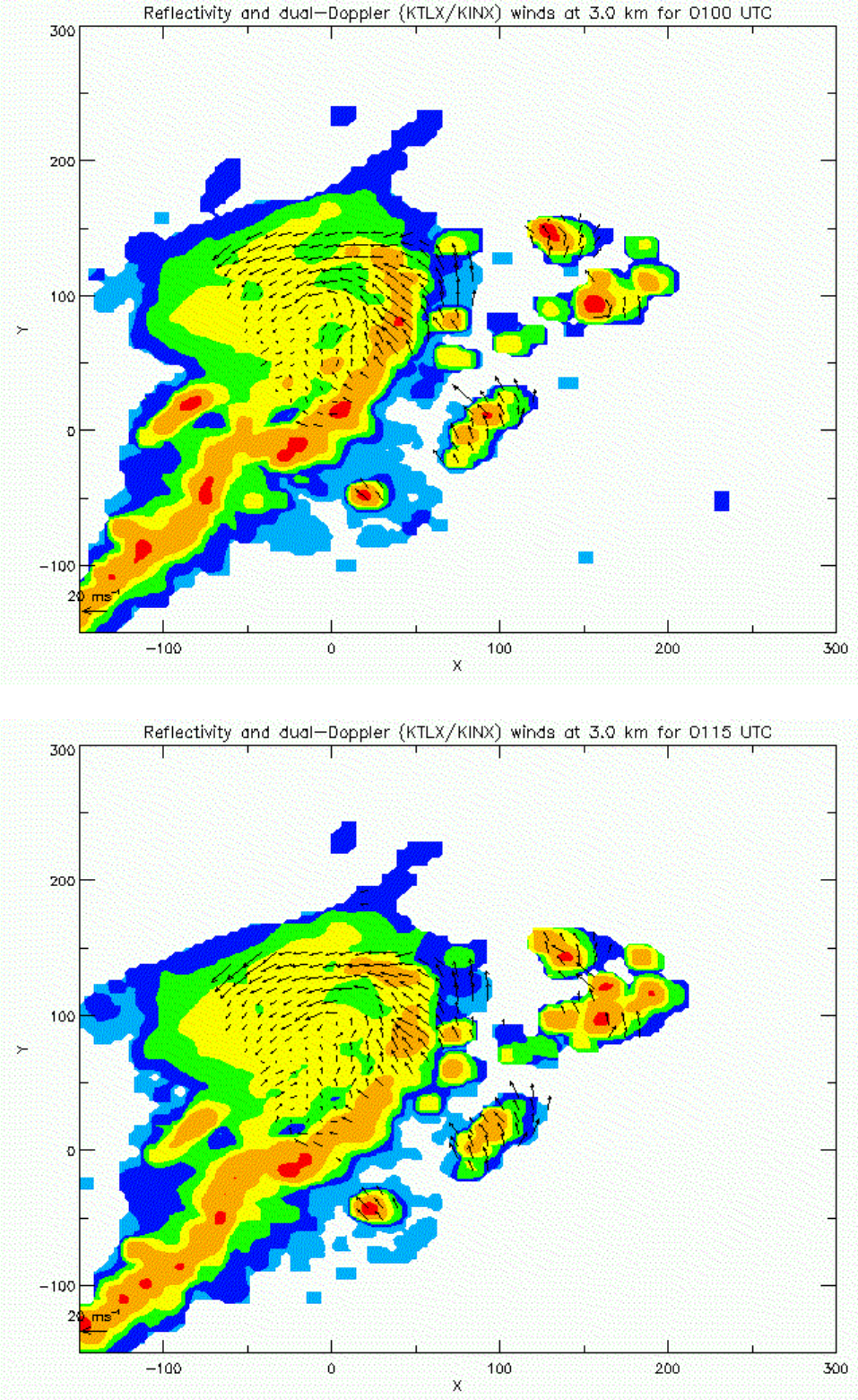

Figure 3.2 continued.

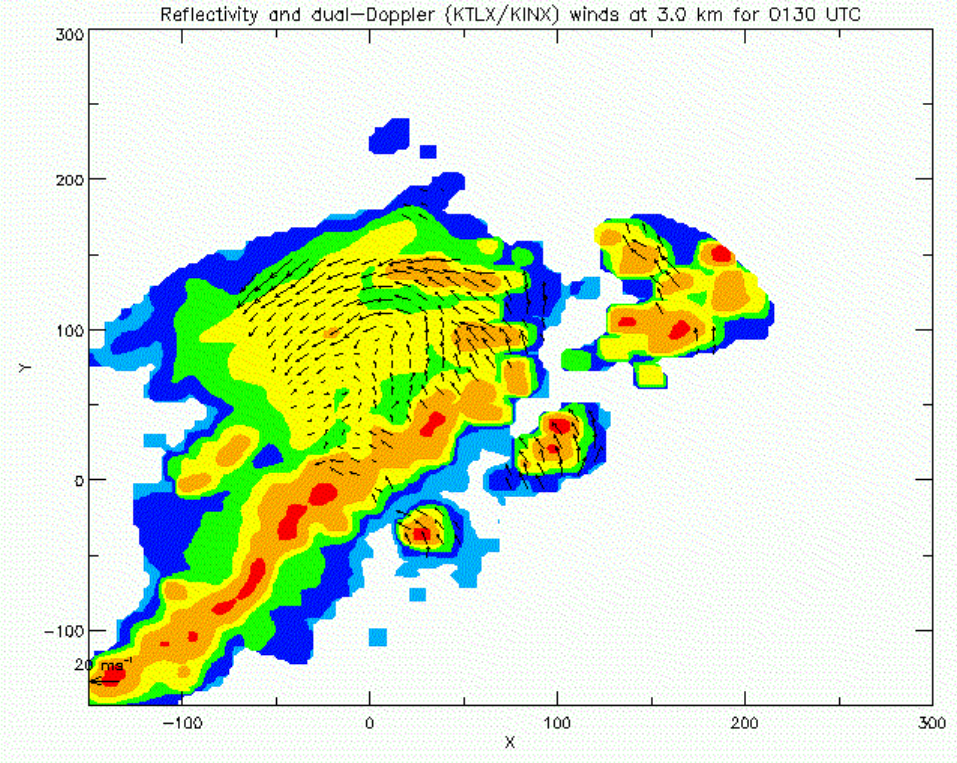

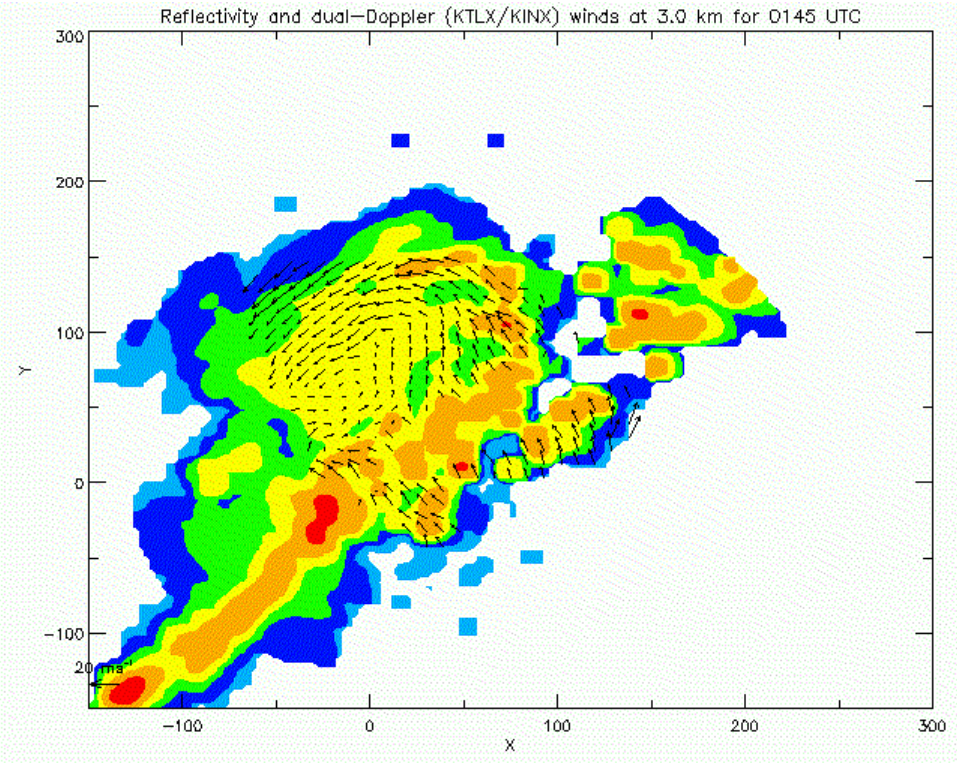

Figure 3.2 continued.

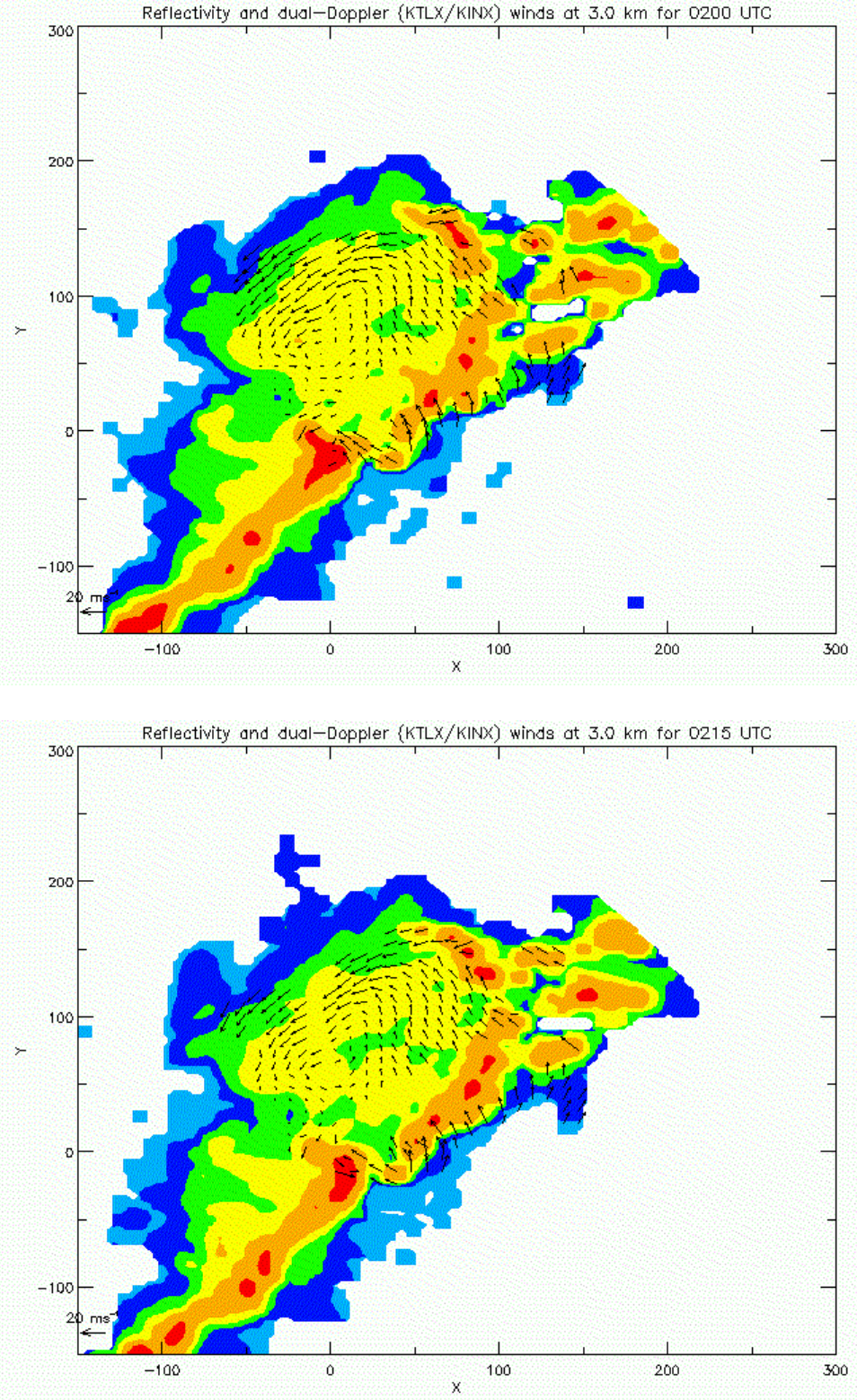

Figure 3.2 continued.

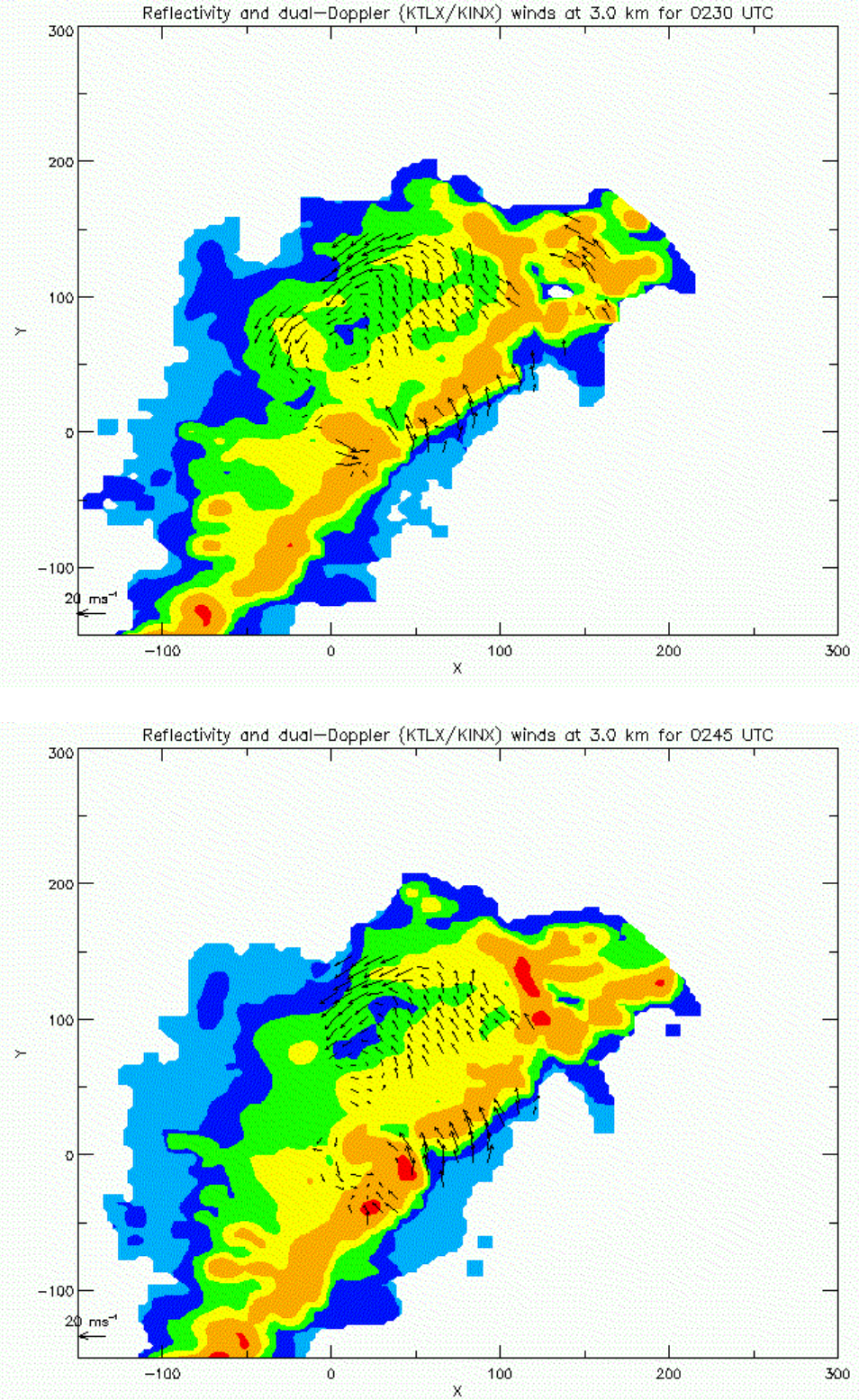

Figure 3.2 continued.

Fig. 3.3 shows reflectivity and storm-relative wind vectors derived from dual-Doppler analysis at 4.5 km altitude for fifteen minute intervals between 0000 and 0245 UTC. At 0000 and 0015 UTC there is no indication of circulation, however the wind vectors closely follow the 40 dBZ contour including where it curves back into the stratiform region as seen in the hook echo at 3.0 km (Fig. 3.2). This suggests that at least at these two times that circulation associated with the MCV might have started at lower levels (i.e., 3.0 km). An hour and a half later, once the MCV has formed and increased in size, decaying cells from the convective leading line clearly feed back into the broader circulation in the stratiform region. It is expected that once mature cells from the leading convective line begin to decay that they are advected back into the stratiform region by the ascending front-to-rear mesoscale flow (Houze et al. 1989). At 0215 UTC, the gap in data at x = -10.0 km that was seen at 3.0 km also occurred at 4.5 km. The MCV has an elliptical southwest to northeast oriented circulation, but the diameter across the longest region of the ellipse is approximately 100 km at this altitude. Of particular interest is another area of cyclonic rotation that developed within the leading convective line that appears just southeast of the KTLX radar located at (x = 0.0, y = 0.0).

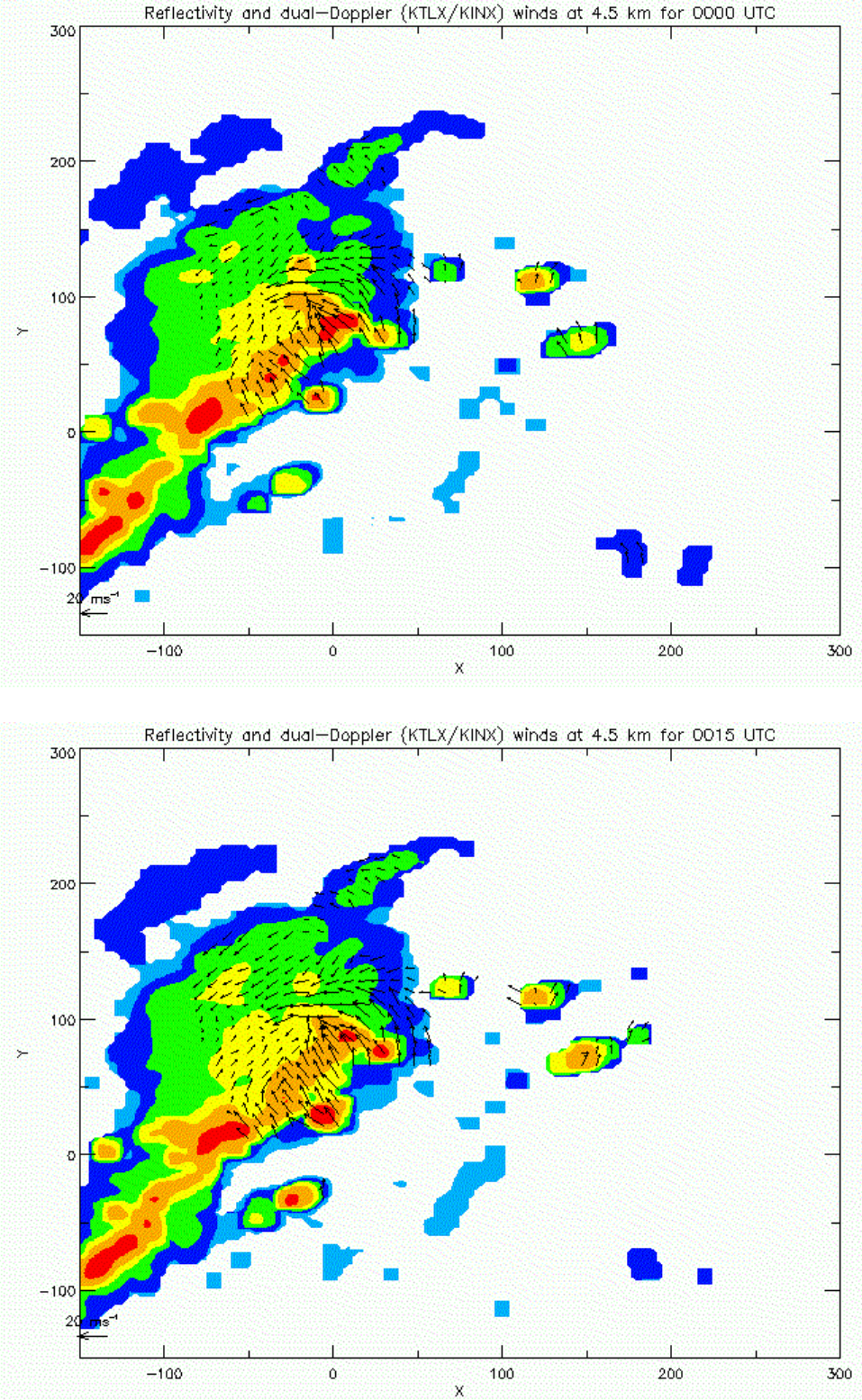

Figure 3.3. Reflectivity and storm-relative wind vectors for fifteen minute intervals between 0000 and 0245 UTC at 4.5 km altitude. Reflectivity scaled in 10 dBZ increments from 0 dBZ (light blue) to 50 dBZ (red).

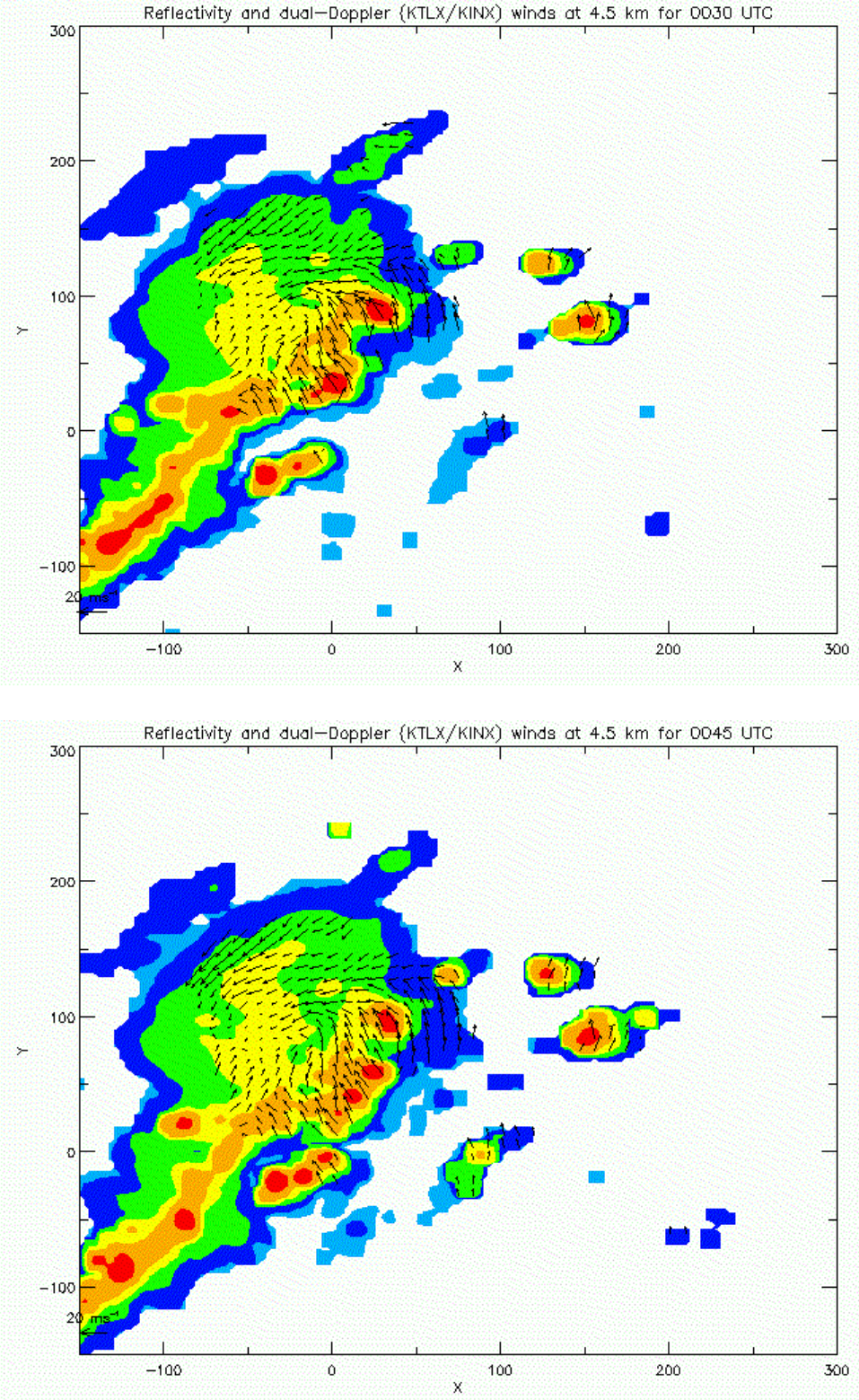

Figure 3.3 continued.

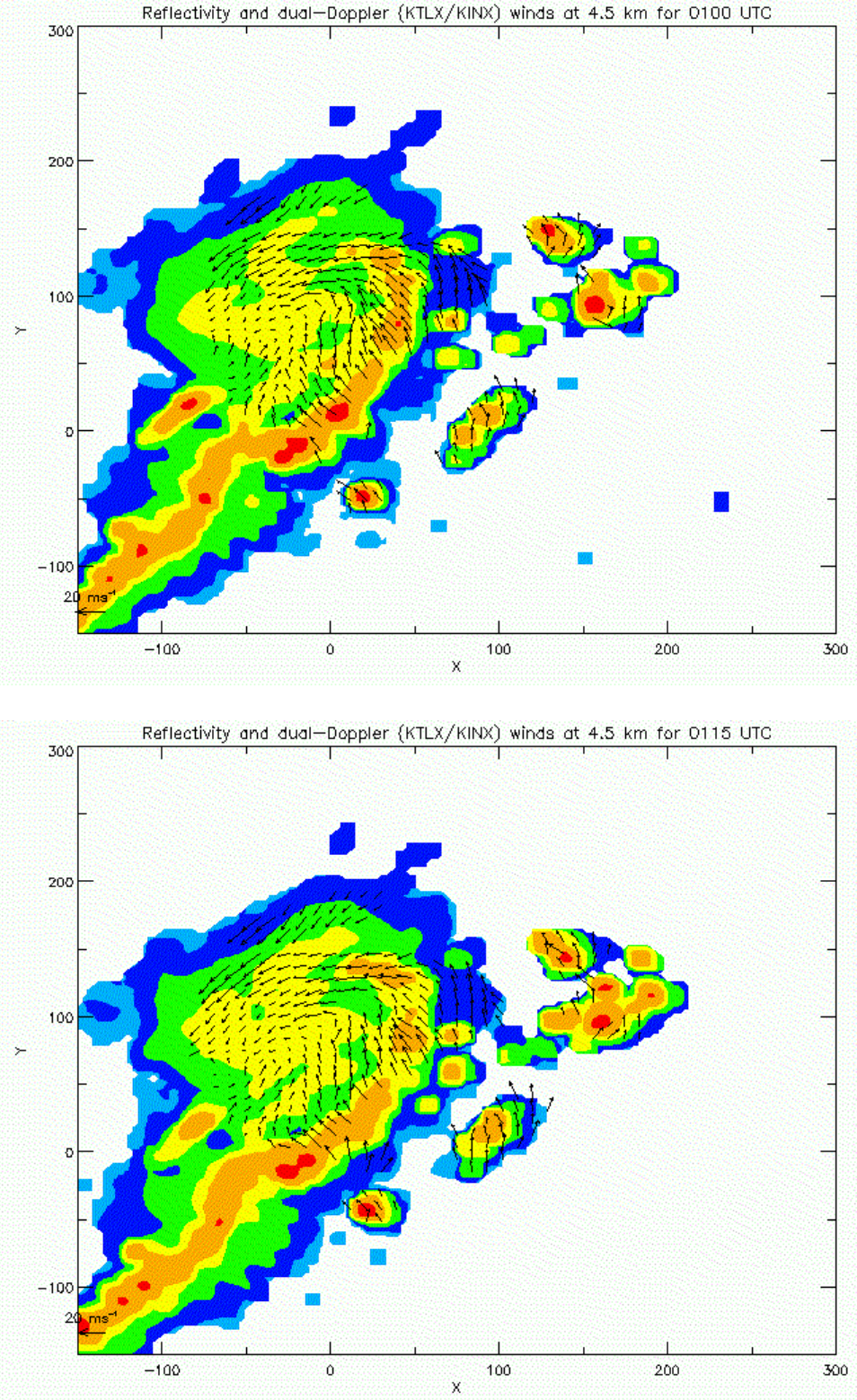

Figure 3.3 continued.

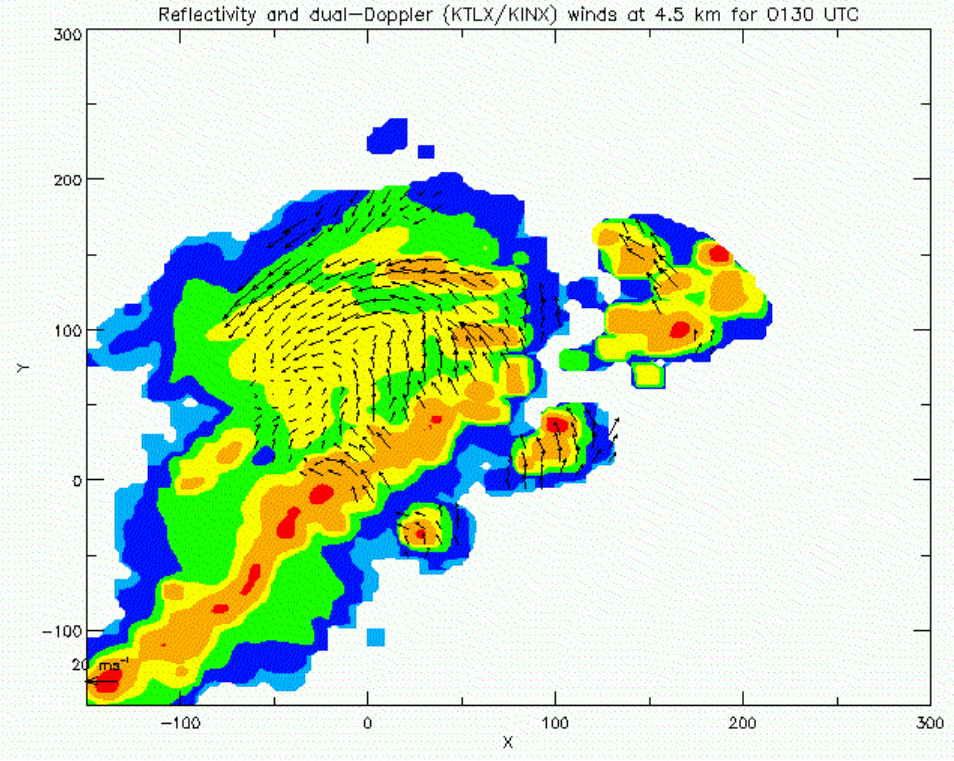

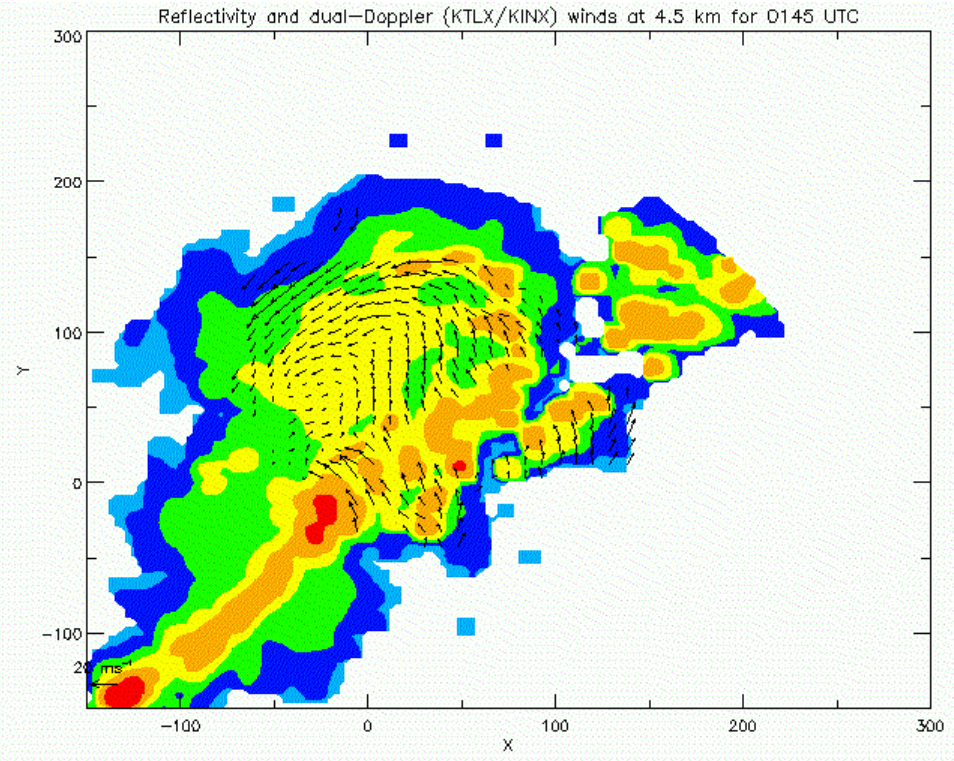

Figure 3.3 continued.

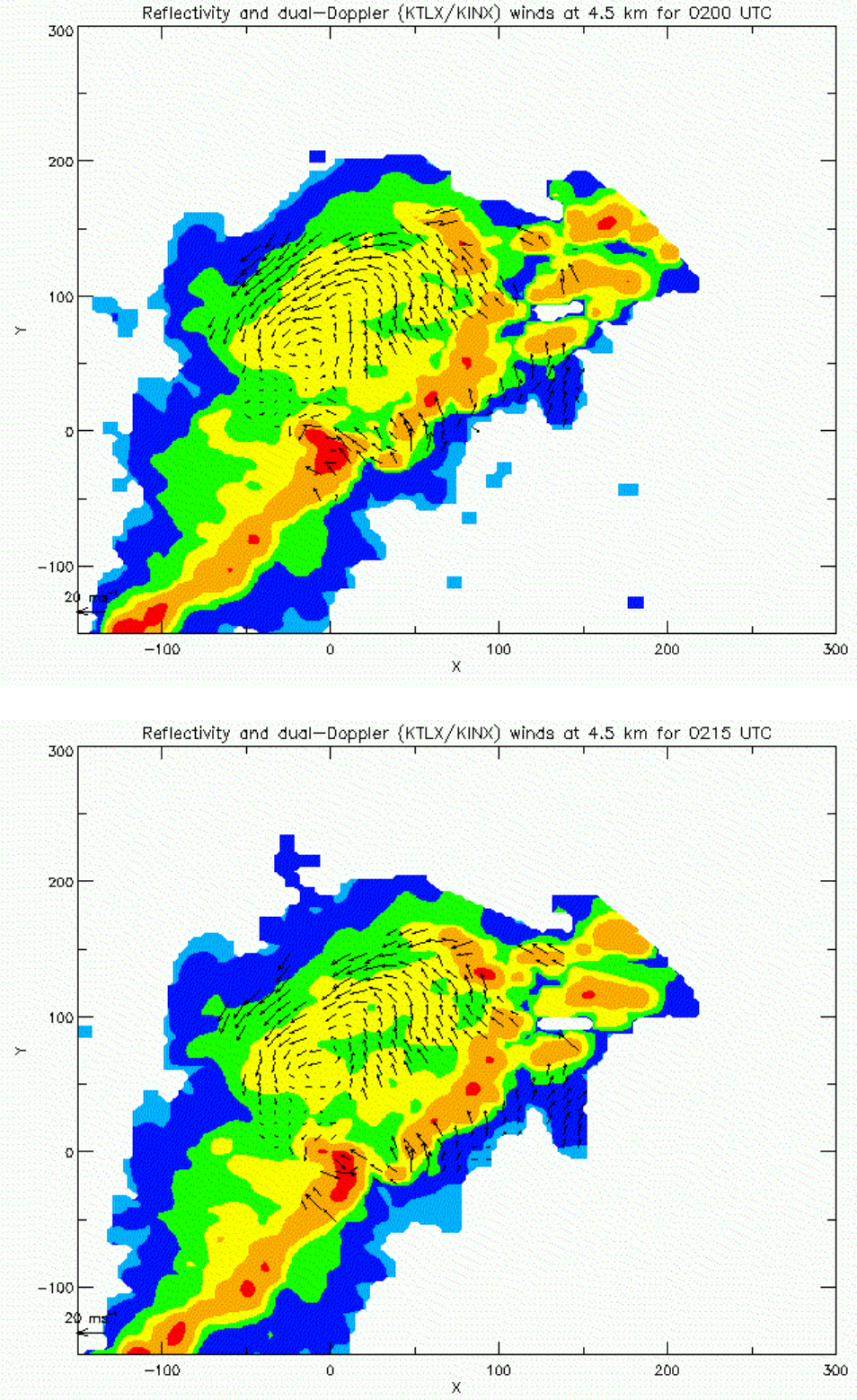

Figure 3.3 continued.

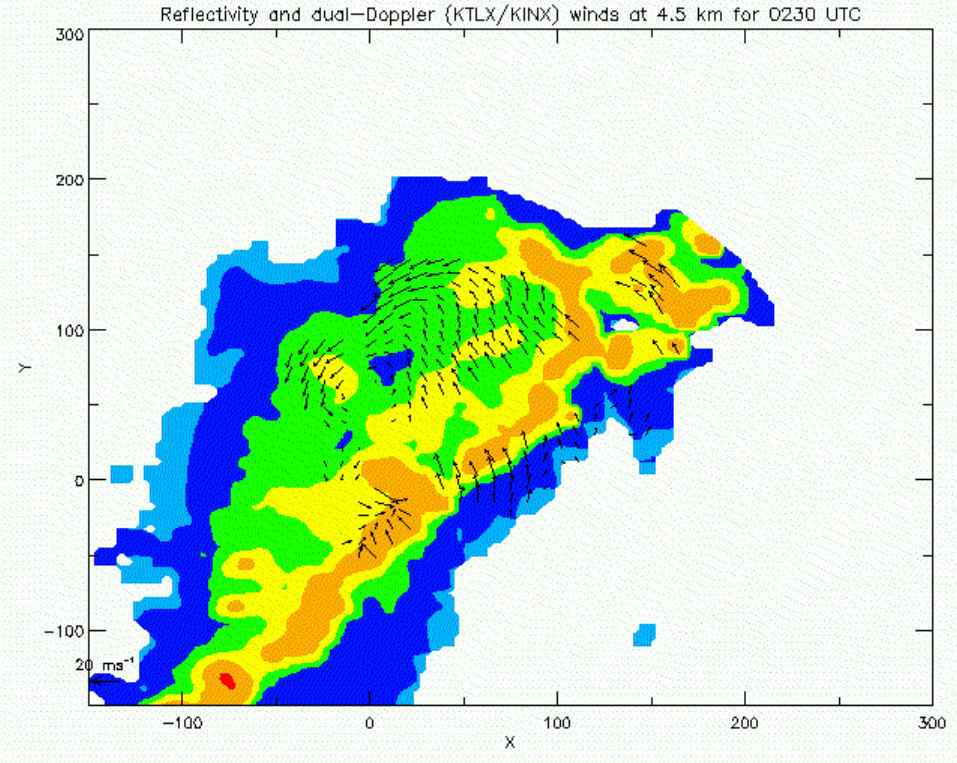

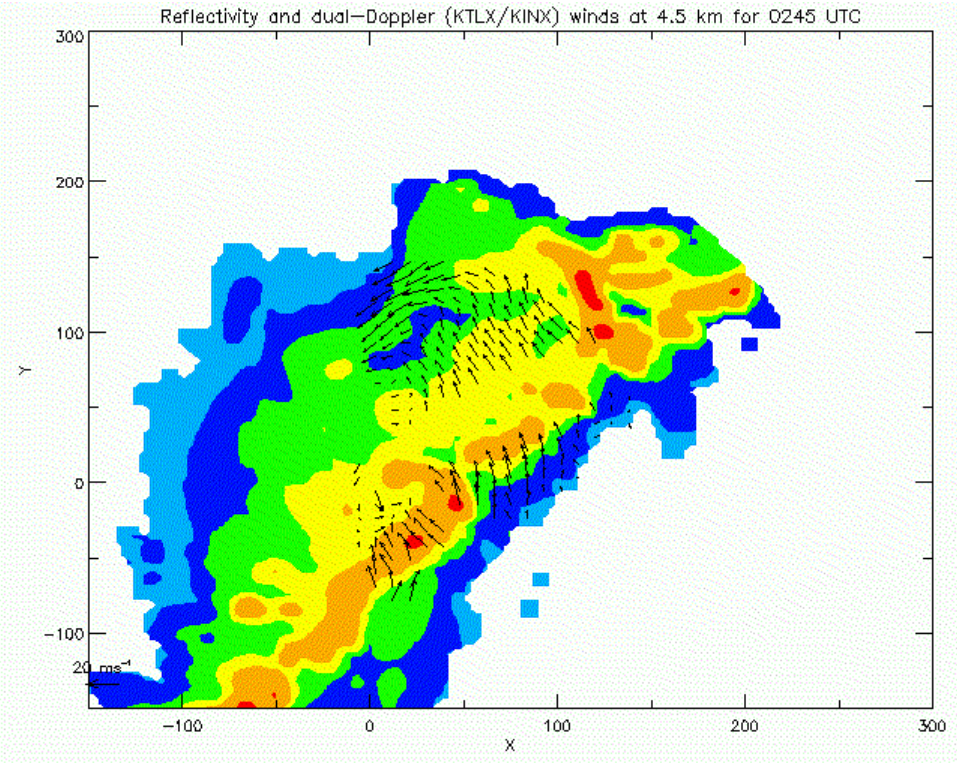

Figure 3.3 continued.

Figure 3.4 shows reflectivity and storm-relative wind vectors derived from dual-Doppler analysis at 5.5 km altitude for fifteen minute intervals between 0000 and 0245 UTC. Convergence but no organized circulation occurs at early times (0000 through 0030 UTC) in the stratiform region in the area of 30 dBZ reflectivity behind the transition zone adjacent to the leading convective line. There is a reflectivity hook that appears at other levels and a sense of some circulation that is definitely not closed. At 0045 UTC, a cyclonic circulation with an elliptical shape becomes more apparent in the dual-Doppler analyses and is located from (x = -10.0, y = 90.0) to (x = -75.0, y = 90.0). An hour later, the circulation associated with the MCV is clearly larger at 0145 UTC. The small vortex located to the southeast of the KTLX radar (x = 0.0, y = 0.0) at 4.5 km is also apparent at 5.5 km altitude by 0215 UTC.

Fig. 3.5 shows reflectivity and storm-relative wind vectors derived from dual-Doppler analysis at 7.0 km altitude for fifteen minute intervals between 0000 and 0245 UTC. Similar to 5.5 km, convergence occurred in the stratiform region up to 0130 UTC. At 0145 UTC there is a suggestion of circulation at the edge of the dual-Doppler lobe (x = -50.0, y = 50.0). Fifteen minutes later it becomes evident that cyclonic rotation extended up to 7.0 km and is centered at approximately (x = -40.0, y = 60.0).

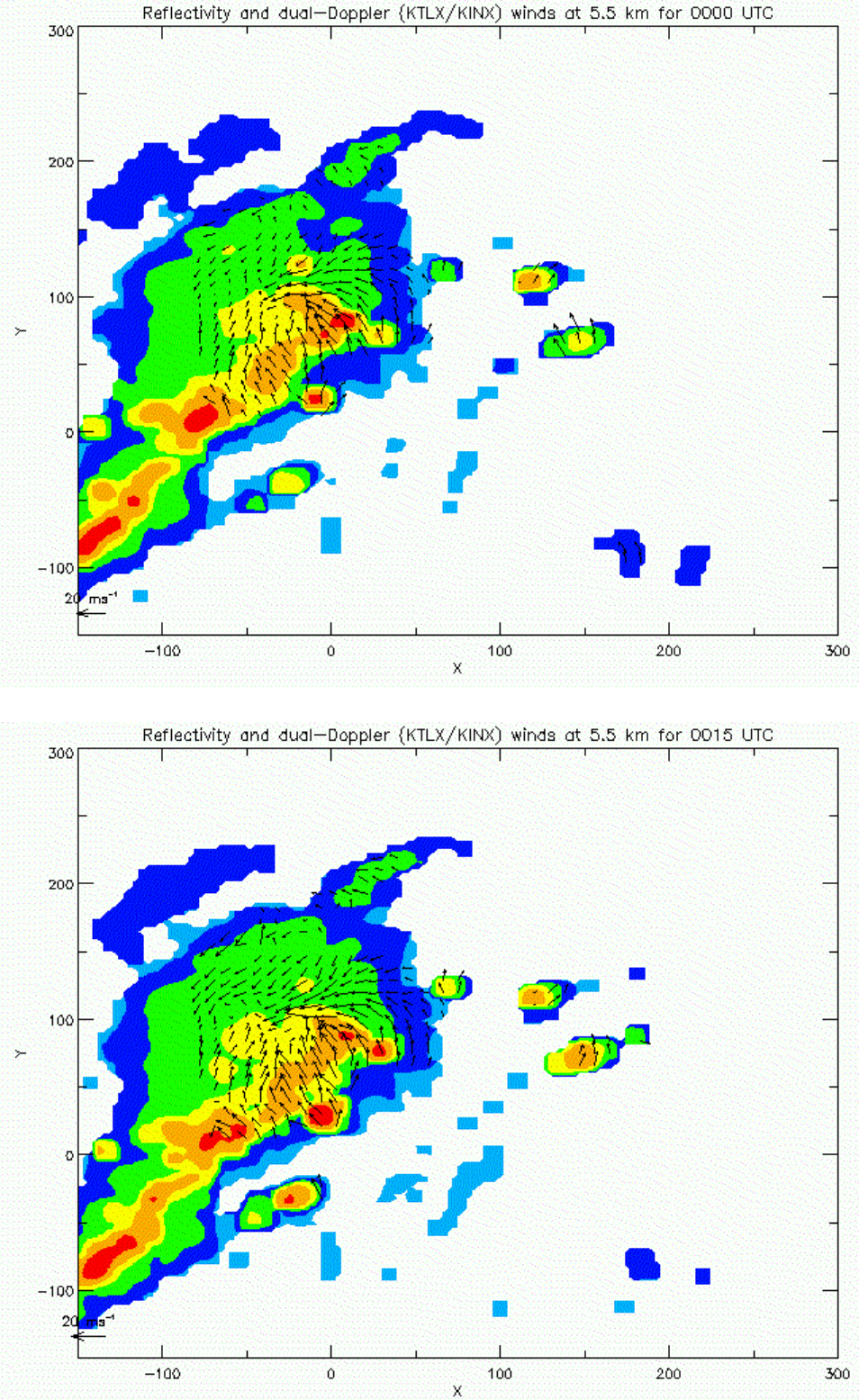

Figure 3.4. Reflectivity and storm-relative wind vectors for fifteen minute intervals between 0000 and 0245 UTC at 5.5 km altitude. Reflectivity scaled in 10 dBZ increments from 0 dBZ (light blue) to 50 dBZ (red).

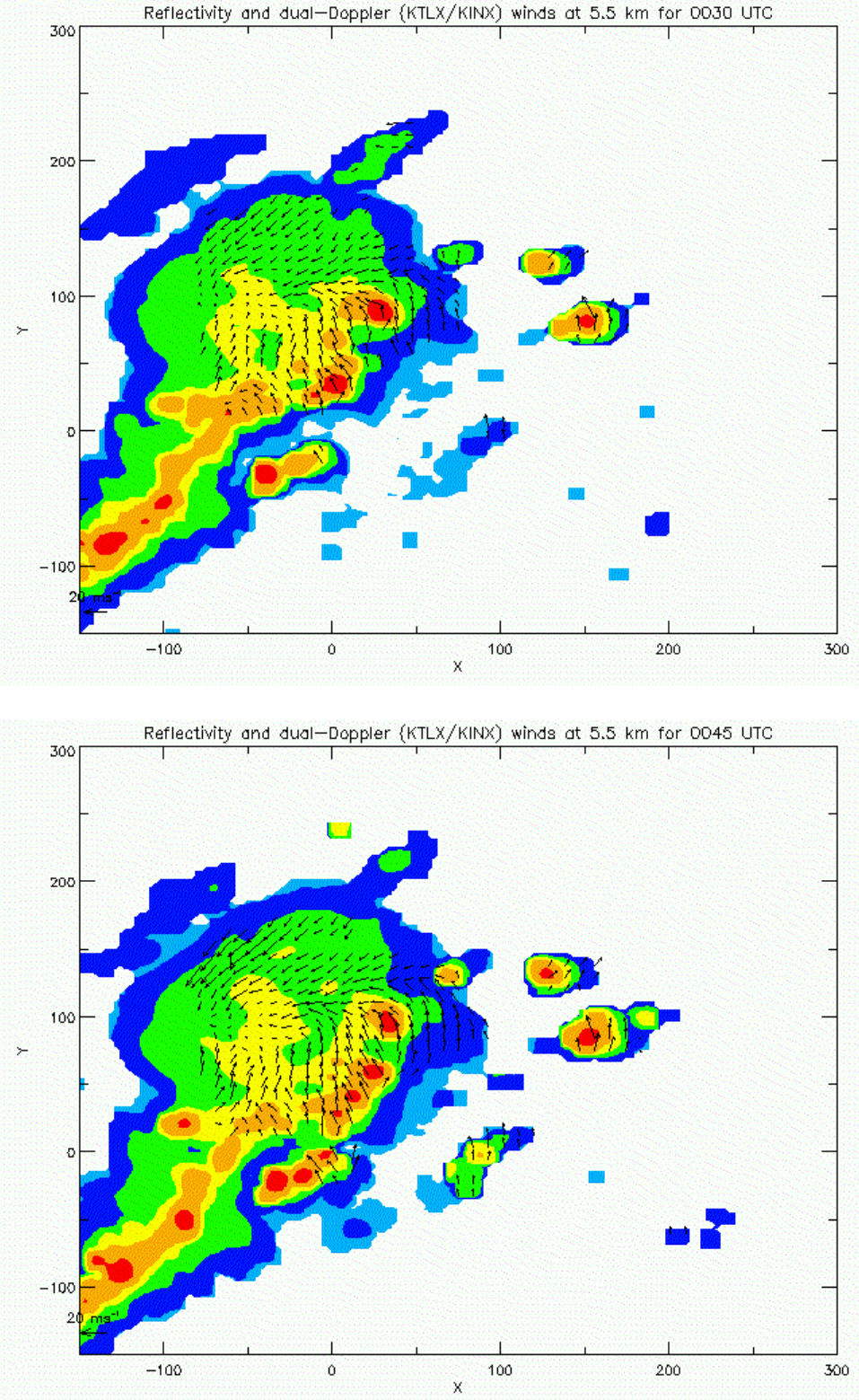

Figure 3.4 continued.

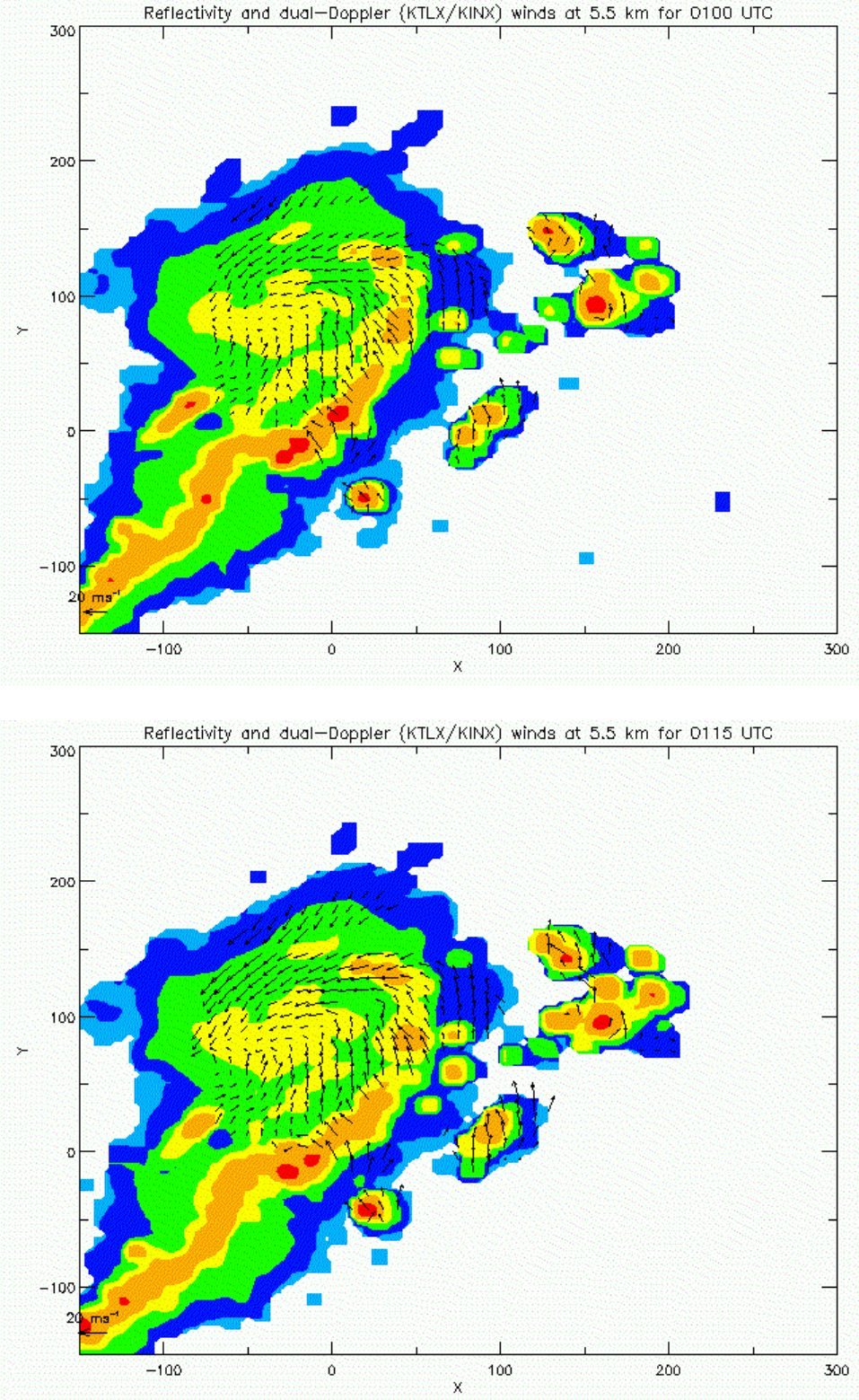

Figure 3.4 continued.

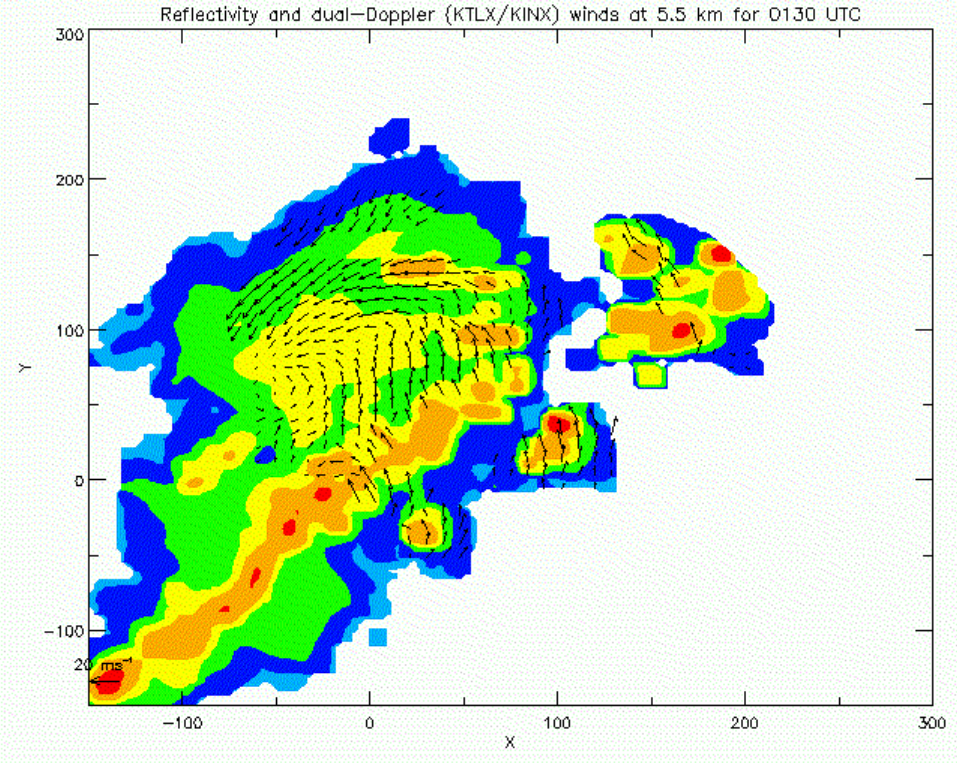

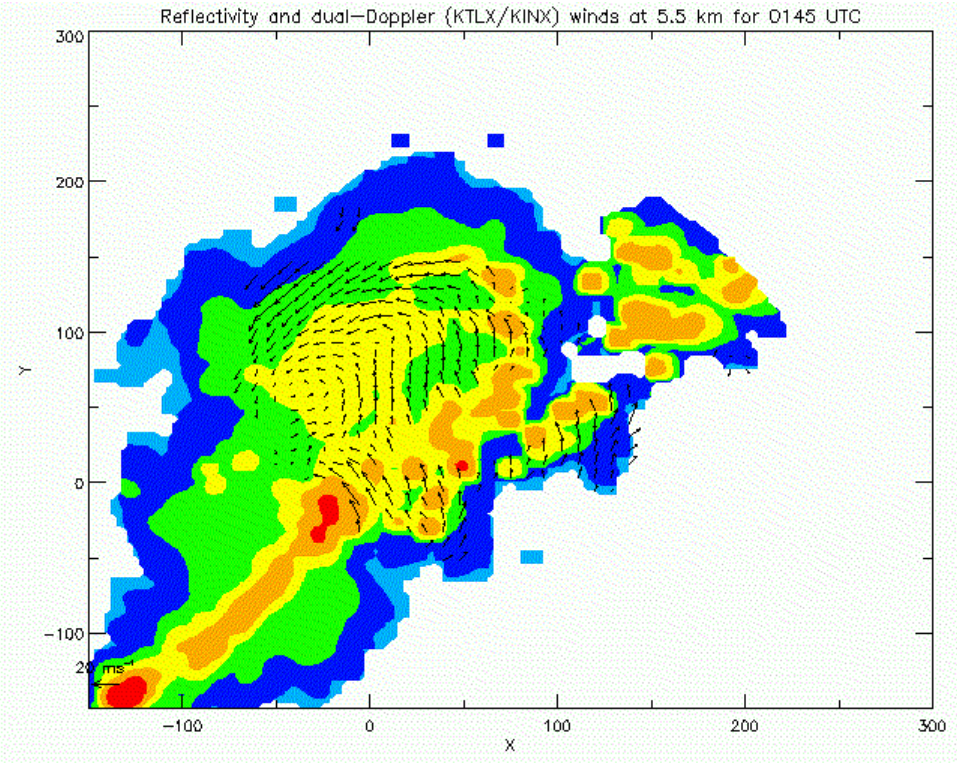

Figure 3.4 continued.

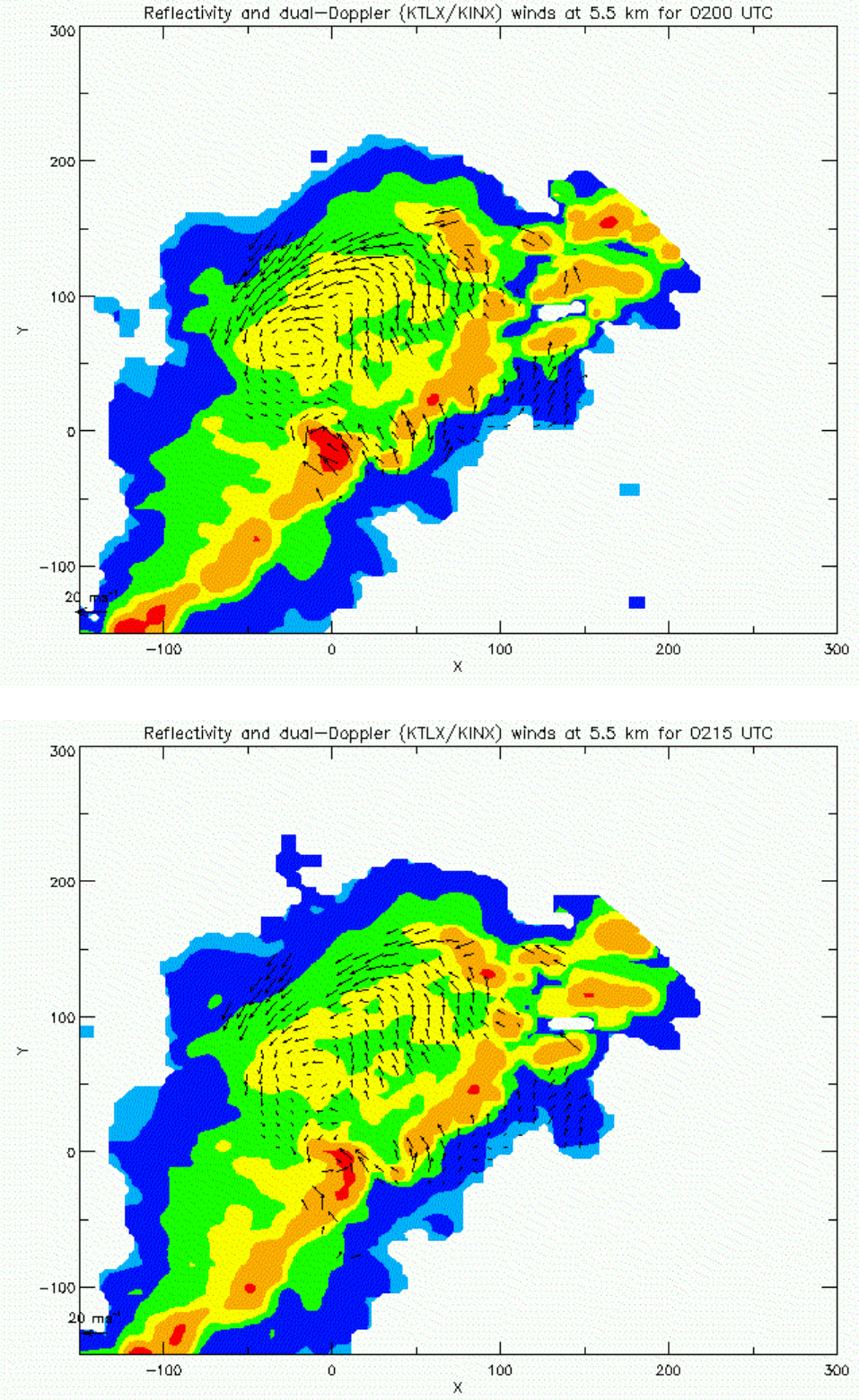

Figure 3.4 continued.

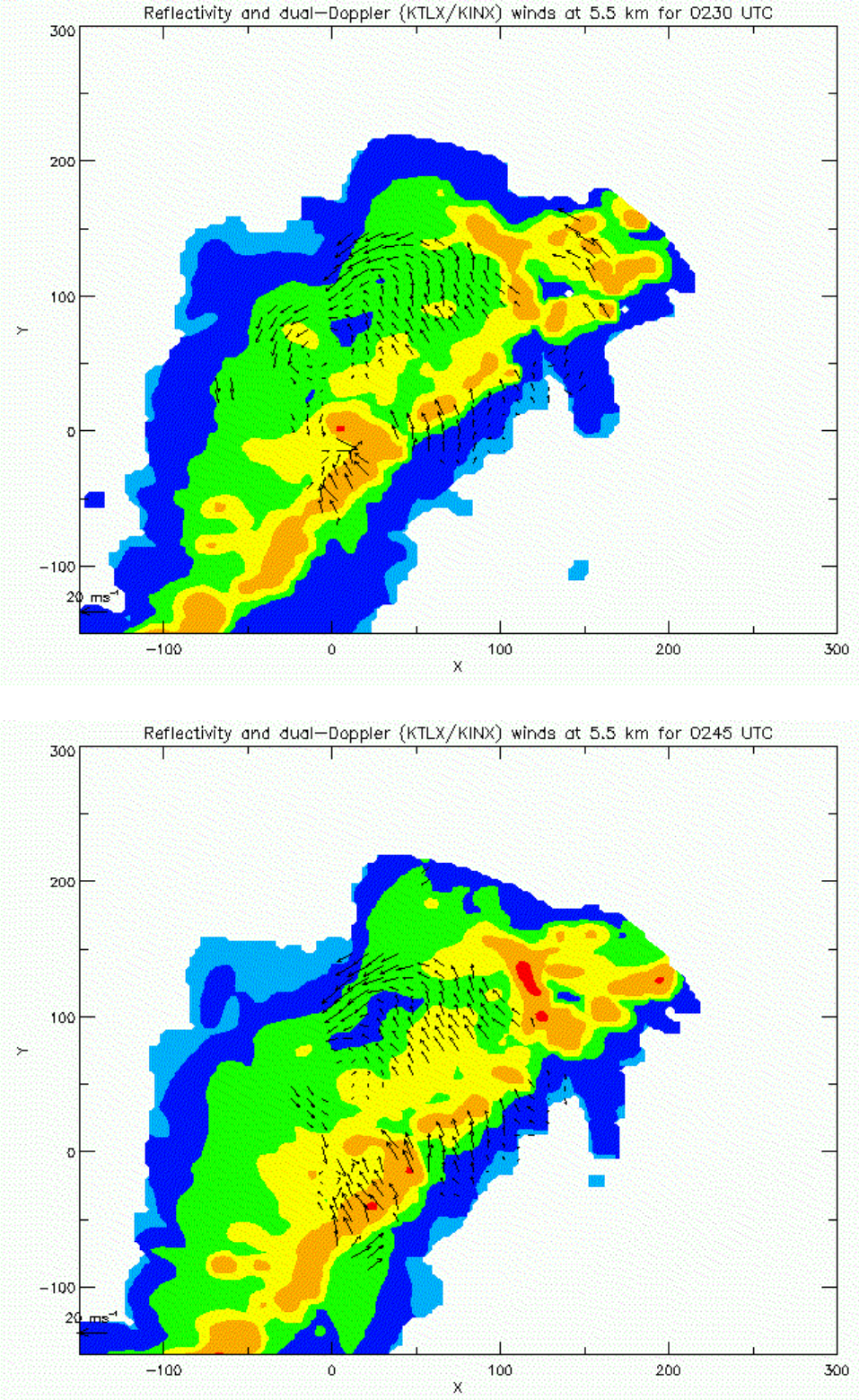

Figure 3.4 continued.

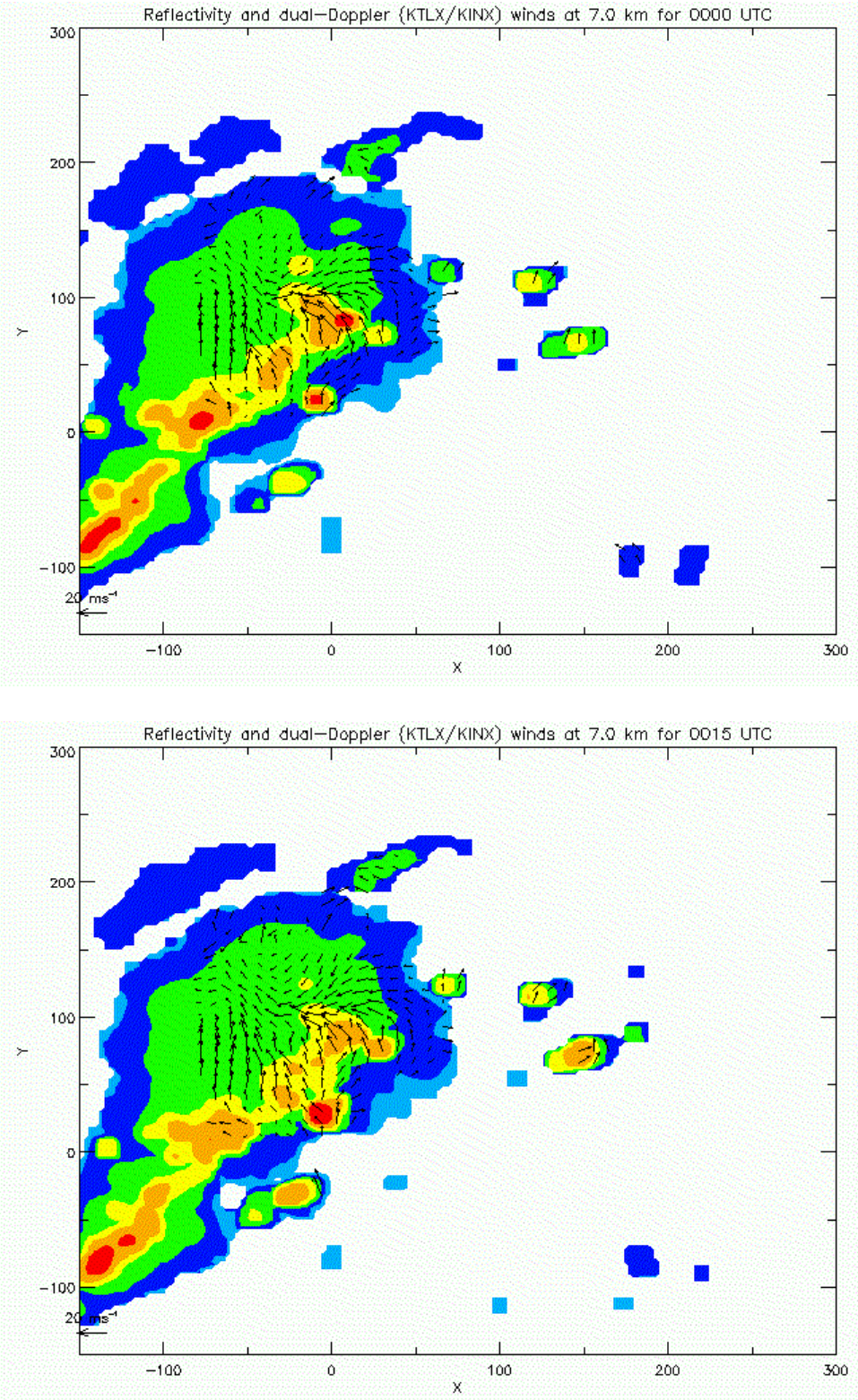

Figure 3.5. Reflectivity and storm-relative wind vectors for fifteen minute intervals between 0000 and 0245 UTC at 7.0 km altitude. Reflectivity scaled in 10 dBZ increments from 0 dBZ (light blue) to 50 dBZ (red).

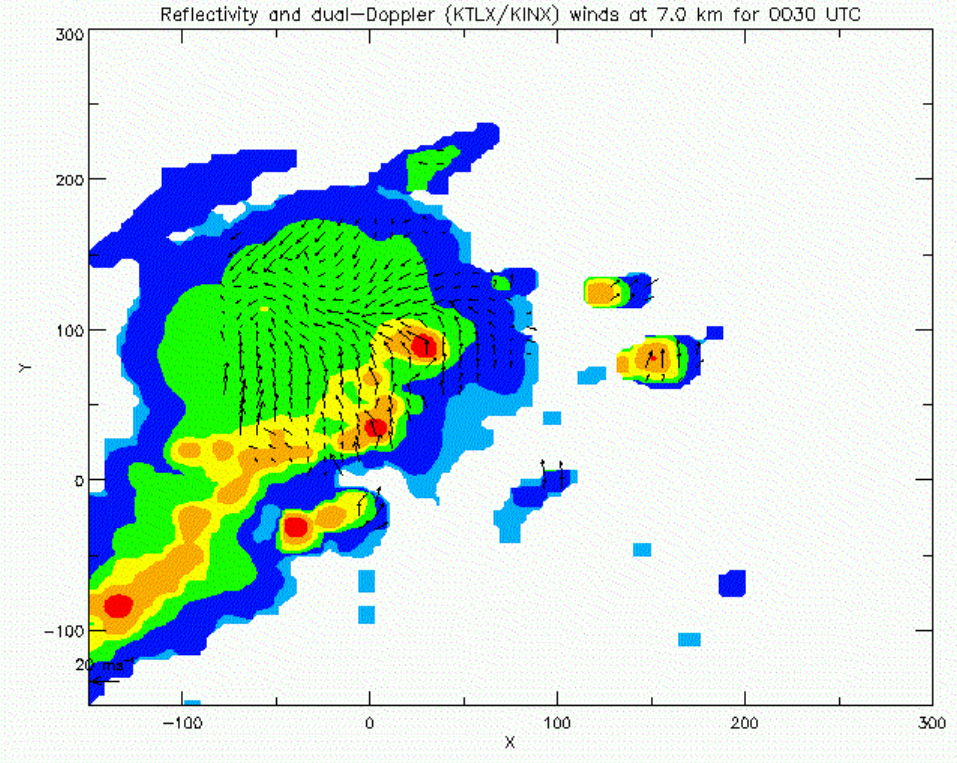

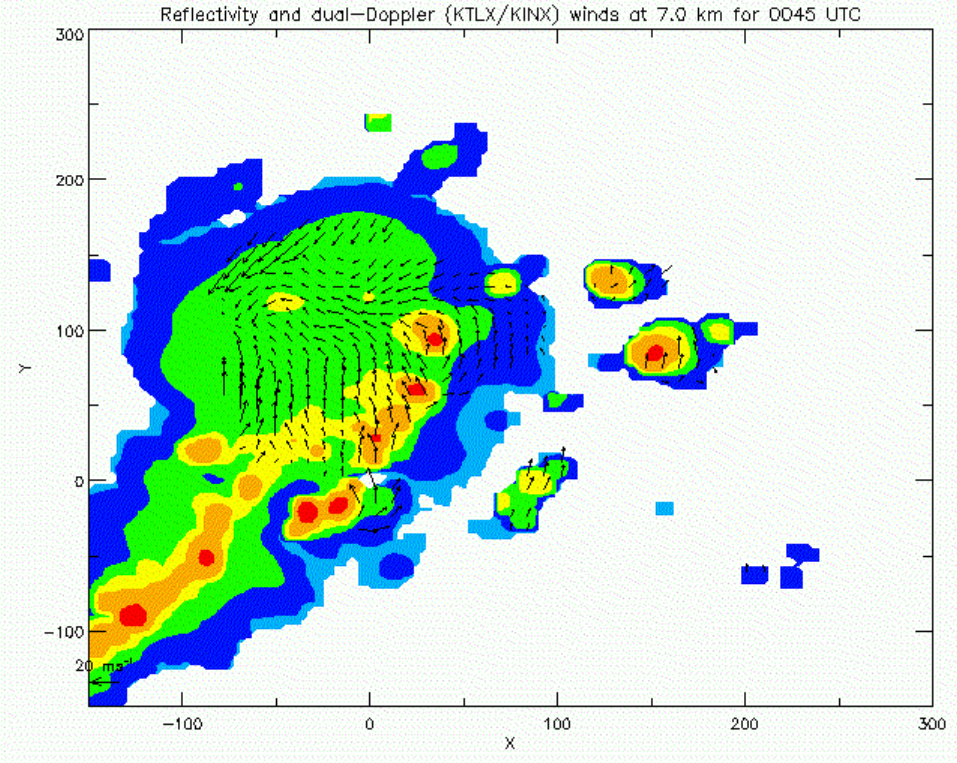

Figure 3.5 continued.

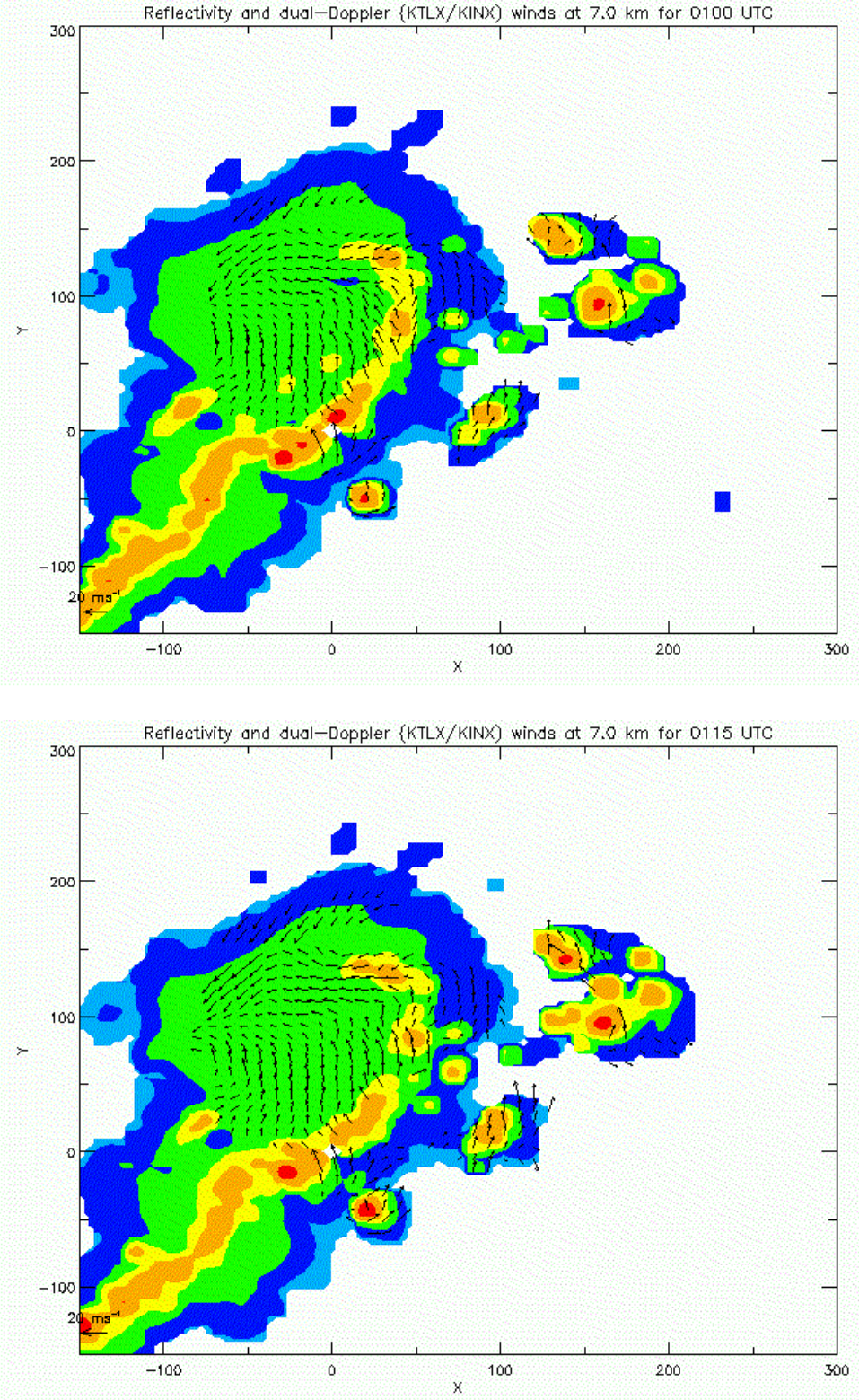

Figure 3.5 continued.

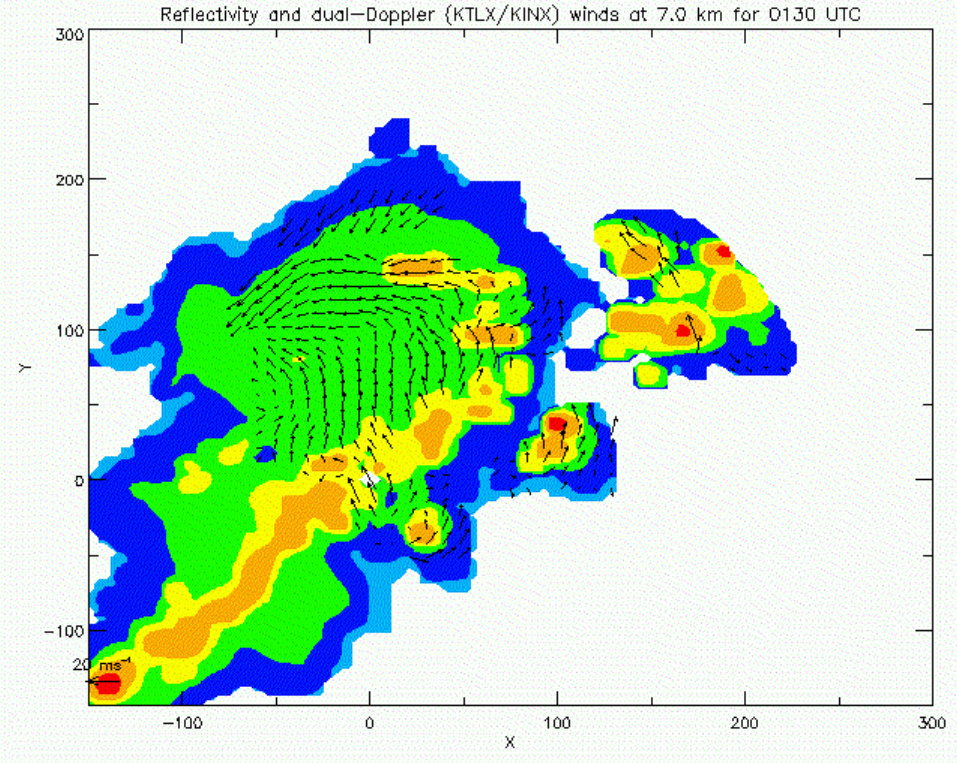

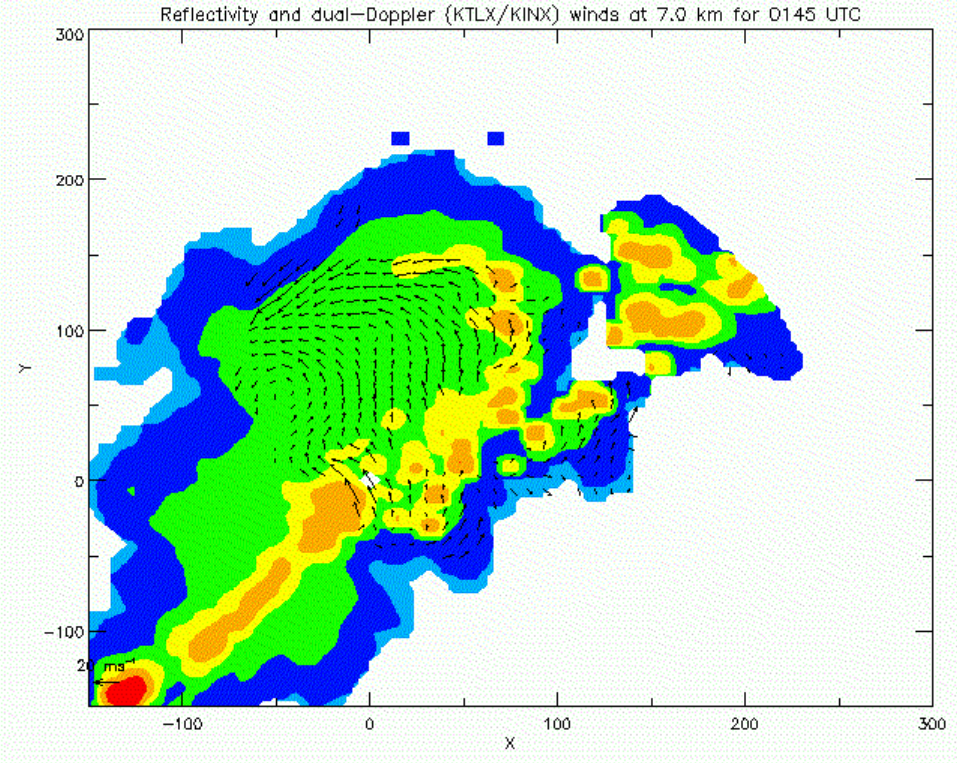

Figure 3.5 continued.

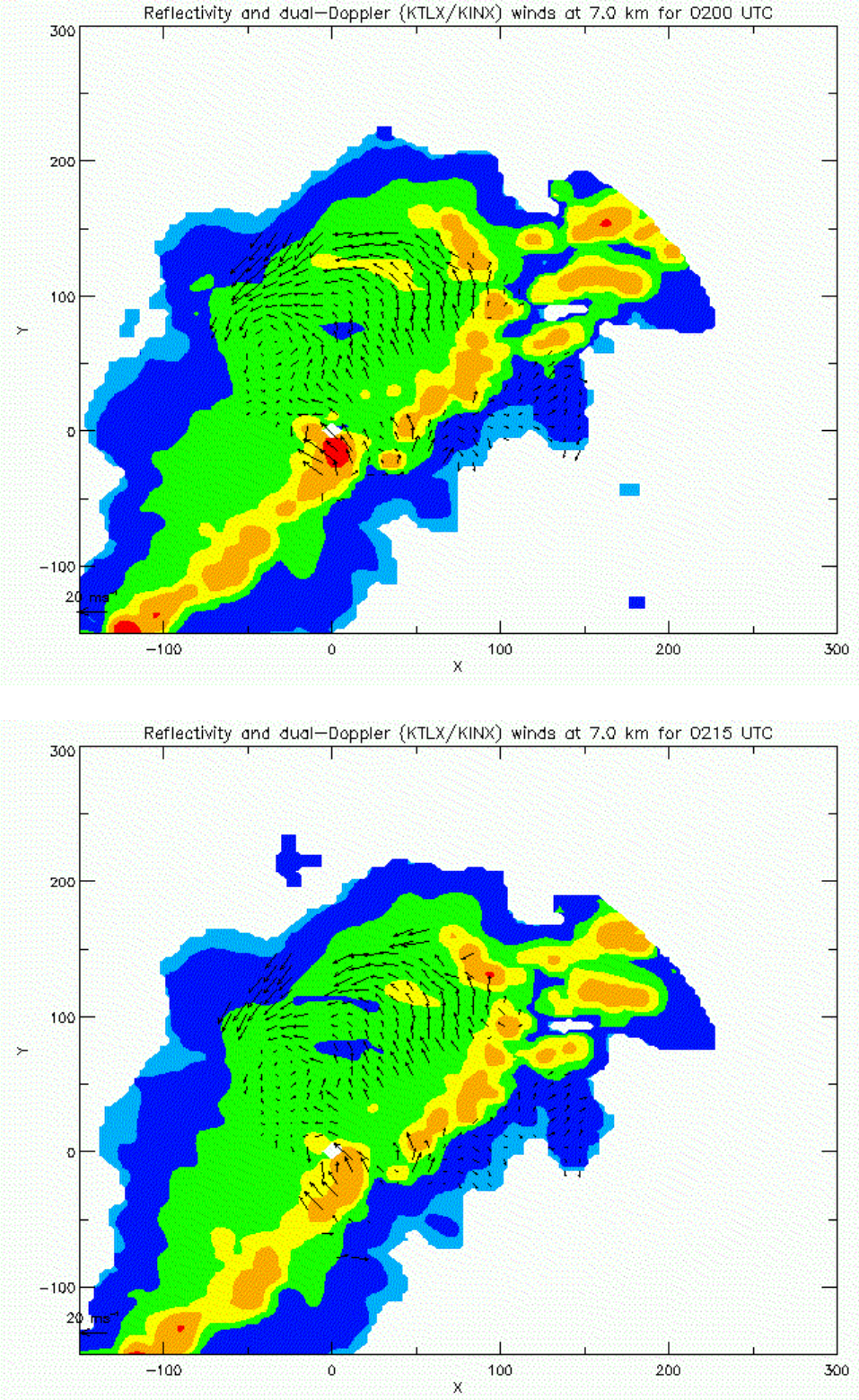

Figure 3.5 continued.

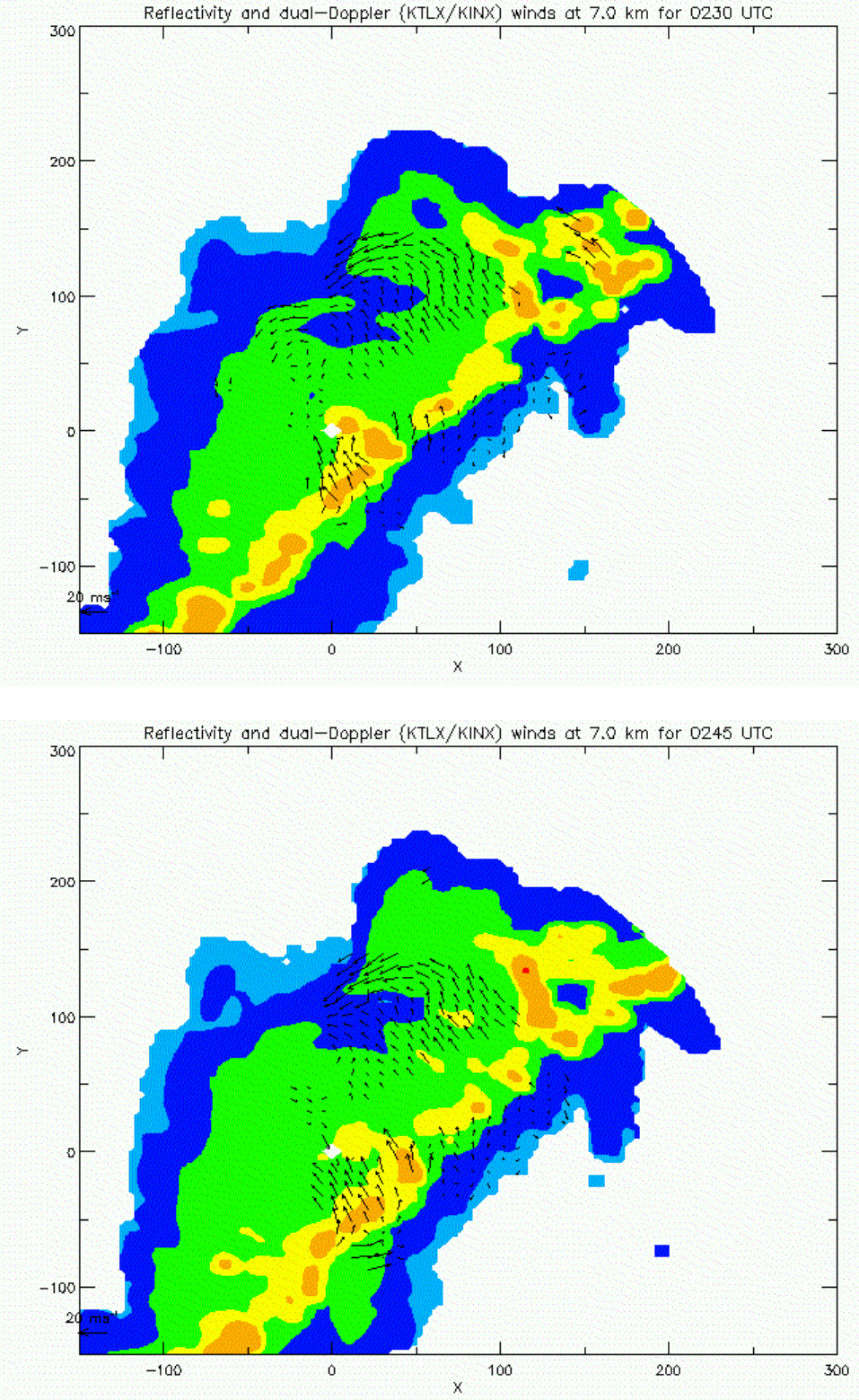

Figure 3.5 continued.

Fig. 3.6 shows reflectivity and storm-relative wind vectors derived from dual-Doppler analysis at 10.0 km altitude for fifteen minute intervals between 0000 and 0245 UTC. Divergent outflow occurs from the convective line at all analysis times which is expected at high altitudes (Houze et al 1989; Biggerstaff and Houze 1991). For example, at 0115 UTC divergent outflow can be seen ahead of the convective line from the front of the leading line and rearwards from the back of the convective line including the curve of the convective line back into the stratiform region located at x = 40.0 between y = 70.0 and y = 150.0 km. This shows that the analyses provide both realistic and reasonable results. This divergence at upper-levels within the MCS creates the cirrus cloud of the anvil as seen in Figs. 1.2 and 1.5. At 0230 UTC, there are banded structures in the reflectivity, which are the result of data gaps due to elevation angles used in VCP-11 by the WSR-88D (see Fig. 2.1), although divergence from the convective line continues to look appropriate to what is expected.

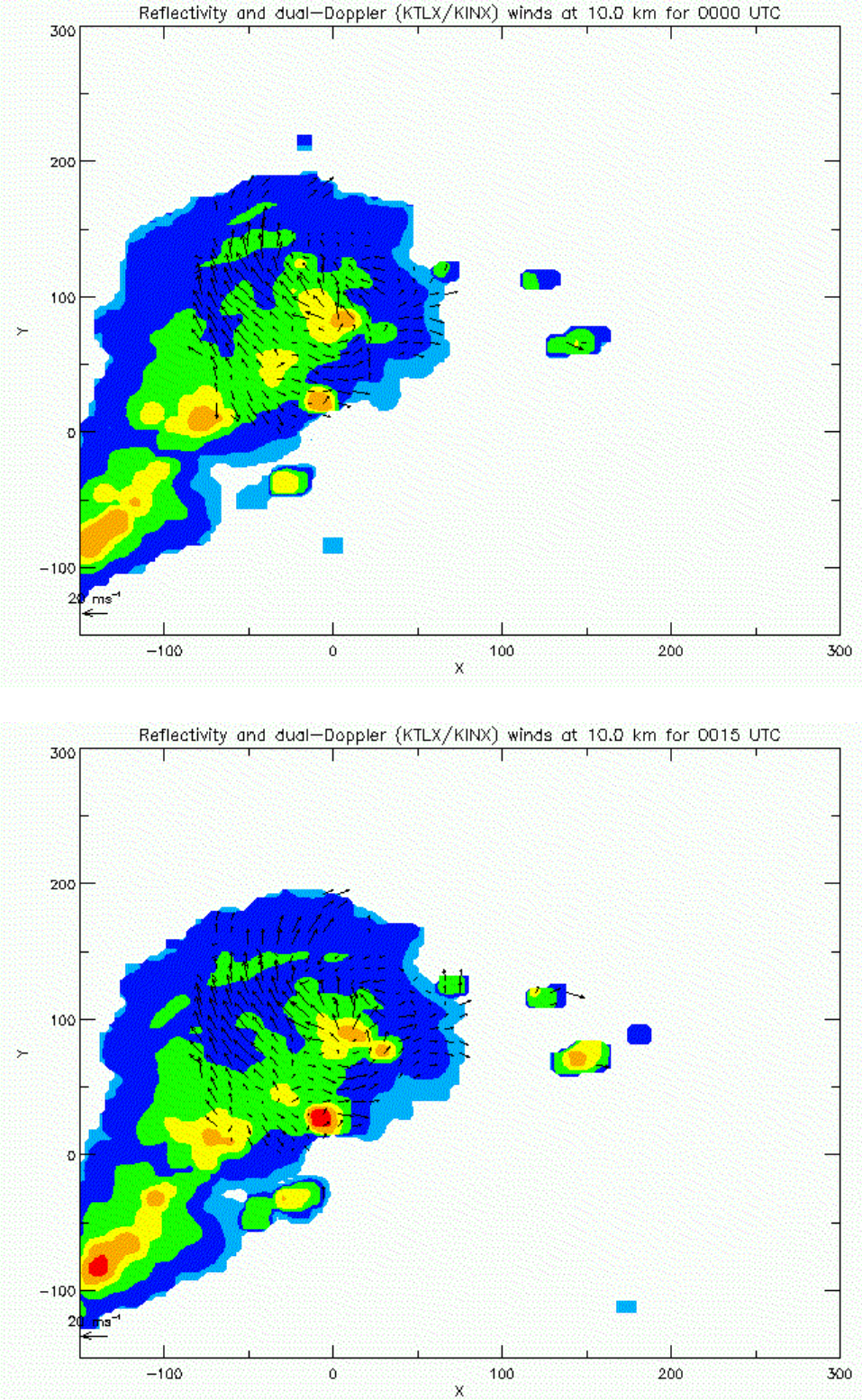

Figure 3.6. Reflectivity and storm-relative wind vectors for fifteen minute intervals between 0000 and 0245 UTC at 10.0 km altitude. Reflectivity scaled in 10 dBZ increments from 0 dBZ (light blue) to 50 dBZ (red).

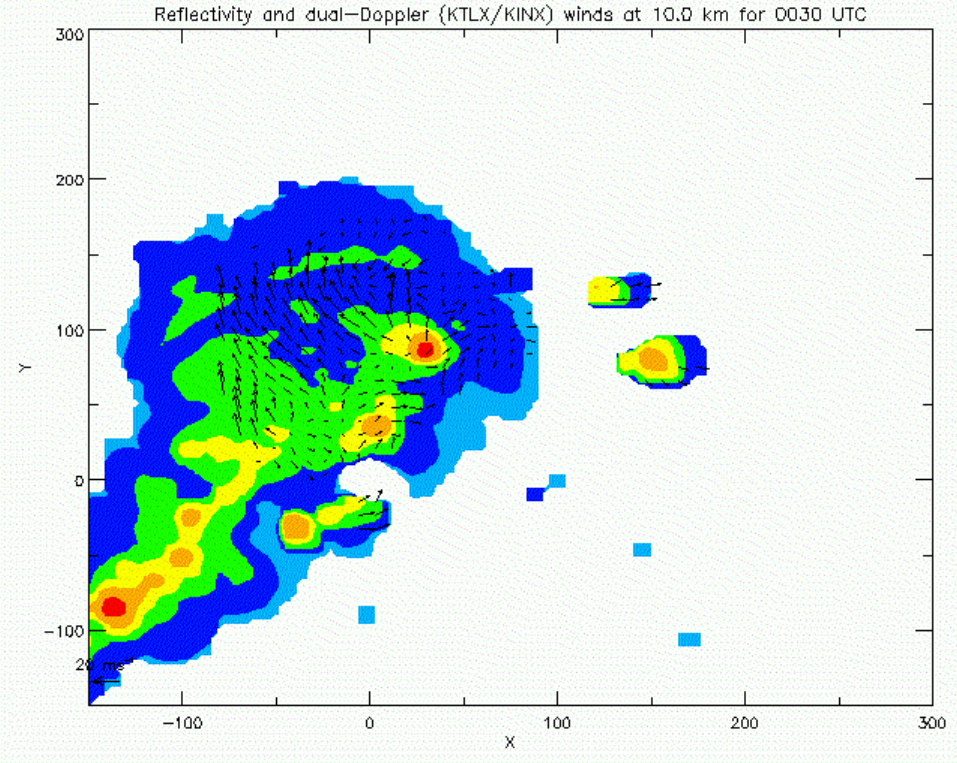

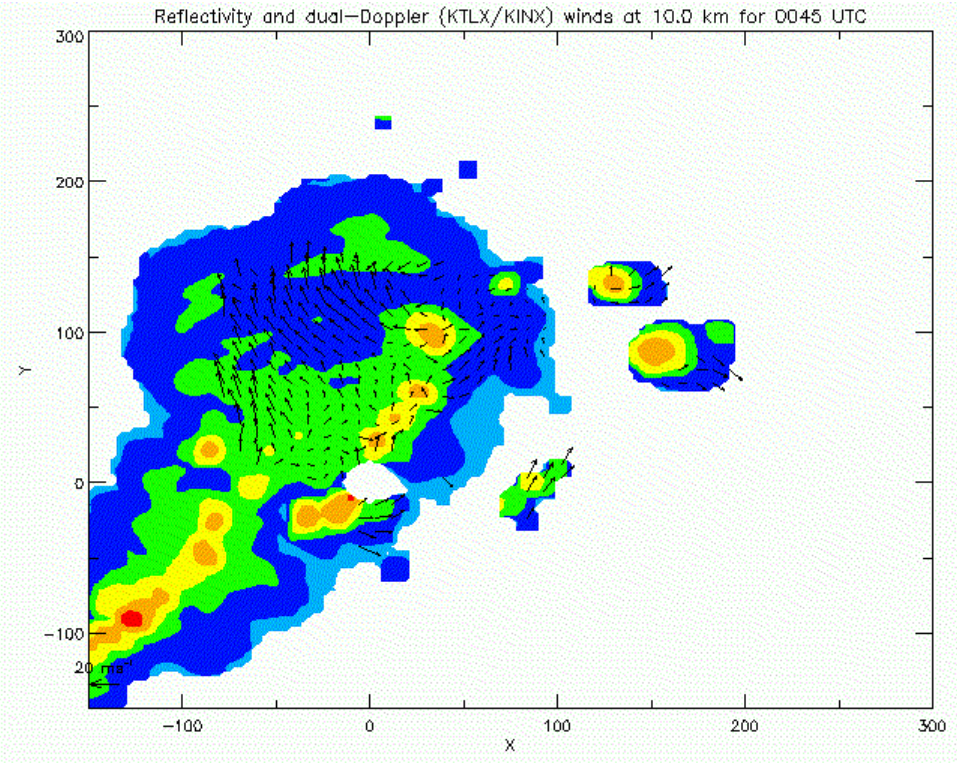

Figure 3.6 continued.

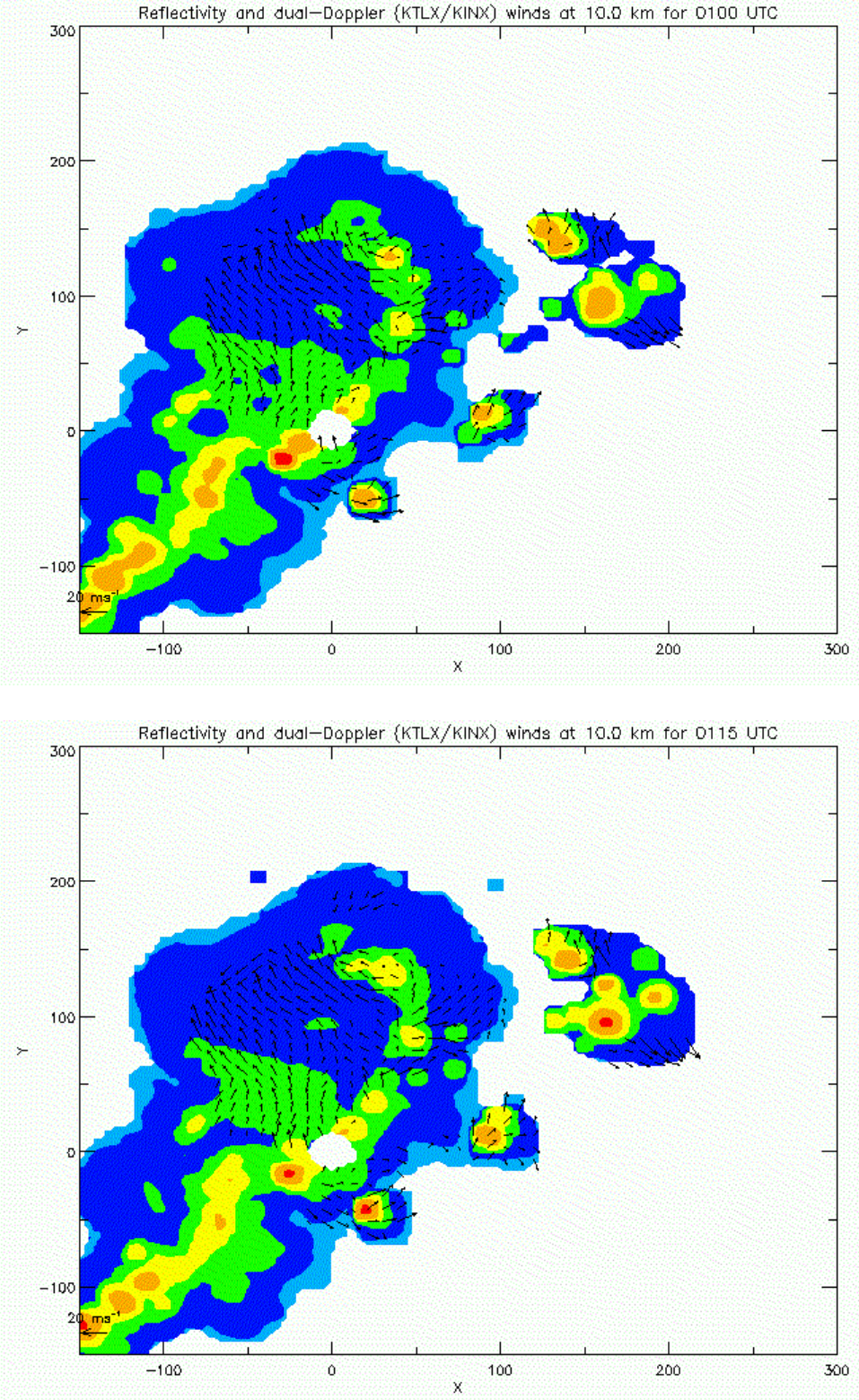

Figure 3.6 continued.

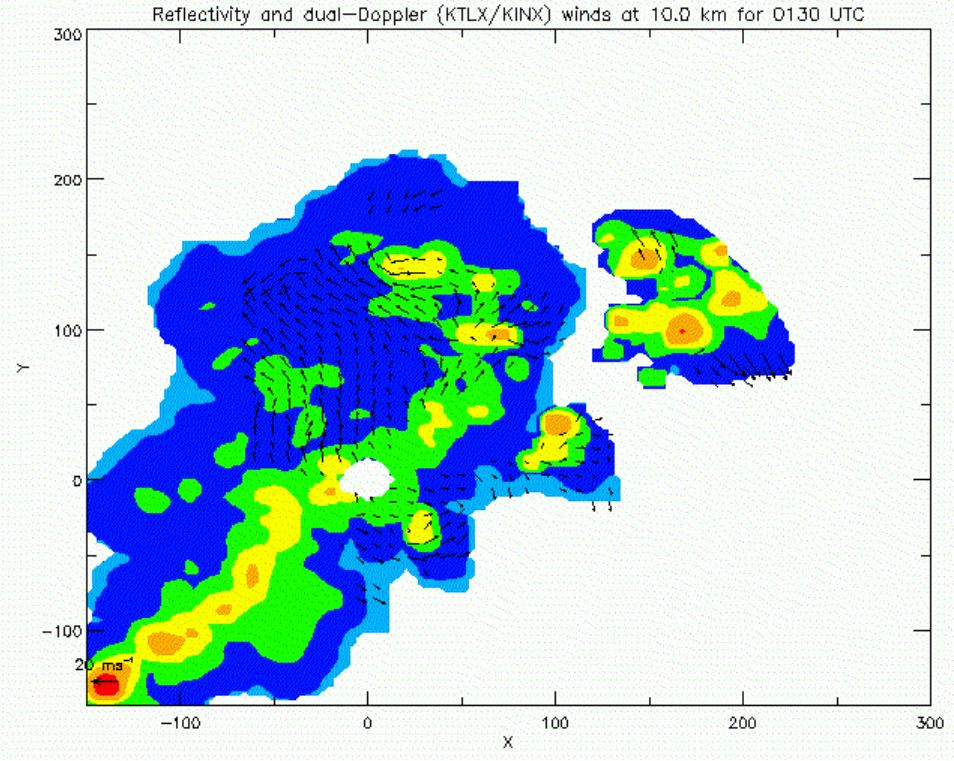

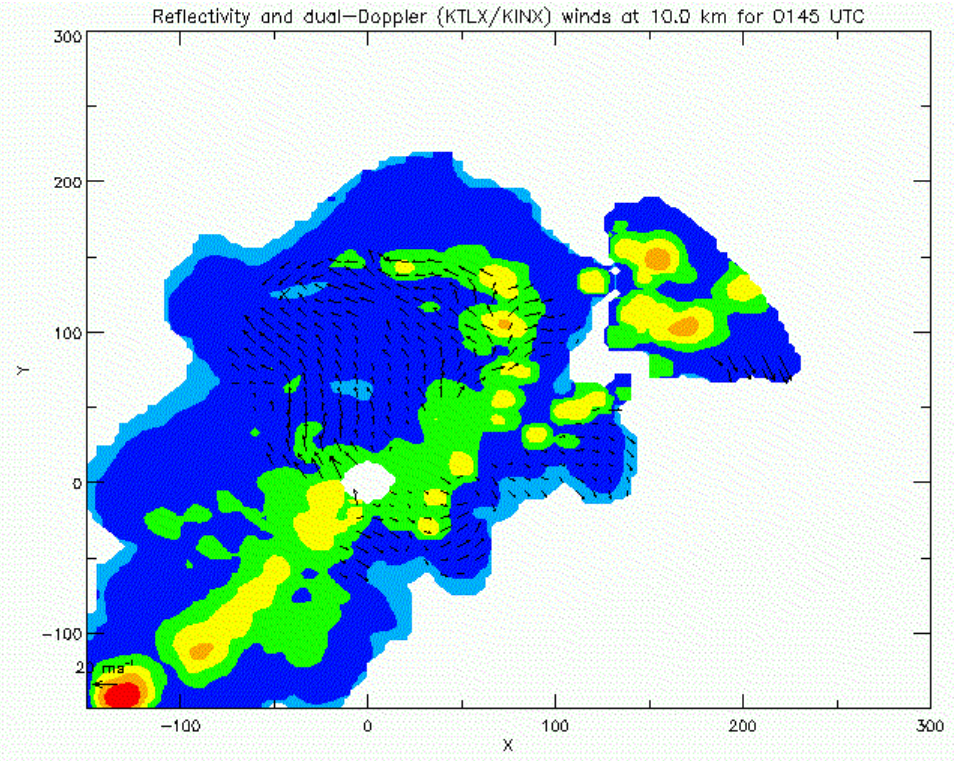

Figure 3.6 continued.

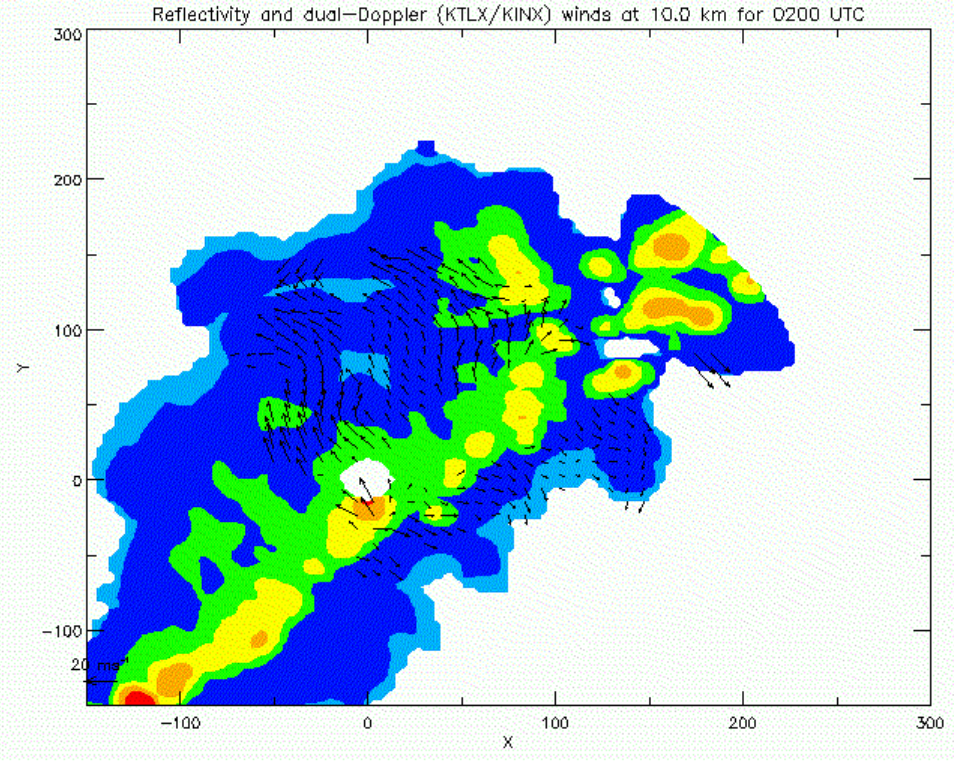

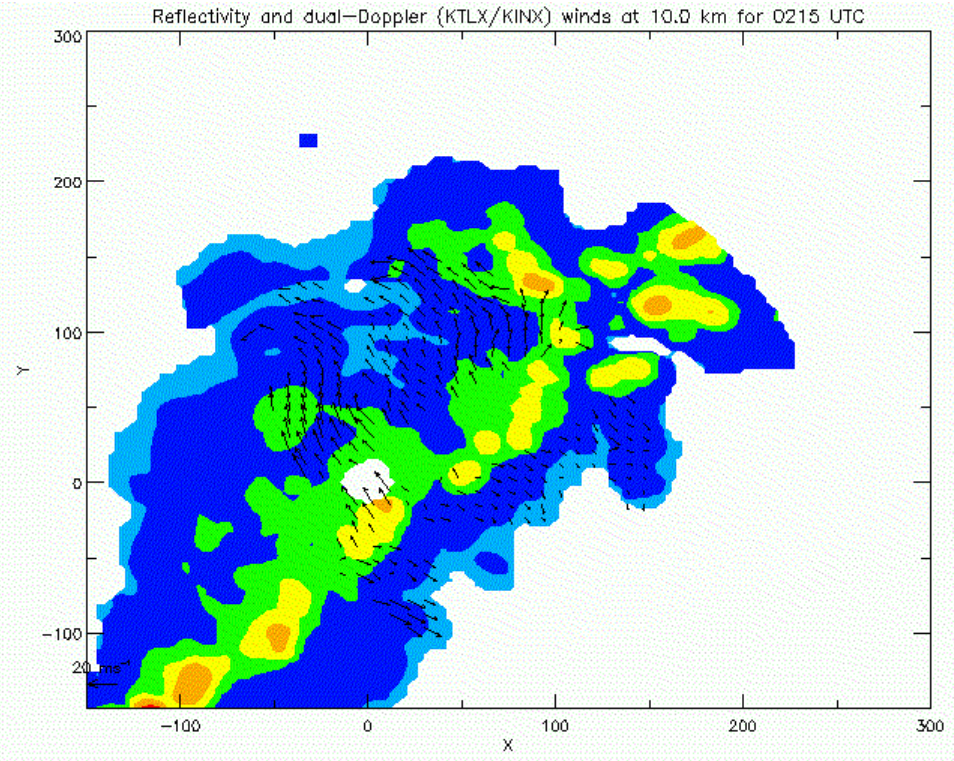

Figure 3.6 continued.

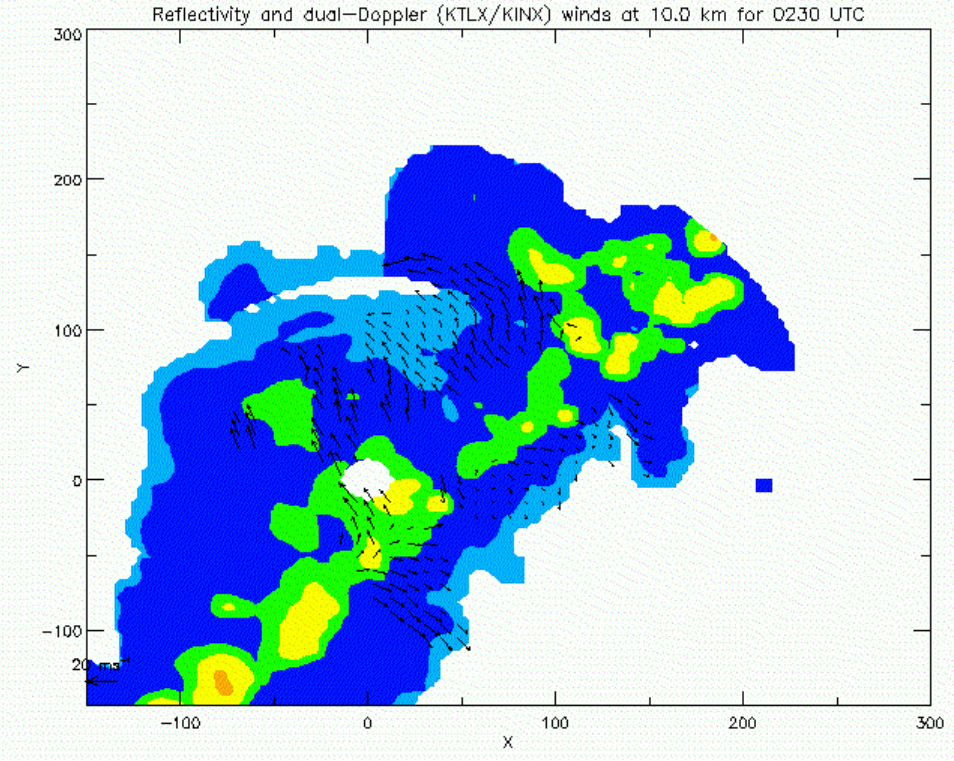

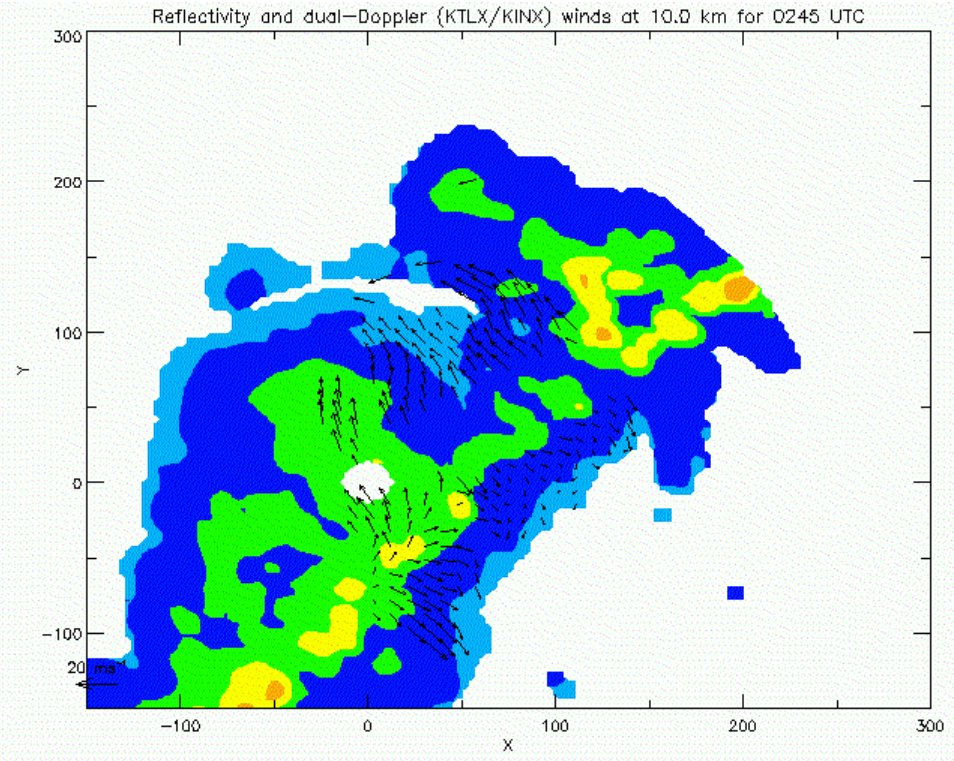

Figure 3.6 continued.

Figs. 3.7, 3.8 and 3.9 show horizontal cross-sections of vertical vorticity contoured at fifteen minute intervals from 0000 to 0245 UTC at altitudes of 1.0, 4.5 and 7.0 km, respectively. Note that the domain of these panels is significantly smaller than previous Figures showing reflectivity and storm-relative dual-Doppler wind vectors. By 0000 UTC at 1.0 km strong vorticity exists (up to 5 x 10^{-3} s^{-1}) but is entirely associated with the convective line (c.f. Figs. 3.7 and 3.1). At this altitude and time, there is coverage of both convective and stratiform regions of the MCS (approximately six times as many points in the stratiform region), but vertical vorticity appears only to exist within the convective line. By 0200 UTC, the area of vorticity associated with the MCV expands and also takes on an elliptical shape as discussed before. It appears that there are also smaller areas of vorticity, which likely originated from the convective line, that were likely incorporated within the larger area of vorticity associated with the MCV. An example of this can be seen at 4.5 km altitude during 0015 and 0030 UTC. The four to five small regions of enhanced vorticity associated with the convective line located at $0.0 < x < 20.0$ and $65.0 < y < 80.0$ at 0015 UTC likely form the "tail" of enhanced vorticity associated with the MCV at 0030 UTC located at ($x = -10.0$, $y = 80.0$). At 7.0 km, the area of vorticity associated with the MCV is located slightly farther west than at lower levels. This suggests that the MCV may have been tilted slightly in the vertical at least in its formative stages as has been seen in previous observational studies (e.g., Yu et al. 1999; Davis and Trier 2007). The development of the MCV can be seen to extend to 7.0 km altitude during this time period. Although vertical vorticity up to 1 x 10^{-3} s^{-1} exists as early as 0015 UTC in an area with a diameter of only 10 km, the magnitude, area, and

gradient of vertical vorticity increases from 0045 to 0230 at this altitude as the MCV develops and expands from lower levels.

Figs. 3.10 and 3.11 show North-South and East-West vertical transects through the MCV at fifteen minute intervals from 0000 to 0245 UTC. During the time period of investigation the North-South transects appear to be wider than the East-West transects which may account for the elliptical shape of the MCV in its formative stages. However, while horizontal expansion continues at 0145 UTC, the vertical vorticity associated with the MCV does not expand above 9.0 km. During the last hour of investigation (0200 UTC and later), the MCV does not extend much farther than 10.0 km but does continue to expand horizontally. The enhanced regions of vertical vorticity at high altitudes that are not connected to regions of vertical vorticity at lower levels are thought to be noise from smoothing techniques of the data in the dual-Doppler analyses. Similar to Scott and Rutledge (1995), if the MCV is defined by a 1×10^{-4} s^{-1} threshold contour, then the MCV expands to a diameter of approximately 100 km at the surface by 0245 UTC in Fig. 3.10. In contrast, the East-West transects in Fig. 3.11 show a much thinner slice of the vortex with a horizontal diameter of approximately 50 km, which is due to the elliptical shape of the MCV.

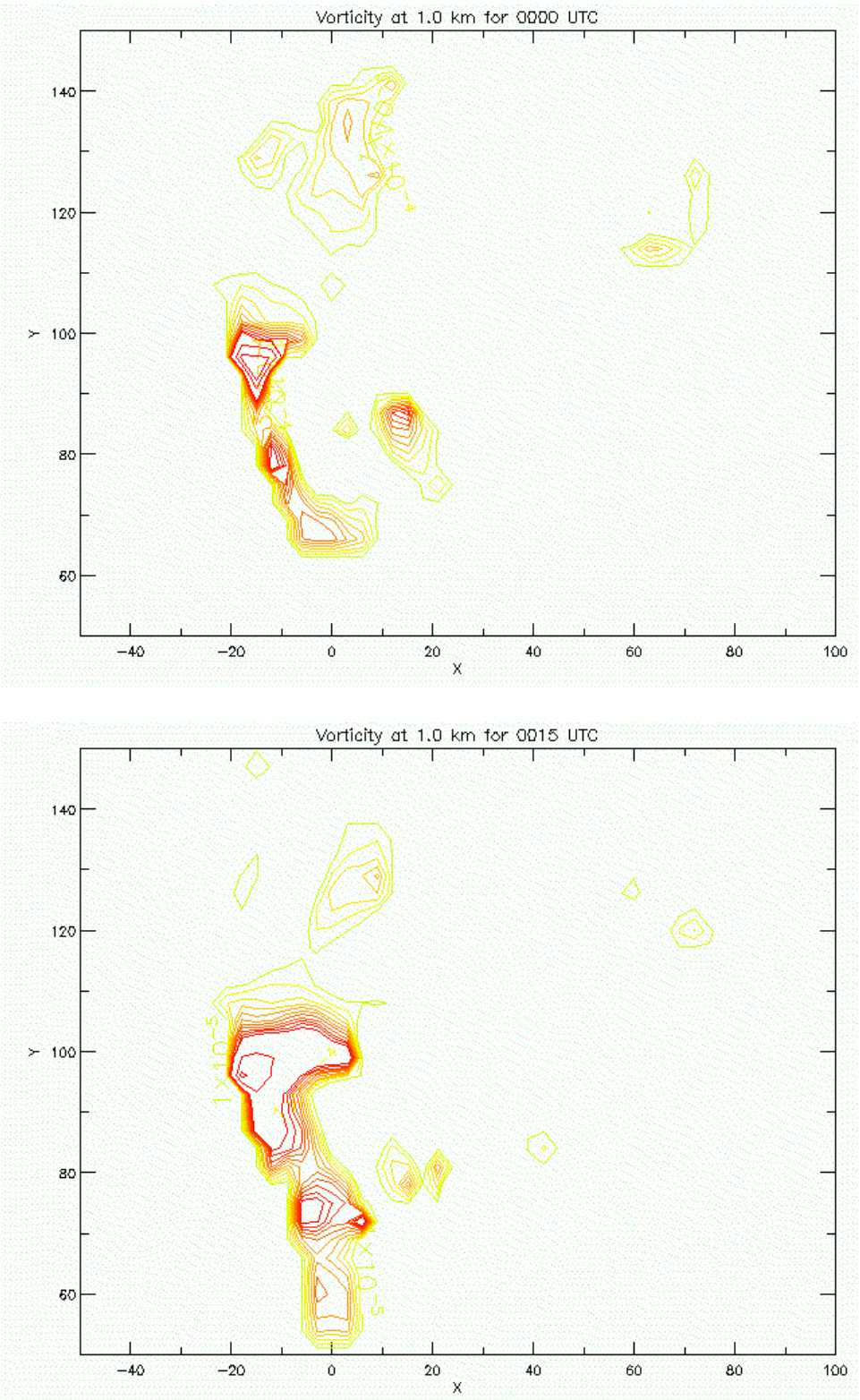

Figure 3.7. Horizontal cross-sections of vertical vorticity at an altitude of 1.0 km for fifteen minute intervals between 0000 and 0245 UTC. The first contour level is 1 x 10^{-5} s^{-1} (green). The next contour level is 1 x 10^{-4} s^{-1} (yellow) with a 1 x 10^{-4} s^{-1} increasing interval thereafter.

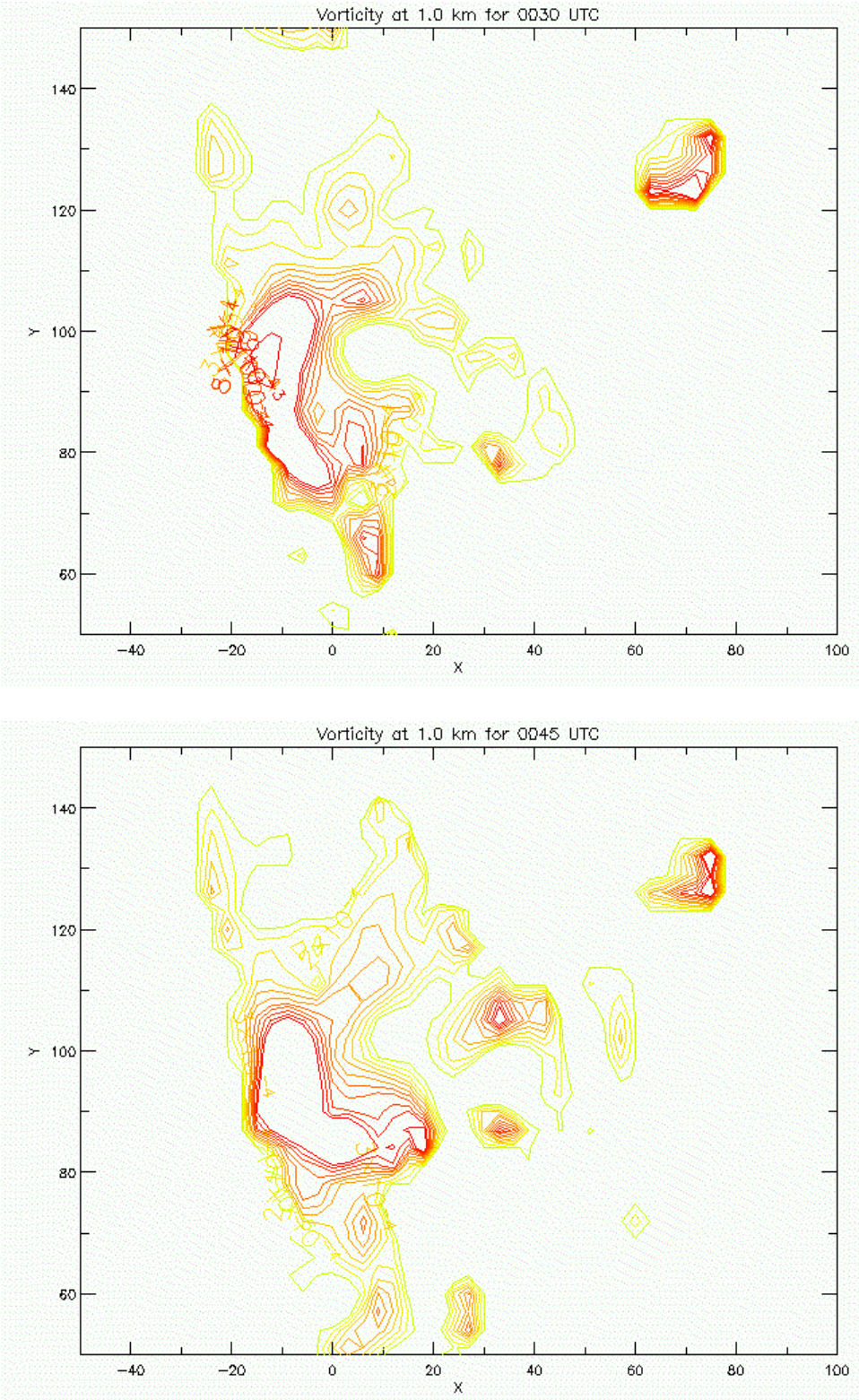

Figure 3.7 continued.

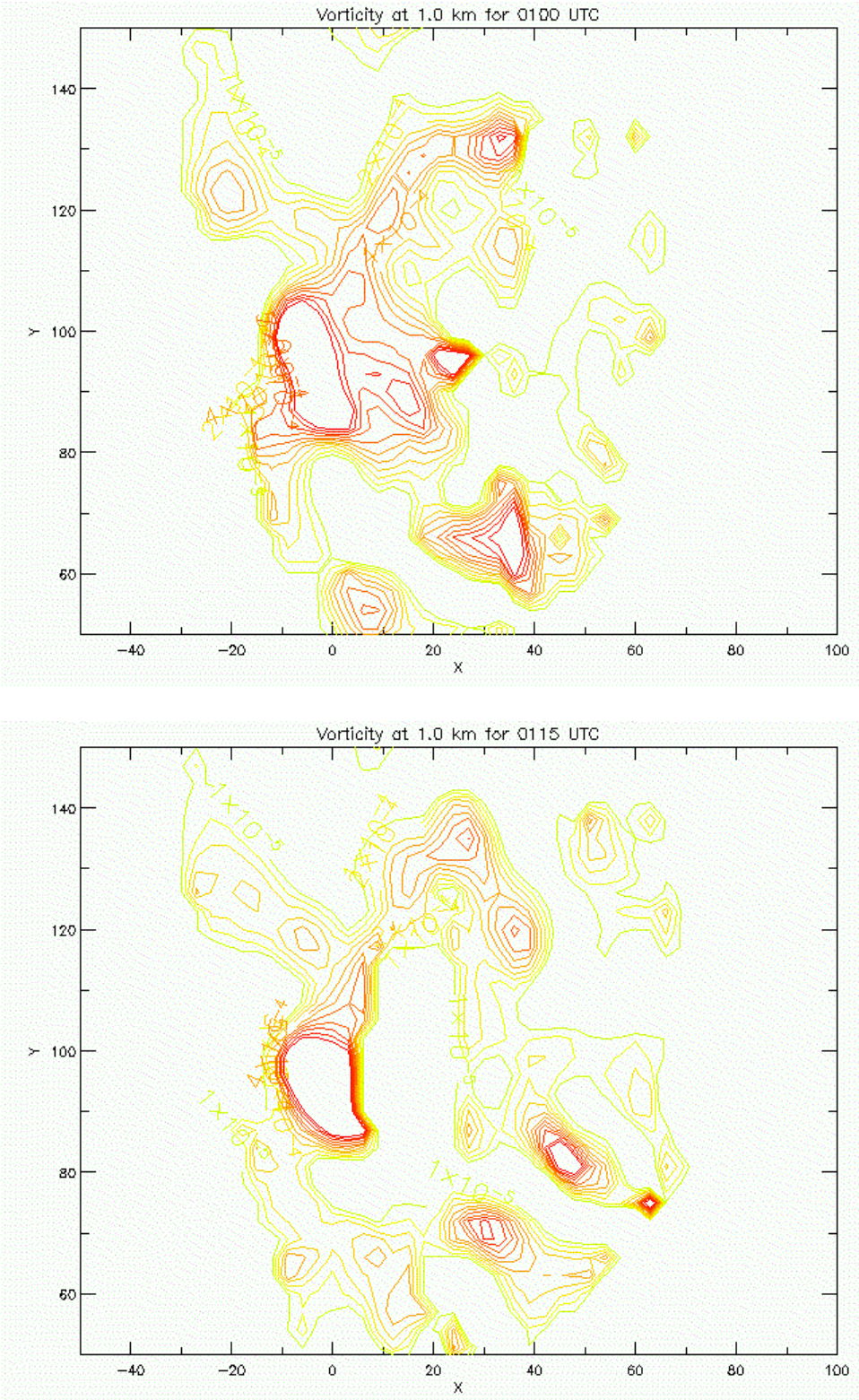

Figure 3.7 continued.

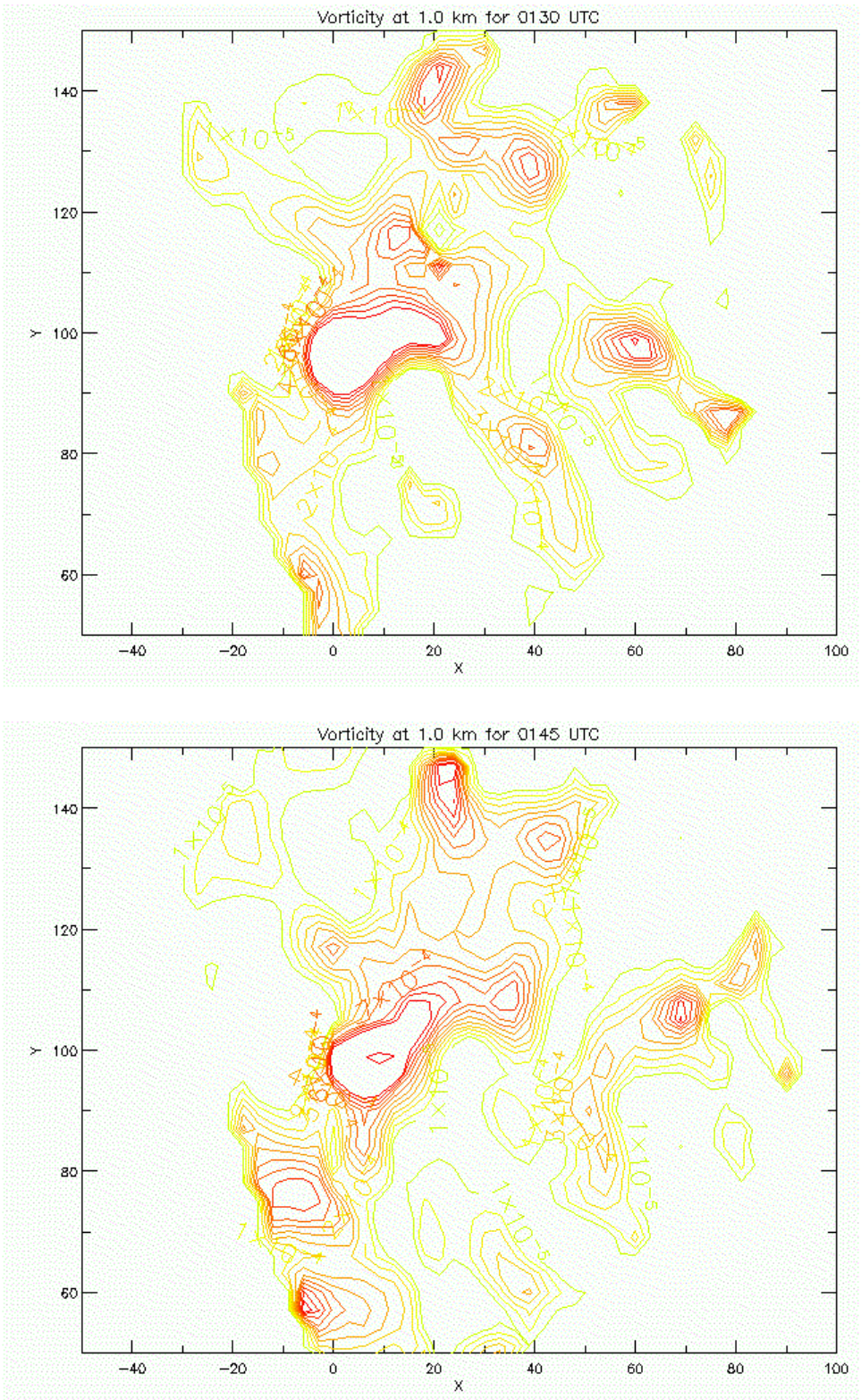

Figure 3.7 continued.

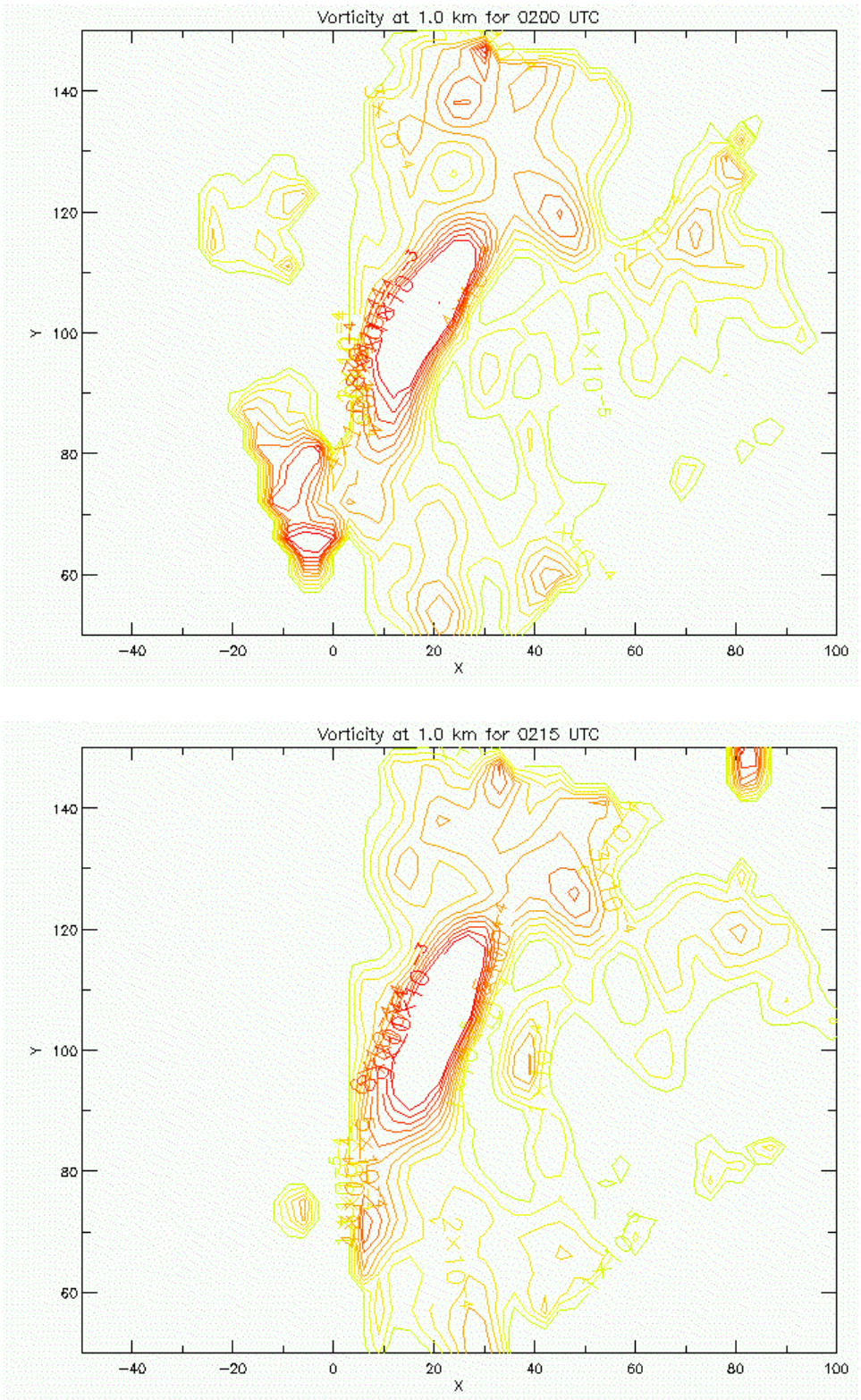

Figure 3.7 continued.

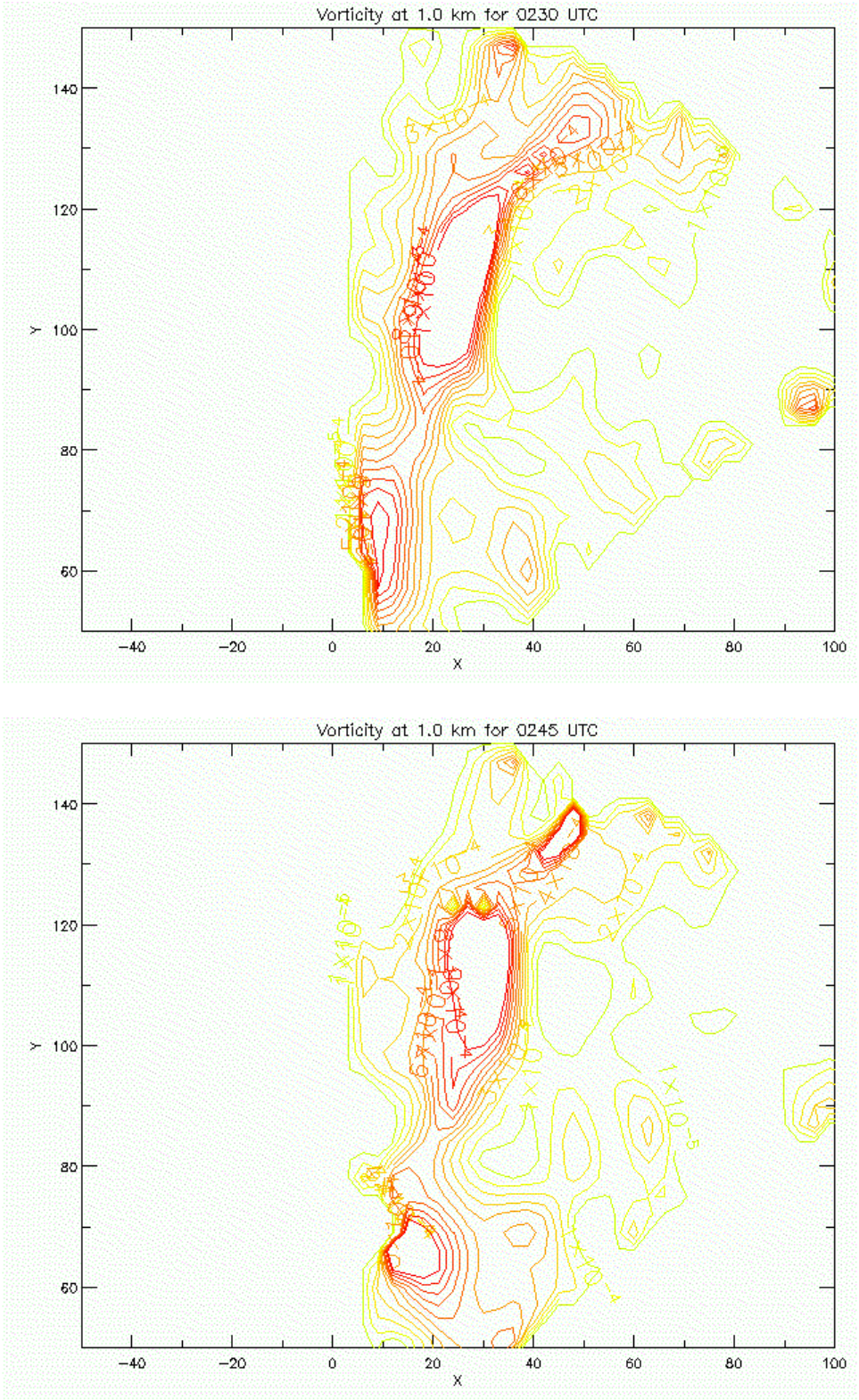

Figure 3.7 continued.

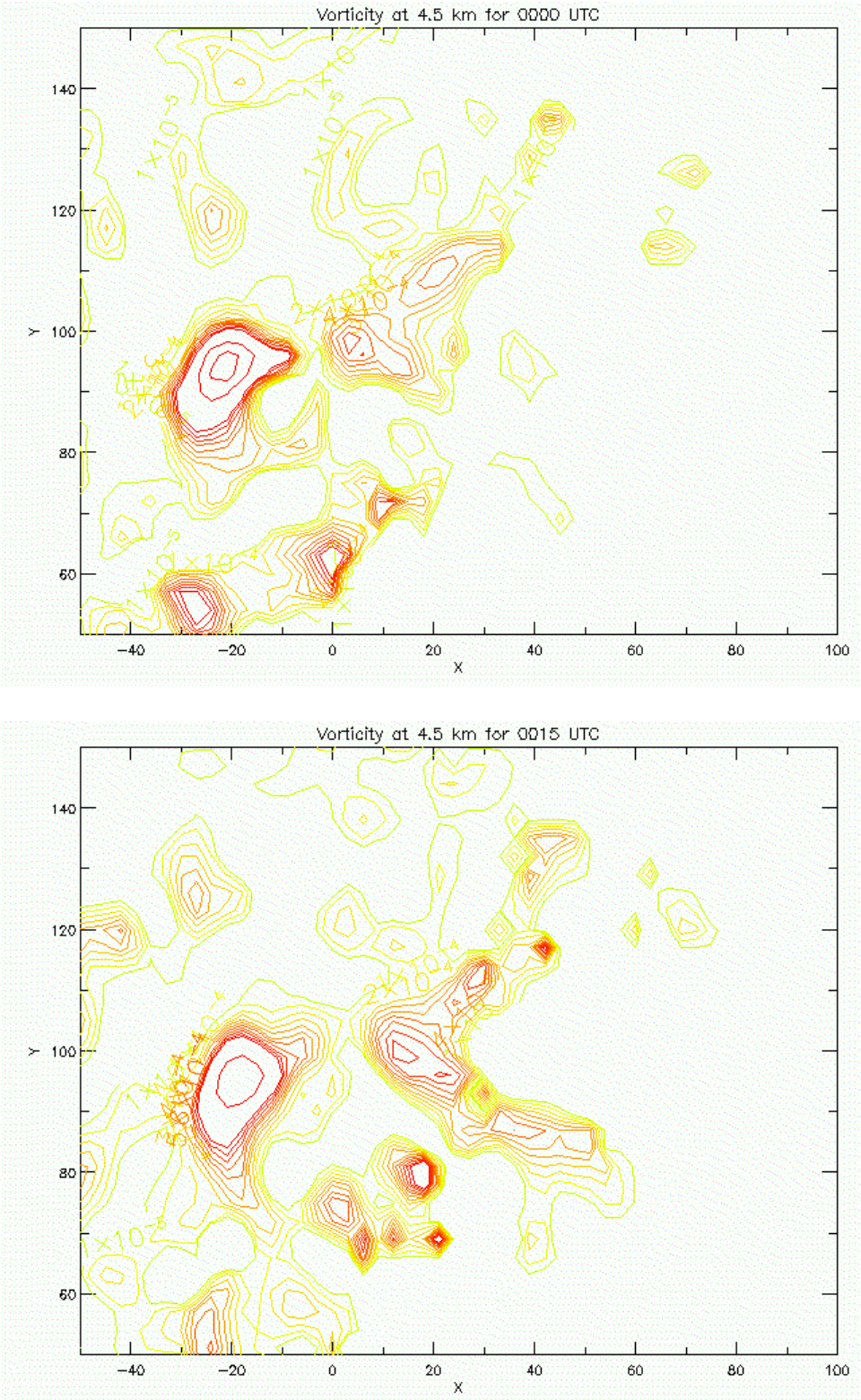

Figure 3.8. Horizontal cross-sections of vertical vorticity at an altitude of 4.5 km for fifteen minute intervals between 0000 and 0245 UTC. The first contour level is 1 x 10^{-5} s^{-1} (green). The next contour level is 1 x 10^{-4} s^{-1} (yellow) with a 1 x 10^{-4} s^{-1} increasing interval thereafter.

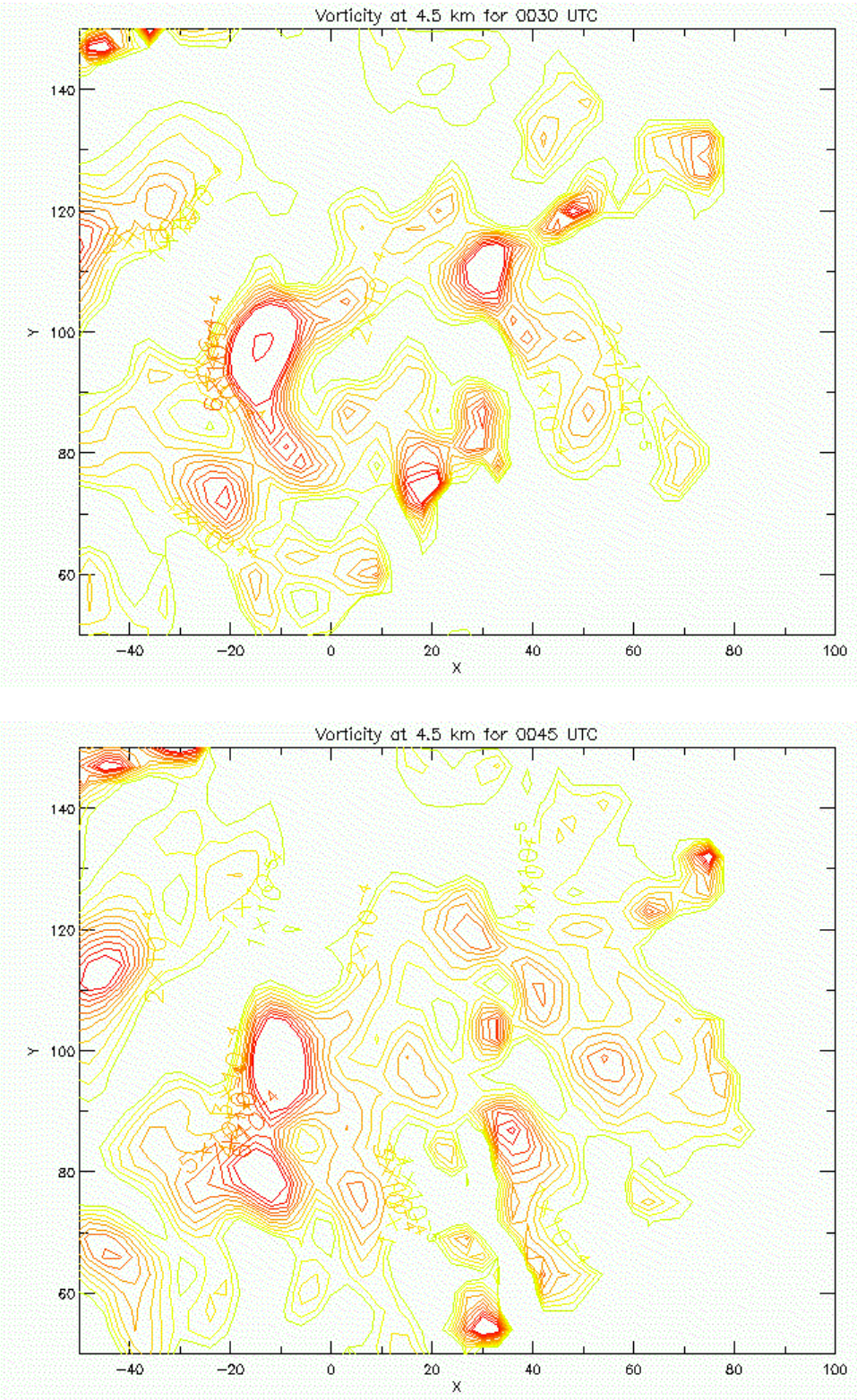

Figure 3.8 continued.

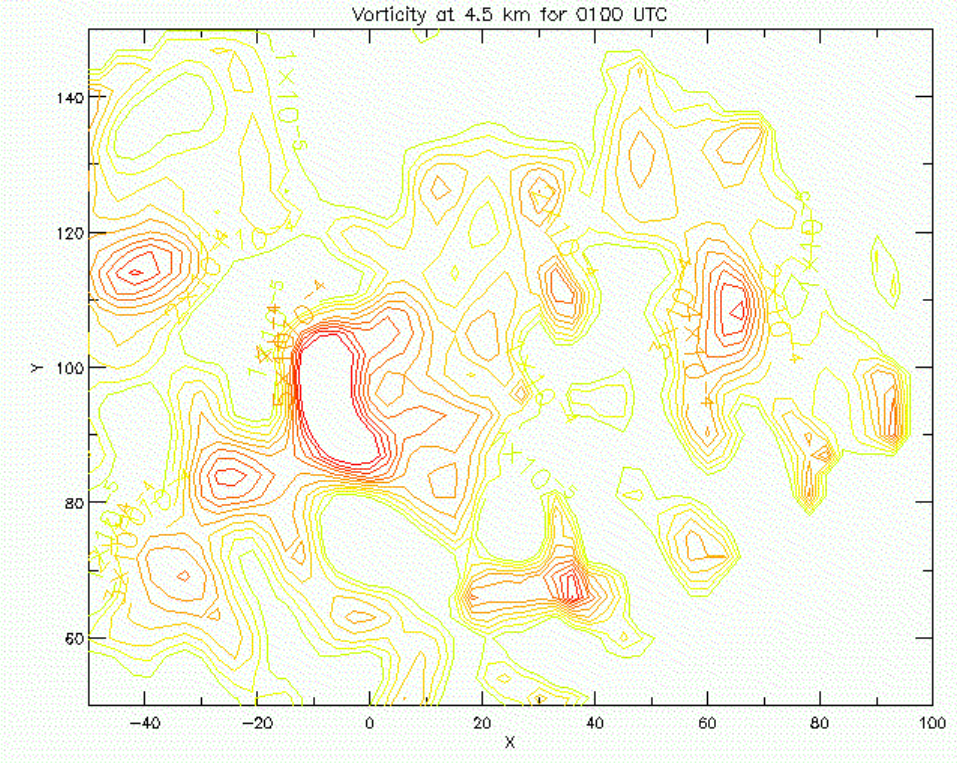

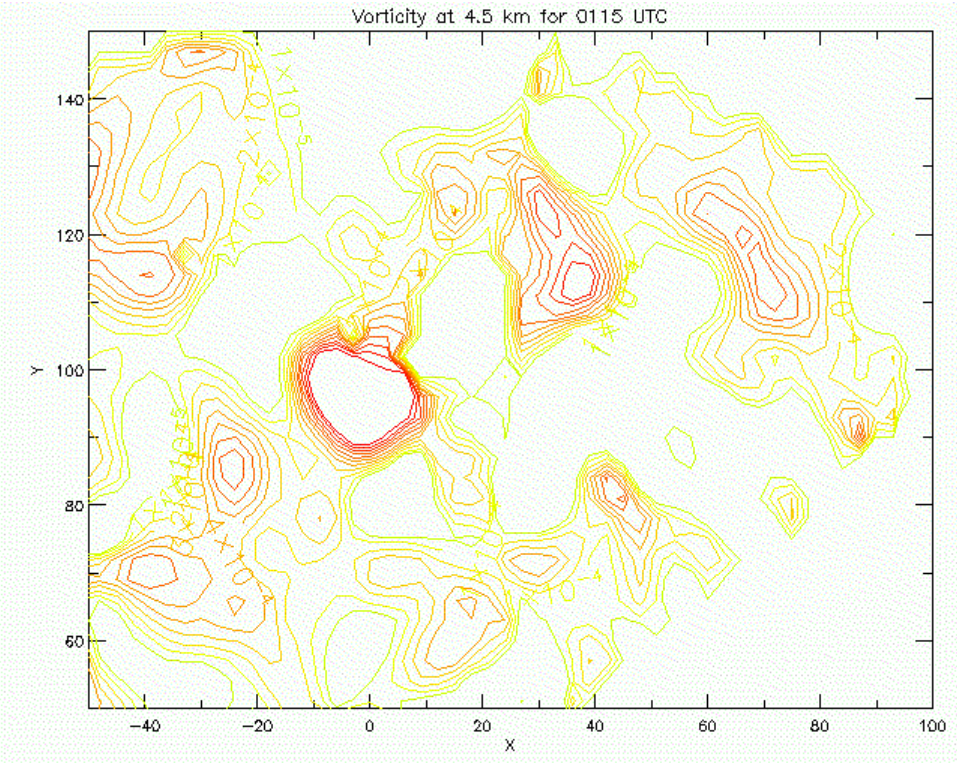

Figure 3.8 continued.

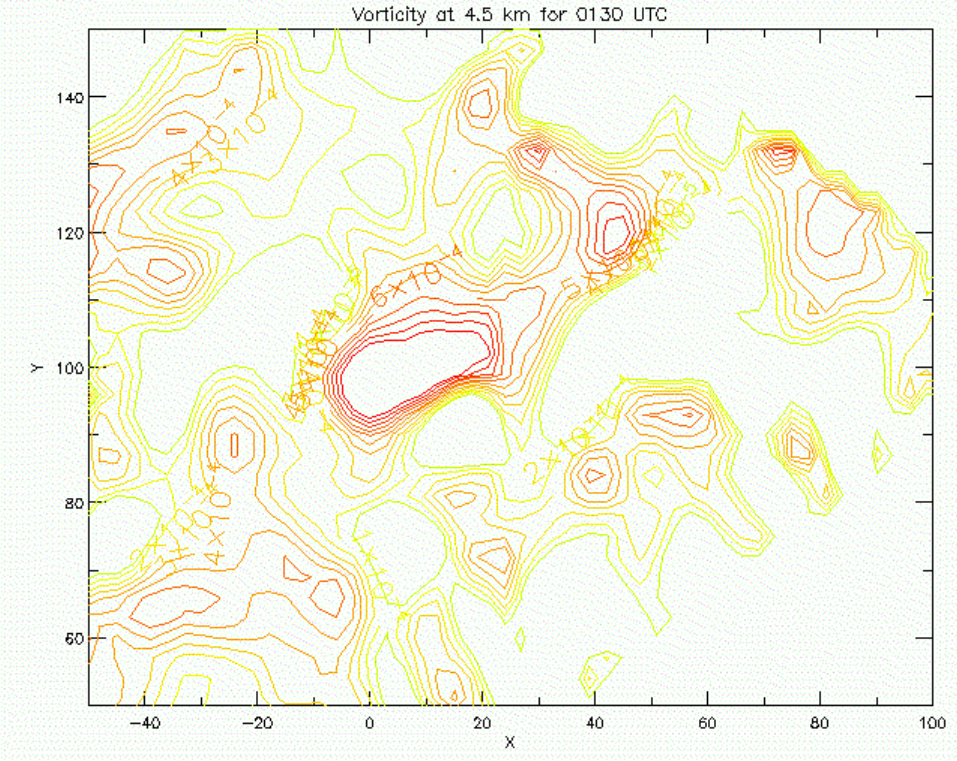

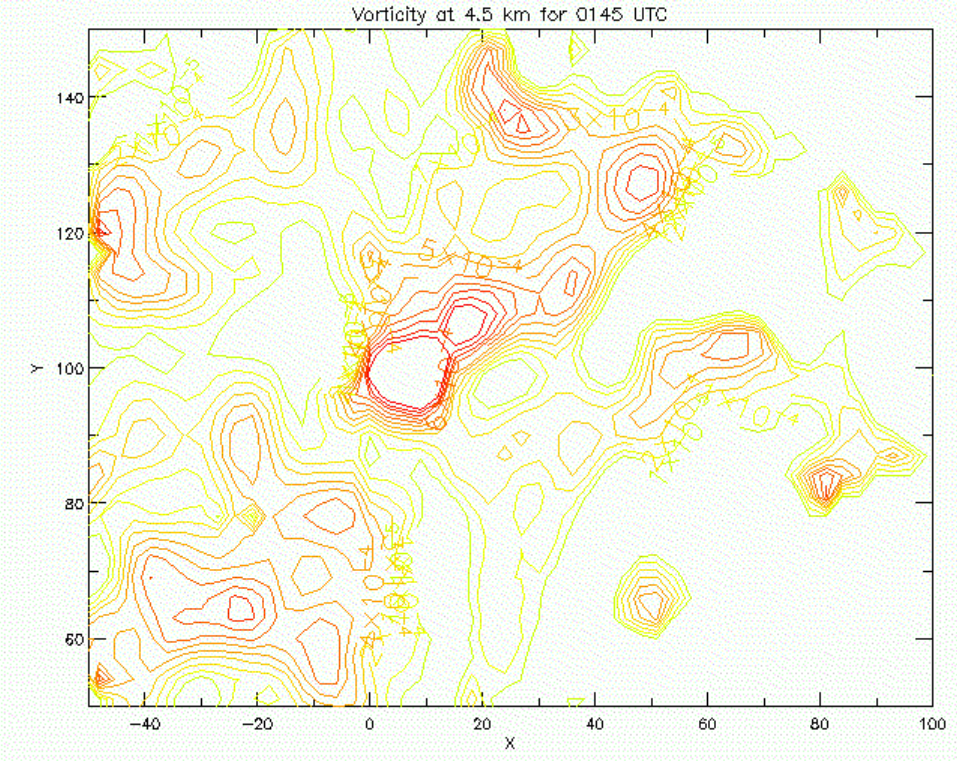

Figure 3.8 continued.

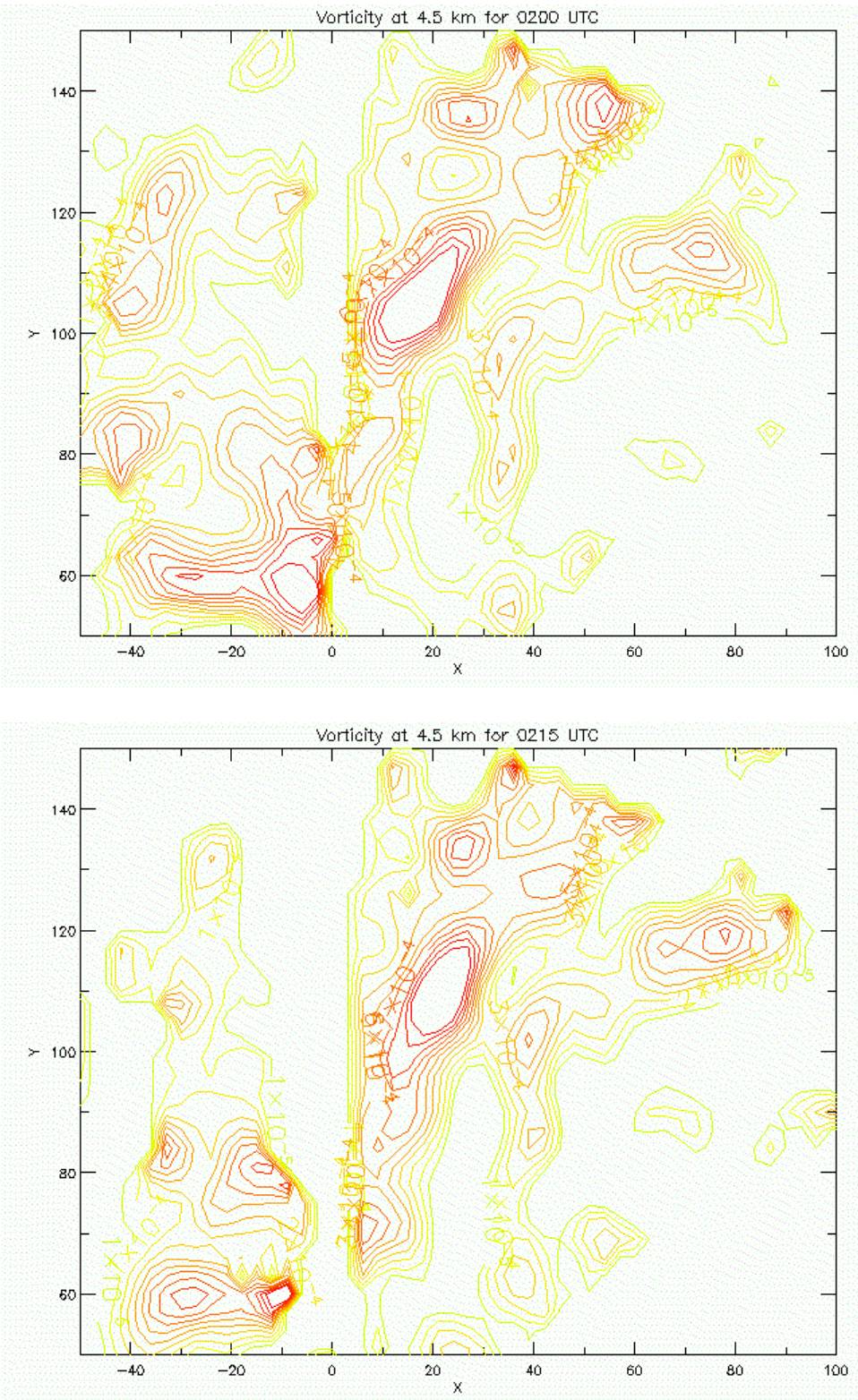

Figure 3.8 continued.

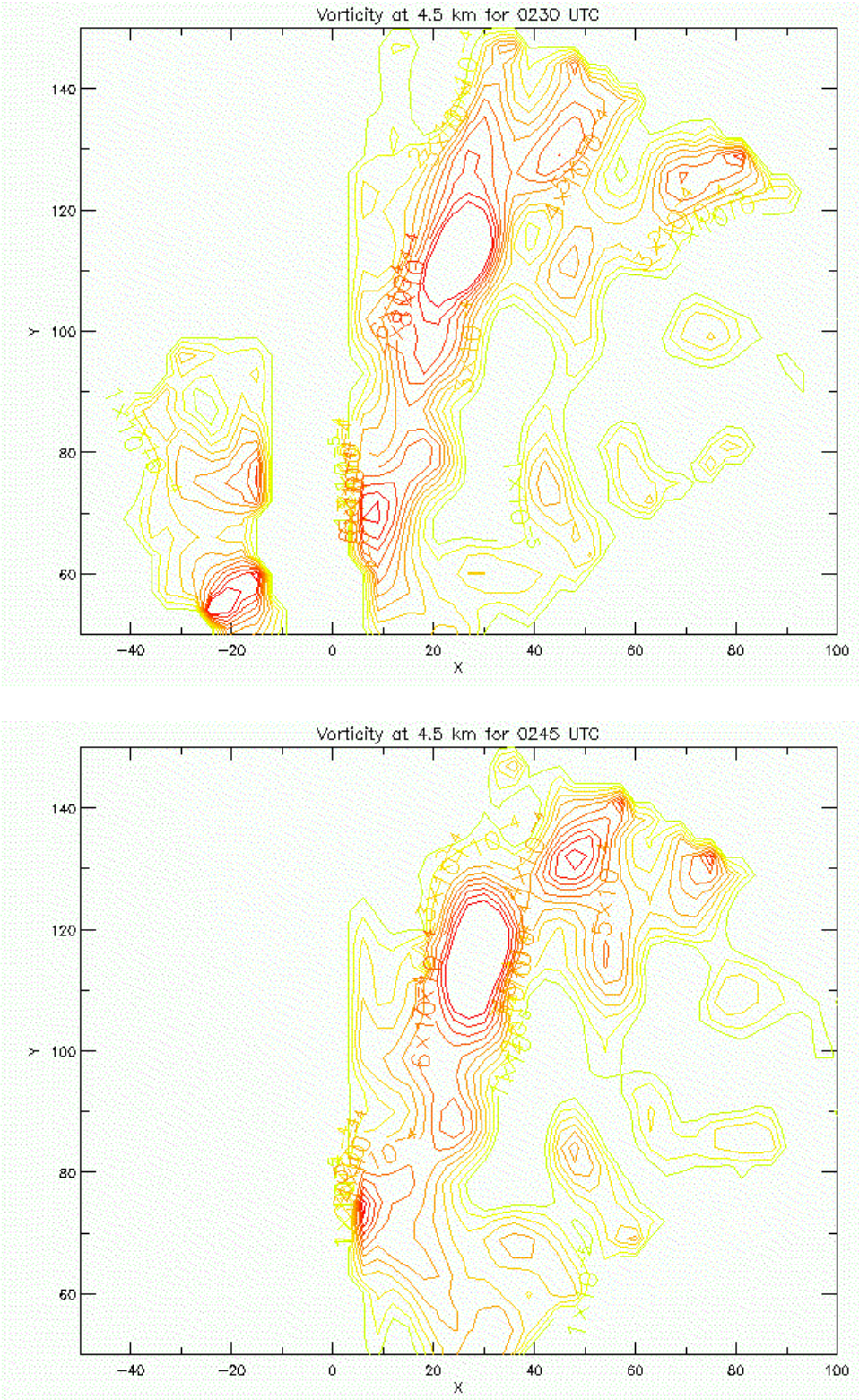

Figure 3.8 continued.

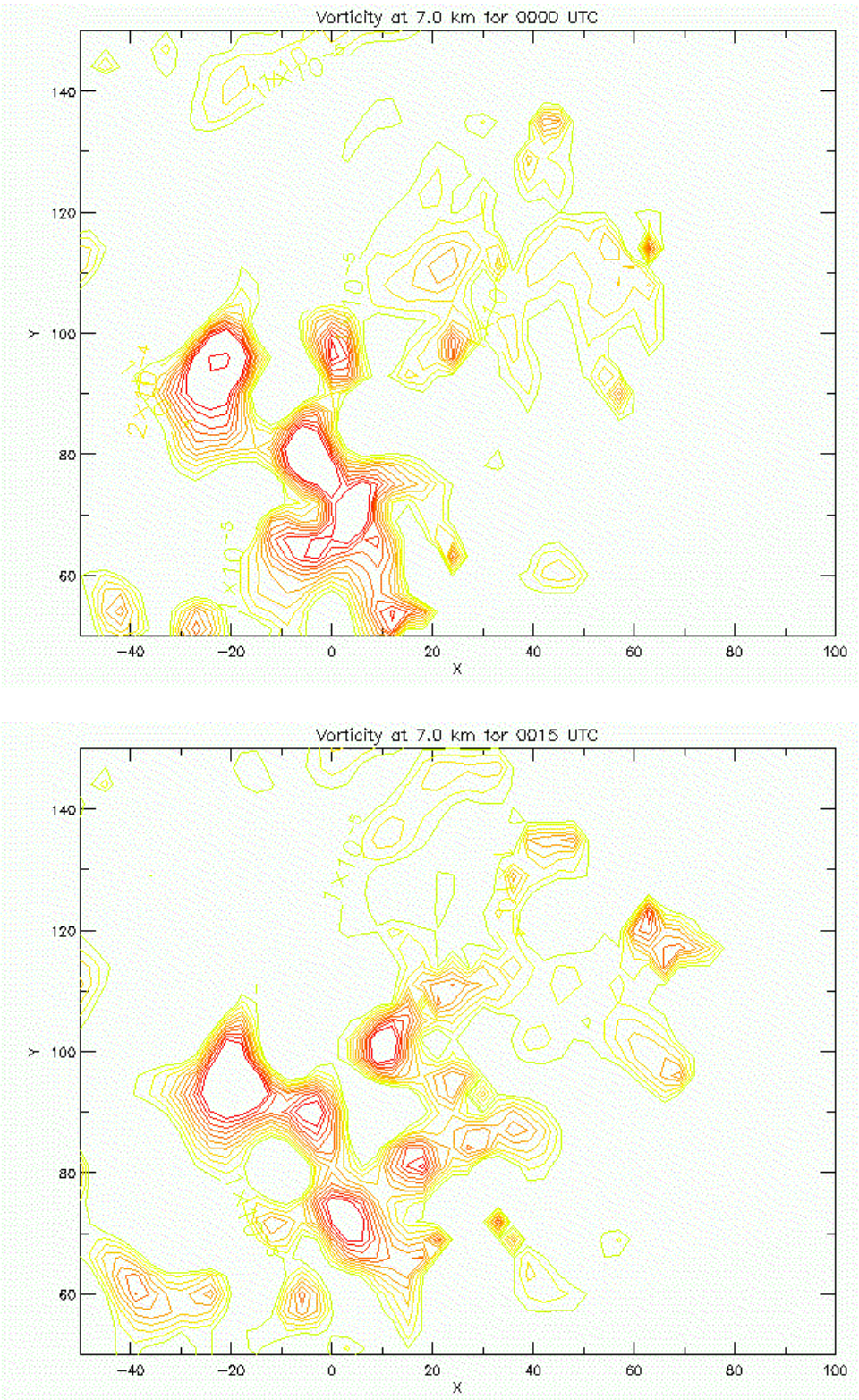

Figure 3.9. Horizontal cross-sections of vertical vorticity at an altitude of 7.0 km for fifteen minute intervals between 0000 and 0245 UTC. The first contour level is 1 x 10^{-5} s^{-1} (green). The next contour level is 1 x 10^{-4} s^{-1} (yellow) with a 1 x 10^{-4} s^{-1} increasing interval thereafter.

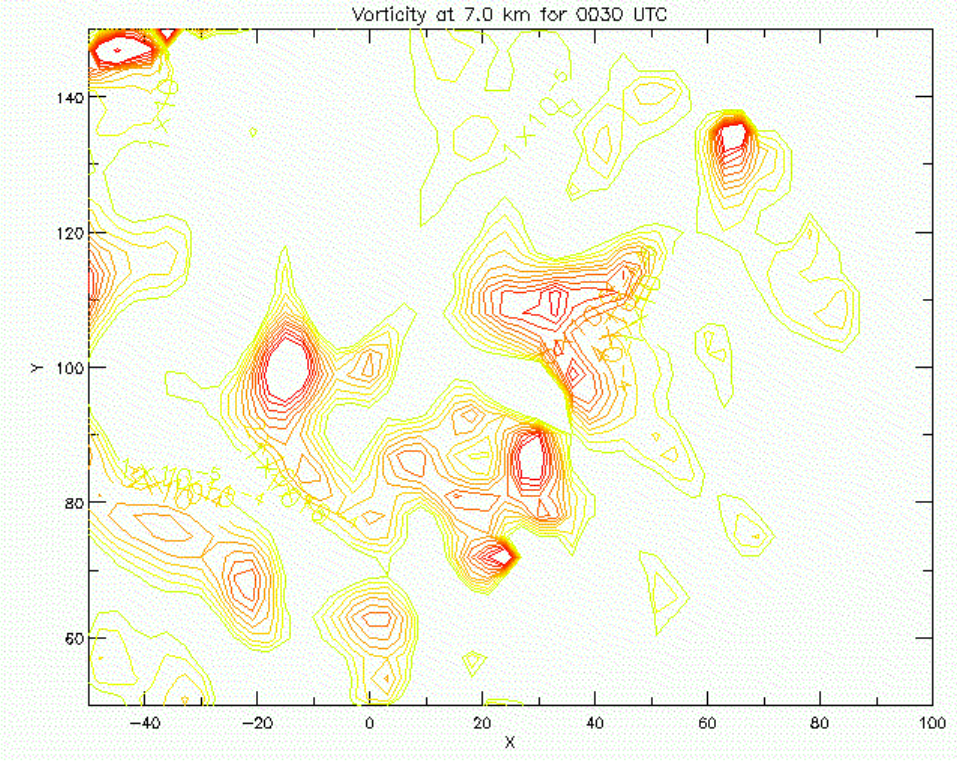

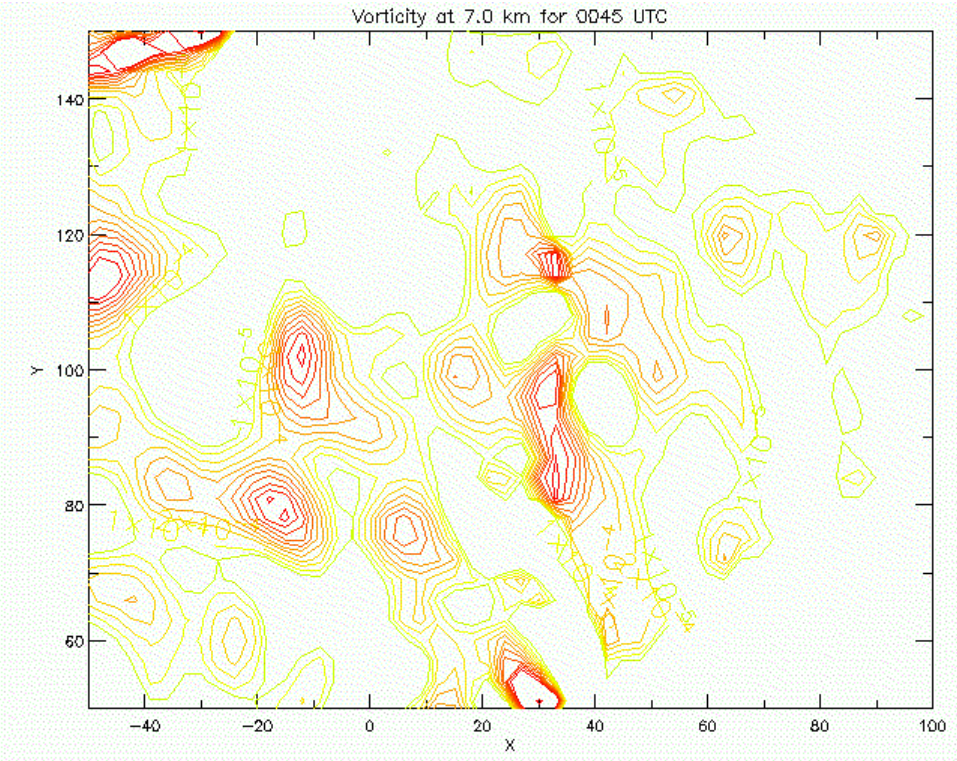

Figure 3.9 continued.

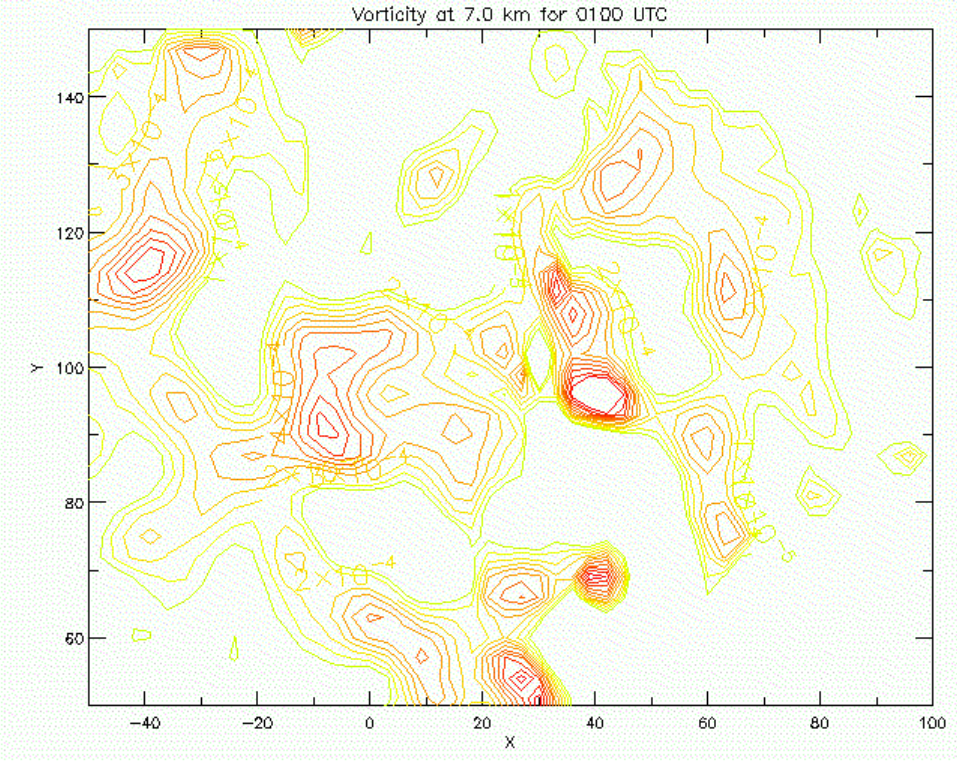

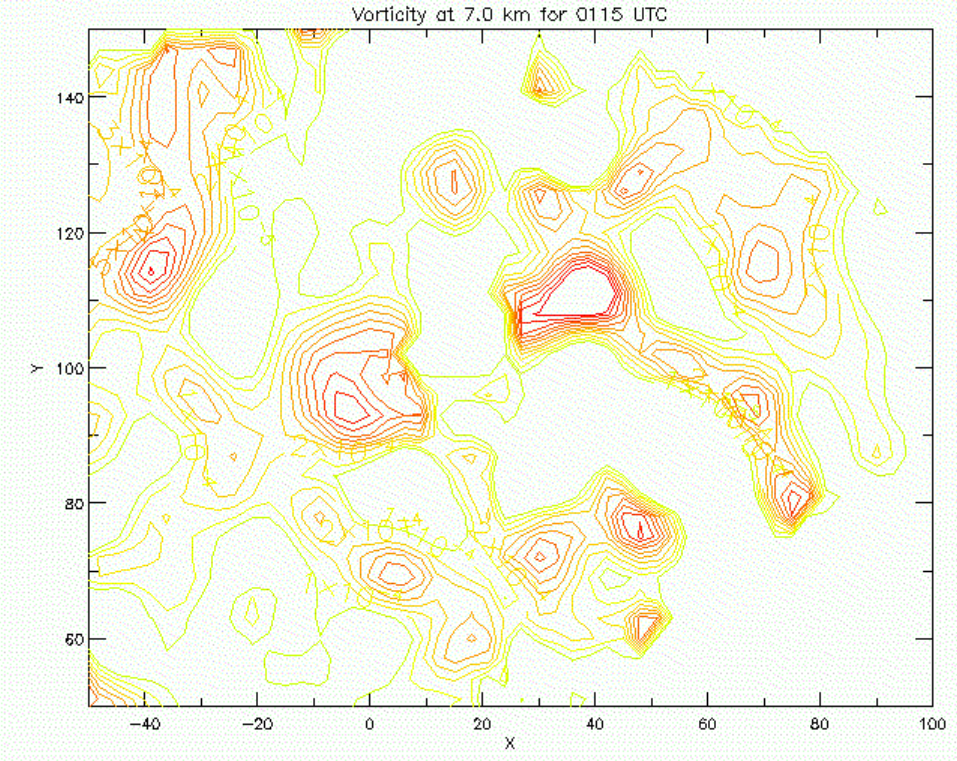

Figure 3.9 continued.

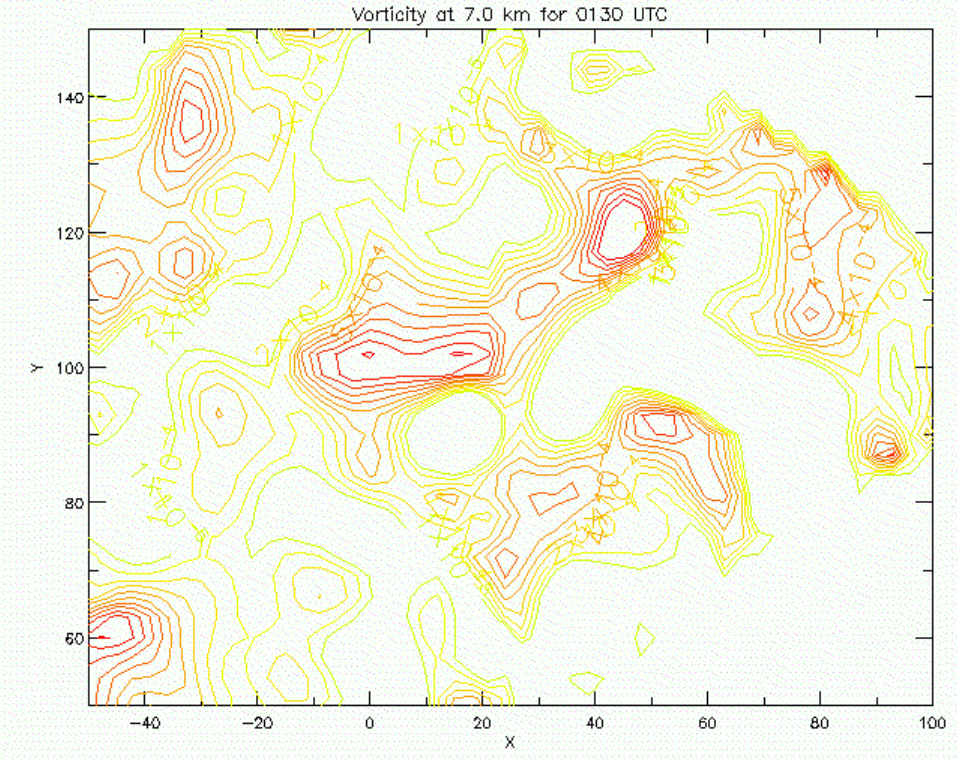

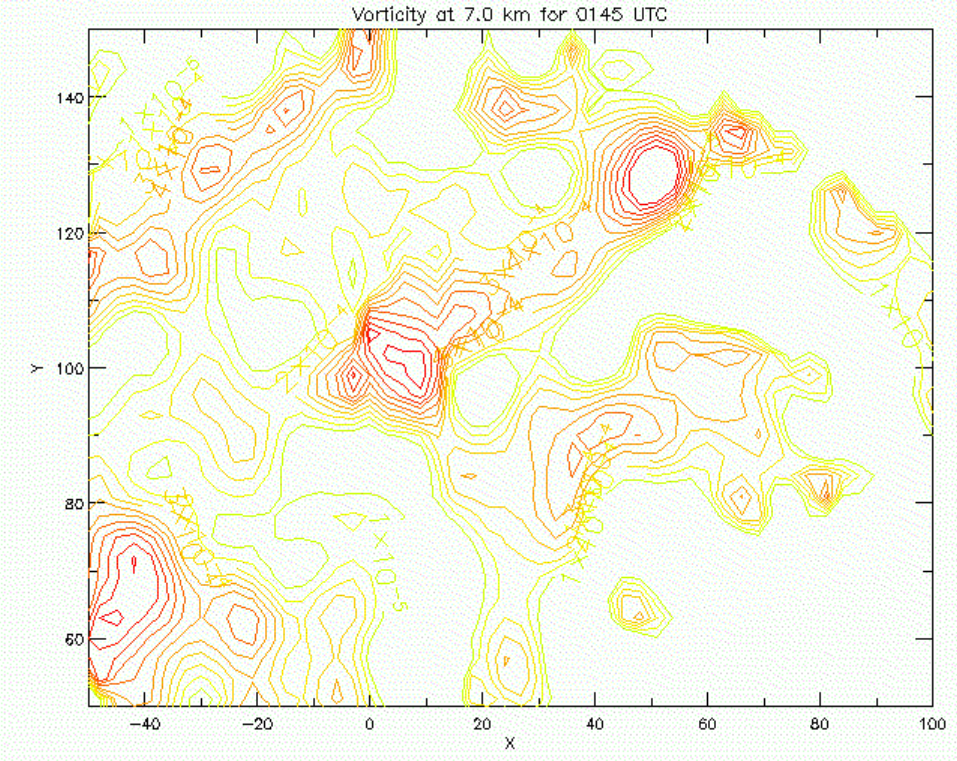

Figure 3.9 continued.

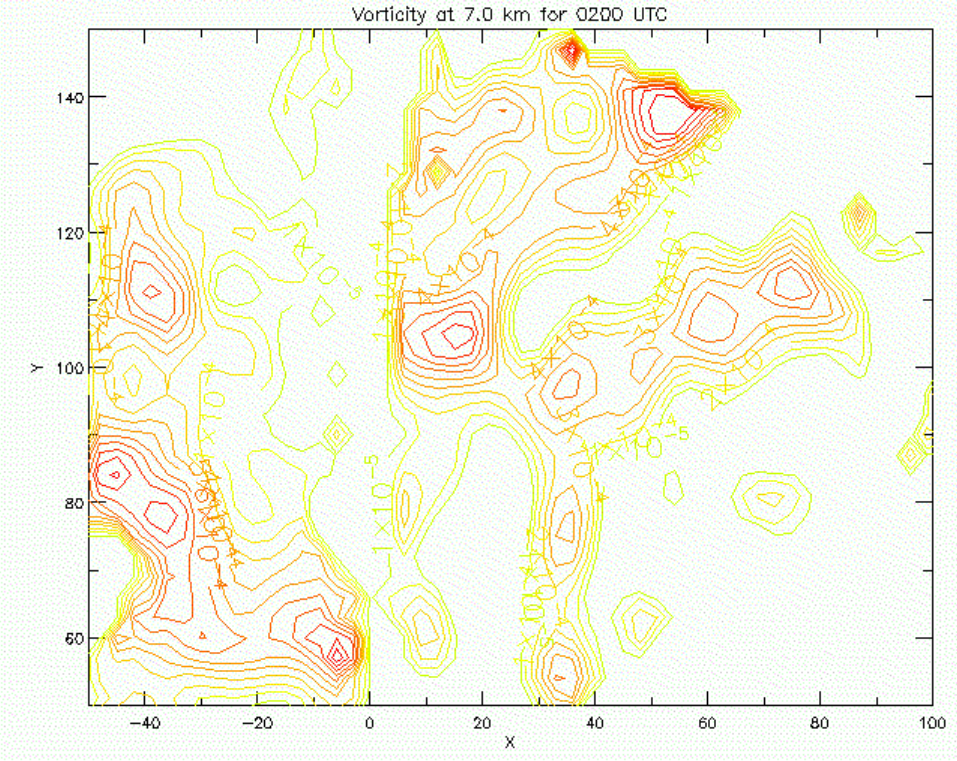

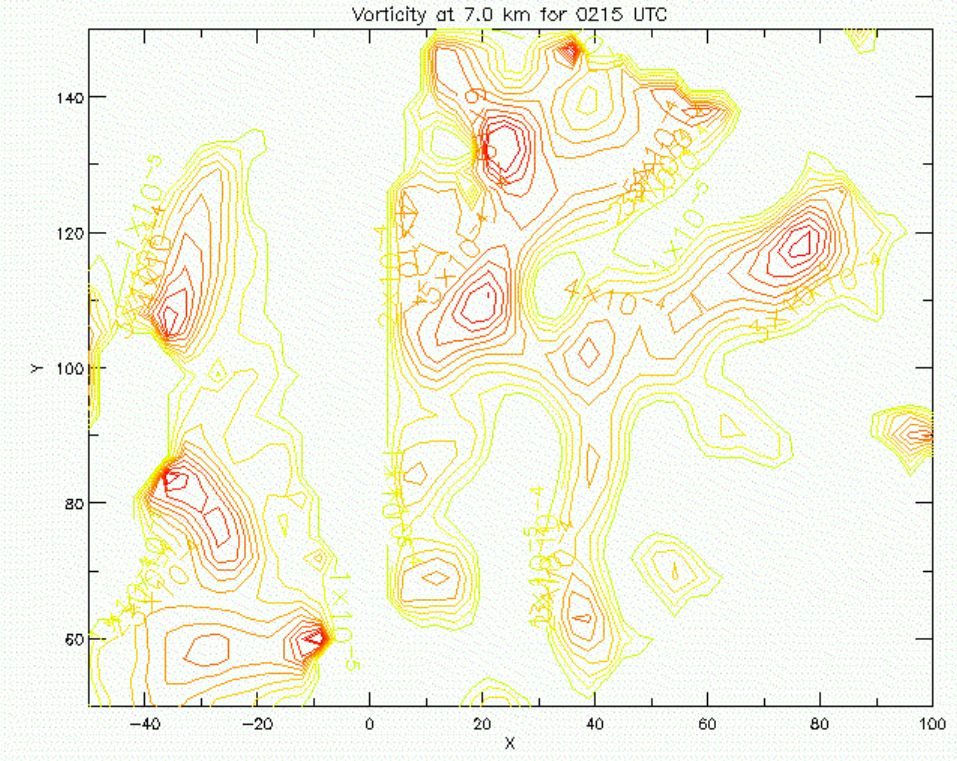

Figure 3.9 continued.

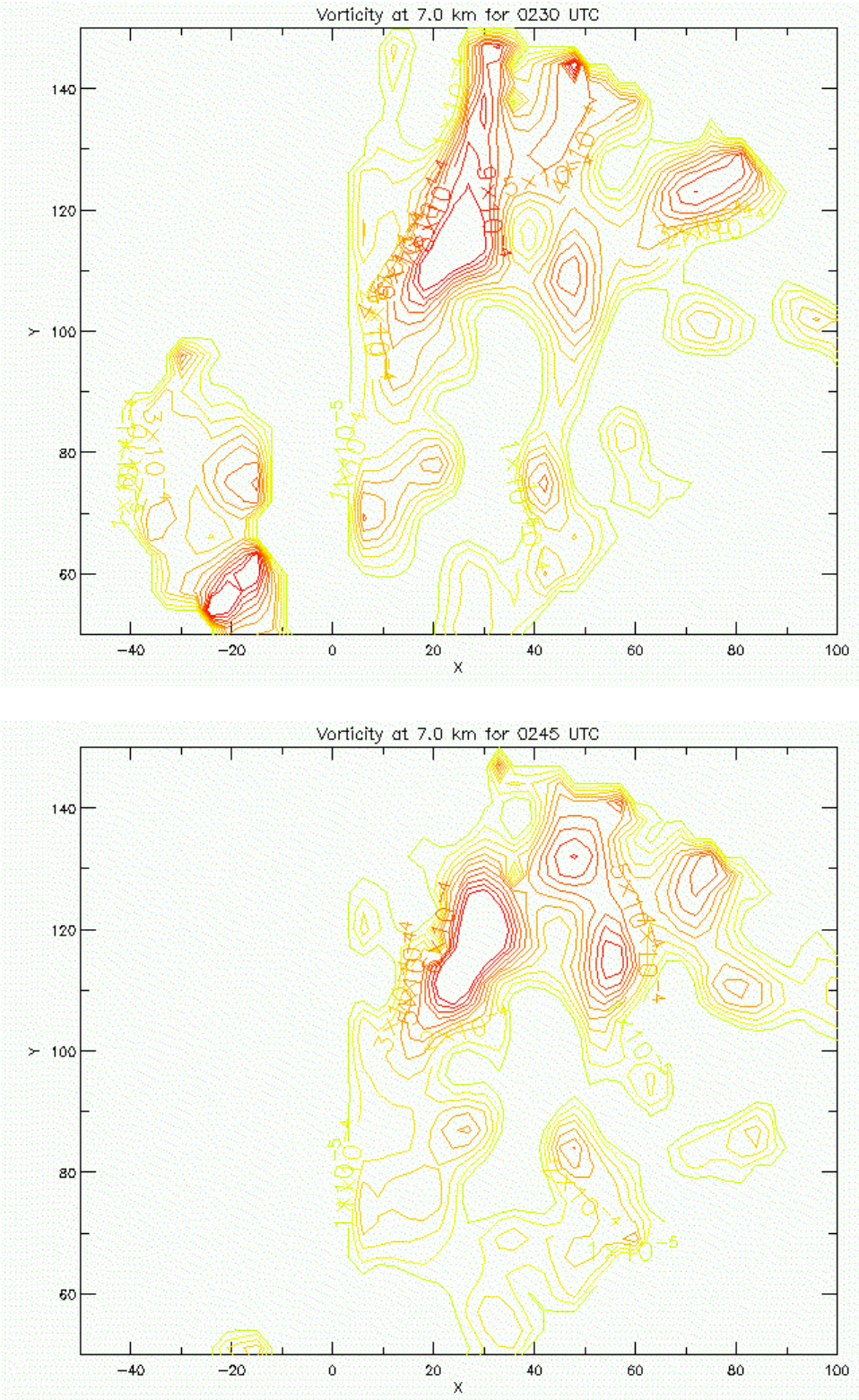

Figure 3.9 continued.

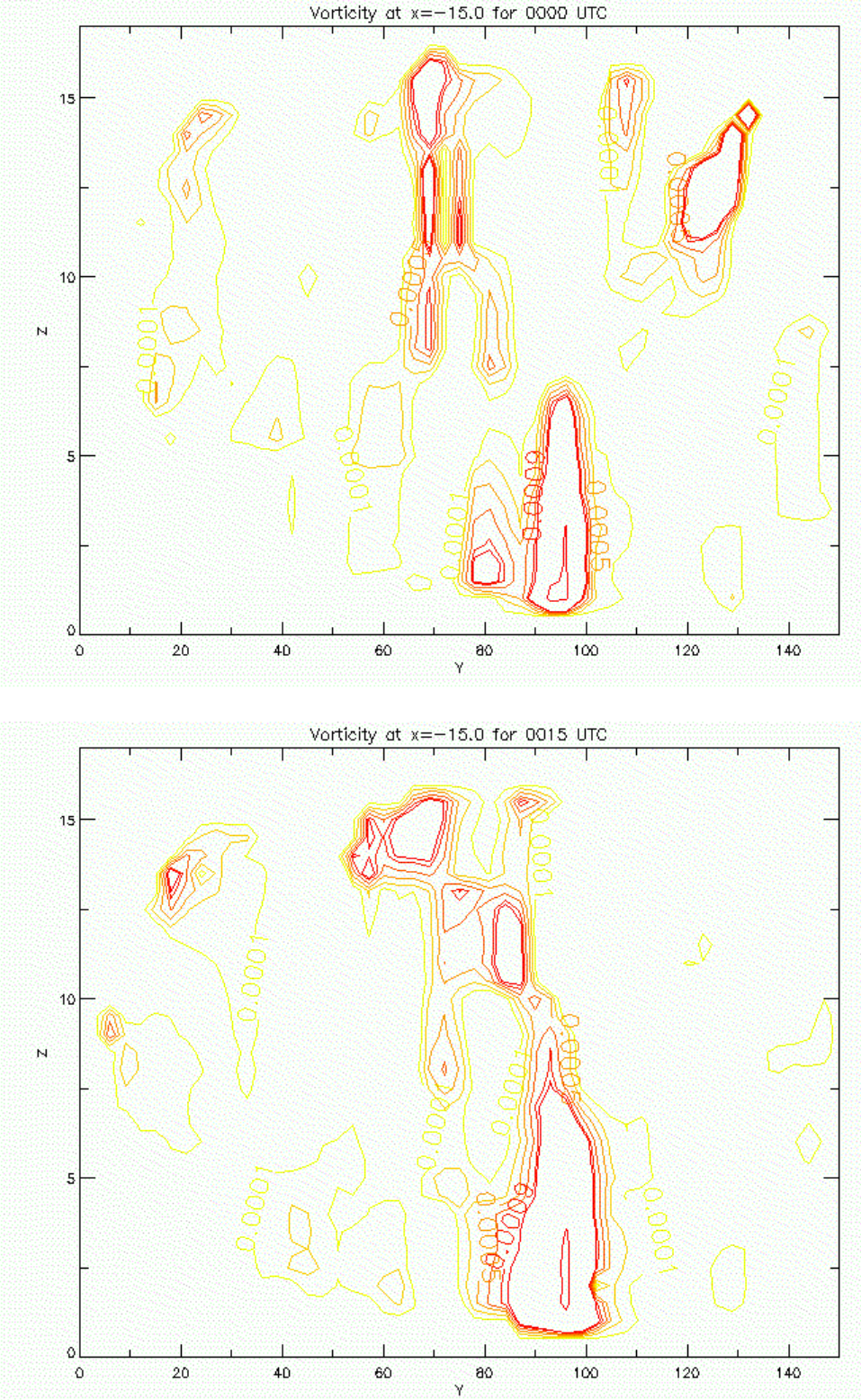

Figure 3.10. Vertical cross-sections for North-South transects through the MCV for fifteen minute intervals between 0000 and 0245 UTC. The first contour is 1 x 10^{-4} s^{-1} (green) with an interval increase of 2 x 10^{-4} s^{-1}. The value of x taken relative to the KTLX radar (0.0,0.0) is noted in each image.

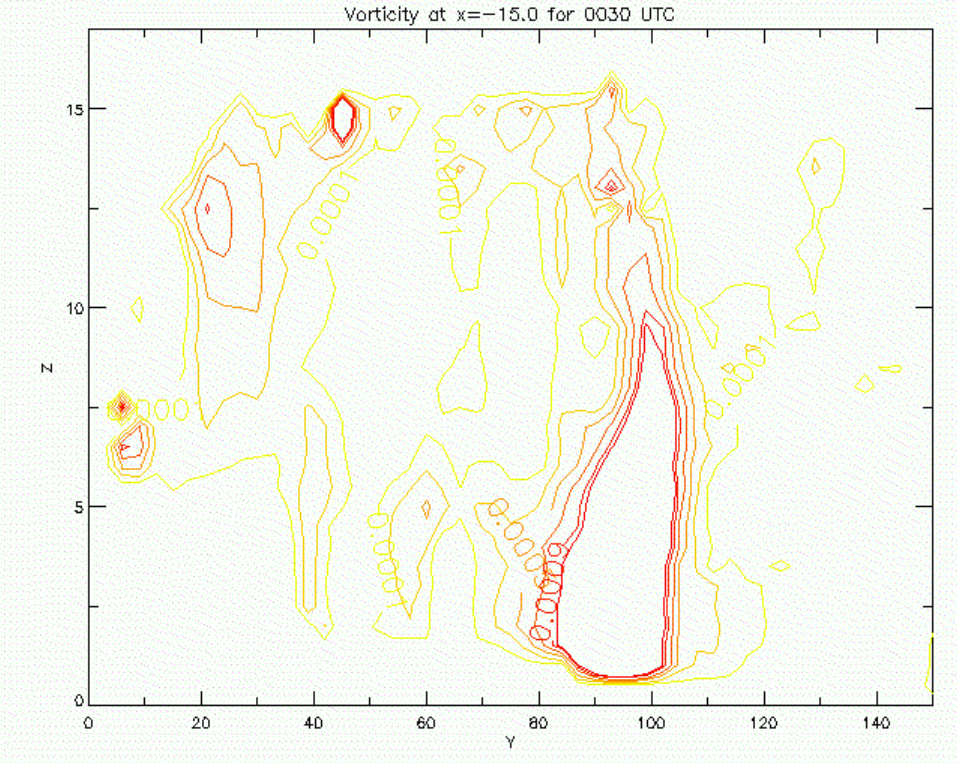

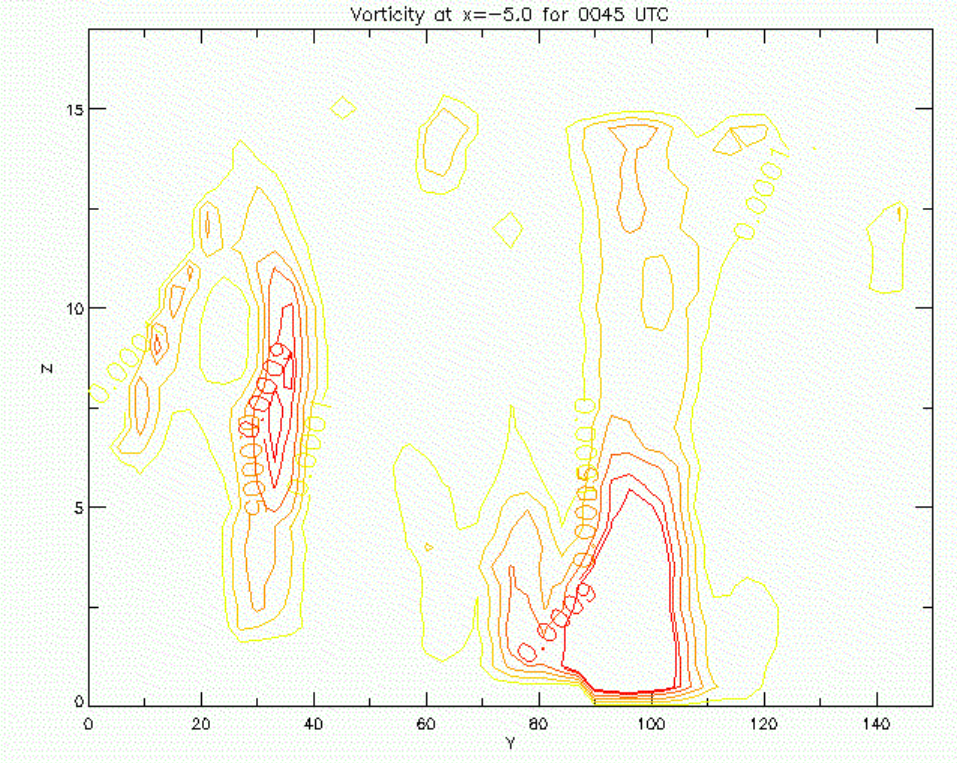

Figure 3.10 continued.

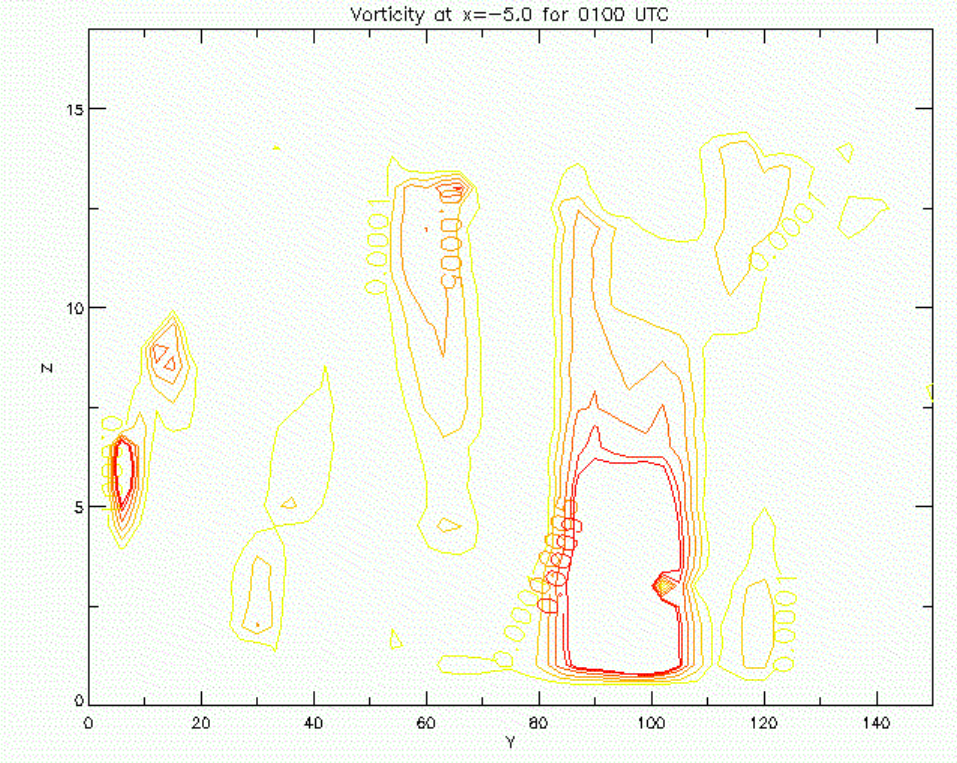

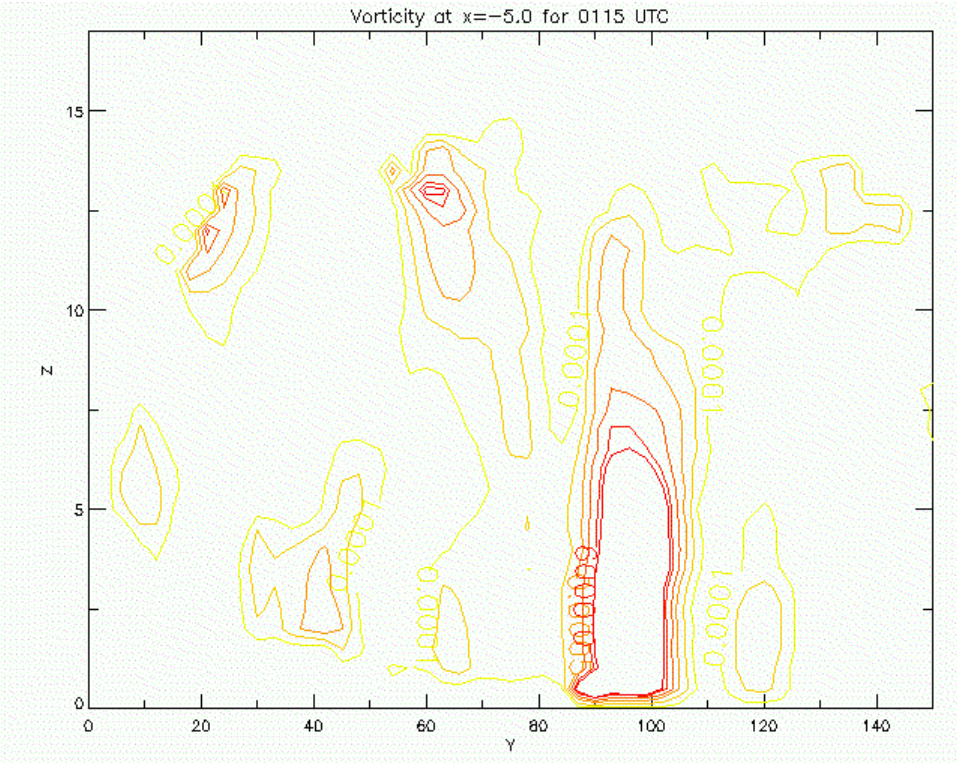

Figure 3.10 continued.

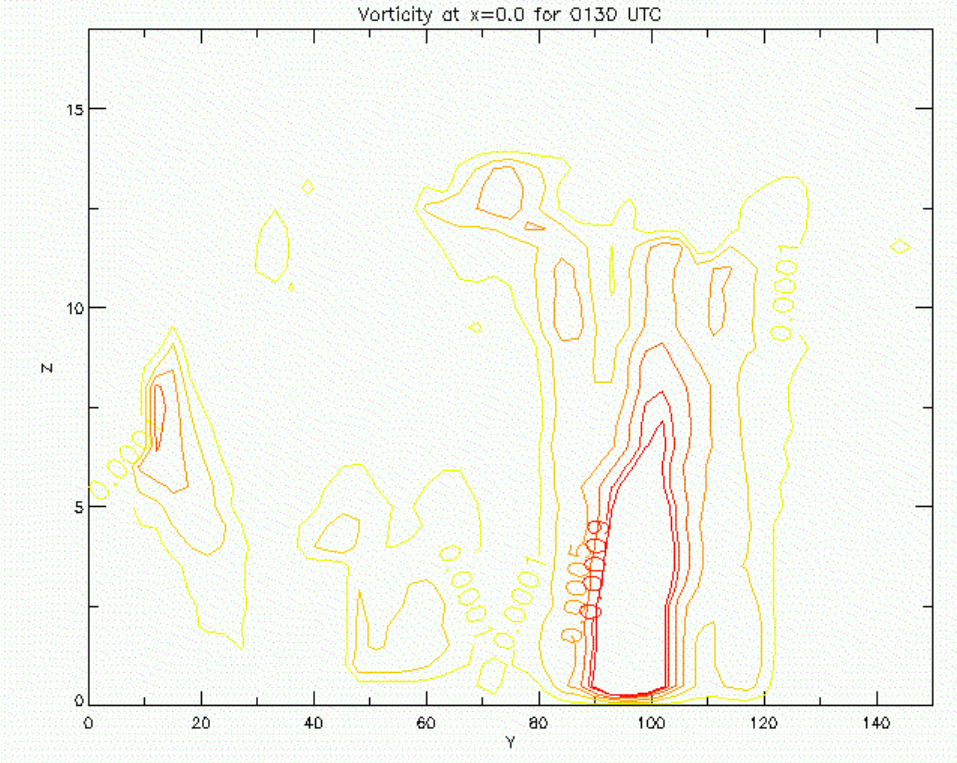

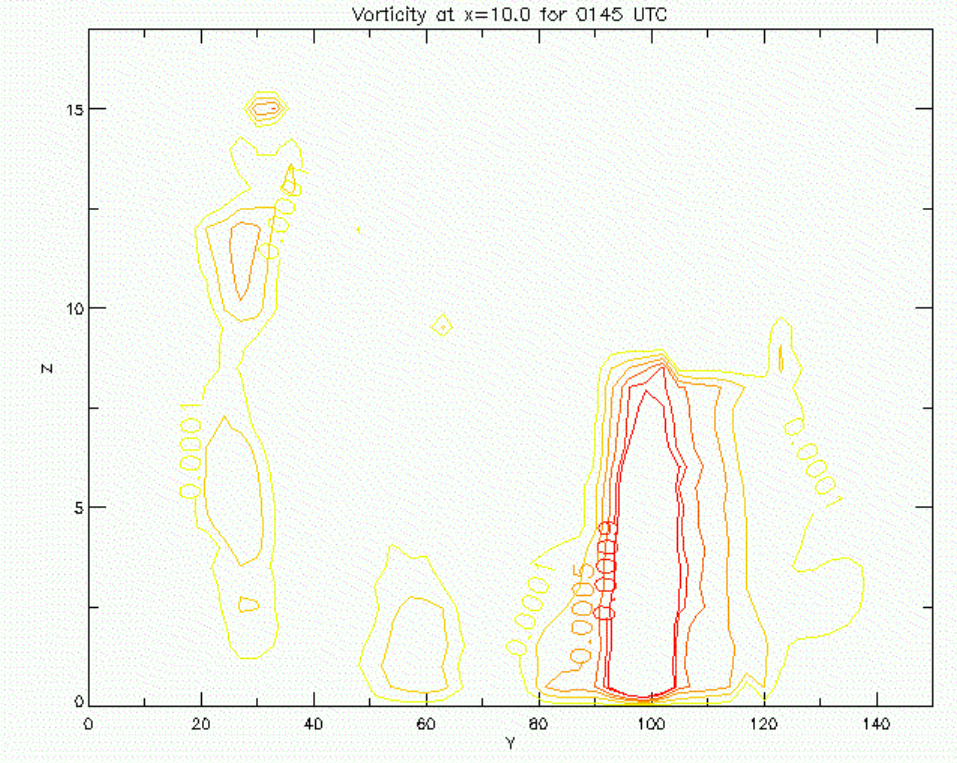

Figure 3.10 continued.

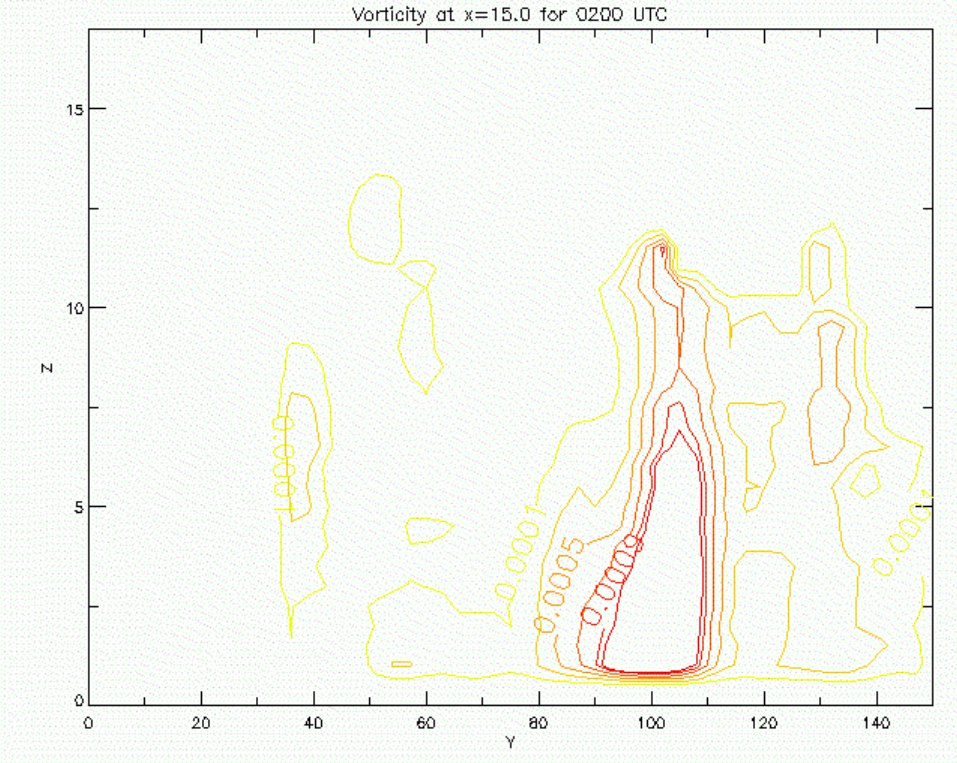

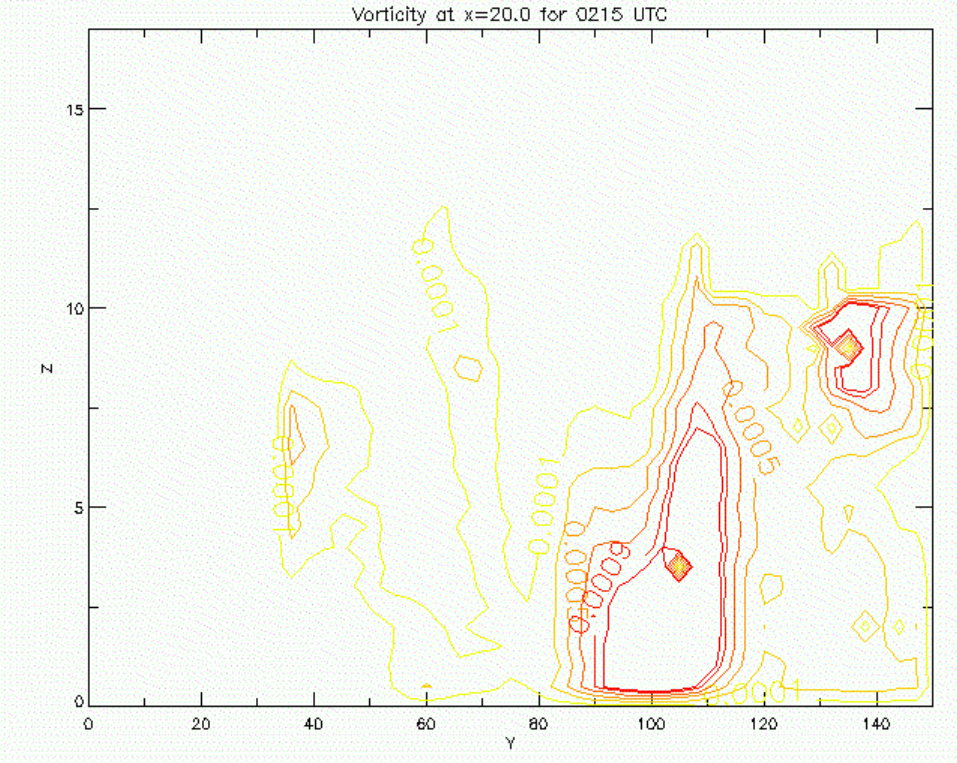

Figure 3.10 continued.

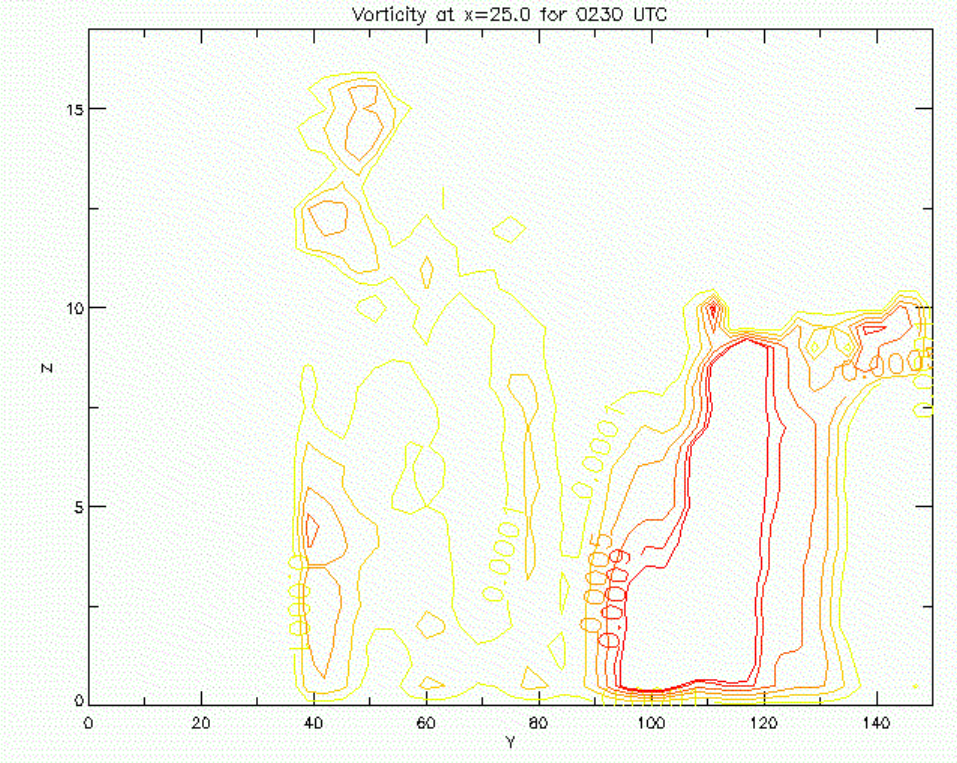

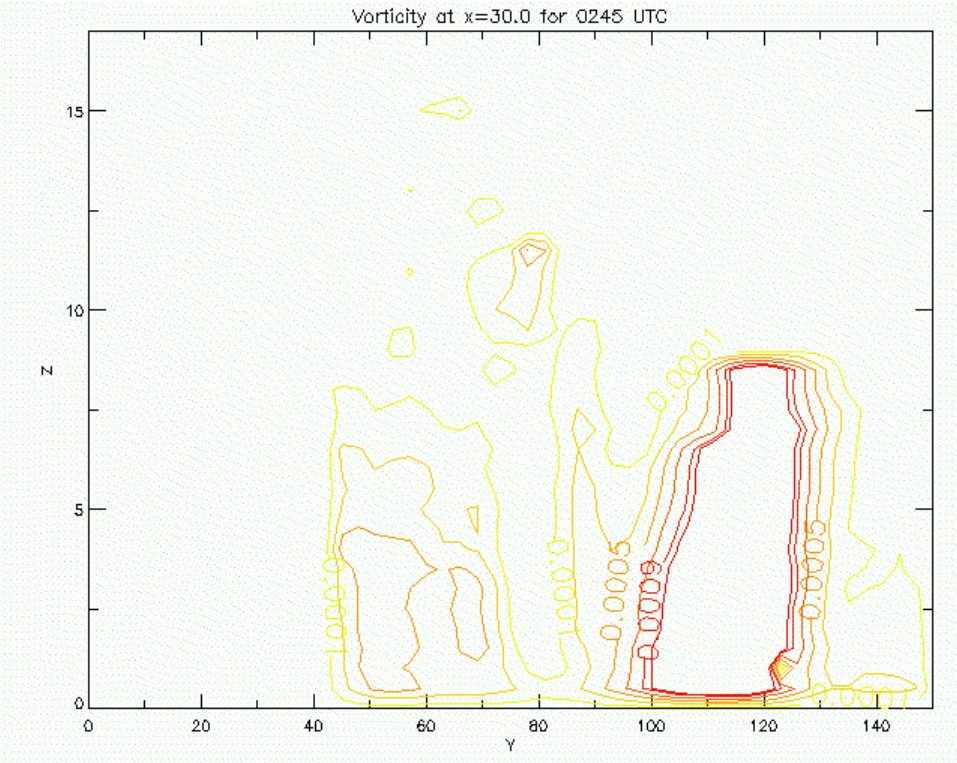

Figure 3.10 continued.

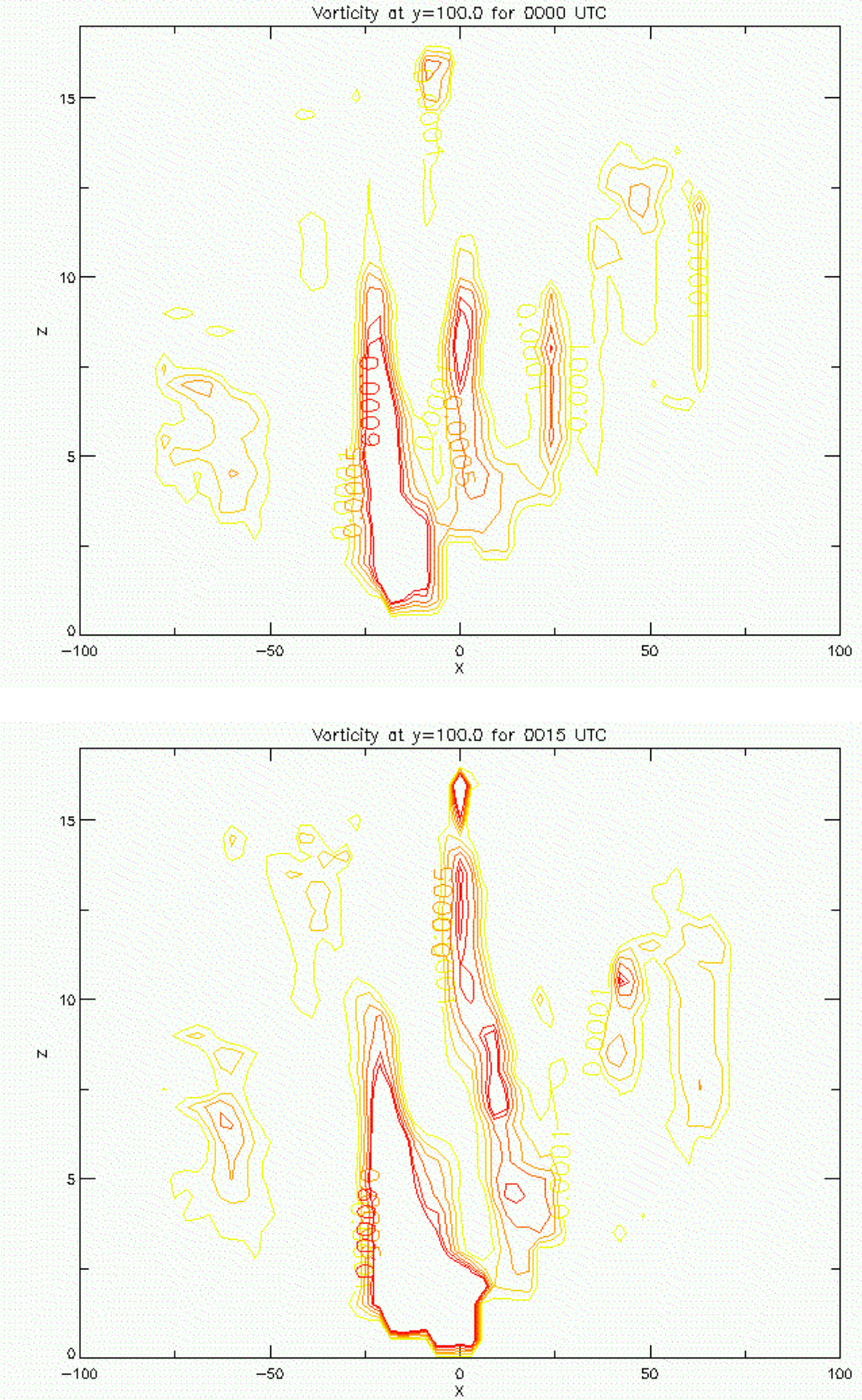

Figure 3.11. Vertical cross-sections for East-West transects through the MCV for fifteen minute intervals between 0000 and 0245 UTC. The first contour is 1 x 10^{-4} s^{-1} (green) with an interval increase of 2 x 10^{-4} s^{-1}. These images were all taken at y = 100.0 relative to the KTLX radar located at (0.0,0.0).

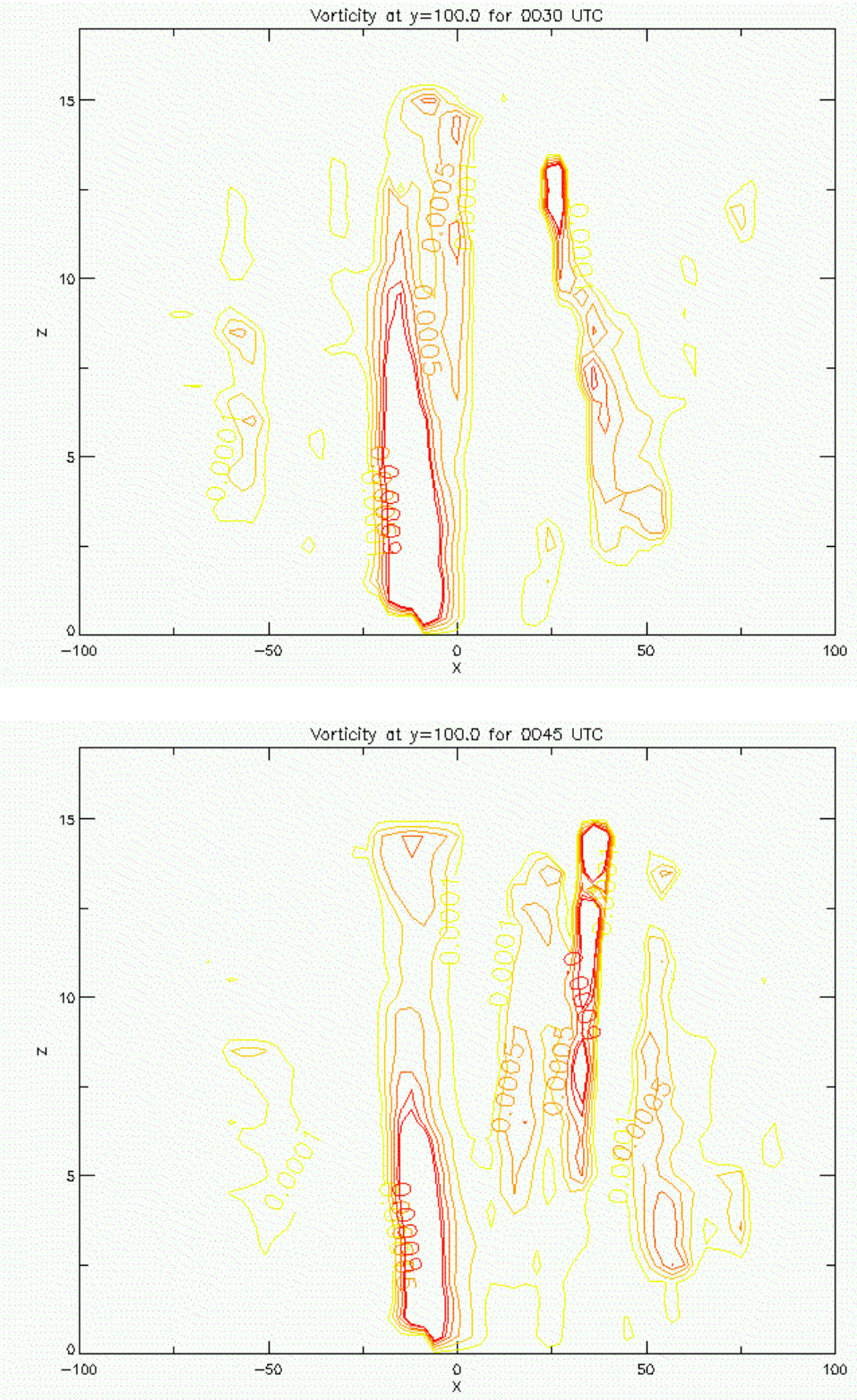

Figure 3.11 continued.

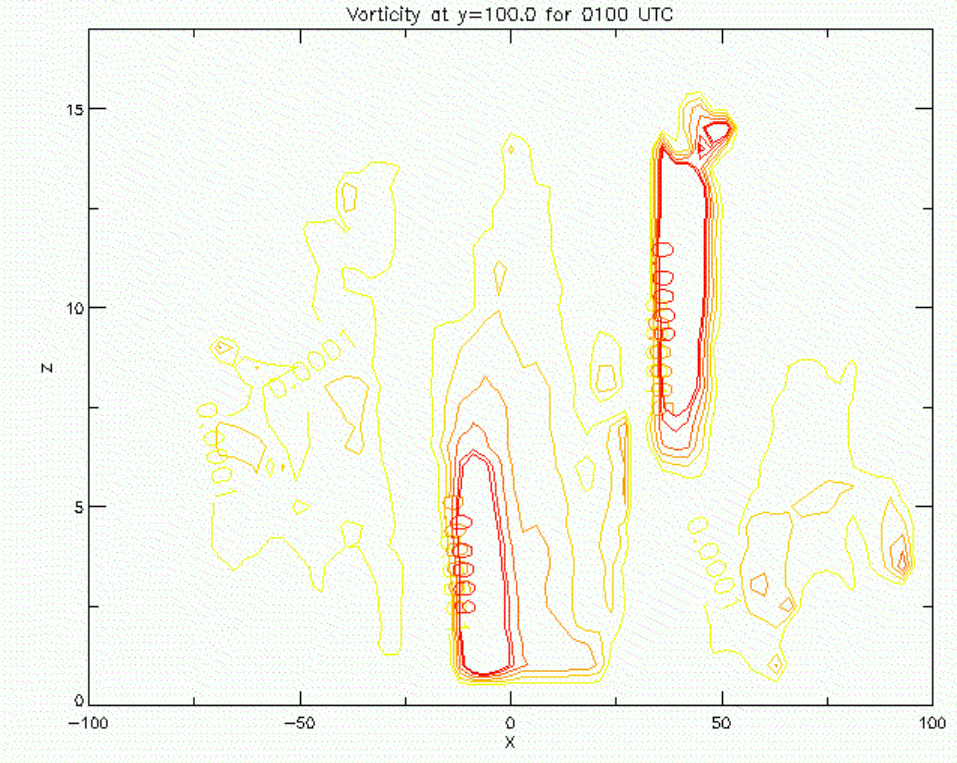

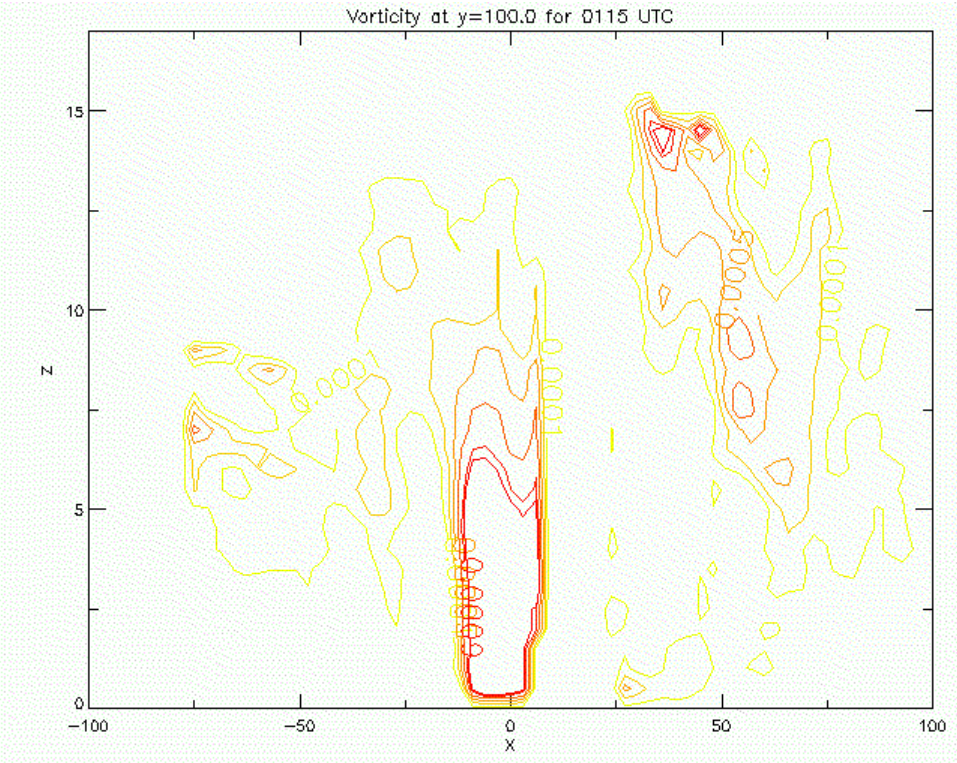

Figure 3.11 continued.

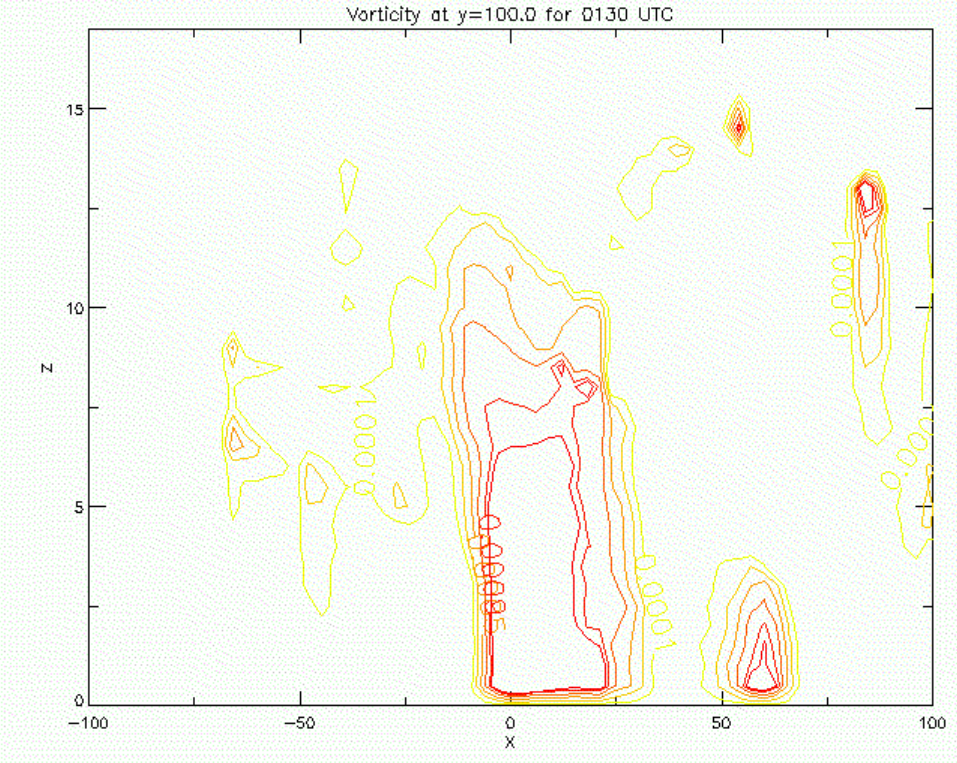

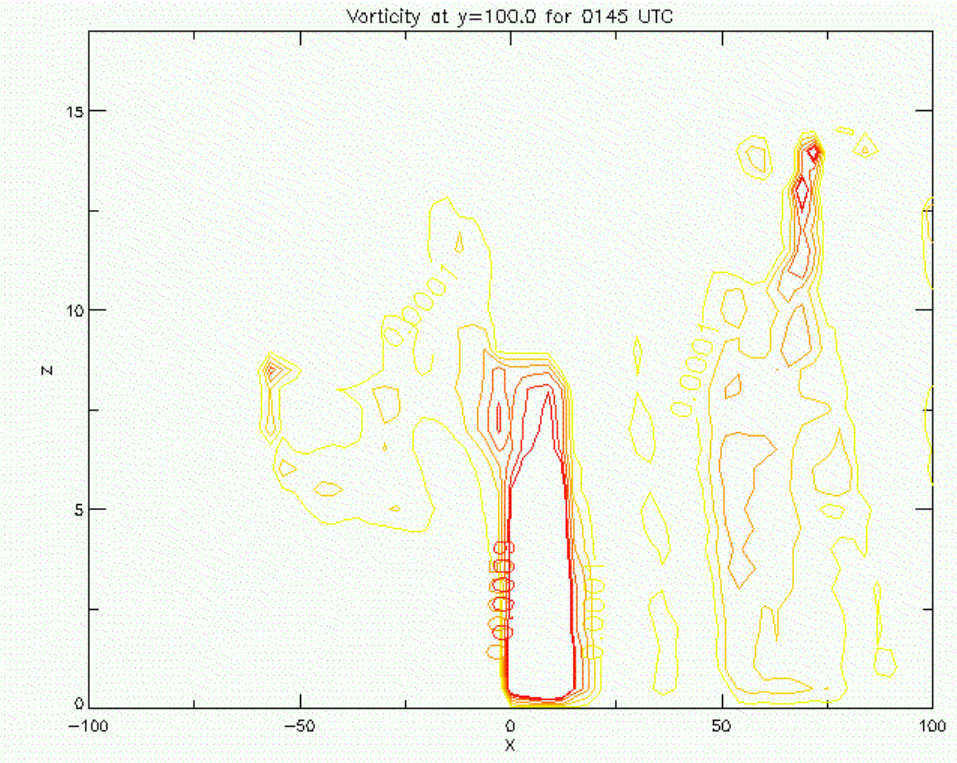

Figure 3.11 continued.

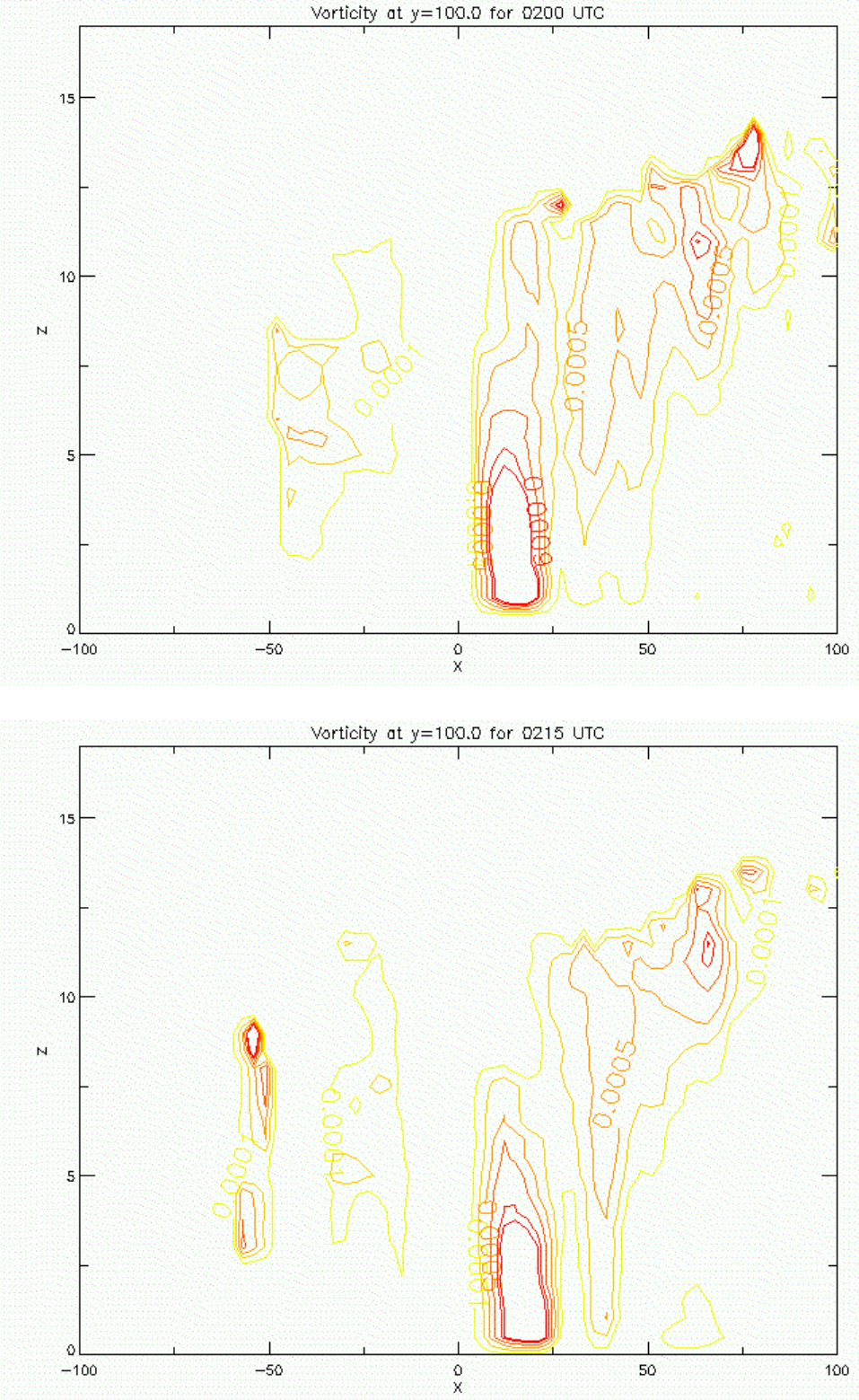

Figure 3.11 continued.

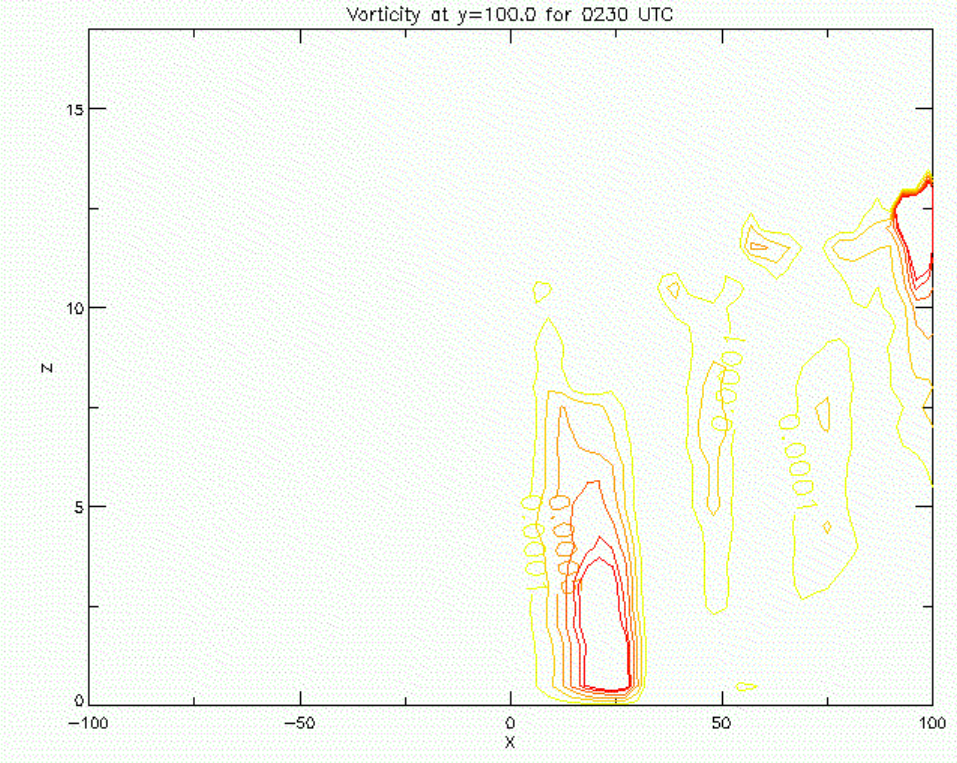

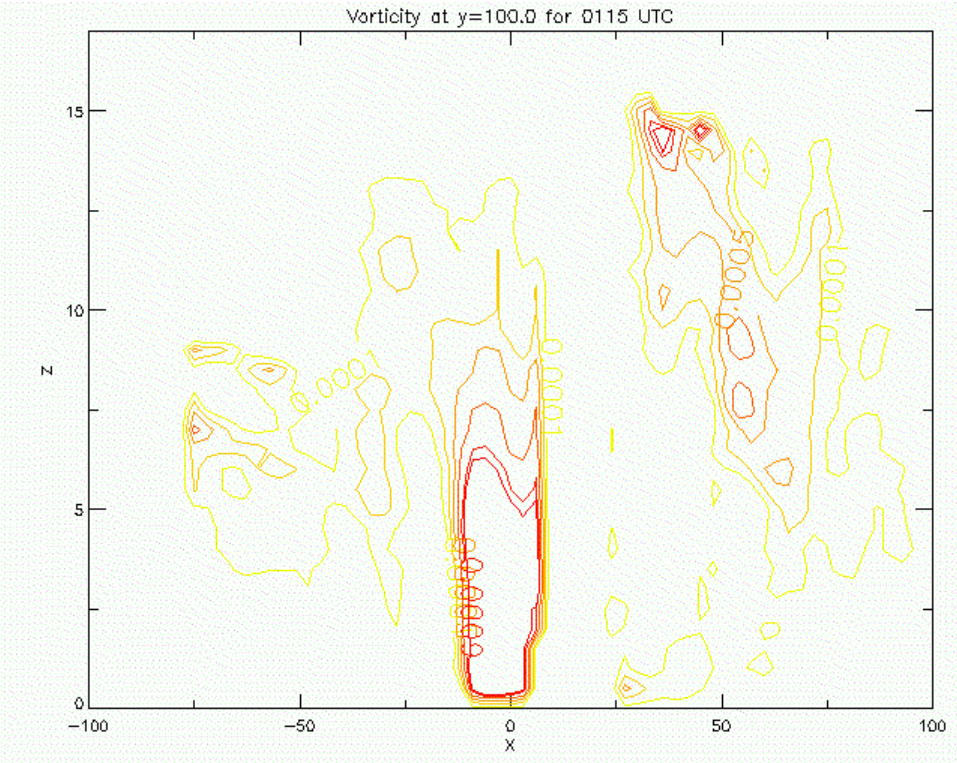

Figure 3.11 continued.

3.2 Time Series of Changes in Reflectivity, Divergence, Vorticity, and Vertical Velocity

Section 3.2 contains time series documenting the total number of data points, the number of convective precipitation data points (loosely defined as having reflectivity greater than 40 dBZ), the number of stratiform precipitation data points (loosely defined as having reflectivity greater than 0 dBZ and less than 40 dBZ), average divergence, average vertical vorticity, and average vertical velocity at 2.0, 3.0, 4.5, 5.5, 7.0, and 10.0 km over the entire dual-Doppler domain to document quantitative changes in reflectivity, divergence, vertical vorticity, and vertical velocity within the MCS where the MCV developed. Data from 1.0 km was not included in the time series because the data were increasingly noisy at the lower boundary of the dual-Doppler analysis.

Fig. 3.12 shows a time series of the total number of data points based on reflectivity greater than 0 dBZ. The lowest number of data points overall occur at 2.0 km. Analyses performed for 2.0 km had approximately 6000 data points until after 0200 UTC when the number of data points at that altitude slightly increased. By 0300 UTC, the number of data points available for analysis at 2.0 km was slightly above 8000. The 3.0 km altitude had a greater number of points to be used in analysis than 2.0 km and also had the most consistent number of analysis points (roughly 7000 until 0300 UTC). This would suggest that comparisons of different quantities at 3.0 km for different times should not be affected by the number of data points used in the calculations. The higher altitudes (4.5 km and greater) started out with lower numbers of data points but surpass the amount of data points available to conduct analyses at 3.0 km by 0100 UTC. For

example, 7.0 km had the greatest number of data points available for analysis after 0030 UTC after the MCS stratiform region entered the dual-Doppler lobe.

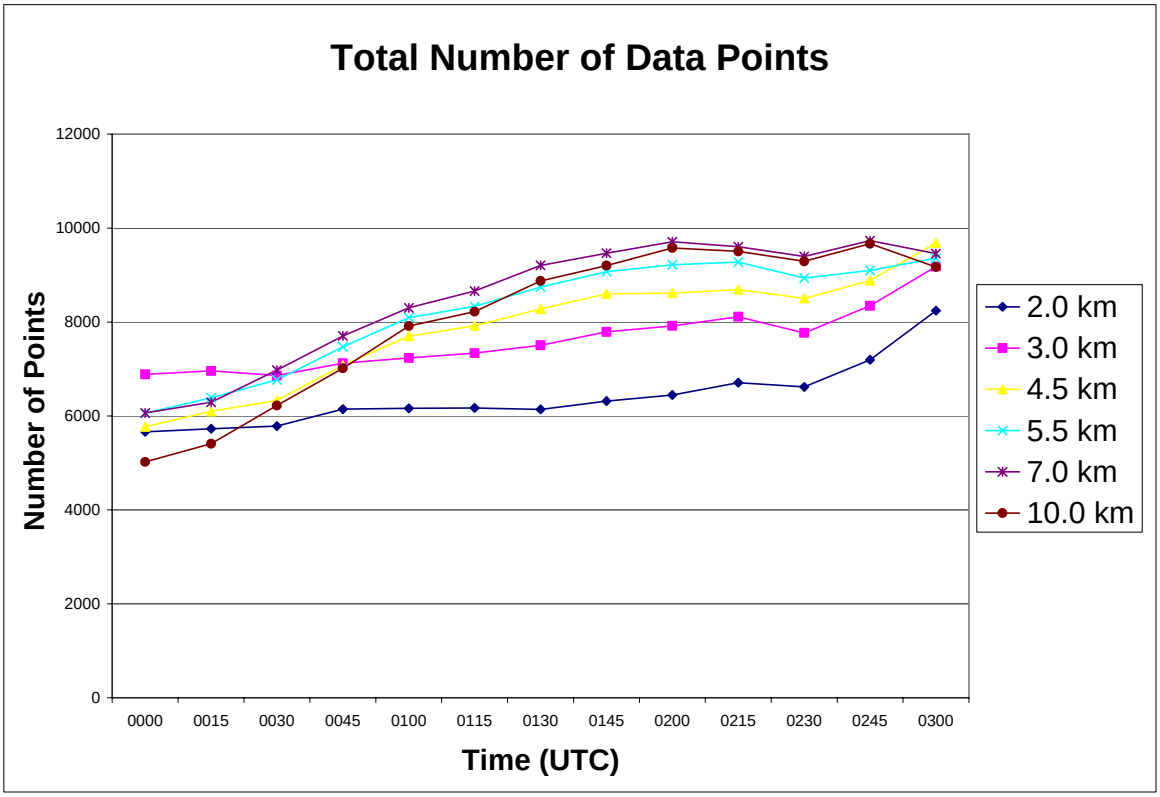

Figure 3.12. The total number of data points based on reflectivity greater than 0 dBZ at different times of dual-Doppler analysis.

Fig. 3.13 shows the number of data points with convective precipitation based on reflectivity greater than 40 dBZ. The lower altitudes (2.0 and 3.0 km) have the greatest number of convective precipitation data points. As developing convective cells, which tend to form just ahead of the leading line of the convective region (see Fig. 1.2), mature they are characterized by strong reflectivity cores that extend down to the surface (Houze et al. 1989). From 0000 to 0100 UTC, there are slightly more convective data points at

2.0 km. However, after 0100 UTC there are slightly more convective data points at 3.0 km. There are consistently fewer convective precipitation data points with increasing altitude as the frequency of 40 dBZ reflectivity decreases with increasing height. Of interest is the relatively high number of convective precipitation data points at 4.5 km. From the 0000 UTC KOUN sounding (Fig. 1.14), the melting level was slightly below 4.5 km, which suggests that the relatively high number of convective precipitation data points are the result of reflectivity values greater than 40 dBZ associated with both the strong convective cores from precipitation in the leading convective line as well as the bright band within the stratiform region.

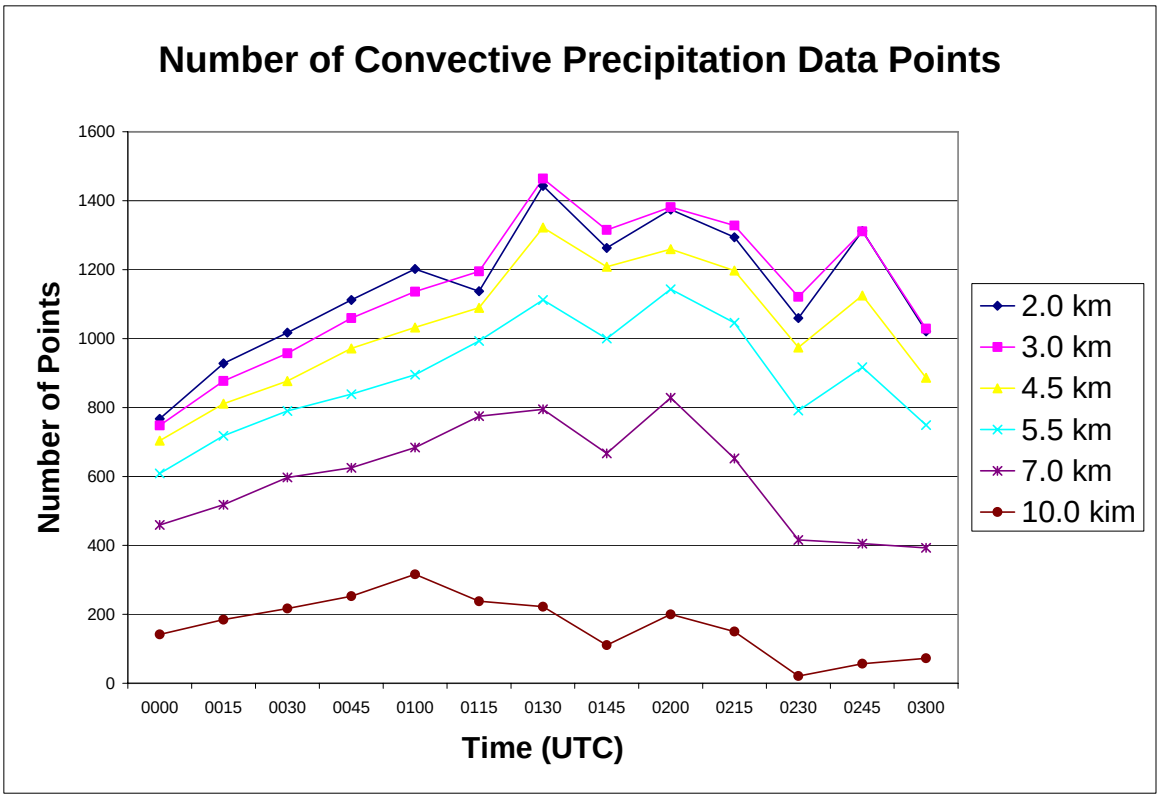

Figure 3.13. The number of data points with convective precipitation based on reflectivity greater than 40 dBZ.

Fig. 3.14 shows the number of data points with stratiform precipitation based on the total number of data points (reflectivity > 0 dBZ) minus the number of convective precipitation data points (reflectivity > 40 dBZ). Most notably, there are four to five times as many data points within the stratiform region than in the convective region at all heights. In contrast to what was found with data points in the convective region, the lowest number of data points from stratiform precipitation occur at the lowest two altitudes (2.0 and 3.0 km). In addition, the number of points at any given altitude and the number of data points overall (between approximately 5,000 and 9,000) are more consistent than what was found in the convective region.

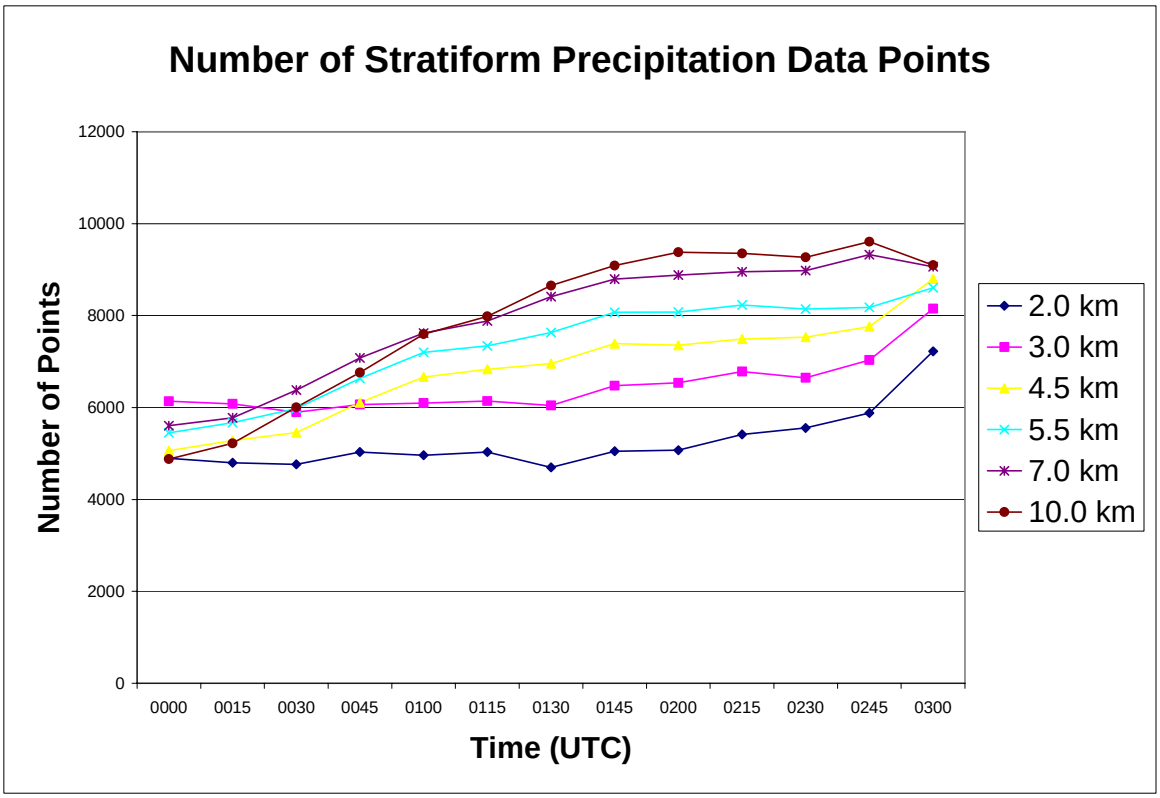

Figure 3.14. The number of data points with stratiform precipitation based on the total number of data points (reflectivity > 0 dBZ) minus the number of convective precipitation data points (reflectivity > 40 dBZ).

Fig. 3.15 shows a time series of average divergence at different altitudes within the dual-Doppler analysis domain of the MCS. At 10.0 km divergence occurs aloft within the MCS which is expected from outflow near the anvil (Houze et al. 1989; Biggerstaff and Houze 1991). Previous studies have shown that in the initial stages of MCV formation, convergence is produced by vorticity generated by the MCV at mid-levels (Johnson and Bartels 1992; Chen and Frank 1993). For this case, the strongest convergence also occurs at 4.5 km. Convergence also occurs at 3.0 km, although the magnitude is generally less than that of convergence at 4.5 km. Of interest are the changes from convergence to divergence at the mid-level altitudes of 5.5 and 7.0 km. At early times, convergence on the order of 2.5×10^{-3} s^{-1} occurs at 7.0 km, and then switches to divergence after 0100 UTC. At 5.5 km (which is approximately 500 mb) convergence occurs up to 0130 UTC, and then switches to divergence, before the flow becomes convergent again at 0215 UTC.

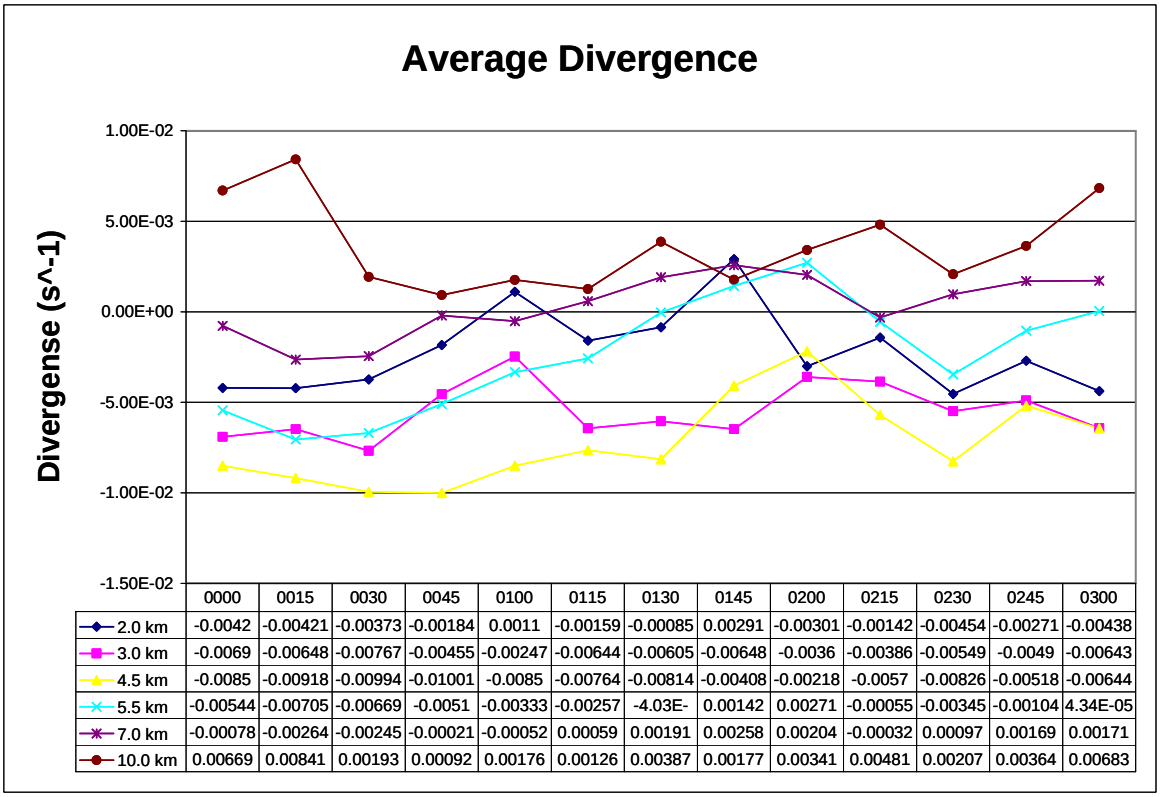

	0000	0015	0030	0045	0100	0115	0130	0145	0200	0215	0230	0245	0300
2.0 km	-0.0042	-0.00421	-0.00373	-0.00184	0.0011	-0.00159	-0.00085	0.00291	-0.00301	-0.00142	-0.00454	-0.00271	-0.00438
3.0 km	-0.0069	-0.00648	-0.00767	-0.00455	-0.00247	-0.00644	-0.00605	-0.00648	-0.0036	-0.00386	-0.00549	-0.0049	-0.00643
4.5 km	-0.0085	-0.00918	-0.00994	-0.01001	-0.0085	-0.00764	-0.00814	-0.00408	-0.00218	-0.0057	-0.00826	-0.00518	-0.00644
5.5 km	-0.00544	-0.00705	-0.00669	-0.0051	-0.00333	-0.00257	-4.03E-	0.00142	0.00271	-0.00055	-0.00345	-0.00104	4.34E-05
7.0 km	-0.00078	-0.00264	-0.00245	-0.00021	-0.00052	0.00059	0.00191	0.00258	0.00204	-0.00032	0.00097	0.00169	0.00171
10.0 km	0.00669	0.00841	0.00193	0.00092	0.00176	0.00126	0.00387	0.00177	0.00341	0.00481	0.00207	0.00364	0.00683

Figure 3.15. A time series of average divergence for altitudes of 2.0, 3.0, 4.5, 5.5, 7.0, and 10.0 km.

Fig. 3.16 shows a time series of average vorticity within the northwest dual-Doppler lobe that represents the area associated with the development of the 11 June 2003 MCV. Between 0030 and 0200 UTC, negative average vorticity occurs at 10.0 km. This is expected because MCVs are generally capped by an anticyclonic circulation at high levels associated with a negative PV anomaly (Raymond and Jiang 1990; Brandes 1990; Verlinde and Cotton 1990; Knievel and Johnson 2002). At all other altitudes average cyclonic vorticity is generally in the range of 1.0 to 2.5 x 10^{-4} s^{-1} during the time period of 0000 to 0300 UTC. The highest values of vertical vorticity occur at low levels such as 2.0 km at 0030 UTC.

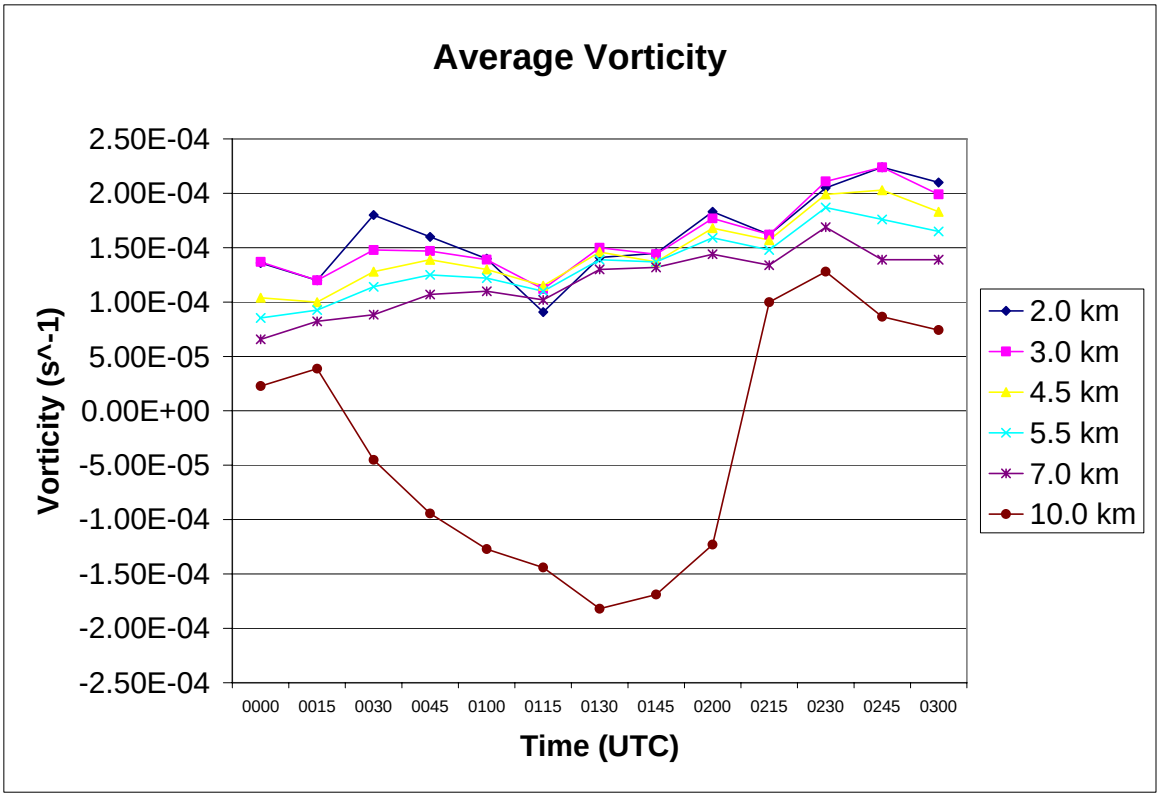

Figure 3.16. A time series of average vorticity for altitudes of 2.0, 3.0, 4.5, 5.5, 7.0, and 10.0 km.

Fig. 3.17 shows a time series of average vertical velocity for different heights. There is positive average vertical velocity (i.e., upward motion) during the entire time period of investigation for 5.5, 7.0, and 10.0 km. There is upward motion of approximately 0.2 m s^{-1} at 4.5 km, which is located just above the melting level, for most times, although downward motion occurs later at 0215 (-0.003 m s^{-1}) and 0230 (-0.12 m s^{-1}) UTC. As has been seen previously in Fig. 3.1, early time periods before 0030 UTC have larger percentages of data from convective precipitation as the leading line of the MCS enters the dual-Doppler lobe. This can also be seen in the relatively high average vertical velocity measurements calculated at these times. There is finally a suggestion of

mesoscale downdraft development at later analysis times. For the 2.0 km altitude there was positive vertical velocity up to 0200 UTC likely associated with the upward motion of developing convection. However after 0200 UTC, average vertical velocity became negative, which suggests the development of a mesoscale downdraft. This average may also be affected by the increasing percentage of stratiform to total precipitation points in the averaging domain as the stratiform region develops with time. Positive average vertical velocity also becomes negative at 0215 UTC for 3.0 and 4.5 km, likely also associated with the development of the mesoscale downdraft and increasing fraction of stratiform precipitation points in the domain.

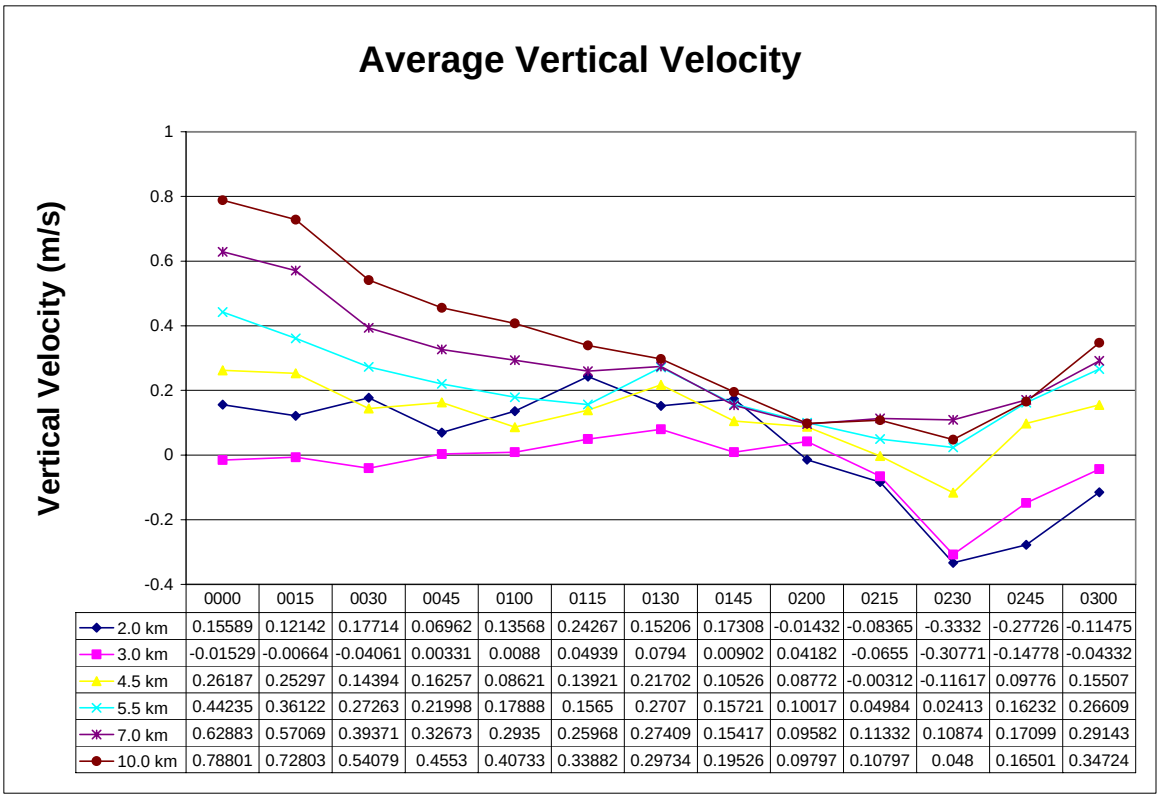

	0000	0015	0030	0045	0100	0115	0130	0145	0200	0215	0230	0245	0300
2.0 km	0.15589	0.12142	0.17714	0.06962	0.13568	0.24267	0.15206	0.17308	-0.01432	-0.08365	-0.3332	-0.27726	-0.11475
3.0 km	-0.01529	-0.00664	-0.04061	0.00331	0.0088	0.04939	0.0794	0.00902	0.04182	-0.0655	-0.30771	-0.14778	-0.04332
4.5 km	0.26187	0.25297	0.14394	0.16257	0.08621	0.13921	0.21702	0.10526	0.08772	-0.00312	-0.11617	0.09776	0.15507
5.5 km	0.44235	0.36122	0.27263	0.21998	0.17888	0.1565	0.2707	0.15721	0.10017	0.04984	0.02413	0.16232	0.26609
7.0 km	0.62883	0.57069	0.39371	0.32673	0.2935	0.25968	0.27409	0.15417	0.09582	0.11332	0.10874	0.17099	0.29143
10.0 km	0.78801	0.72803	0.54079	0.4553	0.40733	0.33882	0.29734	0.19526	0.09797	0.10797	0.048	0.16501	0.34724

Figure 3.17. A time series of average vertical velocity for altitudes of 2.0, 3.0, 4.5, 5.5, 7.0, and 10.0 km.

3.3 Vorticity Budget Analyses

Fig. 3.18 shows the number of data points used to calculate the terms of the vertical vorticity tendency equation during the time period of investigation. Before 0030 UTC there are fewer number of data points available for use in calculating the terms of the vorticity tendency equation. Due to the fact that the MCS in which the MCV developed propagates through a fixed dual-Doppler analysis domain, it is necessary to take into account such biases that might be introduced into the analyses such as those caused by using too few data points. This would suggest that the vorticity budget analyses are most reliable in the time period after 0030 UTC on based on a subjective threshold requiring at least 400 data points at all levels of analysis. This corresponds to an area of an estimated 20 x 20 data points, which with a 3.0 km horizontal grid resolution, corresponds to an area of approximately 60 x 60 km^2.

Fig. 3.19 presents vertical profiles of the vorticity budget terms for fifteen minute intervals from 0000 to 0245 UTC. The first three analyses (0030 UTC and earlier) show that the entire profile is dominated by a lot of noise which is likely due to a larger percentage of data points being convective. Motions on convective scales cannot be resolved for with the 3.0 horizontal grid resolution and likely translates to greater noise in the vorticity budget analyses at earlier times. At later times, there is still noise in the analyses at the top and bottom boundaries due to a reduced number of data points available, but overall trends can be seen from approximately 1.0 to 10.0 km. The vorticity budget at 0215 UTC provides the best example of the vorticity budget analysis profiles due to its lack of noise compared to other times. Below 7.0 km, in the region where the MCV developed, the sum of all four terms of the vertical vorticity tendency equation is

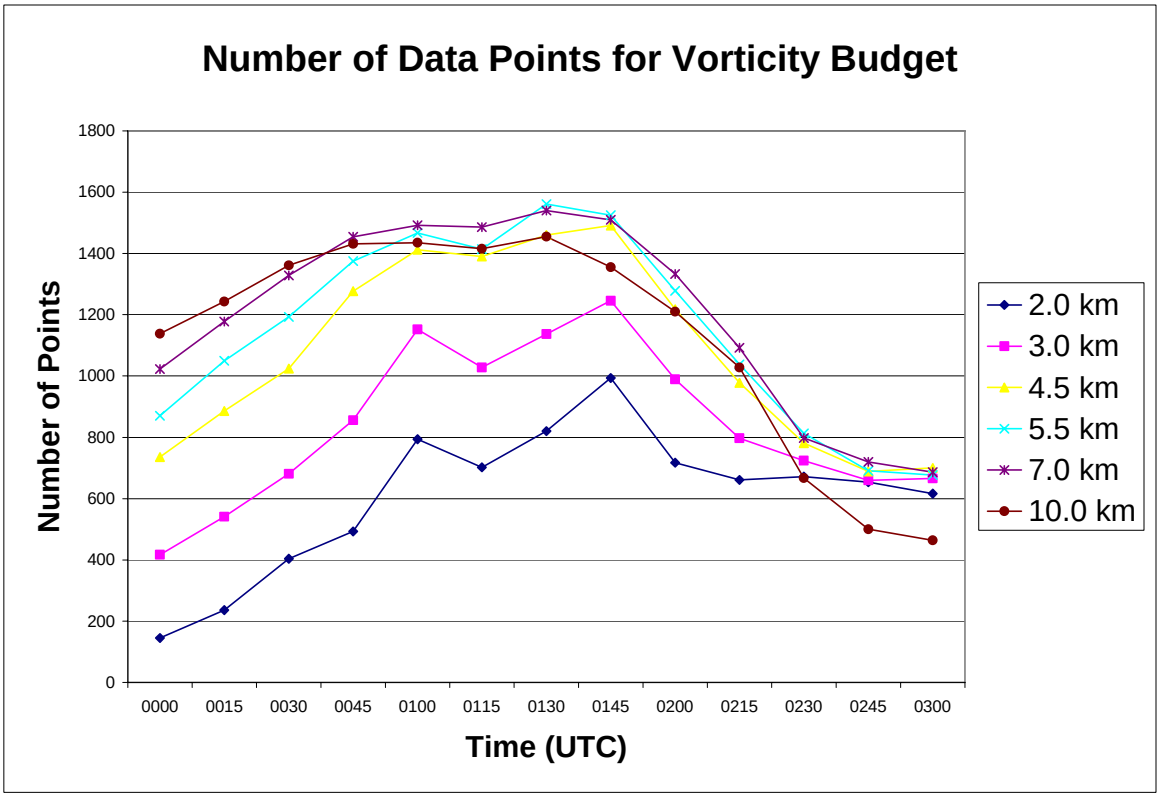

Figure 3.18. The number of data points used to calculate terms of the vorticity tendency equation at each time of analysis.

positive. At this time (0215 UTC), the highest value for the sum of the terms occurred at 4.5 km. The MCV clearly existed at 4.5 km altitude after 0045 UTC. The 4.5 km altitude is also the melting level where the mesoscale updraft and downdraft would provide greatest stretching for the spin up of the MCV. However above 7.0 km, the sum of the four terms from the tendency equation is negative, which is consistent with the development of the previously mentioned anticyclone aloft (Raymond and Jiang 1990; Brandes 1990; Verlinde and Cotton 1990; Knievel and Johnson 2002). At least for this time, these results suggest that horizontal advection, horizontal divergence, vertical advection, and tilting of vertical vorticity all contributed in a positive manner (although at slightly different intensities) to the formation of the 11 June 2003 MCV.

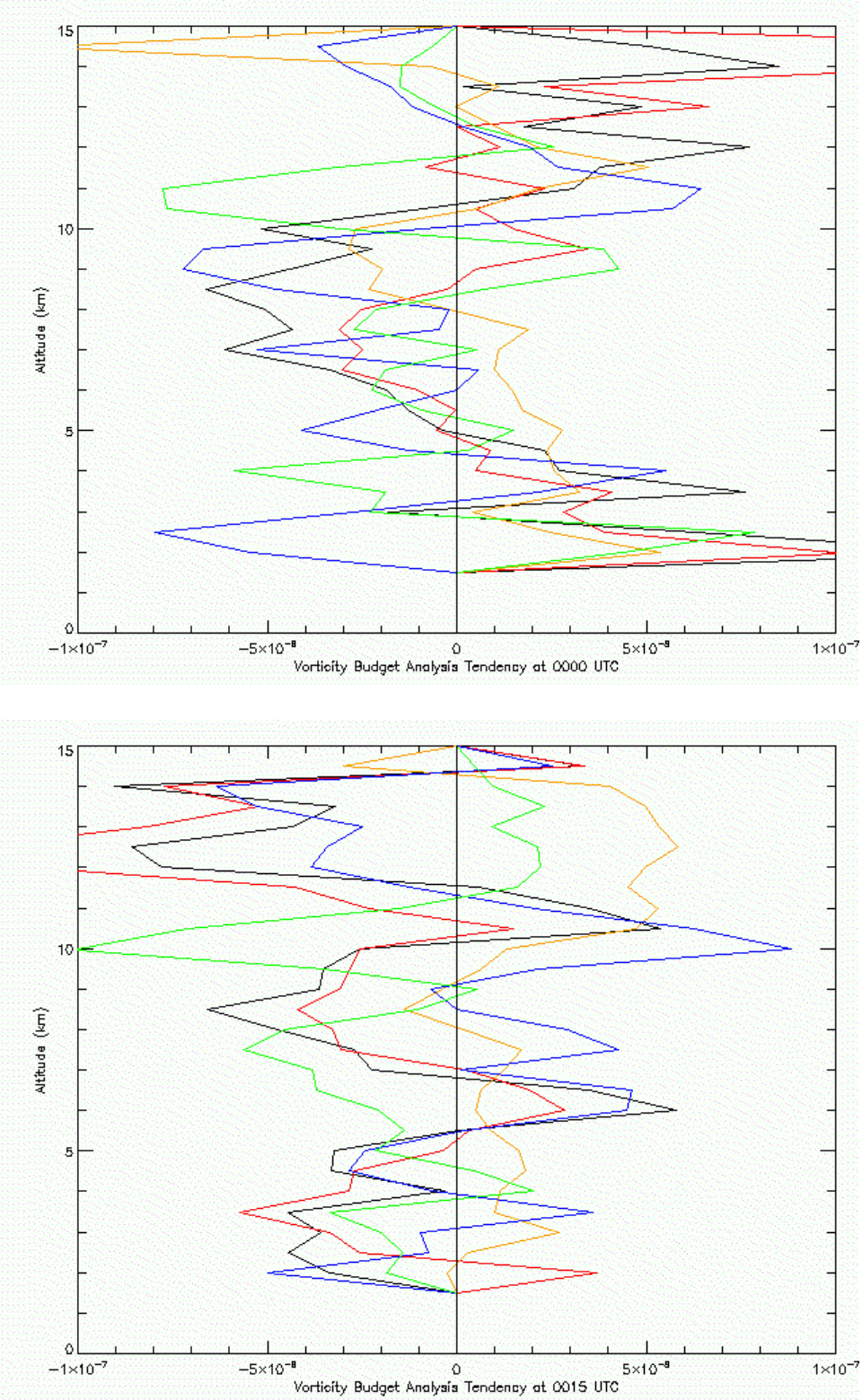

Figure 3.19. Vorticity budgets every fifteen minutes from 0000 to 0245 UTC. Average horizontal advection is in red, average horizontal divergence is in orange, average vertical advection is in blue, the average tilting term is in green, and the sum of all four terms is in black. The units of all terms are s^{-2}.

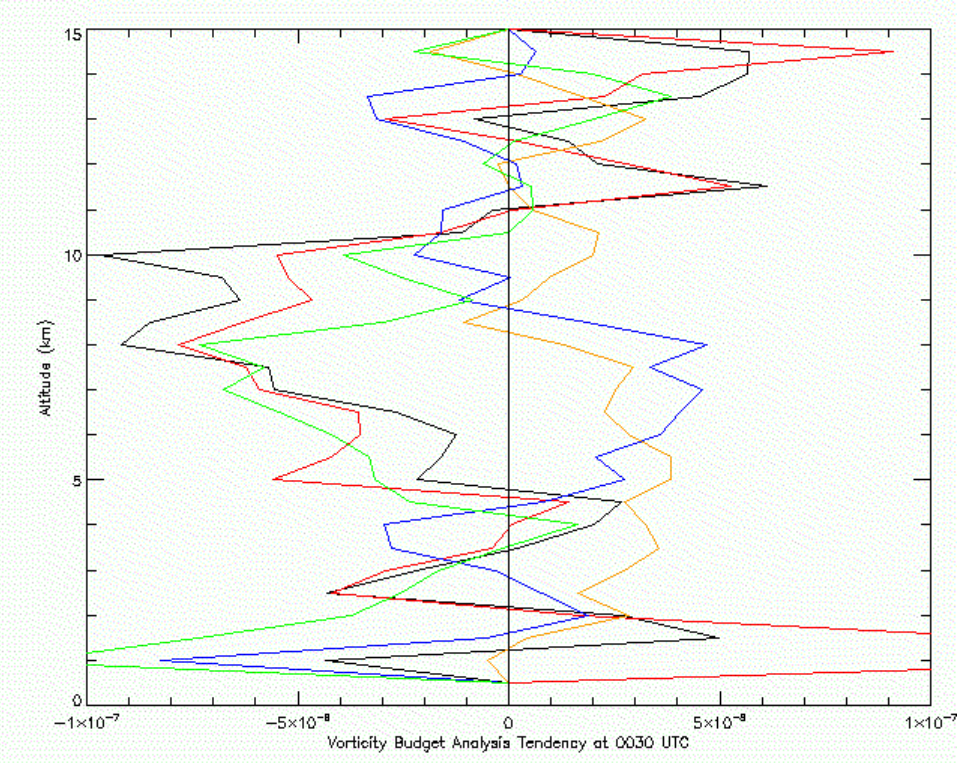

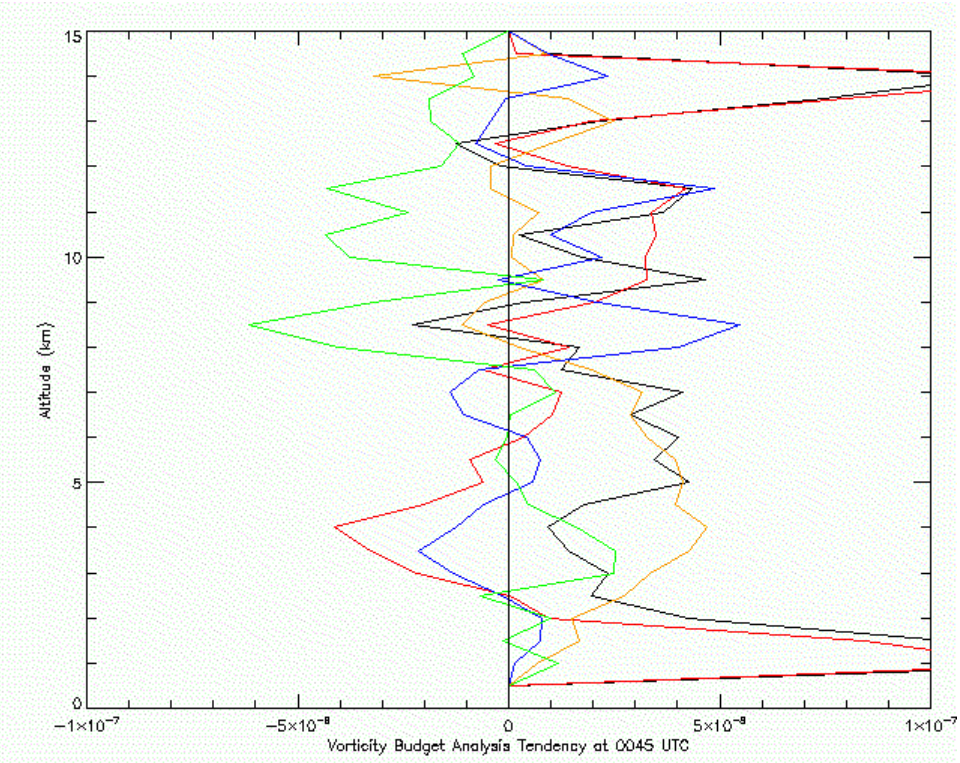

Figure 3.19 continued.

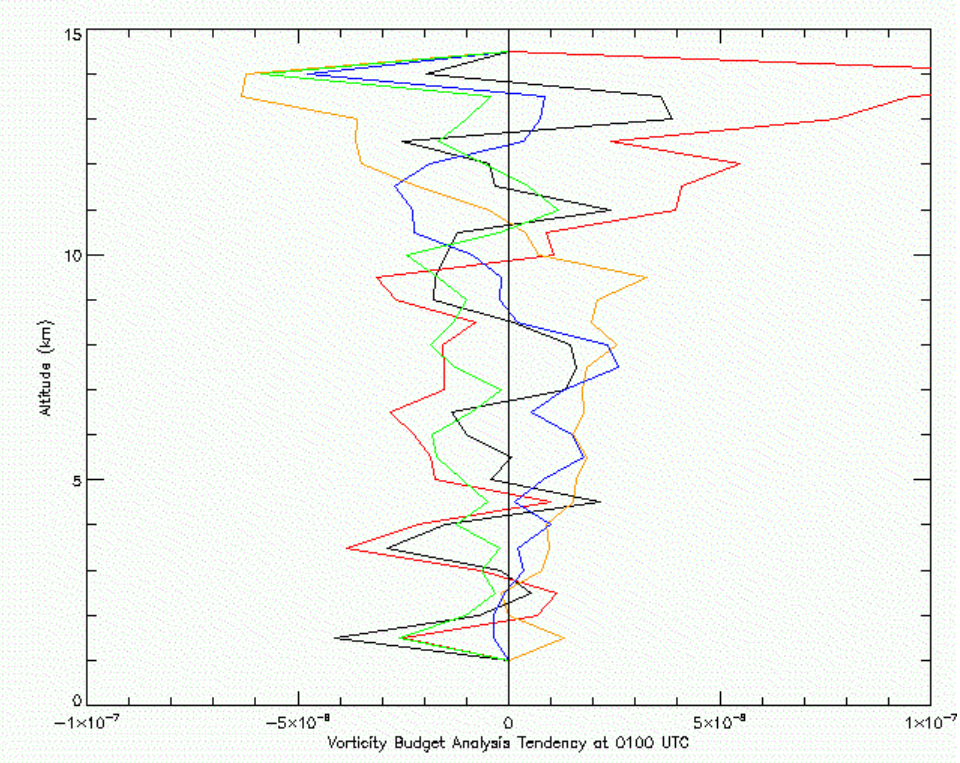

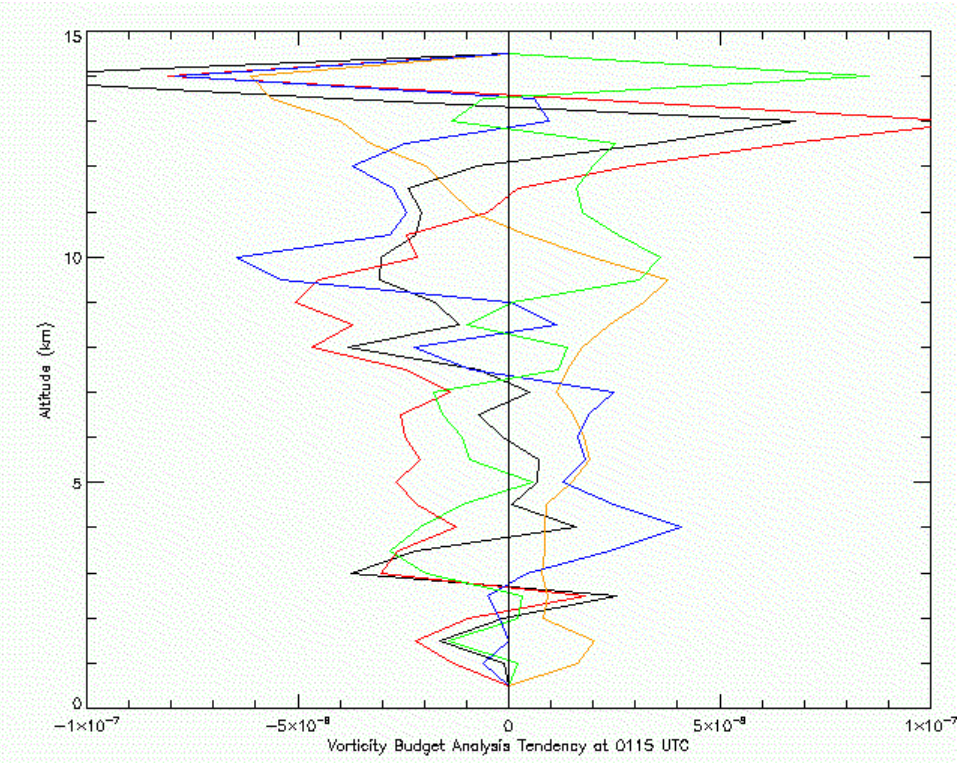

Figure 3.19 continued.

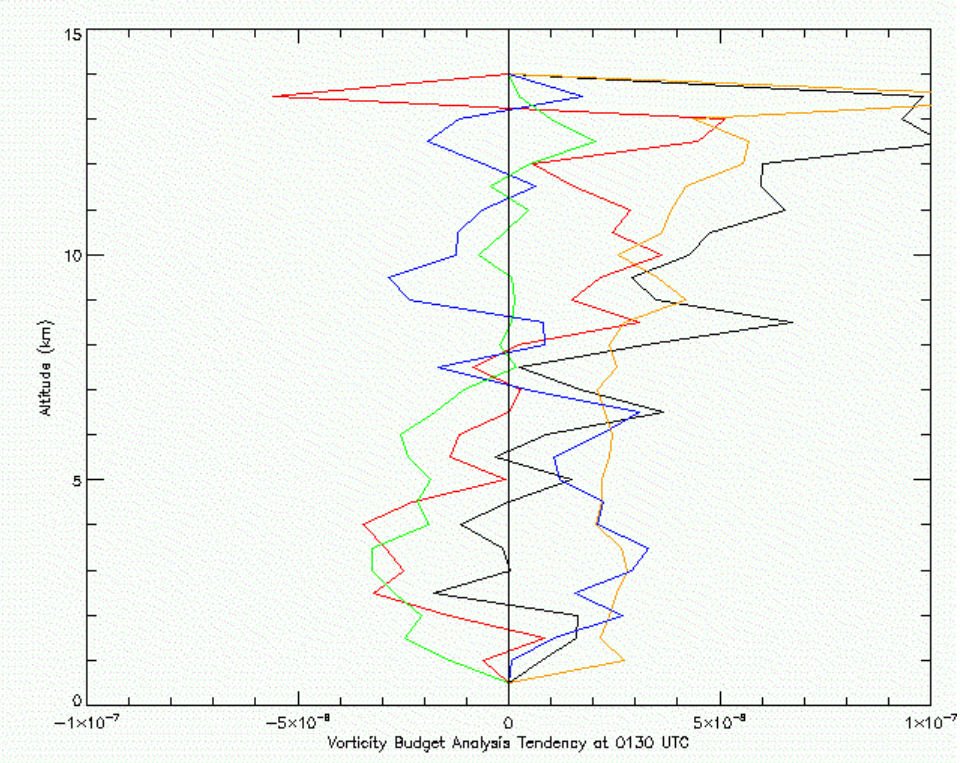

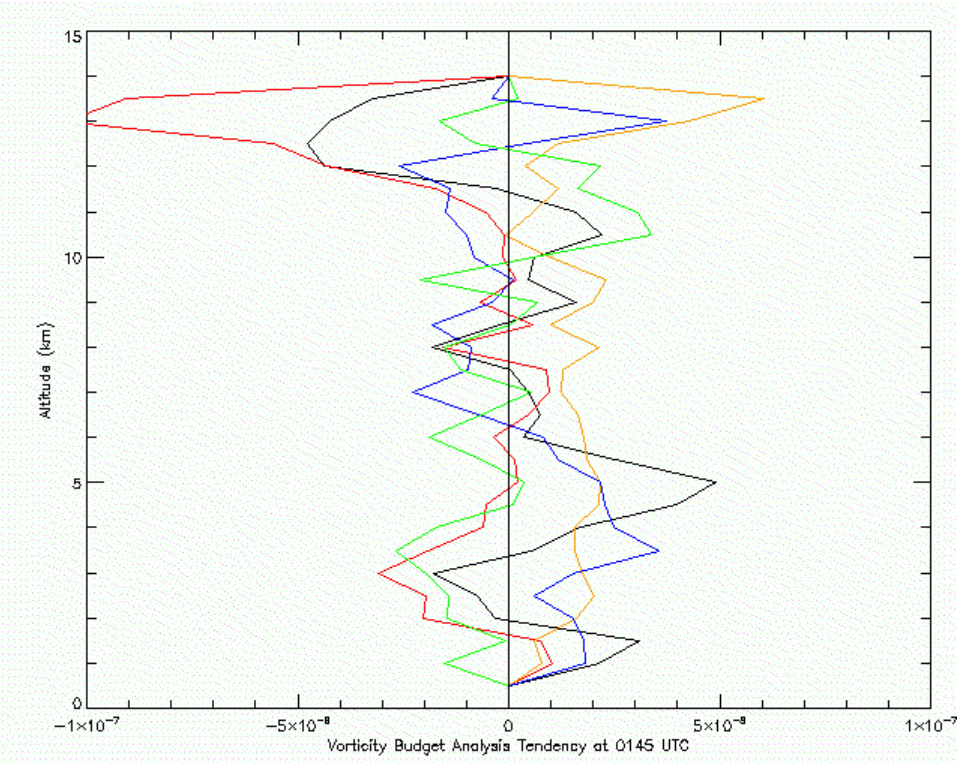

Figure 3.19 continued.

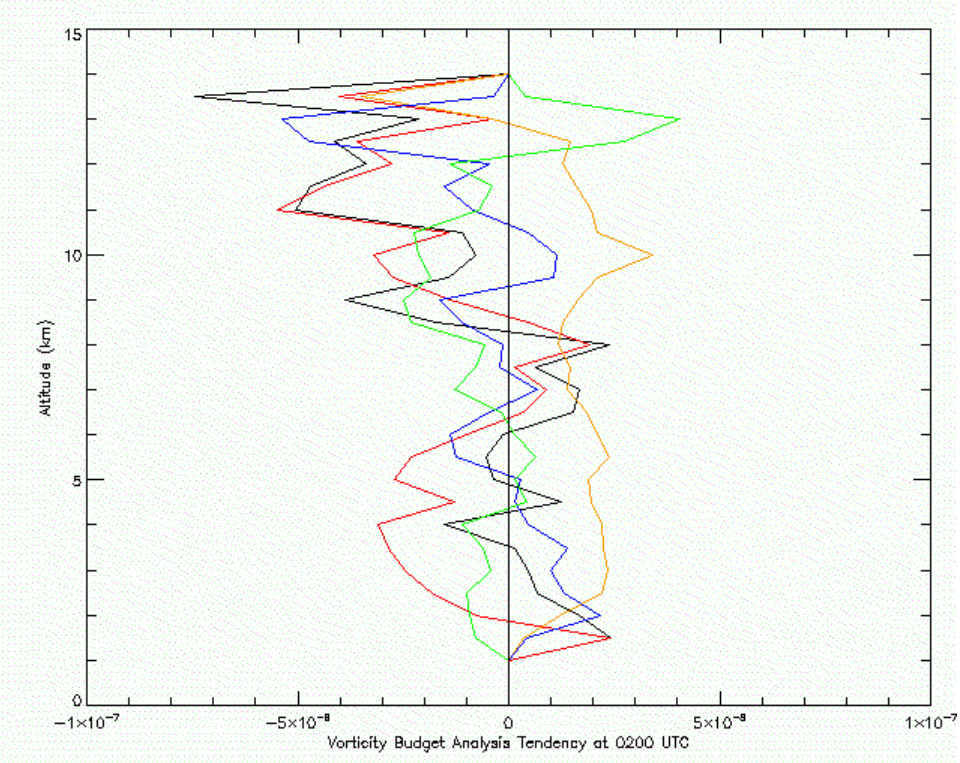

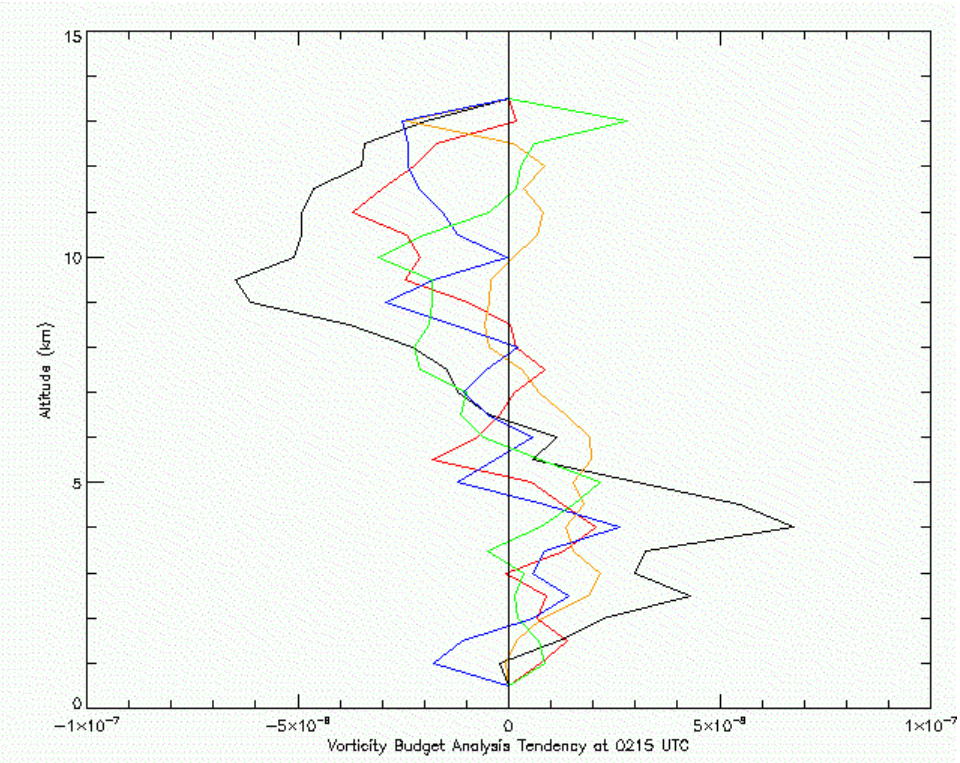

Figure 3.19 continued.

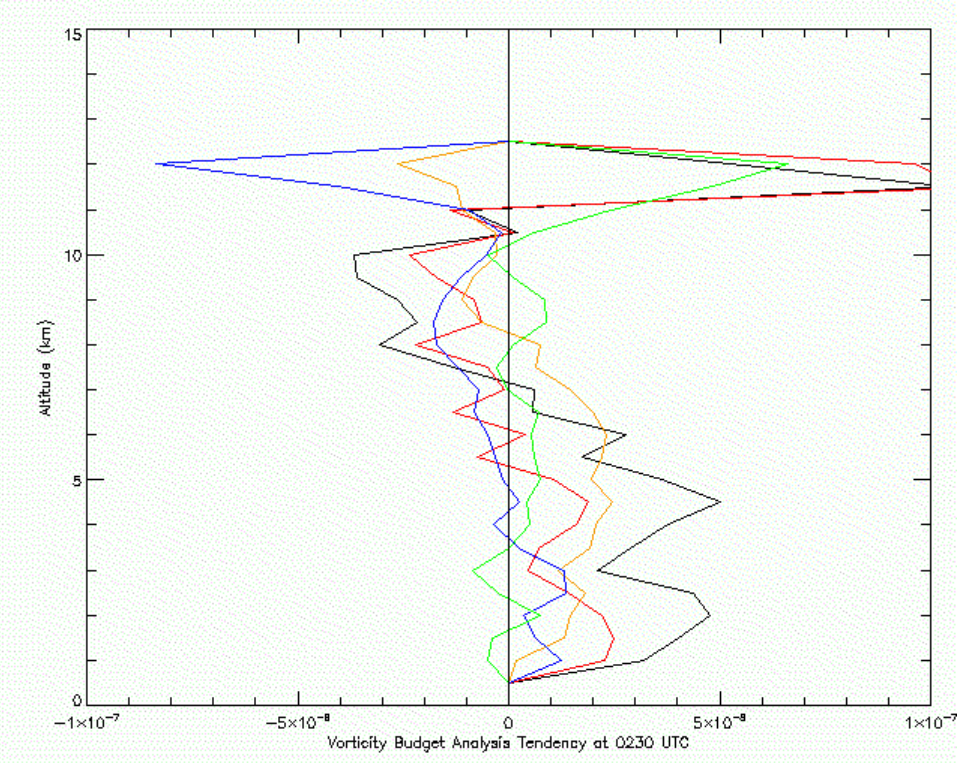

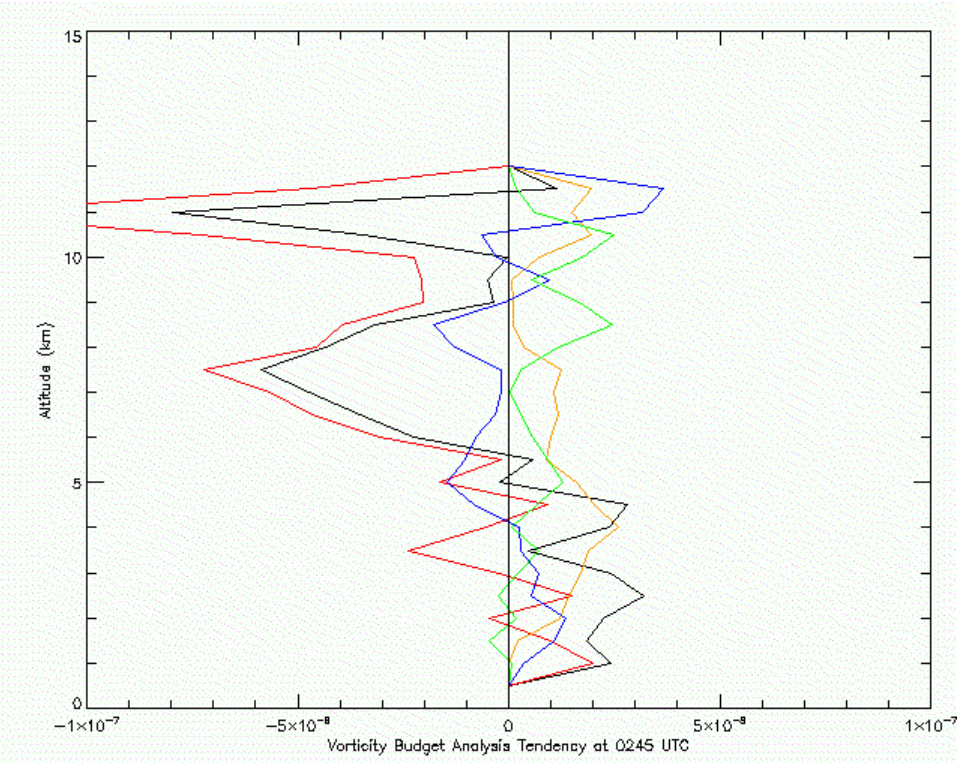

Figure 3.19 continued.

Fig. 3.20 shows the average horizontal advection of vertical vorticity as a function of time for 2.0, 3.0, 4.5, 5.5, 7.0 and 10.0 km. As seen previously, the data at 0000 UTC appear noisy based on a dispersion of values with height, which likely relates back to the fact that at this time the dual-Doppler domain contained a larger percentage of data points within the leading convective line of the MCS. Of particular interest are the high magnitudes of positive average horizontal advection of vorticity at 2.0 km for 0030 (1.25×10^{-7} s^{-2}) and 0045 (7.55×10^{-8} s^{-2}) UTC. These times also correspond to the times when the MCV begins to initiate just to the rear of the convective line (see Figure 3.1). Although horizontal advection at 2.0 km decreases slightly in later times, it is still generally greater than the values of horizontal advection at all other levels. There is also large (5.15×10^{-8} s^{-2}) horizontal advection aloft at 10.0 km at 0045 UTC.

Fig. 3.21 shows the average horizontal divergence of vertical vorticity as a function of time. Before 0100 UTC, there is a positive tendency of vertical vorticity associated with the horizontal divergence (stretching term) at 4.5 and 5.5 km (3.19 to 4.72×10^{-8} s^{-2}). This suggests that at these times and heights within the MCS stretching of vertical vorticity is occurring that could indeed support the genesis of an MCV. More importantly, positive average horizontal divergence exists at all levels (except for 10.0 km from 0000 to 0045 and 0215 to 0230 UTC). This suggests that at least in terms of the tendency of vertical vorticity associated with the horizontal divergence (stretching) term, the environment within which the MCV generates is in fact conducive to its formation. It also implies that as vertical vorticity is generated it will likely be stretched to increase cyclonic rotation. It should be noted, however, that the magnitudes of the contributions of

horizontal divergence are less than for the previously discussed horizontal advection term.

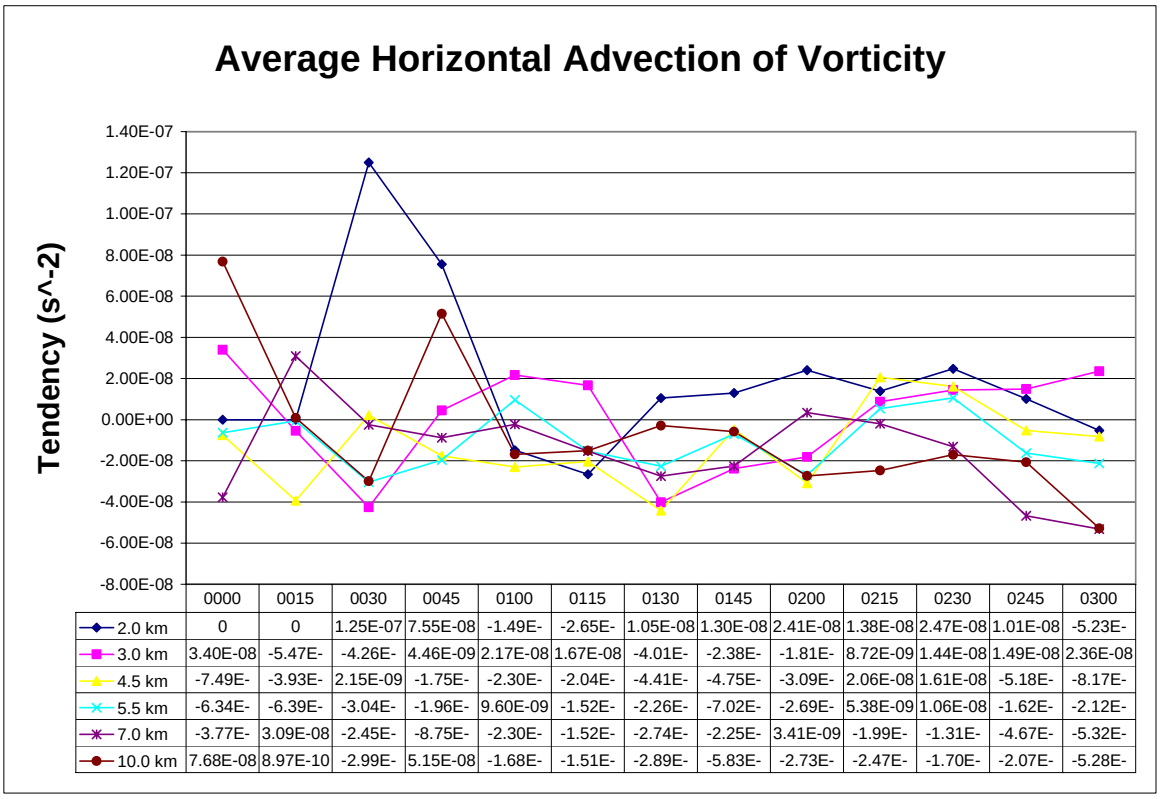

	0000	0015	0030	0045	0100	0115	0130	0145	0200	0215	0230	0245	0300
2.0 km	0	0	1.25E-07	7.55E-08	-1.49E-	-2.65E-	1.05E-08	1.30E-08	2.41E-08	1.38E-08	2.47E-08	1.01E-08	-5.23E-
3.0 km	3.40E-08	-5.47E-	-4.26E-	4.46E-09	2.17E-08	1.67E-08	-4.01E-	-2.38E-	-1.81E-	8.72E-09	1.44E-08	1.49E-08	2.36E-08
4.5 km	-7.49E-	-3.93E-	2.15E-09	-1.75E-	-2.30E-	-2.04E-	-4.41E-	-4.75E-	-3.09E-	2.06E-08	1.61E-08	-5.18E-	-8.17E-
5.5 km	-6.34E-	-6.39E-	-3.04E-	-1.96E-	9.60E-09	-1.52E-	-2.26E-	-7.02E-	-2.69E-	5.38E-09	1.06E-08	-1.62E-	-2.12E-
7.0 km	-3.77E-	3.09E-08	-2.45E-	-8.75E-	-2.30E-	-1.52E-	-2.74E-	-2.25E-	3.41E-09	-1.99E-	-1.31E-	-4.67E-	-5.32E-
10.0 km	7.68E-08	8.97E-10	-2.99E-	5.15E-08	-1.68E-	-1.51E-	-2.89E-	-5.83E-	-2.73E-	-2.47E-	-1.70E-	-2.07E-	-5.28E-

Figure 3.20. Average horizontal advection of vertical vorticity at 2.0, 3.0, 4.5, 5.5, 7.0 and 10.0 km as a function of time.

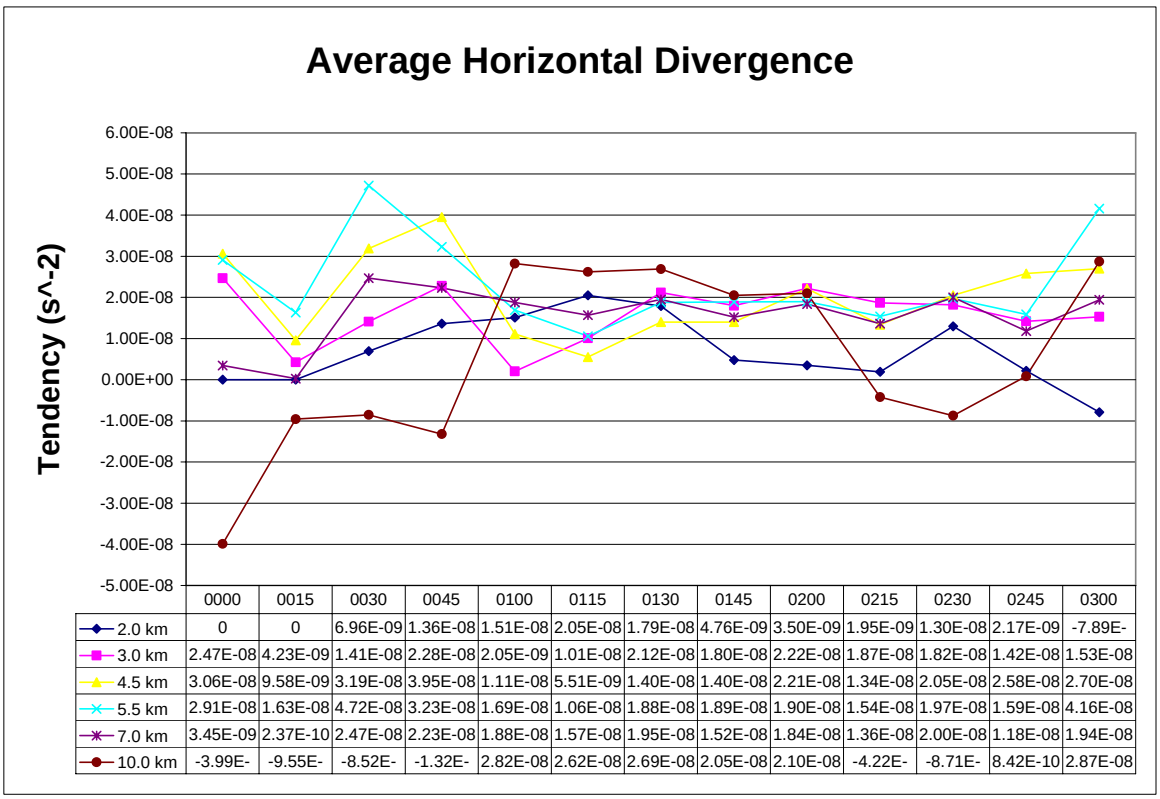

	0000	0015	0030	0045	0100	0115	0130	0145	0200	0215	0230	0245	0300
2.0 km	0	0	6.96E-09	1.36E-08	1.51E-08	2.05E-08	1.79E-08	4.76E-09	3.50E-09	1.95E-09	1.30E-08	2.17E-09	-7.89E-
3.0 km	2.47E-08	4.23E-09	1.41E-08	2.28E-08	2.05E-09	1.01E-08	2.12E-08	1.80E-08	2.22E-08	1.87E-08	1.82E-08	1.42E-08	1.53E-08
4.5 km	3.06E-08	9.58E-09	3.19E-08	3.95E-08	1.11E-08	5.51E-09	1.40E-08	1.40E-08	2.21E-08	1.34E-08	2.05E-08	2.58E-08	2.70E-08
5.5 km	2.91E-08	1.63E-08	4.72E-08	3.23E-08	1.69E-08	1.06E-08	1.88E-08	1.89E-08	1.90E-08	1.54E-08	1.97E-08	1.59E-08	4.16E-08
7.0 km	3.45E-09	2.37E-10	2.47E-08	2.23E-08	1.88E-08	1.57E-08	1.95E-08	1.52E-08	1.84E-08	1.36E-08	2.00E-08	1.18E-08	1.94E-08
10.0 km	-3.99E-	-9.55E-	-8.52E-	-1.32E-	2.82E-08	2.62E-08	2.69E-08	2.05E-08	2.10E-08	-4.22E-	-8.71E-	8.42E-10	2.87E-08

Figure 3.21. Average horizontal divergence of vertical vorticity at 2.0, 3.0, 4.5, 5.5, 7.0 and 10.0 km as a function of time.

Fig. 3.22 shows the average vertical advection of vertical velocity as a function of time. At 0000 UTC, the values at different altitudes are notably different in a random sense, which again suggests that the data at this time are unreliable for vorticity budget analyses. At 2.0 and 3.0 km there is generally less than 2.0 x 10^{-8} s^{-2} of vertical advection of vorticity, which is a relatively small contribution in relation to the other terms of the vorticity tendency equation. There is also negative vertical advection of vorticity at 10.0 km at 0115 and 0130 UTC, which may explain why the MCV failed to extend to that altitude.

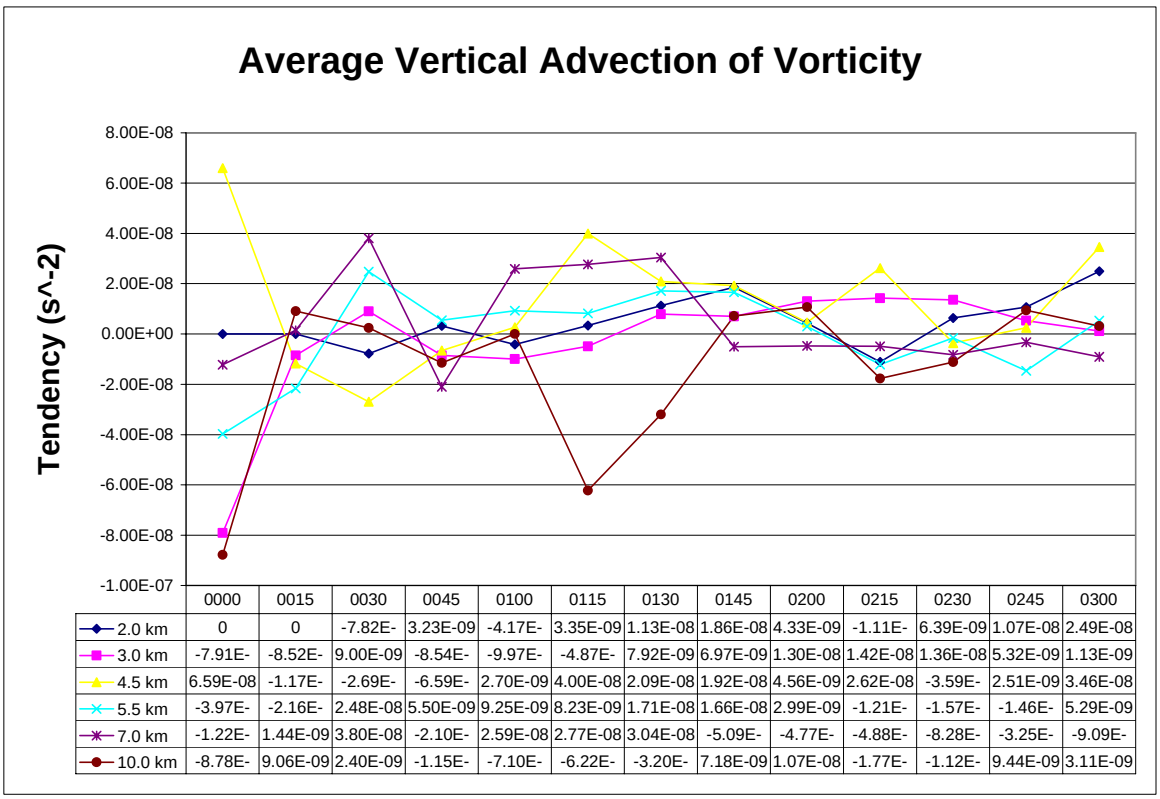

	0000	0015	0030	0045	0100	0115	0130	0145	0200	0215	0230	0245	0300
2.0 km	0	0	-7.82E-	3.23E-09	-4.17E-	3.35E-09	1.13E-08	1.86E-08	4.33E-09	-1.11E-	6.39E-09	1.07E-08	2.49E-08
3.0 km	-7.91E-	-8.52E-	9.00E-09	-8.54E-	-9.97E-	-4.87E-	7.92E-09	6.97E-09	1.30E-08	1.42E-08	1.36E-08	5.32E-09	1.13E-09
4.5 km	6.59E-08	-1.17E-	-2.69E-	-6.59E-	2.70E-09	4.00E-08	2.09E-08	1.92E-08	4.56E-09	2.62E-08	-3.59E-	2.51E-09	3.46E-08
5.5 km	-3.97E-	-2.16E-	2.48E-08	5.50E-09	9.25E-09	8.23E-09	1.71E-08	1.66E-08	2.99E-09	-1.21E-	-1.57E-	-1.46E-	5.29E-09
7.0 km	-1.22E-	1.44E-09	3.80E-08	-2.10E-	2.59E-08	2.77E-08	3.04E-08	-5.09E-	-4.77E-	-4.88E-	-8.28E-	-3.25E-	-9.09E-
10.0 km	-8.78E-	9.06E-09	2.40E-09	-1.15E-	-7.10E-	-6.22E-	-3.20E-	7.18E-09	1.07E-08	-1.77E-	-1.12E-	9.44E-09	3.11E-09

Figure 3.22. Average vertical advection of vertical vorticity at 2.0, 3.0, 4.5, 5.5, 7.0 and 10.0 km as a function of time.

Fig. 3.23 shows the average tilting term of vertical vorticity as a function of time. Before 0100 UTC, while the average tilting term of vorticity at all other altitudes is negative, at 4.5 km it is positive and consistent for three time periods: 0015 (1.97×10^{-8} s^{-2}), 0030 (1.95×10^{-8} s^{-2}), and 0045 UTC (1.63×10^{-8} s^{-2}). The magnitudes of the tendencies associated with the tilting term are less than those found for the tendency terms of horizontal advection and divergence. The consistency of calculations for the tilting term at 4.5 km at these times suggests that the phenomena are real and not a result of the number of data points used in the calculation of the average terms. Of interest is the 4.05×10^{-8} s^{-2} tilting term which occurs at 10.0 km at 0115 UTC. This was also the time and location of interest of negative vertical advection of vorticity seen in Fig. 3.22.

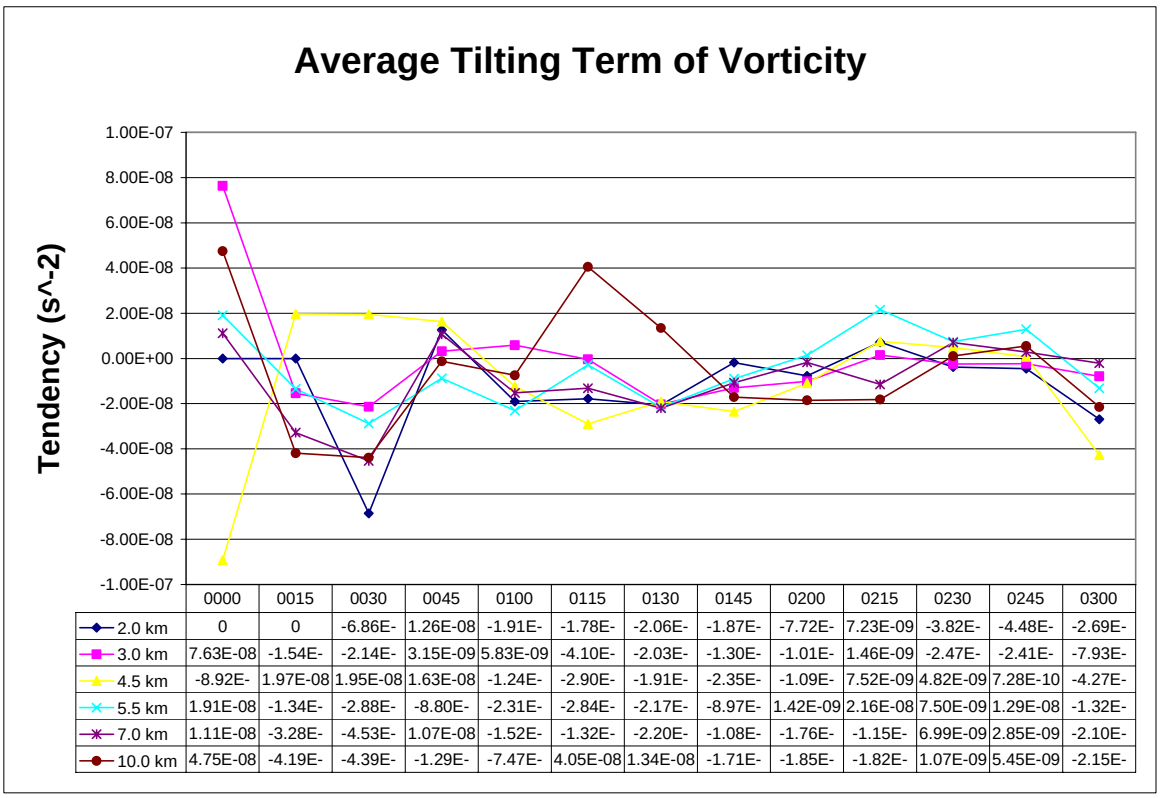

	0000	0015	0030	0045	0100	0115	0130	0145	0200	0215	0230	0245	0300
2.0 km	0	0	-6.86E-	1.26E-08	-1.91E-	-1.78E-	-2.06E-	-1.87E-	-7.72E-	7.23E-09	-3.82E-	-4.48E-	-2.69E-
3.0 km	7.63E-08	-1.54E-	-2.14E-	3.15E-09	5.83E-09	-4.10E-	-2.03E-	-1.30E-	-1.01E-	1.46E-09	-2.47E-	-2.41E-	-7.93E-
4.5 km	-8.92E-	1.97E-08	1.95E-08	1.63E-08	-1.24E-	-2.90E-	-1.91E-	-2.35E-	-1.09E-	7.52E-09	4.82E-09	7.28E-10	-4.27E-
5.5 km	1.91E-08	-1.34E-	-2.88E-	-8.80E-	-2.31E-	-2.84E-	-2.17E-	-8.97E-	1.42E-09	2.16E-08	7.50E-09	1.29E-08	-1.32E-
7.0 km	1.11E-08	-3.28E-	-4.53E-	1.07E-08	-1.52E-	-1.32E-	-2.20E-	-1.08E-	-1.76E-	-1.15E-	6.99E-09	2.85E-09	-2.10E-
10.0 km	4.75E-08	-4.19E-	-4.39E-	-1.29E-	-7.47E-	4.05E-08	1.34E-08	-1.71E-	-1.85E-	-1.82E-	1.07E-09	5.45E-09	-2.15E-

Figure 3.23. Average tilting term of vertical vorticity at 2.0, 3.0, 4.5, 5.5, 7.0 and 10.0 km as a function of time.

Fig. 3.24 shows the average sum of the four terms from the vorticity tendency equation as a function of time. At 2.0 km from 0030 to 0045 UTC, there are relatively strong total tendencies (5.56×10^{-8} s^{-2} and 1.05×10^{-7} s^{-2}). This is predominantly caused by the average horizontal advection of vertical vorticity at 2.0 km at these two times. The average sum of the vorticity budget terms is also negative at 10.0 km before 0045 UTC and from 0200 UTC on. This should be expected at an altitude where anticyclonic rotation associated with upper level outflow would be occurring (Raymond and Jiang 1990; Brandes 1990; Verlinde and Cotton 1990; Knievel and Johnson 2002).

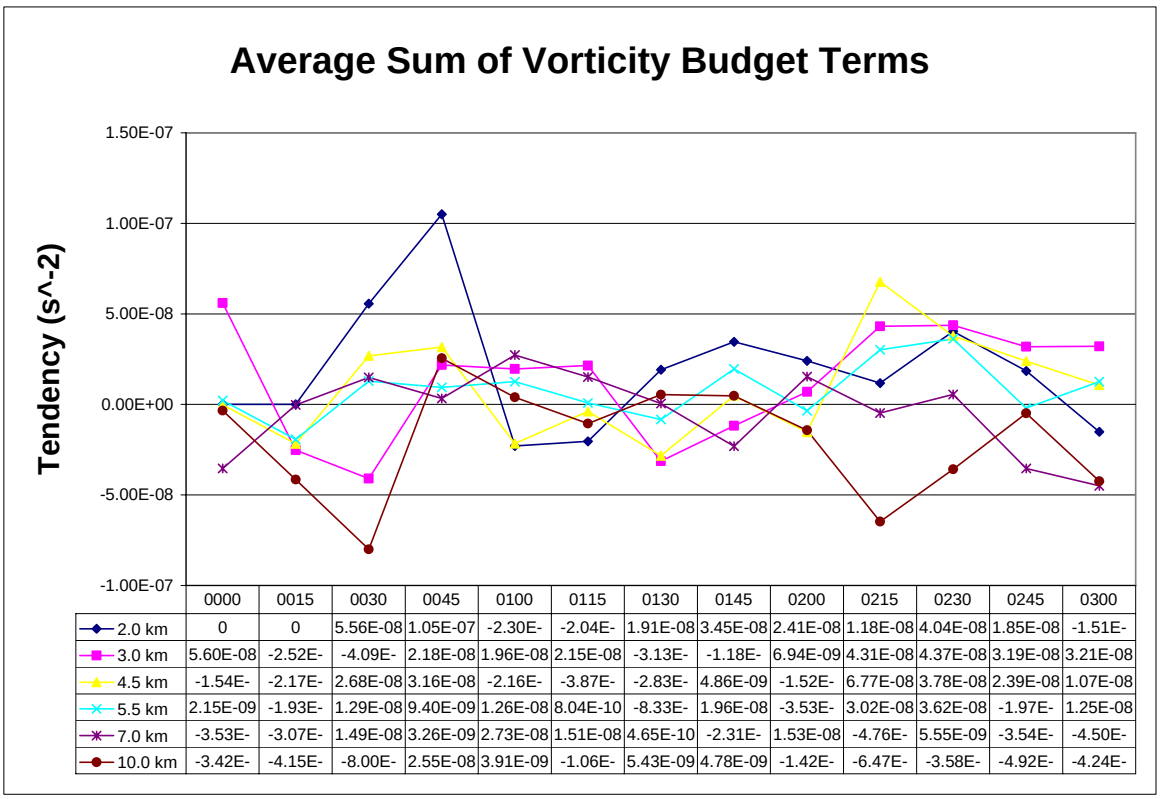

	0000	0015	0030	0045	0100	0115	0130	0145	0200	0215	0230	0245	0300
2.0 km	0	0	5.56E-08	1.05E-07	-2.30E-	-2.04E-	1.91E-08	3.45E-08	2.41E-08	1.18E-08	4.04E-08	1.85E-08	-1.51E-
3.0 km	5.60E-08	-2.52E-	-4.09E-	2.18E-08	1.96E-08	2.15E-08	-3.13E-	-1.18E-	6.94E-09	4.31E-08	4.37E-08	3.19E-08	3.21E-08
4.5 km	-1.54E-	-2.17E-	2.68E-08	3.16E-08	-2.16E-	-3.87E-	-2.83E-	4.86E-09	-1.52E-	6.77E-08	3.78E-08	2.39E-08	1.07E-08
5.5 km	2.15E-09	-1.93E-	1.29E-08	9.40E-09	1.26E-08	8.04E-10	-8.33E-	1.96E-08	-3.53E-	3.02E-08	3.62E-08	-1.97E-	1.25E-08
7.0 km	-3.53E-	-3.07E-	1.49E-08	3.26E-09	2.73E-08	1.51E-08	4.65E-10	-2.31E-	1.53E-08	-4.76E-	5.55E-09	-3.54E-	-4.50E-
10.0 km	-3.42E-	-4.15E-	-8.00E-	2.55E-08	3.91E-09	-1.06E-	5.43E-09	4.78E-09	-1.42E-	-6.47E-	-3.58E-	-4.92E-	-4.24E-

Figure 3.24. Average sum of terms from the vorticity tendency equation at 2.0, 3.0, 4.5, 5.5, 7.0 and 10.0 km as a function of time.

4. DISCUSSION

4.1 Discussion of MCV Evolution

The discussion section is organized into three consecutive times of MCV evolution: 0000 to 0045 UTC, 0100 to 0145 UTC, and 0200 to 0300 UTC. The first period can be characterized as the time when genesis of the 11 June 2003 MCV occurred. The second period can be described as continued genesis and strengthening of the vortex, while the final hour of investigation is characterized by complete MCS maturity and an enlarging MCV. The main characteristics of how the 11 June 2003 MCV originated and evolved are discussed herein synthesizing qualitative characteristics of dual-Doppler analyses and vorticity contours and quantitative results of time series and vorticity budget analyses presented in Section 3.

4.1.1 MCV Evolution during 0000 to 0045 UTC

During the time period of 0000 to 0045 UTC, generation of the 11 June 2003 MCV occurred. At early time periods (0000 and 0015 UTC) Fig. 3.1 shows that the area of the MCS within the dual-Doppler lobe is predominantly convective. The time series (Figs. 3.12 and 3.13) show that at 0000 UTC there were 5663 total data points at an altitude of 2.0 km with 767 of those points being convective. At 0015 UTC, there were 5725 total data points with 928 of those points being convective. At this altitude, the percentage of convective data points was 13.5% and 16.2%, respectively. These values are slightly higher than the average 10% of rain area in MCSs covered by convective rain (Houze 1993). It should be noted, however, that the average reported by Houze 1993 is for all levels within an MCS with lower than 10% averages of convective points at higher

altitudes. The percentage of an MCS that is convective varies and can change due to the location of the MCS (oceanic versus continental) and also within the lifecycle of the MCS. The development of the stratiform rain region during this time period also suggests that the MCS itself was entering a mature phase as the MCV began to generate.

The characteristics of the MCS within which the MCV developed during this time period were also conducive to its formation. At 5.5 km from 0000 to 0030 UTC, before the MCV extended to this altitude at 0045 UTC (Fig. 3.4), convergence, which is often a precursor to rotation, occurred in the stratiform region behind the transition zone (see Fig. 1.3; Biggerstaff and Houze 1991). This convergence at 5.5 km can also be seen in the time series of divergence (Fig. 3.15). At 7.0 km during this time period only convergence occurred with no indication of circulation associated with the MCV at least in dual-Doppler analyses. Divergence from upper-level outflow at 10.0 km suggests that the MCV may eventually extend up to 7.0 km but not to 10.0 km.

The development of cyclonic circulation associated with the MCV occurred mainly during this time period. The first indication of mesoscale circulation associated with the MCV appeared at 0015 UTC at 3.0 km with a weak but closed circulation immediately behind the convective line (see Fig. 3.2). Davis and Trier (2007) suggested that there might have been a remnant of an MCV which formed during the previous evening of 10 June 2003 that may have provided the right conditions for another MCV to form. However, their analysis did not detect an MCV until 0600 UTC (Fig. 1.9). The genesis of an MCV from the convective line in the Yu et al. (1999) case also started and was strongest at 2.5 km, which is consistent with what was observed for this case. Just a half an hour later at 0045 UTC, the MCV extended down to 1.0 km and up to 5.5 km

(Figs. 3.1, 3.4, and 3.5). Vertical transects also show that the area of 1 x 10^{-4} s^{-1} vorticity expanded and deepened significantly from 0015 to 0045 UTC (Figs. 3.10 and 3.11). Mean vertical vorticity also increased slightly during this time period for all levels except 10.0 km (Fig. 3.16).

The vorticity within the convective line is shown to advect rearward in a storm-relative sense into the stratiform region. At 0000 UTC at 1.0 km, horizontal contours of vorticity show 5 x 10^{-3} s^{-1} vertical vorticity associated within a 50 dBZ convective core located at ($-20.0 < x < -10.0$, $y = 95.0$) (Fig. 3.1). At 0000 UTC at 3.0 km, cyclonic rotation was forming in a hook-like appendage which extended back into the stratiform region (Fig. 3.2). This also occurred at 4.5 km at 0000 and 0015 UTC (Fig. 3.3). Although no mesoscale circulation had generated yet in the stratiform region, wind vectors closely followed the curve of the 40 dBZ reflectivity from the convective line back into the stratiform region. There was also a region of 1 x 10^{-5} s^{-1} to 1 x 10^{-4} s^{-1} vertical vorticity which is associated with the 40 dBZ hook at 4.5 km (Fig. 3.3). There were four to five regions of enhanced vorticity associated with the convective line located at $0.0 < x < 20.0$ and $65.0 < y < 80.0$ at 4.5 km at 0015 which were advected north northwest and likely formed the "tail" of enhanced vorticity (1 x 10^{-3} s^{-1}) leading into the MCV at 0030 UTC located at ($x = -10.0$, $y = 80.0$). The highest average values of vertical vorticity are at 2.0 km during this time period, suggesting that vorticity is being generated at low-levels from the convective line.

During this time period, the vorticity budget analyses suggest that generation of low-level vorticity from the convective line is advected rearward and stretched in the stratiform region to generate the MCV. The horizontal advection term (HADV) is

greatest at 2.0 km for 0030 UTC (1.25 x 10^{-7} s^{-2}) and 0045 UTC (7.55 x 10^{-8} s^{-2}). The horizontal advection tendency term is given as follows:

$$\text{HADV} = -\left(u\frac{\partial \zeta}{\partial x} + v\frac{\partial \zeta}{\partial y} \right) \tag{4.1}$$

If rearward (westward) storm relative flow is assumed, as is shown in previous storm-relative dual-Doppler analyses (i.e., Fig. 3.1), then v = 0 and u is negative. In this frame of reference, vorticity is greater in the convective line than where it is being advected to and the $\partial\zeta/\partial x$ term is positive resulting in a positive value of HADV. Stretching of vertical vorticity also occurs at all levels except for 10.0 km before 0100 UTC. The horizontal divergence tendency term (stretching term) is strongest at 5.5 km at 0030 UTC (4.72 x 10^{-8} s^{-2}). These two characteristics suggest that during this time period vertical vorticity is advected rearward from the convective line at low-levels and then stretched in the stratiform region to generate the MCV. The vertical advection tendency term (VADV) is given as follows:

$$\text{VADV} = -w\frac{\partial \zeta}{\partial z} \tag{4.2}$$

Average vertical velocity during this time period is positive so the differential term must be negative for positive tendency of this term to occur. At 5.5 and 7.0 km this is true as there are higher levels of vertical vorticity in mid- to low-levels of the atmosphere. The vertical advection tendency term at 5.5 km is approximately 2.0 x 10^{-8} s^{-2} before 0200 UTC and becomes negative with magnitudes less than 2.0 x 10^{-8} s^{-2} after. At 7.0 km altitude, the vertical advection tendency term is close to zero except for the time period of 0030 to 0130 UTC when it reaches up to 4.0 x 10^{-8} s^{-2}. At low-levels (2.0 and 3.0 km), there is generally less than 2.0 x 10^{-8} s^{-2} of vertical advection of vorticity (Fig. 3.22). This

suggests that stretching, not vertical advection of vorticity, at low-levels occurs in the stratiform region to increase vorticity at mid-levels. At 0030 and 0045 UTC, the most noticeable change in the vorticity tendency equation occurred at 2.0 km (5.56×10^{-8} s^{-2} and 1.05×10^{-7} s^{-2}, respectively). The largest contribution came from the HADV term (up to an order of 1×10^{-7} s^{-2}), while the second largest contribution came from the stretching term (HDIV) (approximately 2×10^{-8} s^{-2}).

The vorticity budgets suggest that different terms of the tendency equation dominate at different levels within the developing MCV. At low levels, the horizontal advection tendency term followed by the horizontal divergence (or stretching) tendency term dominates. At mid-levels, the stretching term dominates, followed by vertical advection and then the tilting tendency term. At upper-levels, there is a negative contribution of the vertical advection tendency term, and a positive contribution of the tilting tendency term.

These results both confirm and extend the knowledge of previous studies of MCVs. Zhang (1992) found that a mature MCV strengthened from convergence and stretching of vertical vorticity. Bartels and Maddox (1991) concluded that MCVs could also be explained by the stretching term of the vorticity equation. The results of this study confirm their finding but also suggest how initial vertical vorticity is generated and moved to the stratiform region where it can be stretched to mid-levels for MCV genesis. Brandes (1990) found that stretching of pre-existing vorticity seemed to be the primary amplification mechanism at mid-levels, which is also supported by these results, however, stretching of vertical vorticity also appears to be occurring at low-levels.

Yu et al. (1999) found that contrary to previously documented MCVs, which have generally been fully developed and observed in the stratiform region of mature MCSs, the vorticity budgets suggested that the mechanisms responsible for the formation of a long-lived MCV are related to the convective, rather than stratiform, precipitation of the developing MCS. According to domain averaged vorticity budgets, Yu et al. (1999) concluded that vertical stretching in the convective region was a primary mechanism contributing to the development of a vortex at low-levels and that the source of vertical vorticity contributing to the initiation of the MCV was likely tilting of horizontal vorticity in the convective region. Due to limitations of horizontal grid resolution of this study (3.0 km), convective scales are unable to be resolved, but it appears that tilting of horizontal vorticity by convective updrafts initially forms the vertical vorticity within the convective line, which is subsequently advected rearward and stretched into an MCV.

4.1.2 MCV Evolution during 0100 to 0145 UTC

During the next time period of 0100 to 0145 UTC, the MCV, which was generated in the previous hour, continued to strengthen through the additional stretching of pre-existing vorticity. At 0100 and 0115 UTC, the MCV developed a 40 km diameter in the stratiform region adjacent to the convective line ($-15.0 < x < 25.0$, $60.0 < y < 100.0$) at 1.0 km. At 0045 at 3.0 km the MCV also had a diameter of approximately 40 km, which suggests that the MCV descended down to 1.0 km at 0100 UTC. By 0130 UTC at 3.0 km, the MCV was centered at approximately (0.0, 50.0) but had an elliptical shape and southwest to northeast orientation. By this time, the circulation at 3.0 km was too large to be captured entirely within the dual-Doppler lobe. By 0145 UTC, the MCV had an elliptical shape at 1.0 km and also was not fully enclosed within the analysis

domain (at least from subjective analysis of Figure 3.1) which suggests that the area of the MCV increased to larger than the size of the dual-Doppler lobe so that southwestern portions of the MCV were no longer visible within the analysis domain. At 4.5 km at 0145 UTC, decaying cells from the convective line located at (50.0, 127.0) and (28.0, 135.0) still appeared to feed back into the broader circulation associated with the MCV and carried maximum values of vertical vorticity of 7 x 10^{-4} s^{-1} into the MCV, which had a maximum value of vertical vorticity at this time of 1 x 10^{-3} s^{-1}.

The MCV also grew horizontally and extended vertically at mid-levels during this time period. By 0145 UTC, the MCV at 5.5 km was located from approximately -60.0 < x < 10.0 and 40.0 < y < 100.0. At this height, initiation of the MCV started at 0045 UTC and in just an hour covered an area of approximately 3300 km^2. At 7.0 km, convergence was present at times up to 0130 UTC in the general area of where the MCV initiated. At 0145 UTC, there was a suggestion of mesoscale cyclonic circulation at the edge of the dual-Doppler lobe. It took much longer for the MCV to extend up to 7.0 km; the MCV initiated at 3.0 km at 0015 UTC and extended vertically to 1.0 and 5.5 km by 0045 UTC. During this time period, vertical transects show that vertical vorticity associated with the MCV expanded both horizontally and vertically as it grew. However, while horizontal expansion continued at 0145 UTC, the vorticity associated with the MCV did not expand above 9.0 km. The failure of the MCV to expand any farther vertically can be explained by the negative sum of vorticity tendency at upper-levels that caused the development of an anticyclone aloft.

The vorticity budgets during this time period suggest that once the MCV was established, it continued to strengthen by continued stretching of pre-existing vorticity.

Average vorticity at these times was consistently cyclonic (generally between 1.0 to 1.5 x 10^{-4} s^{-1}) for all altitudes except 10.0 km where anticyclonic rotation occurred. All altitudes also had positive average vertical velocity during this time period. The vorticity budgets reveal that the stretching term and vertical advection tendency term were generally positive, while the horizontal advection term and tilting term were generally negative. However, the horizontal advection term could turn negative and still indicate rearward advection of vorticity if vorticity in the MCV was greater than that in the convective line. During this time period, there were the most number of points available to calculate the vorticity budgets. The positive stretching term at 10.0 km may suggest how the MCV was able to expand vertically at least up to 7.0 km. However, this could have been opposed by negative vertical advection tendency at 0115 (-6.22 x 10^{-8} s^{-2}) and 0130 UTC (-3.20 x 10^{-8} s^{-2}). Vertical vorticity appeared to be increasing with height and vertical velocity was positive but vertical advection of vorticity was negative, which may be one explanation for why the MCV extended up to 7.0 km an hour after it appeared at 5.5 km. These results agree with the findings of Zhang (1992) in which a mature MCV strengthened from convergence, although these results suggest that horizontal advection and stretching instead of tilting caused the initiation of the MCV. Knievel and Johnson (2003) also suggested that tilting was responsible for MCV initiation, but they examined an already mature MCV and were not able to account for MCV genesis.

4.1.3 MCV Evolution during 0200 to 0300 UTC

During the final period of investigation, dual-Doppler analyses, horizontal and vertical contours of vorticity, and time series reflect what occurred in the stratiform region of the mature MCS and enlarging MCV. At 1.0 km, the MCV retained its elliptical

shape, and while the center of the MCV was still within the northwestern dual-Doppler lobe, by this time it appeared that the MCV had grown large enough that not all (particularly southwestern) portions of the MCV were captured in the analysis domain. Also by this time period, the MCV was well within the stratiform region of the MCS. The MCV continued to propagate eastward but not at the same rate as the leading convective line, therefore it appeared to move rearward in an MCS-relative sense. At 0245 UTC, the center of the MCV was located at approximately (25.0, 55.0). The independent movement of an MCV relative to its parent MCS has been documented before by Raymond and Jiang (1990) and Fritsch et al. (1994) and appears to be a characteristic of long-lived MCVs. At 5.5 km, the flow became convergent again at 0215 UTC. Averages for the time series were taken over the entire domain of the MCS. The number of convective points within the domain decreased rapidly after 0200 UTC (Fig. 3.13) but the number of stratiform points continued to increase (Fig. 3.14). The convergent result at 5.5 km therefore is likely an indication of convergence in the stratiform region associated with MCV spin up (Johnson and Bartels 1992). After 0200 UTC, the flow became cyclonic again at 10.0 km. One would expect anticyclonic flow at this level associated with a negative PV anomaly (Raymond and Jiang 1990; Brandes 1990; Verlinde and Cotton 1990). However, the MCV has likely expanded beyond the bounds of the dual-Doppler analysis domain at this time and the results of averaging for the time series may reflect that. There is also a suggestion of mesoscale downdraft development, which signifies a mature MCS (Biggerstaff and Houze 1992), at later times. After 0200 UTC, average vertical velocity at 2.0 km became negative and might suggest the development of a mesoscale downdraft. The downdraft formed at and below the melting level, as is

expected as the stratiform region develops and matures due to the cooling of midtropospheric environmental air by melting and evaporation of hydrometeors as they descend through the stratiform cloud (Houze 2004). Positive vertical velocity also became negative at 0215 for 3.0 and 4.5 km. This could also be the result of averaging over a greater percentage of stratiform points within the dual-Doppler lobe. The development of a mature MCS with a mesoscale downdraft provides evidence of the conduciveness of environment in which the MCV generated to its formation.

During this time period, the characteristics of the MCV and MCS environment became more homogeneous at 3.0, 4.5, and 5.5 km. At 0245 UTC, there was another small vortex at approximately (49.0, -10.0) in a reflectivity hook near KTLX (0.0, 0.0) at 3.0 (Fig. 3.2), 4.5 (Fig. 3.3), and 5.5 km altitude (Fig. 3.4). Although the analysis region limits what can be said about where this vortex moved in a storm-relative sense, if it followed a similar pattern to what occurred with vorticity generated farther north in the convective line (resolved by dual-Doppler domain), then it would move rearward and eventually become incorporated into the growing MCV. At 4.5 km the diameter across the longest region of the elliptical MCV was approximately 100 km. The extent of the MCV was larger aloft than at the surface as seen by Chen and Frank (1993) and Johnson and Bartels (1992), among others. The banded structure of reflectivity also became apparent at 10.0 km starting at 0200 UTC. These were also a result of data gaps due to decreasing vertical coverage of scanning elevation angles at greater heights. Even with this banded structure within the reflectivity, divergent flow, which is expected near the anvil (Houze 1989; Biggerstaff and Houze 1991), did not appear to be affected.

Horizontal and vertical transects of vertical vorticity also give an improved qualitative sense of how the MCV evolved during this time period. Although the MCV was seen from subjective analysis of dual-Doppler reflectivity and storm-relative wind vectors at 0145 UTC, the MCV clearly strengthened at 7.0 km from 0200 and 0215 to 0230 and 0245 UTC centered approximately at (27.0, 115.0) in Figure 3.5. From the North-South vertical transects, the MCV did not extend much above 10.0 km but did continue to expand horizontally. If it is assumed that an MCV can be defined by a 1.0 x 10^{-4} s^{-1} contour (as done by Scott and Rutledge 1995), at 0230 and 0245 UTC, the MCV extended to approximately 100 km at the surface. In contrast, the East-West transects show a much "thinner" slice of the vortex (horizontal diameter of approximately 50.0 km), which is the result of the elliptical shape of the MCV.

The vorticity budgets during the time period of 0200 to 0300 UTC began to resemble previous studies of vorticity budgets of mature MCVs. From 0200 UTC on, the number of data points used to calculate the vorticity budgets decreased but remained above 500 points at all levels. Starting at 0230 UTC, the number of data points at 10.0 km became less than that at 2.0 km which is likely due to the MCS moving through the dual-Doppler lobe and the area remaining in the analysis domain being predominantly stratiform. The appearance of an "S-curve", which is an indication of negative vertical vorticity tendency at mid- to upper-levels and positive vertical vorticity tendency at low- to mid-levels, in the sum terms is suggested at 0200 UTC and is well established from 0215 UTC on. The sum of the tendency terms is positive below 6.5 (0215 UTC), 7.0 (0230 UTC) and 5.5 km (0245 UTC) and negative above which indicates likelihood of the formation of a cyclonic MCV below and anticyclone aloft above the level where the

sum of the tendency terms changes sign (Knievel and Johnson 2003). The HADV term was basically positive at mid- to low-levels (except at 3.0 to 4.0 km at 0245 UTC) and also highest at 2.0 km which suggests that vertical vorticity may still have been advected rearward into the stratiform region to be stretched vertically. The HDIV term was also generally positive while the VADV term was either small or negative during this time period which also supports rearward horizontal advection and stretching of vertical vorticity as the main mechanism for generating and maintaining the MCV. However the tilting term was generally negative which appears to contradict what Brandes (1990) and Zhang (1992) found that tilting of vorticity at low-levels caused MCV formation. These studies assumed that horizontal vorticity rolls were the initial source of vorticity that needed to be turned vertically by convective updrafts to generate an MCV. However, the results presented in this study suggest that vertical vorticity already existed within the convective line and requires rearward horizontal advection and stretching to form and subsequently strengthen an MCV.

5. CONCLUSIONS

The three main objectives of this investigation and corresponding main conclusions are given below.

5.1 Document Mesoscale Development of 11 June 2003 MCV

- The genesis of the 11 June 2003 MCV occurred at approximately 0015 UTC at 3.0 km altitude and expanded vertically to 1.0 km and 5.5 km in half an hour. The longest extent of the MCV at the surface during the 0000 to 0300 UTC time period was approximately 100.0 km.
- Vertical vorticity was clearly generated in the convective line although the convective scale process for how this exactly occurred could not be resolved.
- In the last hour, the MCV began to exhibit features as seen in previous studies of mature MCVs, such as independent movement from its parent MCS (Raymond and Jiang 1990; Fritsch et al. 1994), while still remaining in the stratiform region.

5.2 Document Quantitative Changes in Reflectivity, Divergence, Vorticity, and Vertical Velocity within MCS

- The number of stratiform reflectivity points in the MCS steadily increased, suggesting the maturity of the MCS with the appearance of a growing stratiform rain region.
- Convergence was strongest at 4.5 and 3.0 km altitude where the magnitude of vertical vorticity associated with the MCV was strongest.

- Average vorticity over the entire dual-Doppler domain increased for low- to mid-levels, which suggests the continued development and strengthening of the MCV.
- The development of a mesoscale downdraft at low-levels in the last hour of analysis also signified MCS maturity.

5.3 Investigation of Generation of Vertical Vorticity within MCV

- It appears that tilting of horizontal vorticity by convective updrafts initially forms the vertical vorticity within the convective line, which is subsequently advected rearward and stretched into an MCV. This is consistent with what Bartels and Maddox (1991) concluded that MCVs could be explained by the stretching term of the vorticity tendency equation, but suggests how initial vertical vorticity is generated.
- The MCV, which established itself in the first hour, strengthened in magnitude and increased in volume likely through continued stretching of pre-existing vertical vorticity which was advected into the stratiform region.
- The appearance of an "S-curve" in vorticity budgets, which indicate formation of cyclonic rotation below from positive tendency terms and anticyclonic rotation above from negative tendency terms, occurred in the last hour of analysis and showed the continued development and maturity of the MCV (Scott and Rutledge 1995; Yu et al. 1999; Knievel and Johnson 2003).

Future work involves a further investigation of the MCS within which the MCV developed, including vertical profiles of averaged divergence, vorticity, and vertical velocity and perhaps contoured-frequency-with-altitude diagrams (CFADs) (Yuter and Houze 1995) to give a better 3-D description of what occurs within the MCS. WSR-88D data is recorded and archived daily. It is clear that this technique can be used in the future as well by other investigators to study mesoscale phenomena that occur in central and eastern Oklahoma within the dual-Doppler lobes of the KTLX and KINX radars.

REFERENCES

Bartels, D. L., and R. A. Maddox, 1991: Midlevel cyclonic vortices generated by mesoscale convective systems. *Mon. Wea. Rev.*, **119,** 104-118.

Biggerstaff, M. I., and R. A. Houze Jr., 1991: Kinematic and precipitation structure of the 10-11 June 1985 squall line. *Mon. Wea. Rev.*, **119,** 3034-3065.

Blanchard, D. O., 1990: Mesoscale convective patterns of the Southern High Plains. *Bull. Amer. Meteor. Soc.*, **71,** 994-1005.

Bluestein, H. B., S. D. Hrebenach, C.-F. Chang, and E. A. Brandes, 1994: Synthetic dual-Doppler analysis of mesoscale convective systems. *Mon. Wea. Rev.*, **122,** 2105-2124.

Brandes, E. A., 1990: Evolution and structure of the 6–7 May 1985 mesoscale convective system and associated vortex. *Mon. Wea. Rev.*, **118**, 109–127.

Brown, P. S., 1976: Sources of computational instability in numerical solution of the Stochastic collection equation. *J. Atmos. Sci.*, **33**, 1375-1378.

Chen, S. S., and W. M. Frank, 1993: A numerical study of the genesis of extratropical convective mesovortices. Part I: Evolution and dynamics. *J. Atmos. Sci.*, **50**, 2401-2426.

Cressman, G. P., 1959: An operational objective analysis system. *Mon. Wea. Rev.*, **87,** 367-374.

Crum, T. D., R. L. Alberty, and D. W. Burgess, 1993: Recording, archiving, and using WSR-88D data. *Bull. Amer. Meteor. Soc.*, **74**, 645-653.

Davies-Jones, R. P., 1979: Dual-Doppler radar coverage area as a function of measurement accuracy and spatial resolution. *J. Appl. Meteor.*, **18,** 1229-1233.

Davis, C. A., and M. L. Weisman, 1994: Balanced dynamics of mesoscale vortices produced in simulated convective systems. *J. Atmos. Sci.*, **51**, 2005-2030.

_____, D. A. Ahijevych, and S. B. Trier, 2002: Detection and prediction of warm season, midtropospheric vortices by the Rapid Update Cycle. *Mon. Wea. Rev.*, **130,** 24-42.

_____, N. Atkins, D. Bartels, L. Bosart, M. Coniglio, G. Bryan, W.Cotton, D. Dowell, B. Jewett, R. Johns, D. Jorgensen, J. Knievel, K. Knupp, W.-C. Lee, G. McFarquhar, J. Moore, R. Przybylinski, R. Rauber, B. Smull, J. Trapp, S. Trier, R. Wakimoto, M. Weisman, and C. Ziegler, 2004: The Bow-Echo And MCV Experiment (BAMEX): Observations and opportunities, *Bull. Amer. Meteor. Soc.*, **85**, 1075-1093.

_____, and S. B. Trier, 2007: Mesoscale convective vortices observed during BAMEX. Part I: Kinematic and thermodynamic structure. *Mon. Wea. Rev.*, **135,** 2029-2049.

Doviak, R. J., P. S. Ray, R. G. Strauch, and L. J. Miller, 1976: Error estimation in wind fields derived from dual-Doppler radar measurements. *J. Appl. Meteor.*, **15,** 868-878.

Galarneau, T. J., and L. F. Bosart, 2005: An examination of the long-lived MCV of 10-13 June 2003. *Preprints, 11th AMS Conference on Mesoscale Processes*. Am. Meteor. Soc. Paper JP5J.7.

Gunn, R., and G. D. Kinzer, 1949: The terminal velocities of fall for water droplets in stagnant air. *J. Meteor.*, **6,** 243-248.

Fritsch, J. M., R. J. Kane, and C. R. Chelius, 1986: The contribution of mesoscale convective weather systems to the warm-season precipitation in the United States. *J. Appl. Meteor.*, **25,** 1333-1345.

_____, J. D. Murphy, and J. S. Kain, 1994: Warm core vortex amplification over land. *J. Atmos. Sci.*, **51**, 1780-1807.

Fujita, T.T., 1978: Manual of downburst identification for project NIMROD. Satellite and Mesometeorology Research Paper No. 156, Department of Geophysical Sciences, University of Chicago, 104 pp.

Houze, R. A. Jr., S. A. Rutledge, M. I. Biggerstaff, and B. F. Smull, 1989: Interpretation of Doppler radar displays of midlatitude mesoscale convective lines. *Bull. Amer. Meteor. Soc.*, **70,** 608-619.

_____, B. F. Smull, and P. Dodge, 1990: Mesoscale organization of springtime rainstorms in Oklahoma. *Mon. Wea. Rev.*, **118,** 613-654.

_____, 1993: *Cloud Dynamics*. Academic, San Diego, CA, 573 pp.

_____, 2004: Mesoscale convective systems. *Reviews of Geophysics*, **42**, RG4003, doi:10.1029/2004RG000150.

Johnson, R. H., and D. L. Bartels, 1992: Circulations associated with a mature-to-decaying midlatitude mesoscale convective system. Part II: Upper-level features. *Mon. Wea. Rev.*, **120**, 1301-1321.

Knievel, J. C., and R. H. Johnson, 2002: The kinematics of a midlatitude, continental mesoscale convective system and its mesoscale vortex. *Mon. Wea. Rev.*, **130**, 1749-1770.

_____, and R. H. Johnson, 2003: A scale-discriminating vorticity budget for a mesoscale vortex in a midlatitude, continental mesoscale convective system. *J. Atmos. Sci.*, **60**, 781-794.

Leary, C. A., and R. A. Houze Jr., 1979: Melting and evaporation of hydrometeors in precipitation from the anvil clouds of deep tropical convection. *J. Atmos. Sci.*, **36**, 669-679.

Lhermitte, R. M., and L. J. Miller, 1970: Doppler radar methodology for the observation of convective storms. *Preprints 14th Conf. Radar Meteorology*, Tuscon, Amer. Meteor. Soc., 133-138.

Loehrer, S. M., and R. H. Johnson, 1995: Surface pressure and precipitation life cycle characteristics of PRE-STORM mesoscale convective systems. *Mon. Wea. Rev.*, **123,** 600-621.

Mohr, C. G., L. J. Miller, R. L. Vaughan, and H. W. Frank, 1986: The merger of mesoscale datasets into a common Cartesian format for efficient and systematic analyses. *J. Atmos. Oceanic Technol.*, **3**, 143–161.

Nathanson, F. E., 1969: *Radar Design Principles*. McGraw-Hill, New York, NY, 596 pp.

Oye, D. and M. Case, 1995: REORDER: A program for gridding radar data. Research Data program, Atmospheric Technology Division, National Center for Atmospheric Research, Boulder, CO.

Parker, M. D., and R. H. Johnson, 2000: Organizational modes of midlatitude mesoscale convective systems. *Mon. Wea. Rev.*, **128**, 3413-3436.

Raymond, D. J., and H. Jiang, 1990: A theory for long-lived mesoscale convective systems. *J. Atmos. Sci.*, **47**, 3067-3077.

Rinehart, R. E., 2001: *Radar for Meteorologists*. 3d ed. Rinehart Publications, Columbia, MO, 428 pp.

Rutledge, S. A., and D. R. MacGorman, 1988: Cloud-to-ground lightning activity in the 10-11 June 1985 mesoscale convective system observed during the Oklahoma-Kansas PRE-STORM Project. *Mon. Wea. Rev.*, **116**, 1393-1408.

_____, R. A. Houze Jr., M. I. Biggerstaff, and T. Matejka, 1988: The Oklahoma-Kansas mesoscale convective system of 10-11 June 1985: Precipitation structure and single-Doppler radar analysis. *Mon. Wea. Rev.*, **116**, 1409-1430.

_____, C. Lu, and D. R. MacGorman, 1990: Positive cloud-to-ground lightning in mesoscale convective systems. *J. Atmos. Sci.*, **47,** 2085-2100.

Scott, J. D. and S. A. Rutledge, 1995: Doppler radar observations of an asymmetric mesoscale convective system and associated vortex couplet. *Mon. Wea. Rev.*, **123**, 3437-3457.

Sirmans, D., and R. J. Doviak, 1973: Meteorological radar signal intensity estimation. NOAA Tech. Memo. ERL-NSSL 64.

Skamarock, W. C., M. L. Weisman, and J. B. Klemp, 1994: Three-dimensional evolution of simulated long-lived squall lines. *J. Atmos. Sci.*, **51**, 2563-2584.

Smull, B. F., and R. A. Houze Jr., 1985: A midlatitude squall line with a trailing region of stratiform rain: Radar and satellite observations. *Mon. Wea. Rev.*, **113**, 117-133.

Steiner, M., R. A. Houze Jr., and S. E. Yuter, 1995: Climatological characterization of three-dimensional storm structure from operational radar and rain gauge data. *J. Appl. Meteor.*, **34,** 1978-2007.

_____, and J. A. Smith, 2002: Use of three-dimensional reflectivity structure for automated detection and removal of nonprecipitating echoes in radar data. *J. Atmos. Oceanic Technol.*, **19**, 673-686.

Trier, S. B., C. A. Davis, and J. D. Tuttle, 2000: Long-lived mesoconvective vortices and their environment. Part I: Observations from the central United States during the 1998 warm season. *Mon. Wea. Rev.*, **128**, 3376-3395.

_____, and C. A. Davis, 2002: Influence of balanced motions on heavy precipitation within a long-lived convectively generated vortex. *Mon. Wea. Rev.*, **130**, 877-899.

_____, and C. A. Davis, 2007: Mesoscale convective vortices observed during BAMEX. Part II: Influences on secondary deep convection. *Mon. Wea. Rev.*, **135**, 2051-2075.

Verlinde, J., and W. R. Cotton, 1990: A mesoscale vortex couplet observed in the trailing anvil of a multicellular convective complex. *Mon. Wea. Rev.*, **118**, 993-1010.

Wakimoto, R. M., H. V. Murphy, C. A. Davis, and N. T. Atkins, 2006: High winds generated by bow echoes. Part II: The relationship between the mesovortices and damaging straight-line winds. *Mon. Wea. Rev.*, **134**, 2813-2829.

Weisman, M. L., 1993: The genesis of severe, long-lived bow echoes. *J. Atmos. Sci.*, **50**, 645-670.

_____, and C. A. Davis, 1998: Mechanisms for the generation of mesoscale vortices within quasi-linear convective systems. *J. Atmos. Sci.*, **55**, 2603-2622.

Yu, C.-K., B. J.-D. Jou, and B. F. Smull, 1999: Formative stage of a long-lived mesoscale vortex observed by airborne Doppler radar. *Mon. Wea. Rev.*, **127**, 838-857.

Yuter, S. E., and R. A. Houze Jr., 1995: Three-dimensional kinematic and microphysical evolution of Florida cumulonimbus, Part III, Vertical mass transport, mass divergence, and synthesis. *Monthly Weather Review*, **123**, 1964-1983.

Zhang, D.-L., and J. M. Fritsch, 1987: Numerical simulation of the meso-β scale structure and evolution of the 1977 Johnstown flood. Part II: Inertially stable warm-core vortex and the mesoscale convective complex. *J. Atmos. Sci.*, **44**, 2593–2612.

_____, 1992: The formation of a cooling-induced mesovortex in the trailing stratiform region of a midlatitude squall line. *Mon. Wea. Rev.*, **120,** 2763-2785.

VITA

Amber Elizabeth Reynolds received her Bachelor of Science degree in Meteorology from The Pennsylvania State University in 2004. She entered the Atmospheric Science program at Texas A&M University in September 2004 and graduated in December 2007. Her research interests include radar and satellite meteorology and civil engineering as it relates to structural damage caused by severe weather.

Ms. Reynolds may be reached at amber.reynolds@ttu.edu. Written correspondence may be sent to:

Department of Atmospheric Sciences

c/o Dr. Fuqing Zhang

Texas A&M University M.S. 3150

College Station, TX 77843